Max-Planck-Institut
für Meteorologie

MAX-PLANCK-GESELLSCHAFT

International Max Planck Research School
on Earth System Modelling

Atmospheric Chemistry Reactions in a Turbulent Flow: Application to an Urban Environment

Wing Yi Li

Hamburg 2019

Berichte zur Erdsystemforschung
Reports on Earth System Science

217
2019

Hinweis

Die Berichte zur Erdsystemforschung werden vom Max-Planck-Institut für Meteorologie in Hamburg in unregelmäßiger Abfolge herausgegeben.

Sie enthalten wissenschaftliche und technische Beiträge, inklusive Dissertationen.

Die Beiträge geben nicht notwendigerweise die Auffassung des Instituts wieder.

Die "Berichte zur Erdsystemforschung" führen die vorherigen Reihen "Reports" und "Examensarbeiten" weiter.

Notice

The Reports on Earth System Science are published by the Max Planck Institute for Meteorology in Hamburg. They appear in irregular intervals.

They contain scientific and technical contributions, including Ph. D. theses.

The Reports do not necessarily reflect the opinion of the Institute.

The "Reports on Earth System Science" continue the former "Reports" and "Examensarbeiten" of the Max Planck Institute.

Anschrift / Address

Max-Planck-Institut für Meteorologie
Bundesstrasse 53
20146 Hamburg
Deutschland

Tel./Phone: +49 (0)40 4 11 73 - 0
Fax: +49 (0)40 4 11 73 - 298

name.surname@mpimet.mpg.de
www.mpimet.mpg.de

Layout

Bettina Diallo and Norbert P. Noreiks
Communication

Copyright

Atmospheric Chemistry Reactions in a Turbulent Flow: Application to an Urban Environment

Wing Yi Li

Hamburg 2019

Wing Yi Li
aus Hongkong

Max-Planck-Institut für Meteorologie
The International Max Planck Research School on Earth System Modelling
(IMPRS-ESM)
Bundesstr. 53
20146 Hamburg

Universität Hamburg
Geowissenschaften
Meteorologisches Institut
Bundesstr. 55
20146 Hamburg

Tag der Disputation: 18. April 2019

Folgende Gutachter empfehlen die Annahme der Dissertation:
Prof. Dr. Guy Brasseur
Prof. Dr. Martin Claussen

Vorsitzender des Promotionsausschusses:
Prof. Dr. Dirk Gajewski

Dekan der MIN-Fakultät:
Prof. Dr. Heinrich Graener

Berichte zur Erdsystemforschung / Max-Planck-Institut für Meteorologie 217
Reports on Earth System Science / Max Planck Institute for Meteorology 2019

ISSN 1614-1199

Abstract

Turbulence mixes initially-segregated chemical species in the atmosphere and hence affects the actual rate of chemical reactions. The significance of such interaction between turbulent motions and chemical reactions can be evaluated from the Damköhler number (Da), the ratio between the turbulent and the chemical timescale. For fast chemistry in which the reaction takes place before the chemicals are well mixed by turbulence ($Da \geq 1$), the inefficient turbulent mixing can significantly affect the actual rate of chemical reaction. Such interaction is however unresolved in operational chemical-transport models. Low-resolution chemical-transport models dilute and mix precursors instantly in a coarse grid, and hence miscalculate chemical reactions, for example ozone chemistry. This treatment is particularly unsuitable for urban environments where the anthropogenic emissions of pollutants are strong and highly localised. The objective of this thesis is to explore a way to provide a suitable parametrisation of this subgrid chemical-turbulence interaction for large-scale models with focus on urban environments. To achieve this purpose, this thesis systematically quantifies the effect of turbulent transport on chemical reactions in an urban boundary layer using regional-scale and turbulent-resolving approaches, and a combination of the two.

The problem is first illustrated by a study on sensitivity of ozone chemistry to model resolution in the region of Hong Kong with the chemical transport model WRF-Chem and a 1 km-resolution emission inventory. The results between the models at different horizontal resolutions (27, 9, 3, 1 km) are compared to account for the impact of increasing resolution to the calculated chemistry of ozone and its precursors. The model fails to reproduce the meteorological and chemical variations associated with local topography and emission hotspots at lower resolutions. With increasing resolution, the model shows a larger segregation between ozone and its precursors, and gives a lower net ozone production rate. However, the results of the chemical calculations at resolutions of 3 km and 1 km in general do not show statistically significant differences.

In order to explicitly quantify the effect of turbulent motions on the rate of chemical reactions in an urban boundary layer, direct numerical simulations are performed with two initially segregated chemicals reacting in a second-order chemical scheme. In a top-bottom entrainment-emission configuration, the inefficient turbulent mixing of the segregated reactants can cause a 15-35% reduction in reaction rate from the imposed

value for the fast-chemistry cases ($Da = 1$ -10). Strong emission fluxes and heterogeneous surface emissions can further reduce the reaction rate to less than 5% of the imposed rate. Such reduction in reaction rate due to the inefficient mixing of chemicals by turbulence is highly dependent on the instantaneous Da and the ratio between the corresponding Da of the two reactants. The results are then degraded to lower resolutions to mimic the calculation in a regional model. They reveal that at a horizontal resolution of 1 km, the overestimation of the chemical reaction rate by the model is moderated to 4-22% for the previous fast-chemistry cases. With the $NO-NO_2-O_3$ chemical scheme, the resultant effective reaction rate is $\sim 85\%$ of the imposed rate when the NO emission flux is strong, and a 1 km-resolution model overestimates the actual rate by $\sim 9\%$.

At last, the effective chemical reaction rate due to the segregation of reactants by inefficient turbulent mixing is parametrised as a function of Da. Such parametrisation is then applied specifically to the reaction between NO and O_3 as a test of its application to the WRF-Chem model in the region of Hong Kong. We find that the effect of the parametrisation is small ($< 2\%$) on the modelled NO_X concentrations, and is significant on the modelled O_3 concentration only right above an emission hotspot. It is speculated that when the parametrised effective reaction rate is largely deviated from the original rate, where the NO_X emission is strong, the modelled concentrations are dominantly affected by other processes such as emission and advection. Further research is required to explore if such parameterisation of the subgrid chemical-turbulence interaction leads to significant effect when applied also to other chemical reactions.

Zusammenfassung

Turbulenz mischt zunächst entmischte chemische Spurenstoffe in der Atmosphäre und beeinflusst somit die tatsächliche Geschwindigkeit chemischer Reaktionen. Die Bedeutung der Wechselwirkung zwischen turbulenten Bewegungen und chemischen Reaktionen kann anhand der Damköhler-Zahl (Da), dem Verhältnis zwischen turbulenter und chemischer Zeitskala, bewertet werden. Bei einer schnellen Chemie, in der die Reaktion stattfindet, bevor die Spurenstoffe durch Turbulenzen gut gemischt wurden ($Da \geq 1$), kann das ineffiziente turbulente Mischen die tatsächliche Reaktionsgeschwindigkeit der Spurenstoffe erheblich beeinflussen. Eine solche Wechselwirkung ist jedoch in chemischen Transportmodellen nicht berücksichtigt. Chemisch-Transportmodelle mit niedriger Auflösung verdünnen und mischen die chemischen Vorläufersubstanzen instantan innerhalb einer grossräumigen Modellgitterbox. Dieser Modellansatz führt dann zu einer fehlerhaften Berechnung der chemische Reaktionen, beispielsweise in der Ozonchemie. Der Ansatz ist insbesondere für städtische Umgebungen ungeeignet, in denen die anthropogenen Schadstoffemissionen räumlich konzentriert auftreten.

Das Ziel dieser Arbeit ist es, eine geeignete Parametrisierung dieser innerhalb der Gitterbox bisher unaufgelösten Chemie-Turbulenz-Interaktion für großräumigen Modellanwendungen mit Fokus auf urbane Umgebungen bereitzustellen. Um dieses Ziel zu erreichen, wird in dieser Dissertation der Einfluss des turbulenten Transports auf chemische Reaktionen in einer urbanen Grenzschicht systematisch mittels regionaler und turbulenzauflösender Ansätze und einer Kombination der beiden quantifiziert.

Die Problemstellung wird zunächst in einer Studie zur Empfindlichkeit der Ozonchemie gegenüber der Modellauflösung in der Region Hongkong veranschaulicht. Die Studie basiert auf dem chemischen Transportmodell WRF-Chem und einem Emissionsinventar mit einer Auflösung von 1 km. Die Modellergebnisse bei verschiedenen horizontalen Auflösungen (27, 9, 3 und 1 km) werden verglichen, um die Auswirkungen der zunehmenden Auflösung auf die berechnete Ozonchemie und die Vorläufersubstanzen zu analysieren. Bei niedrigeren Auflösungen kann das Modell die meteorologischen und chemischen Variationen der lokalen Topographie und der Emissionsquellen nicht reproduzieren. Mit zunehmender Auflösung zeigt das Modell eine stärkere räumliche Trennung zwischen Ozon und seinen Vorläufern, was zu einer niedrigeren Netto-Ozonproduktionsrate führt. Die Ergebnisse der chemischen Berechnungen bei Auflösungen von 3 km und 1

km zeigen im Allgemeinen keine statistisch signifikanten Unterschiede.

Um den Einfluss turbulenter Bewegungen auf die Geschwindigkeit chemischer Reaktionen in einer urbanen Grenzschicht explizit zu quantifizieren, werden direkte numerische Simulationen mit zwei zunächst getrennten Spurenstoffen durchgeführt, die in einem Reaktionsschema zweiter Ordnung reagieren. In einer Top-Bottom-Entrainment Emissionskonfiguration und in Fällen schneller Chemie ($Da = 1$ -10) kann das ineffiziente Turbulenzmischen der getrennten Reaktanten eine Verringerung der Reaktionsrate um 15-35% vom vorgeschriebenen Wert verursachen. Starke Emissionsflüsse und heterogene Oberflächenemissionen können die Reaktionsrate weiter auf weniger als 5% der vorgeschriebenen Rate reduzieren. Die Verringerung der Reaktionsgeschwindigkeit aufgrund der ineffizienten Turbulenzmischung von Spurenstoffen hängt stark von dem momentanen Da und dem Verhältnis der Da-Werte der beiden Reaktanten ab. Die Ergebnisse werden dann auf eine niedrigere Auflösung übertragen, um die Berechnung in einem regionalen Modell nachzuahmen. Es zeigt sich, dass bei einer horizontalen Auflösung von 1 km die Überschätzung der Reaktionsraten durch das Modell bei Fällen mit schneller Chemie auf 4-13% abgemildert wird. Mit dem chemischen Schema $NO-NO_2-O_3$ beträgt die resultierende effektive Reaktionsrate 85% des vorgeschriebenen Wertes, wenn der NO-Emissionsfluss stark ist. Ein Modell mit einer Auflösung von 1 km überschätzt die tatsächliche Rate um $\sim 9\%$.

Schließlich wird die effektive chemische Reaktionsgeschwindigkeit der aufgrund ineffizienter Turbulenzmischung segregierten Reaktanten als Funktion von Da parametrisiert. Um die Anwendung im WRF-Chem-Modell in der Region Hongkong zu testen, wird diese Parametrisierung speziell auf die Reaktion zwischen NO und O_3 angewendet. Es zeigt sich, dass der Effekt der Parametrisierung auf die berechneten NO_X-Konzentrationen nicht signifikant ist ($< 2\%$). Der Effekt ist hingegen signifikant für die berechnete O_3 -Konzentration direkt über einer starken Emissionsquelle. Es wird vermutet, dass bei einer starken Abweichung der parametrisierten effektiven Reaktionsrate von der ursprünglichen vorgeschriebenen Rate, wenn die Emission von NO_X stark ist, die vom Modell berechneten Konzentrationen mageblich von anderen Prozessen wie Emission und Advektion beeinflusst werden. Weitergehende Studien müssen klären, ob diese explizite Parameterisierung von Chemie-Turbulenz-Interaktionen zu signifikanten Änderungen der Modellergebisse führt, wenn sie auch auf andere chemische Reaktionen angewendet wird.
.

Acknowledgements

I would like to take this chance to acknowledge all the people that make this thesis possible.

First I express my deepest gratitude to my supervisor, Prof. Dr. Guy Brasseur, for his guidance and support to me and to this thesis. Thanks to him, I smoothly shifted my academic profession from the field of astronomy to atmospheric science in the past 4 years. It is no doubt my honour to work with him and to be his student. I also sincerely thank the other members in my advisory panel, my panel chair Prof. Dr. Martin Claussen and my co-advisor Dr. Hauke Schmidt, for their insightful discussions and instant help in the administrative arrangements with MPI-M and UHH, and Dr. Juan Pedro Mellado, for his help to set up the DNS model and his comments on Chapter 3 of this thesis.

My sincere thanks also extend to the members in the Environmental Modelling group for their support, specially to Idir Bouarar for his help to set up the WRF-Chem model, Angelika Heil for translating the abstract of this thesis to German, Nico Caltabiano for providing writing advices, Ina Döge for helping with daily simultaneous problems, and also to Natalia Sudarchikova, Katinka Petersen, Ali Hoshyaripour, Claire Granier, Yuting Wang, Xiaoqin Shi and Cornelia Sengbusch.

It was my privilege to share the same floor with Prof. Dr. Hartmut Graßl and Prof. Dr. Klaus Fraedrich for their profound knowledge and experience in science and other aspects of life.

I am also grateful to the researchers I have worked with during conferences and scientific visits, in particular to Dr. Chun-Ho Liu for his contribution to the budget analysis in Chapter 3 of this thesis.

I furthermore show my appreciation to my fellow students in the IMRPS graduate school, Manita Chouksey, Melinda Galfi, Sirisha Kalidindi, Hao-wei Wey, Jörg Burdanowitz, Sebastian Müller and Johannes Winkler for their aid and company inside and outside the institute. I express my special thanks to Antje Weitz and Cornelia Kampmann for their continuous help in the progression and administrative work of the PhD programme including the submission of this thesis.

I show my thankfulness to the friends I met in Hamburg, especially to Chunjung Chen, Tingchen Chen and Rowting Huang for their friendship, which make my life in Hamburg enjoyable.

Last but not least, I would like to thank my parents for their unconditional love and endurance for all these years. Without their support, I would never be able to pursue my PhD studies in Germany.

Contents

List of Figures

List of Tables

Chapter 1

Introduction

The chemical composition of the Earth's atmosphere is subject to multi-scale variations in response to various dynamical and photochemical processes with consequences to human population. One foremost example highly influencing modern societies is the problem of air pollution, in which excess emission of pollutants worsens air quality and brings adverse effect on human health. Understanding the chemistry in atmospheric flows is therefore important, and one of the common means to extend our knowledge on atmospheric chemistry is through numerical simulations.

The rates at which chemical reactions between two reactive species occur are described by rate constants that are measured in the laboratory under specified conditions inside a reaction vessel. The rate at which the product of a reaction is formed is proportional to the concentrations of the reactants, and the corresponding proportionality constant is precisely the reaction rate constant. Contrary to the preset conditions in the laboratory, concentrations of the reactants are often affected by turbulent motions in the atmosphere. The distributions of these species are hence very irregular in space and time. Therefore, the actual production rate of the product deviates from the laboratory-measured value and cannot be assumed to be proportional only to the spatial- and temporal-averaged concentrations of the reactants.

Two major types of models, the Eulerian and the Lagrangian models, can be applied to calculate the transport of reactive species in geophysical flows. In the Eulerian approach, the Earth is covered with a three-dimensional grid and the physical and chemical quantities considered are derived within each grid mesh. The geometric size of the mesh defines the spatial resolution of the model. Model grids represent the structure that allows the governing equations to be discretised. Physical and chemical quantities such as the concentrations of chemical species are assumed to be uniform inside each grid box. In other words, the approach implicitly assumes that chemical species are completely mixed within each grid cell. For example, if two chemical species A and B are released from two distant sources located within a given grid cell, they will react instantly in the model, even though they may not rapidly mix in the real world.

In the Lagrangian approach, the fluid is represented by a large number of air parcels to which values of the variables considered are attached. These parcels are displaced by the motion of the fluid and the identities of these parcels are not altered during their displacement. These air parcels do not mix in the flow unless specific action is undertaken in the model to ensure some mixing between parcels. The Lagrangian model may therefore underestimate the rate at which species A and B react with each other.

The situation in the real atmosphere can be described somehow intermediately between the two extreme scenarios prescribed by the Eulerian and Lagrangian methods. If the flow is purely laminar and uniform, the two species A and B that are emitted from two separated point sources will advect on parallel trajectories. The two species will remain segregated and will not react with each other, a situation that is close to what would be assumed in a Lagrangian model. On the other hand, in the planetary boundary layer, where the flow is usually turbulent (see Section 1.1), eddies are generated and mix species A and B, and hence partially reduce their segregation. This allows chemical reactions to occur, in some extent similar to the approach in an Eulerian model.

The degree of mixing between two initially segregated species depends on the respective chemical lifetimes of the species and the timescale characterising the strength of turbulence in the atmosphere (refer to Section 1.3). Species with long lifetimes such as carbon dioxide or methane are generally well mixed in the atmosphere, while fast-reacting species, such as nitrogen monoxide (NO), isoprene and hydroxyl radical (OH) are strongly affected by chemistry before being mixed by turbulence (refer to Table 1.1). In turbulent flows, such species are distributed with multi-scale spatial and temporal fluctuations. If they are emitted at different locations, they may still be partially segregated when the reaction takes place, and the resultant reaction will be at a rate considerably lower than what is assumed when they are totally mixed. In this case, the reaction rate is therefore affected by the strength of the turbulence.

Current chemical transport models do not consider the effect of inefficient turbulent mixing of segregated chemical species inside their grid meshes, and hence tend to overestimate the reaction rates between fast-reacting primary species in turbulent flows, especially in the boundary layer near emission sources. This can, in principle, lead to substantial errors in the calculated concentrations of secondary species, in particular those in nonlinear chemical systems. For example, it is known that ozone is formed in a complex chemical cycle involving volatile organic compounds (VOCs) and nitrogen oxides ($NO_X = NO + NO_2$). The resultant production rate of ozone is highly nonlinear, and the number of ozone molecules produced per NO_X molecule lost is higher when the NO_X concentration is low (refer to Figure 1.1, also see Section 1.2). As a result, the amount of ozone produced in a given area (corresponding to a grid mesh of an Eulerian model) will be different even with a fixed total quantity of NO in that area, depending if NO is emitted uniformly in the area (less concentrated) or at separated point sources

(more concentrated). Additionally, if the emissions of NO and VOCs are not located at the same spot within a given area, ozone is only produced when the air masses carrying NO and VOC respectively gradually mix. Hence the production rate of ozone will also depend on the rate at which mixing takes place.

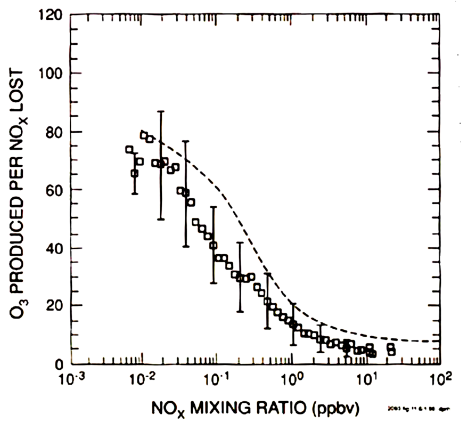

Figure 1.1: The number of ozone molecules produced for each NO_X molecule lost against the NO_X mixing ratio. The broken line refers to the results from a box model with fixed NO_X and hydrocarbons at 3 pm EST, altitude 0-1800 m in clear sky values (Liu et al. 1987). The open square refers to the boundary layer averaged values calculated from a 3D model, with the bars representing two standard deviations. Figure and description adopted from Brasseur et al. (1999). This shows that the number of ozone molecules produced per NO_X molecule is a function of NO_X mixing ratio and decreases with increasing NO_X concentration, resulting in the non-linearity of ozone chemistry.

The issue of segregation versus mixing is particularly important in urban areas since the emissions of different species are highly localised and generally not co-located. For example, NO is released by vehicles within street canyons in the centre of the city; while VOCs are released elsewhere. For example, isoprene is emitted from vegetations, and is particularly concentrated at the outskirt of the city. Furthermore, fast reactions between species such as NO_X at the surface and a compound entrained from the free troposphere such as ozone are strongly affected by turbulent mixing within the urban boundary layer complicated by the complex urban structures.

This thesis addresses the issue of how turbulent motion affects chemical reactions in the air, and how the ability or inability of resolving these motions in a numerical model impacts the resulting chemical calculations. The study focuses on urban environments particularly on their strong emission fluxes and segregated sources. The problem is first illustrated by a study on the sensitivity of ozone chemistry to model resolution of a regional model. The effect of turbulence on chemical reactions is then examined by means of a turbulence-resolving explicitly resolves turbulent motions in the planetary boundary layer. At last the knowledge attained from the turbulence-resolving simulations is applied to the regional model to assess the impact of such application.

1.1 Planetary boundary layer

The investigation in this thesis is centred on the relations between turbulent motions and chemical reactions in the planetary boundary layer. The dynamics and structure of the planetary boundary layer are therefore briefly introduced here. One can also refer to Stull (2012) for a more detailed review.

The *planetary boundary layer*[1] (PBL, Figure 1.2) refers to the part of the troposphere that is directly influenced by the presence of the Earth's surface, and responds to surface forcing, such as heat transfer and pollution emission, with a timescale of an hour or less. It extends typically to 1-3 km above the surface. Above the PBL is the inversion layer, where the potential temperature increases with height, and hence the inversion layer is stably stratified. Rising air from the PBL is often unable to penetrate this inversion layer, making it a cap to the PBL. Above the inversion layer is the free troposphere, where the air is also stably stratified and has a general slow sinking model.

The transport of quantities in the PBL, such as momentum and pollutants, occurs mainly by the dominating wind horizontally and by turbulent motions vertically. Turbulence occurs relatively frequently during daytime, and is mainly generated by mechanically by rough surface elements and buoyantly by surface heating. The mechanical turbulence is generated as the friction of the ground and other surface structures drags the air flowing over the ground surface and develops wind shears. The buoyant turbulence occurs as solar radiation heats up the ground and makes thermals of warm air to rise. These air plumes rise up to the base of the subsidence inversion, where it is radiatively cooled and sinks. These updrafts and downdrafts of air are also the strongest eddies and are most efficient in mixing quantities in the boundary layer. At the other end of the size range, the smallest eddies have sizes of a few millimetres. They are weak and are quickly dissipated by viscosity, and hence are believed to have less contribution to the mixing of quantities (e. g. Krol et al. (2000)).

Over land surfaces, the PBL has a well-developed structure which evolve with the diurnal cycle (from left to right of Figure 1.2). During daytime, the PBL is strongly influenced by solar heating of the Earth's surface and is highly convective. Due to its convective nature, the daytime PBL is also known as the *convective boundary layer*. The convective boundary layer (CBL) consists on three major components - the surface layer, the mixed layer and the entrainment zone. The *surface layer* is the bottom 10% of the boundary layer, in which turbulence is mainly generated by mechanical shear. Above the surface layer is the *mixed layer*, where the buoyant turbulence dominates. The mixed layer grows in depth with time after sunrise as the solar heating becomes more intense, and reaches its maximum height in late afternoon. It grows by slowly mixing down the air from the inversion layer, or in this context, the *entrainment zone*,

[1] also referred as the boundary layer

a layer of stable air on top of the mixed layer. The entrainment zone serves as a lid to the rising thermals, and also to the pollutants in polluted regions.

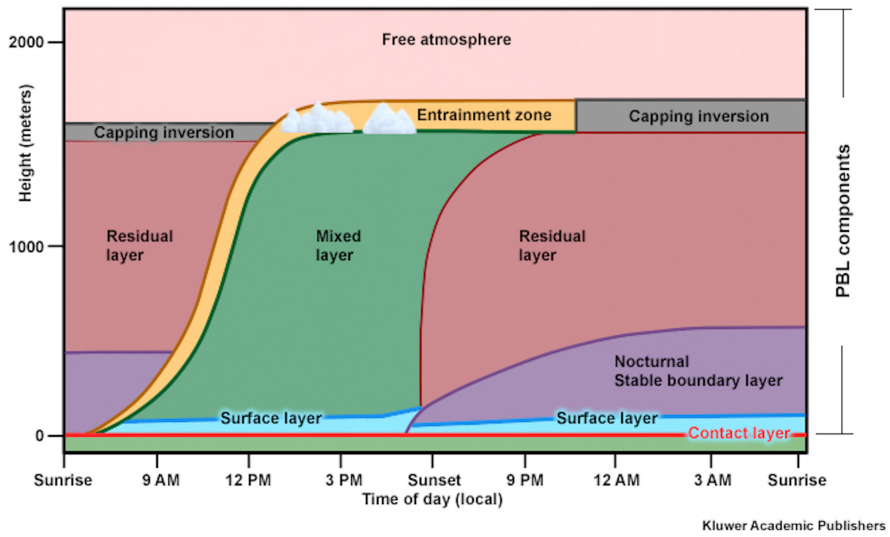

Figure 1.2: Schematic diagram showing different layers in the planetary boundary layer (PBL) (along the y-axis), and their evolution with time of day beginning from sunrise (along the x-axis). Diagram courtesy for COMET/METED.

After sunset, the mixed layer rapidly collapses due to the suppressed surface heating. Turbulence in the mixed layer decays and the mixed layer transits to the residual layer. During nighttime, the bottom portion of the residual layer is cooled radiatively and transformed into a stable boundary layer. This nocturnal boundary layer is characterised by statically stable air, which suppresses turbulence and vertical mixing of quantities.

The dynamics of the PBL plays an important role in changing the chemical concentrations in the surface air. For instance, for an inert chemical continuously emitted from the surface, its concentration drops upon sunrise as the PBL grows in depth and dilutes its chemical composition. After sunset, as the PBL shrinks, the chemical species released at the surface remain in the shallow surface layer and accumulate in the surface air. On the other hand, for chemicals originated from the free troposphere, their concentration increases after sunrise as they are entrained from aloft with the growth of the mixed layer. After sunset, the entrainment ceases and stops replenishing the chemicals, leaving the chemicals depleted within the boundary layer in the course of the night by deposition to the surface.

Over the ocean, the diurnal cycle of the surface heating and cooling is minimal due to the large heat capacity of water. The marine boundary layer remains neutral throughout the day, in which vertical mixing is maintained mainly by mechanical turbulence. It typically extends to around 1 km above sea level and is often capped by a shallow

cumulus or stratus cloud layer.

In urban areas, the surface is rough and complex with buildings and other large urban structures, which modify the turbulent transfer and the structure of the boundary layer. The portion of planetary boundary layer that is affected by the presence of the urban area is called the urban boundary layer. The urban boundary layer (UBL) is characterised by its complex surface layer, which can be further divided to the urban canopy layer[2], the roughness sublayer[3] and the inertial sublayer[4]. These sublayers are influenced by the urban structures at different extents. One can refer to Oke (1997) for more details. The UBL also consists of a mixed layer, in which the turbulence properties are probably independent of the surface roughness. Therefore, an urban boundary layer can also be approximated with an extended surface layer imbedding the urban features with CBL on top (Onomura et al. (2015), also see Figure 1.3). The direct numerical simulations conducted in Chapter 4 refer to this CBL above the extended urban surface layer.

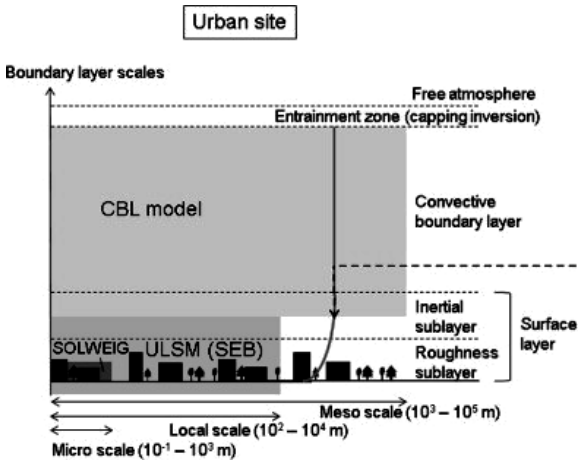

Figure 1.3: The potential combination of a CBL and urban models in representing key features in the UBL in Onomura et al. (2015). Schematic diagram showing the relation between the boundary layer scales, the structure of the UBL, and the different models adopted. A CBL model is coupled with the urban land surface model (ULSM) to study the meteorological forcing in urban sites. Figure adopted from Onomura et al. (2015).

For instance, the direct numerical simulations are conducted under the conditions in

[2]The assembly of buildings, trees and other objects which compose a town or a city, and the spaces between them.

[3]A layer includes the urban canopy layer, and extends from the surface up to two to five times the height of the roughness elements.

[4]A sublayer in wall-boundded shear flows characterised by a sufficiently large Reynolds number and a logarithmic velocity profile.

a clear CBL[5], in which buoyancy is a main driving force of turbulence. Buoyancy[6] is responsible to drive the motion of convective thermals, which make a larger contribution to vertical chemical transport than mechanical turbulence. It can be calculated from the virtual potential temperature[7] profile θ_v with the expression

$$b = g(\theta_v - \theta_{v,0})/\theta_v, \tag{1.1}$$

where g is the gravitational constant and $\theta_{v,0}$ is the reference virtual potential temperature. With a surface buoyancy flux B_0[8], the positively-buoyant thermals of warm air rise as they are less dense than the surrounding air. Negatively-buoyant thermals of cool air, on the other hand, sink from the cloud top. These updrafts and downdrafts correspond to the largest eddies in the boundary layer, and have sizes of the boundary layer height. The transition of the sign of buoyancy between the thermal updrafts and downdrafts defines the size of these eddies, and hence defines the boundary layer height. Therefore, the boundary layer height z_i is defined in this thesis as the height where the buoyancy variance $\langle b'b' \rangle$ is maximum away from the surface (Garcia and Mellado 2014). The convective timescale t_c, which is related to the convective velocity w_c by

$$t_c = \frac{z_i}{w_c}. \tag{1.2}$$

This convective timescale represents the dynamical timescale involved in convective (or buoyant) turbulent motions in the CBL. As the buoyant turbulence plays a much bigger role in mixing of chemical species in a CBL than the mechanical turbulence, in the context of this thesis, we will refer turbulent motions to those driven by the buoyancy. Therefore, the turbulent timescale in this thesis is referred to the convective time scale ($t_{turb} = t_c$) (Deardorff 1970). The convective velocity is defined as (Deardorff 1970)

$$w_c = \left[\frac{g}{T_v} z_i \overline{w'\theta'_v}|_0 \right]^{1/3} = (B_0 z_i)^{\frac{1}{3}}, \tag{1.3}$$

where T_v is the virtual temperature, and $\overline{w'\theta'_v}|_0$ is the kinematic vertical turbulent flux of the virtual potential temperature at the surface. The convective velocity is related to

[5]In a clear CBL, the atmosphere is assumed to be dry and no saturation is taking place. With clear CBL conditions, the mixed-layer theory is valid (Lilly 1968) and its governing equations can be derived in a non-dimensional form with the scaling of convective velocity, timescale and the boundary layer height (de Arellano et al. 2015).

[6]Here, buoyancy refers to the buoyancy force per unit mass, which is the upward force exerted upon air parcel with unit mass in a gravitational field due to the density difference between the parcel and that of the surrounding air (AMS Glossary).

[7]The theoretical potential temperature of dry air that would have the same density as moist air (AMS Glossary)

[8]The flux that is proportional to buoyancy at the surface (AMS Glossary)

the surface buoyancy flux B_0 and the boundary layer height z_i with the expression

$$B_0 = (g/T_v)\overline{w'\theta'_v}|_0.$$

1.2 Ozone chemistry

A simplified overview of ozone chemistry in the troposphere is presented to provide the reader with sufficient background to understand the results in Chapter 3. One can refer to Brasseur et al. (1999) and Brasseur and Jacob (2017) for more details.

In the troposphere, the chemistry of ozone (O_3) is initiated by the formation of the hydroxyl radical OH by the following processes

$$\begin{aligned} O_3 + h\nu &\longrightarrow O(^1D) + O_2 \\ O(^1D) + H_2O &\longrightarrow 2\,OH \end{aligned}$$

Here $O(^1D)$ represents the electronically excited oxygen atom, and $h\nu$ refers to a solar photon. Note that this initial step requires the presence of O_3, which can be for example transported from the stratosphere. Additional O_3 molecules are produced by the photochemical oxidation of carbon monoxide (CO) or of volatile organic compounds (VOCs) by OH in the presence of nitrogen oxides, which includes nitrogen monoxide and dioxide ($NO_X = NO + NO_2$). In the case of CO, the following sequence of reactions leads to the formation of ozone molecules:

$$CO + OH \xrightarrow{+O_2} CO_2 + HO_2 \tag{1.4}$$

$$k_2 : HO_2 + NO \longrightarrow OH + NO_2 \tag{1.5}$$

$$J_1 : NO_2 + h\nu \xrightarrow{+O_2} NO + O_3 \tag{1.6}$$

$$Net : CO + 2\,O_2 + h\nu \longrightarrow CO_2 + O_3.$$

Here, the constant k_i is the rate constant of the corresponding reaction i, and J_i refers to the photolysis coefficient of the corresponding photochemical reaction i. In the case of VOCs, the first step is an abstraction of a hydrogen atom by reaction with OH, to produce an organic radical R, that is subsequently added to oxygen O_2 to form an organic peroxyl radical $R\,O_2$:

$$R\,H + OH \xrightarrow{+O_2} R\,O_2 + H_2O \tag{1.7}$$

When the concentration of NO_X is sufficiently high, which is said to be in a high-NO_X

regime, the $R\,O_2$ radicals react with NO:

$$k_3 : R\,O_2 + NO \longrightarrow R\,O + NO_2 \tag{1.8}$$

and NO_2 is photolysed to produce NO and O_3 as Reaction 1.6. When the concentration of NO_X is low (the low-NO_X regime), the $R\,O_2$ radicals react with the peroxyl radical HO_2 instead, which produces no ozone. The above chemical sequences of CO and VOCs provide the dominant source of ozone in the troposphere, and Reaction 1.5 and 1.8 are the limiting reactions. Therefore, the ozone production rate can be formulated as

$$P(O_3) = k_2\langle HO_2\rangle\langle NO\rangle + \sum k_{3,i}\langle RO_{2,i}\rangle\langle NO\rangle \tag{1.9}$$

, where $\langle HO_2\rangle$ and $\langle NO\rangle$ refer to the instantaneous concentrations of HO_2 and NO (in this session the quantities bracketed with $\langle\rangle$ refer to the concentrations of the corresponding chemical species). $\langle RO_{2,i}\rangle$ refers to several types of peroxyl radicals produced by the oxidation of VOCs by the OH radical from Reaction 1.7, and $k_{3,i}$ refers to their corresponding rate coefficients with NO in Reaction 1.8. The downward transport of ozone from the stratosphere also serves as an additional source of ozone.

The loss of ozone in the troposphere takes place by the photolysis of ozone to $O(^1D)$ followed by the reaction of $O(^1D)$ with H_2O:

$$\begin{aligned} O_3 + h\nu &\longrightarrow O(^1D) + O_2 \\ k_4 : O(^1D) + H_2O &\longrightarrow 2\,OH, \end{aligned} \tag{1.10}$$

with Equation 1.10 being the rate limiting step. Ozone is also consumed by HO_2 and OH:

$$k_5 : O_3 + OH \longrightarrow HO_2 + O_2 \tag{1.11}$$

$$k_6 : O_3 + HO_2 \longrightarrow OH + 2\,O_2 \tag{1.12}$$

$$Net : 2\,O_3 \longrightarrow 3\,O_2,$$

and by unsaturated VOCs (Johnson and Marston 2008)

$$k_7 : O_3 + R\,H \longrightarrow \text{carbonyls} + \text{Criegeebiradicals}. \tag{1.13}$$

The cycling of NO and NO_2 produces no net effect on ozone:

$$k_1 : NO + O_3 \longrightarrow NO_2 + O_2 \tag{1.14}$$

$$J_1 : NO_2 + h\nu \xrightarrow{+O_2} NO + O_3 \tag{1.15}$$

$$Net : \text{No change in } O_3.$$

This cycle is very rapid on a timescale of few minutes in daytime, and NO, NO_2 and O_3 are typically equilibrated on a timescale of a few minutes, in a condition called photostationary state. However, during nighttime, NO_2 is oxidised by ozone to produce NO_3 instead, which is further converted to N_2O_5 and HNO_3:

$$\mathrm{NO_2 + O_3 \longrightarrow NO_3 + O_2} \tag{1.16}$$

$$\mathrm{NO_2 + NO_3 + M \longrightarrow N_2O_5 + M}$$

$$k_8 : \mathrm{N_2O_5 + H_2O \xrightarrow{aerosol} 2\,HNO_3} \tag{1.17}$$

$$Net : \mathrm{2\,NO + 3\,O_3 + H_2O \longrightarrow 2\,HNO_3}$$

Nitric acid (HNO_3) is removed from the atmosphere by wet deposition. This chain of reaction usually occurs during nighttime, as with daylight NO_3 is photolysed to return NO_2 in a lifetime of only a minute. When the NO_X concentration is very high, NO_2 can also react with OH to form HNO_3:

$$k_9 : \mathrm{NO_2 + OH \xrightarrow{M} HNO_3}. \tag{1.18}$$

Together with the reaction between NO_2 and $R\,O_2$

$$k_{10} : \mathrm{NO_2 + R\,O_2 \longrightarrow ROONO_2} \tag{1.19}$$

and the reaction between VOCs and NO_3

$$k_{11} : \mathrm{NO_3 + R\,H \longrightarrow R'ONO_2} \tag{1.20}$$

(Roberts 1990), these reaction constituent a loss for NO_2 and NO_3, which prohibit NO_2 cycling back to O_3, and in turn suppress the production of ozone. Summing up the effect from Reaction 1.10, 1.11, 1.12, 1.13, 1.17, 1.18, 1.19 and 1.20, the loss rate of ozone is given by (Wang et al. 2017):

$$\begin{aligned} L(\mathrm{O_3}) =& k_4\langle \mathrm{O(^1D)}\rangle\langle \mathrm{H_2O}\rangle + k_5\langle \mathrm{OH}\rangle\langle \mathrm{O_3}\rangle + k_6\langle \mathrm{HO_2}\rangle\langle \mathrm{O_3}\rangle \\ &+ \sum k_{7,i}\langle \mathrm{VOC}_i\rangle\langle \mathrm{O_3}\rangle + 3\times k_8\langle \mathrm{N_2O_5}\rangle + k_9\langle \mathrm{NO_2}\rangle\langle \mathrm{OH}\rangle \\ &+ \sum k_{10,i}\langle R\,\mathrm{O}_{2,i}\rangle\langle \mathrm{NO_2}\rangle + \sum k_{11,i}\langle \mathrm{VOC}_i\rangle\langle \mathrm{NO_3}\rangle. \end{aligned} \tag{1.21}$$

There is also an ozone sink from deposition to the surface. The lifetime of ozone ranges from days in the boundary layer to months in the upper troposphere.

The ozone production rate depends on the abundance of NO_X, VOCs and CO, and the cycling of odd hydrogen radicals HO_X (HO_X = OH + HO_2) in competition with the HO_X sink. In the troposphere under normal condition, OH mainly reacts with CO and VOCs in the afore-mentioned sequences to produce HO_2. Whether ozone production

takes places depends on the competition between the reaction of HO_2 with NO to produce ozone (Reaction 1.5), and its reaction with another HO_2 radicals to produce peroxides H_2O_2:

$$HO_2 + HO_2 \longrightarrow H_2O_2 + O_2,$$

which is then washed out by precipitation. In this case, the ozone production rate increases nearly linearly with NO_X concentrations[9], but is independent of the CO and VOC concentrations. Thus, this is called the *NO_X-limited regime*.

On the other hand, when NO_X concentrations are high, or when the UV radiation is low, the formation of HNO_3 by Reaction 1.18 becomes the dominant sink of HO_X[10]. In this case, the competition is instead between the reactions of the OH radicals with VOCs and CO (Reaction 1.4 and 1.7, which subsequently produce ozone) and Reaction 1.18. The ozone production rate therefore increases with the VOCs and CO concentrations, but decreases with the NO_X concentrations[11]. This regime is called the *VOC-limited regime*.

Figure 1.4 shows the net ozone production rate ($P(O_3) - L(O_3)$) as a function of NO_X concentration. For very low NO_X concentrations (such as in remote areas or over the ocean), the net ozone production rate is negative. It then increases nearly linearly with NO_X concentrations at low NO_X concentrations. When NO_X concentration reaches beyond the level of $\sim O(1)$ ppbv, the net production rate then begins to fall off with increasing NO_X concentration as the concentrations of HO_2 and RO_2 start to collapse (Monks 2005). When NO_X concentrations exceed a level of around 20 ppbv (in very polluted areas), the net ozone production rate becomes negative again and the ozone chemistry system is in titration conditions (Reactions 1.14 and 1.18 dominants). Figure 1.5 shows an ozone isopleth diagram which illustrates the dependence of ozone concentration on the concentrations of both NO_X and VOCs, and indicates the corresponding VOC/NO_X ratios and VOCs and NO_X concentrations of the NO_X- and VOC-limited regimes respectively. The VOC-limited regime is typical in highly polluted urban areas, while the NO_X-limited regime is typical in locations downwind of urban and suburban areas. For example, the domain that the study is focusing in South China and Hong Kong, which has a typical NO_X concentration of around 20 ppbv, is mainly in the VOC-limited regime.

From the above description, one can see that the chemistry of ozone is highly non-linear in polluted areas. A misrepresentation of precursor concentrations, possibly due

[9] At low NO_X concentrations, HO_X production and destruction are not affected by NO_X concentrations. Also, the concentration of HO_2 is much larger than that of OH at low NO_X condition, such that the majority amount of HO_X is constituent of HO_2. Therefore, in remote atmosphere, where HO_2 is more abundant than RO_2, $P(O_3) \approx k_2\langle HO_2\rangle\langle NO\rangle \propto \langle NO\rangle$ (Logan et al. 1981; Brasseur et al. 1999).

[10] At high NO_X concentration, the ratio of HO_2/OH is affected by NO_X, and HO_2 no longer dominates over OH (Logan et al. 1981; Brasseur et al. 1999).

[11] The term $k_2\langle HO_2\rangle\langle NO\rangle$ becomes non-linear because $\langle HO_2\rangle$ is dependent on $\langle NO\rangle$.

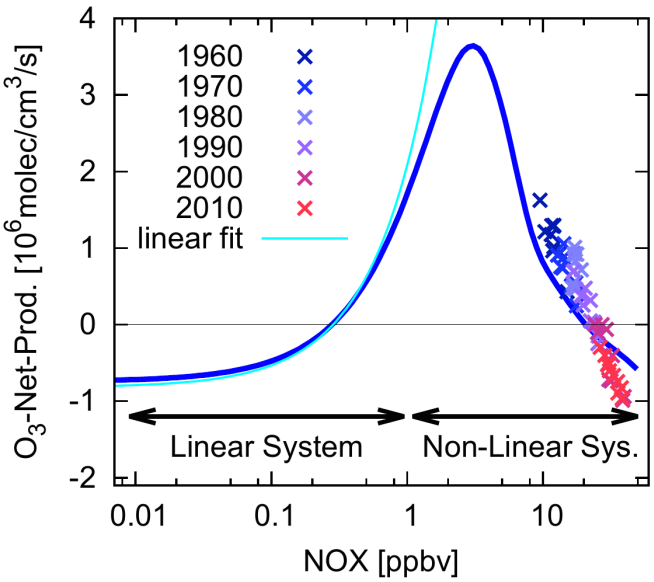

Figure 1.4: Net ozone production rate as a function of NO_X concentration. The solid blue line shows the result based on box model simulations at 50°N in Europe for summer conditions, which were constrained by values from the global chemistry climate simulation. The crosses indicate the results from comprehensive climate-chemistry ensemble simulations and are colour-coded with respect to time from 1960s to 2010s. Increasing global NO_X emissions in the period 1960 to 2019 results in the decrease in net ozone production rate. The light blue line shows a linear fit of the net production rate in the NO_X regime, which appears in the logarithmic scale (x-axis) as an exponential function, indicating a linear relation between the net production rate and the NO_X concentration. Figure and description adopted from Grewe et al. (2012).

to artificial mixing within a model grid mesh and errors from emission inventory, may therefore push the scenario from one regime to another, and give very different results in ozone concentrations. In general, the ozone production rate per NO_X molecule is higher when the NO_X concentration is low (see Figure 1.1). Therefore, low-resolution model tends to dilute NO hotspots, and produces an excess amount of ozone (e. g. Arunachalam et al. (2006)).

To further investigate the relation between ozone and NO_X, one can analyse the interconversion of O_3, NO and NO_2 (see Figure 1.6). Under atmospheric conditions, the interconversion of O_3, NO and NO_2 is generally dominated by the null cycle of Equations 1.14 and 1.15 (Leighton 1960). This cycle has no net change to ozone concentration and only partitions NO_X(= NO + NO_2) and the oxidant O_X (=NO_2 + O_3) between its constituent components, but does not change the total mixing ratio of both NO_X and O_X. Figure 1.6(a) shows the variation of O_3 and NO_2 concentrations with NO_X concentration under polluted conditions. It clearly shows the interconversion of O_3 and NO_2 as a function of NO_X. With the interconversion of NO_2 and O_3 within the combined mixing ratio of O_X, one can make a linear plot of the O_X concentrations against NO_X concentrations to check the local and regional contribution of NO_X to O_X (Clapp and

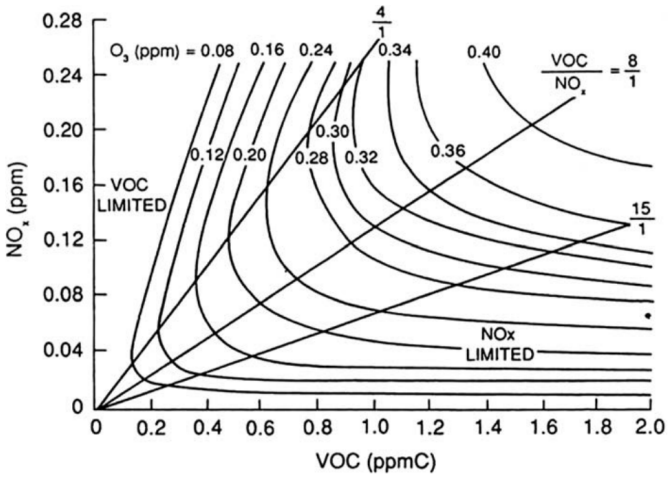

Figure 1.5: Ozone isopleth diagram showing the ozone concentration as a function of the concentrations of NO_X and VOC. The VOC-limited regions are characterised by its high NO_X concentrations and/or low VOC/NO_X ratio, and are typical for highly polluted urban areas, such as the domain in this study in South China and Hong Kong. The NO_X-limited regionals are characterised by its low NO_X concentrations and/or high VOC/NO_X ratio, and are typical of locations downwind of the urban and suburban areas. Figure and text adopted from Brasseur and Jacob (2017).

Jenkin 2001; Mazzeo et al. 2005; Song et al. 2011) (see Figure 1.6(b)). Since O_3 can only be produced with the presence of NO_X, the intercept of the O_X-NO_X linear relation (at which $\langle NO_X \rangle = \langle NO_2 \rangle = 0$) represents the background O_3 level by regional transport. Above that background level of O_X, the O_X concentrations increase linearly with NO_X concentrations. In this NO_X-dependent regime, the slope of the O_X-NO_X linear relation correlates the local contribution of NO_X to O_X composition (on the other hand, the level of primary pollution).

1.3 Impact of inefficient turbulent mixing on chemical reaction

In real-life environments, chemical species are normally emitted from segregated sources. Atmospheric turbulence mixes these initially-segregated species to allow possible chemical reactions. The actual rate of chemical reaction therefore depends on the efficiency of turbulence to mix the corresponding chemicals. This effect of turbulent motions on chemical reactions can be estimated from the ratio between the turbulent and chemical timescales (the Damköhler number Da (Damköhler 1940)). For instance, for a second-order chemical reaction, where a chemical species A reacts with another species B to form the product C with an imposed rate constant k:

$$\mathrm{A} + \mathrm{B} \xrightarrow{k} \mathrm{C},$$

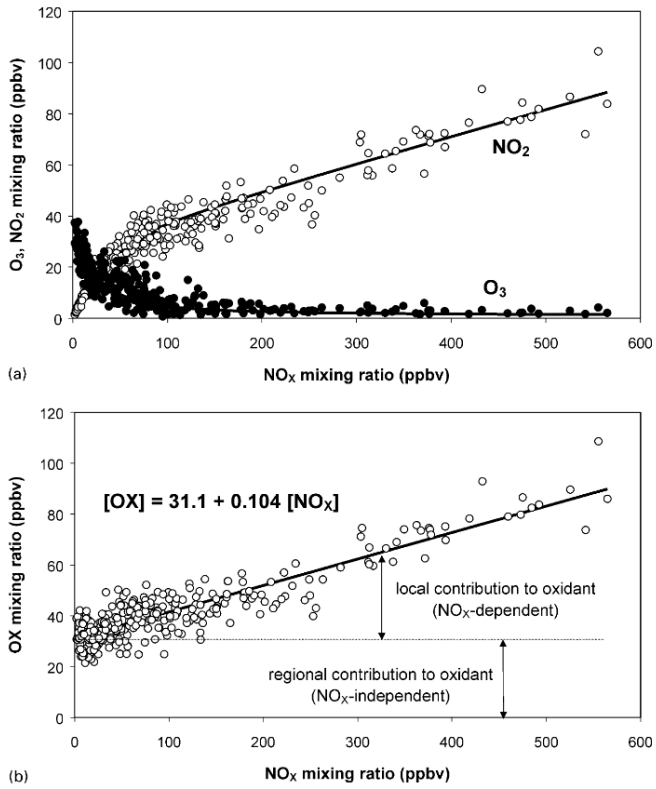

Figure 1.6: (a) Variation of daytime average mixing ratios of O_3 and NO_2 with NO_X mixing ratio. Note that when ozone is almost completely removed when the NO_X concentration reaches ∼100 ppbv, the concentration of NO_2 concentration keeps on increasing. The lines were calculated with the assumption of photostationary state. (b) Variation of daytime average mixing ratios of the oxidant O_X with NO_X mixing ratios. The line was defined by linear regression analysis. From the result of the linear regression, the background O_3 level is 31.1 ppbv, and the local contribution to O_X is 10.4% of the NO_X level. In both figure, the dots present data for each day of November 1998 and 1999 at six observational sites in the UK. Figure and part of the caption adopted from Clapp and Jenkin (2001).

the chemical timescale of the species A is:

$$t_{chem,A} = \frac{1}{k\langle B\rangle}, \tag{1.22}$$

where $\langle B\rangle$ is the volumetric-averaged concentration of the species B. Together with the turbulent timescale calculated from Equation 1.2 and 1.3, the Damköhler number of the species A is given by

$$Da_A = \frac{t_{turb}}{t_{chem,A}} = \frac{z_i/w_c}{1/k\langle B\rangle} = k\langle B\rangle \left(\frac{z_i^2}{B_0}\right)^{\frac{1}{3}}. \tag{1.23}$$

And similarly the Damköhler number of the species B can be written as

$$Da_B = k\langle A\rangle \left(\frac{z_i^2}{B_0}\right)^{\frac{1}{3}}. \tag{1.24}$$

For slow chemistry with $Da \ll 1$, the chemical lifetime of the reactant is long enough for turbulence to mix them well in the boundary layer before they react, such that the production rate of species can be approximated as the product of k and the volumetric-mean of the reactants ($k\langle A\rangle\langle B\rangle$). On the other hand, for fast reactions with $Da > 1$, such that the chemical timescale of the reactant is comparable to or shorter than the turbulent timescale of the atmosphere, the reactants are not well mixed by turbulence before the chemical reaction takes place. In that case species A and B only react when turbulent motion brings the two species together, and hence the production rate of species C also depends on the turbulent timescale. For instance, the turbulent timescale t_{turb} for large-scale eddies in a CBL is typical $10^2 - 10^3$ s. With the reference of Table 1.1, the chemical lifetime of NO_X and O_3 in the boundary layer is comparable to t_{turb}. Therefore, the turbulent motions in the CBL potentially affect the chemical reactions involving NO_X and O_3.

The state of mixing of species A and B in the boundary layer can be represented by the segregation coefficient (e. g. Danckwerts (1952); Vinuesa and de Arellano (2003)):

$$I_S = \frac{\langle A'B'\rangle}{\langle A\rangle\langle B\rangle},$$

which is the ratio between volumetric-averaged values of the concentration covariance ($\langle A'B'\rangle$) and the product of the mean concentrations ($\langle A\rangle\langle B\rangle$). If species A and B are completely well mixed to uniform distribution , then $I_S = 0$. If species A ad B are completely segregated, then $I_S = -1$. If species A and B are emitted in the same direction and their concentrations are correlated, then $I_S > 1$. By Reynolds decomposition, the concentration of species A can be broken down as the sum of the mean term $\langle A\rangle$ and the turbulent term A', as similarly for species B as $B = \langle B\rangle + B'$. The segregation coefficient can then be related to the volumetric-averaged chemical production term $\langle R\rangle$ by

$$\begin{aligned}\langle R\rangle &= -k\langle AB\rangle \\ &= -k\left(\langle A\rangle\langle B\rangle + \langle A'B'\rangle\right) \\ &= -k(1 + I_S)\langle A\rangle\langle B\rangle \\ &= -k_{eff}\langle A\rangle\langle B\rangle.\end{aligned}$$

The effective chemical reaction rate k_{eff} then quantitatively measures the actual chemical reaction rate under the influence of turbulent motions (Vinuesa and de Arellano

2003). It can illustrate the influence compared to a complete-mixing model, in which both species A and B are assumed to be evenly distributed throughout the boundary layer. Therefore, its normalised value with the imposed chemical reaction rate, k_{eff}/k, is employed as an assessment of the strength of the impact of turbulence on chemical reactions in Chapter 3:

$$\frac{k_{eff}}{k} = 1 + I_S = 1 + \frac{\langle A'B' \rangle}{\langle A \rangle \langle B \rangle}. \tag{1.25}$$

It can also potentially serve as a correction factor to the rate constant employed in a chemical-transport model to take into the account of the corresponding subgrid effect (Vinuesa and de Arellano (2005), also see Chapter 4).

In the context of an urban environment, the second-order chemical reaction mentioned above can be analogous to the reaction between $R\,O_2$ and NO, which is the limiting reaction of forming ozone (Reaction 1.8). The VOCs are often emitted from sources segregated from NO. With the intense emission fluxes of these precursors in an urban area, their resultant concentrations are also high. From Equation 1.22, the timescales of the involved chemical reactions are relatively fast. The impact of turbulence mixing on these chemical reactions are hence potentially important in cities.

1.4 Past work on related topics in multiple scales

Chemical composition in the atmosphere is affected by various physical and chemical processes (Figure 1.7), which can be mainly divided into four general types: transport, chemistry, emissions and deposition (Jacob 1999). Numerical models are employed to calculate the spatial and temporal variations of the chemical composition in the air. However, these models have technical limitations, so that they can only do the calculations with a restrained resolution in order to cover a designated simulation domain. In general, a model can only resolve processes with a length scale larger than its grid mesh (or with a timescale longer than a timestep). Processes with a length scale shorter than the model resolution are considered as subgrid effects, and can only be approximated by corresponding parametrisation schemes. However, these parametrisation schemes are usually based on certain specific assumptions, which may not accurately represent the real-life situation, especially for complex scenarios. Therefore, scientists usually employ different types of models with suitable respective resolution to solve their problems involving processes with a particularly length scale (refer to Figure 1.8). For instance, for the interest of this thesis, which is to investigate the influence of turbulence on chemical reaction in urban environments, the range involved covers the microscale and local scale, as indicated in the grey-shaded box in Figure 1.8. As a result, the problem can be addressed by means of direct numerical simulation, large eddy simulation and mesoscale models.

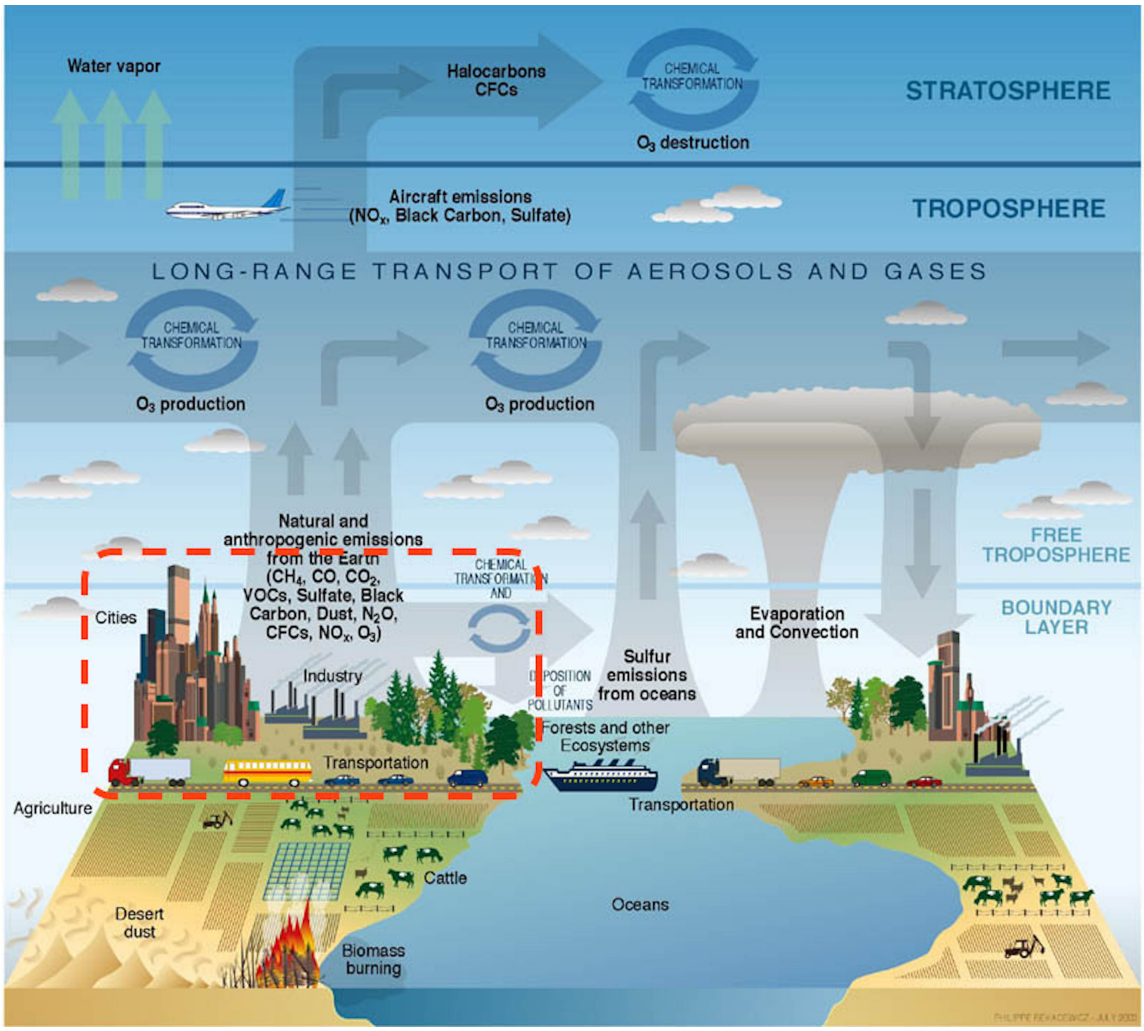

Figure 1.7: Schematic diagram showing examples of physical and chemical processes related to atmospheric composition. The processes of interest in this work, in the urban environment in the boundary layer, is highlighted in the red dashed box. Figure adopted from Rekacewicz (2003).

The application of atmospheric models in daily practices is highly diversified in monitoring and forecasting a wide variety of atmospheric phenomena. For instance, chemical-transport models are commonly employed for air quality monitoring and foresting in regions and cities. *Chemical transport models* (CTMs) consist of mathematical representations of the relevant physical and chemical atmospheric processes, which are solved using numerical algorithms to obtain chemical concentrations as a function of space and time for a given set of chemical emissions and meteorological conditions (Seigneur and Moran 2004). For the interest of air quality modelling, a regional CTM is usually employed with a finer resolution of ∼10 km to represent the characteristics in a regional scale (also refer as the mesoscale in Figure 1.8). As a result, the question of how the model resolution affects the calculations of a CTM has been raised. Spatial resolution

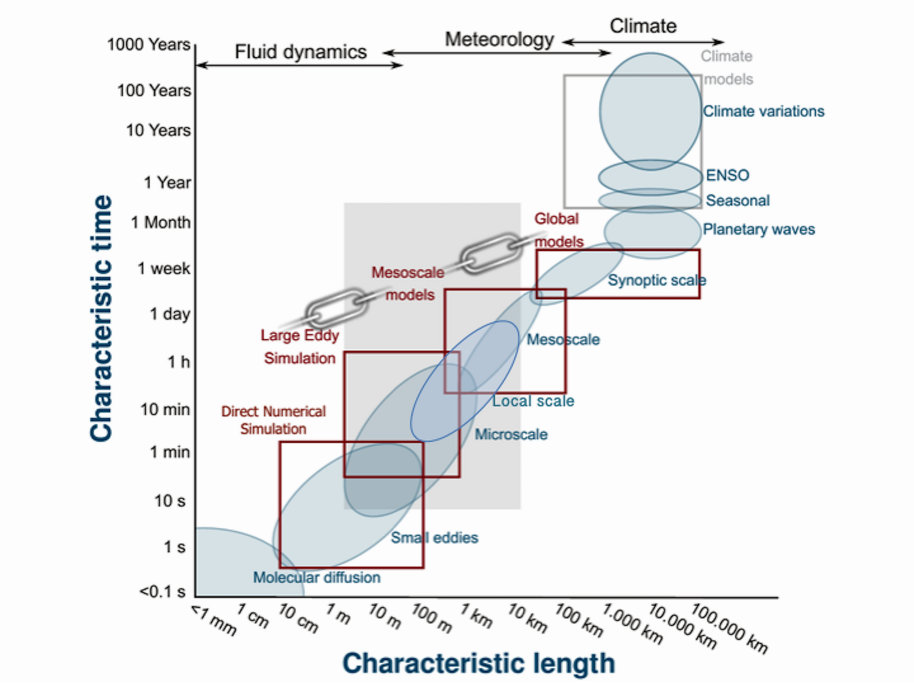

Figure 1.8: Time and length scales of atmospheric dynamical phenomena and the hierarchy of atmospheric numerical models superposed on the scale classification of phenomena. The range of time and length scales of interest in this work is highlighted in the grey-shaded box. Figure adopted from Montornes et al. (2017) and text from Steyn (2015).

of the model affects calculation in three main aspects - meteorology, emission and deposition (Tie et al. 2010). With these effects, the CTMs with different resolutions give different results on chemical concentrations and distributions, which may potentially impact the subsequent chemical calculations, especially for non-linear chemistry like ozone chemistry.

Several studies have conducted simulations of a number of CTMs on the sensitivity of ozone chemistry to model resolution over the US and Europe (∼50 km) and high (∼10 km) resolution (e g. Jang et al. (1995); Cohan et al. (2006); Queen and Zhang (2008); Valari and Menut (2008); Arunachalam et al. (2006); Schaap et al. (2015); Yu et al. (2016); Tie et al. (2010); Pfister et al. (2014); Tan et al. (2015)). All studies reported that the high-resolution model showed emission hotspots of ozone precursors, while low-resolution dilutes these emissions. Most of the studies also reported excess in ozone production in low-resolution models (e. g. Pfister et al. (2014)). In particular, Yu et al. (2016) reported that only their high-resolution model (0.25°× 0.3125°, around 18 km) can recover the negative correlation between isoprene and NO, as observed in airborne measurements, and hence give different ozone formation pathways. However, model performance does not necessarily improve with increasing model resolution. Yu et al. (2016) also reported that spatial concentration correlations between modelled and observed values improve as the resolution increases from 4°× 5° to 2°× 2.5°, but then

Chemical species	Approximate timescale (s)	Atmospheric phenomena
OH, HO_2 (HO_X)	$10^{-1} - 1$	Smallest turbulent eddies
NO, NO_2 (NO_X)	$10^2 - 10^3$	Large eddies in PBL/Thermal updrafts
Isoprene	$10^3 - 10^4$	Convection
O_3^b*	$10^3 - 10^5$	Large eddies/Convection
O_3^t, CO	10^7	General circulation
CH_4	$10^8 - 10^9$	Climate change

Table 1.1: Typical time scales of transformation of chemical species and their related atmospheric phenomena (species with superscript b refer to the species in the boundary layer, while those with superscript t refer to the species in the free troposphere). Table content mostly adopted from de Arellano et al. (2004).
*: The timescale of O_3 in the boundary layer ranges from hours to 1-2 days depending on the extent of pollution in the region (Monks et al. 2015; Fowler et al. 2008).

worsen at their highest resolution at $0.25° \times 0.3125°$. They suggested that is because finer modes of variability are more difficult to capture in the models with high resolution. Schaap et al. (2015) with their investigation with a number of European CTMs at resolutions ranging from 56 to 7 km also noticed that the model improvement with increasing resolution is less significant in rural areas and for secondary species.

Studies also report similar findings for modelling ozone concentrations in a single city. Based on their studies in Mexico city, Tie et al. (2010) suggested the threshold resolution of a model, that is the minimum resolution adopted before the modelled concentrations are very different from the observed values, is around one-sixth of the size of the city. Beyond that resolution, the improvement of model performance with increasing resolution is not so significant. Valari and Menut (2008) conducted a set of simulations with fixed model resolution at 6 km but with 10 varied resolutions of emission data (from 6 km- to 48 km-resolutions) in Paris, and showed that the optimal resolution is at 12 km, instead of at their highest resolution of 6 km. They suggested that is due to the equilibrium between the model resolution and the input errors, which can be errors from a range of sources such as emission inventories or model algorithms. All these studies suggest that merely increasing the model resolution may not be an effective measure for improving model performance.

One of the possible input errors may come from the subgrid effects that CTMs fail to resolve within a grid mesh. For example, even at a resolution of 1 km, a CTM cannot resolve the turbulent motions inside its grid mesh (for comparison, the length scale of turbulence is $\sim O(10)$ m). Since Donaldson and Hilst (1972), it is known that turbulence process plays a role in the transformation of chemical species in the flow. To assess the effect of turbulence on chemical reactions in the atmosphere, other studies have investigated the specific conditions and scaling parameters of which chemistry is significantly affected by turbulence under various boundary layer flows (e. g. Brost et al. (1988), Gao and Wesely (1994), Verver et al. (1997), Galmarini et al. (1997)). The results from these studies concluded that when the timescale of the chemical reaction involved is of similar

order as the timescale of turbulent mixing (i. e. $Da \sim 1$), atmospheric turbulence controls chemical reaction. The method these author used is mainly to include the chemical terms in the discretised turbulence governing equations to see how the equations with the chemical terms deviate from those with inert tracers. However, with this method, one need a parametrisation for vertical turbulent mixing. Therefore, the research advanced by conducting similar investigation by means of large eddy simulations.

Large-eddy simulation (LES) is a three-dimensional numerical simulation of turbulent flow, in which large eddies are resolved, while the effect of the smaller eddies are parametrised (AMS glossary). With higher resolving power, LES allows further investigation on the governing parameters and the main characteristics of turbulent reacting flows (de Arellano et al. 2004). Schumann (1989) conducted the first LES of a CBL with reactive species. In his simulation, the segregation of the species is due to the coherent structure of the CBL, with one species A emitted from the surface and another species B entrained from the free troposphere. He showed that the chemical reaction between species A and B is slowed down due to insufficient turbulent mixing. The investigation is then continued by a number of studies with similar configurations but with extension to a variety of initial and boundary conditions, such as with a more complex chemical scheme (e. g. Krol et al. (2000) with the RH-O_3 cycle, and Li et al. (2016) with biogenic VOC chemistry), with different weather conditions (e. g. Vilà-Guerau de Arellano et al. (2005) with shallow cumulus), and with heterogeneous fluxes of surface emission (e. g. Krol et al. (2000) with a Gaussian-function emission and Ouwersloot et al. (2011) with varied isoprene flux) and of surface heat (e. g. Ouwersloot et al. (2011)). However, it was found that with strong emission fluxes ($\sim O(0.1)$ ppb m s^{-1}), subgrid turbulent parametrisation in the LES simulations may induce signicant error, especially near the surface where the species is emitted (Vinuesa and de Arellano 2005; Vinuesa and Porté-Agel 2008).

To apply the findings from these LES studies to large-scale models, there are also different attempts to parametrise the effect of turbulence on chemical reactions. A common approach is to calculate the vertical fluxes and covariances of the chemical concentrations using first-order (e. g. Petersen and Holtslag (1999), Geyer and Stutz (2004) and Vinuesa and de Arellano (2005)) and second-order (e. g. Verver et al. (1997) and Lenschow et al. (2016a)) closure methods. These parametrisation schemes were tested in one-dimension and box models, and showed results with good agreement with the LES results. Methods have also been suggested on how to apply these schemes to large-scale models by calculating the segregation coefficient I_S from other quantities of the corresponding turbulent reacting flows such as updraft and downdraft concentrations, and entrainment and emission fluxes (Petersen and Holtslag 1999; Vinuesa and de Arellano 2005), but none of the studies have applied any of these schemes to an operational CTM so far.

1.5 Thesis motivation and objectives

Despite a number of studies have discussed how model resolution affects chemical calculations or model performance of a CTM and how turbulent motions affect chemical reactions in a boundary layer, no study has explicitly examined how the inability to resolve turbulent motions impacts the calculation of chemical reactions in a CTM. Aiming to close this gap at the same time to explore a suitable parametrisation of this subgrid chemical-turbulence interaction for a CTM, this thesis systematically quantifies the effect of turbulent transport on chemical reactions in the boundary layer using a combination of turbulence-resolving and regional scales approaches. The question is put into the context of conditions in urban environments. To achieve the objective of the thesis, the following research questions are raised:

- How does the calculation of ozone chemistry change with grid and emission resolution in a regional chemical-transport model over an urban environment?
- How do turbulent motions affect the rate of chemical reactions of two initially-segregated species in the boundary layer under conditions of urban environments?
- How significant is this effect of inefficient turbulent mixing on chemical reactions in models with grid resolution commensurable with regional CTMs?
- How significant is this effect when applied to an operational regional chemical-transport model?

This thesis is constructed of 3 main chapters: In *Chapter 2*, a study on the sensitivity of ozone chemistry to model resolution is conducted with a WRF-Chem model around the region of Hong Kong. The highly urbanised city of Hong Kong is chosen as a subject of our study because the emissions are relatively strong and highly localised, the flow is particularly complex with multi-scale turbulence, and surface measurements of key chemical species are available. Several simulations are conducted with gradually increased spatial resolution, and statistical quantities related to ozone chemistry are derived in a given domain. Instead of focusing on comparing model results with observational data to assess the improvement on model performance as in the past work, this work puts its focus on comparing model results at different resolutions in order to examine the effect of increasing resolution on the related physical and chemical processes and its reasons behind.

In *Chapter 3*, *direct numerical simulations*[12] (DNS), which explicitly resolve turbulent motions in a convective boundary layer, are conducted with two reacting and initially

[12]The DNS model adopted here has an equivalent resolving power as in a LES model with a suitable Reynolds number adopted. One should refer to Section 3.2.1 for more details on the comparison between the DNS and LES model.

segregated species to explicitly quantify the effect of turbulent motions on chemical reactions in an urban environment. Previous studies on the effect of turbulence on chemical reactions focus either on agricultural/rural conditions, or on urban environments with complex chemistry schemes involving multiple chemical reactions. None of these cases can provide a generalised picture on the question in urban conditions. Therefore, this study addresses the issue with a second-order chemical reaction in the urban PBL under conditions of strong emission fluxes and heterogeneous surface emissions, and with the chemistry between NO and ozone entrained from the free troposphere. The results are then degraded to lower resolution to mimic the calculation in a regional model. Based on the DNS simulations, the effective reaction rate with the influence of turbulence is expressed as a function of the physical and chemical variables of the simulations, in a way that can be applied to our model in Chapter 4.

In *Chapter 4*, the parametrisation formulation deduced from Chapter 3 is applied to the calculation of chemical reaction in the regional model in Chapter 2 to account for the influence of turbulence on the reaction rate of initially segregated species. This will be the first attempt to apply a parametrisation scheme of such effect to a 3D operational Eulerian CTM. It also serves as a bridge between the knowledge of the topic in turbulent-resolving scale and larger-scale models. Statistical quantities related to ozone production are compared between the original and modified models to assess the importance of the subgrid influence of turbulent mixing on chemical reactions in a regional scale.

The overall conclusion and an outlook are given in *Chapter 5*.

Chapter 2

Sensitivity of ozone chemistry to grid and emission resolution in a regional chemical transport model

2.1 Introduction

2.1.1 Chapter objective and outline

Air pollution is a multi-scale problem that spans from local to intercontinental scale. To monitor and understand the nature of air pollution, chemical transport models are employed at a range of resolutions according to the extent of the interested areas. Chemical transport models (CTMs) are particularly sensitive to grid resolution when simulating pollutant concentrations. Spatial resolution of a model can affect model calculations in aspects of the meteorological effect, emissions and chemical processes. These factors change the pollutant distributions in the model, and hence alter the calculation of their chemistry. Due to its non-linear nature, ozone chemistry is prone to be sensitive to model resolution. The ozone production efficiency, i. e. the ozone production rate per unit NO_X, is higher in low-NO_X concentrations (Liu et al. (1987), also known as the NO_X-limited regime). Low-resolution models tend to dilute the precursor concentrations due to their coarse grid size, leading to overestimation in ozone production. Ozone titration by NO may also be suppressed due to the diluted NO_X concentrations, again resulting in enhanced ozone values, especially during nighttime. Moreover, other ozone precursors, such as VOCs, are emitted in sources at different specific locations. For example, isoprene is mainly found in forested areas, while NO_X are emitted in urban areas with highly localised sources. However, in a low-resolution model, all these sources may be included within one coarse grid. In contrast, a high-resolution model recovers the sharp gradient and the segregation of tracer concentrations in the simulated areas, in particular in urban areas, and hence is expected to produce more accurate ozone values.

In this chapter, the sensitivity of the calculation of ozone chemistry to grid resolution in the regional CTM Weather Research and Forecasting model coupled with Chemistry (WRF-Chem) is assessed. Unlike the previous studies (e. g. Jang et al. (1995); Cohan et al. (2006); Queen and Zhang (2008); Valari and Menut (2008); Arunachalam et al. (2006); Schaap et al. (2015); Yu et al. (2016); Tie et al. (2010); Pfister et al. (2014); Tan et al. (2015), also read Section 1.4), this chapter focuses on comparing analysis of the results between different resolutions in order to examine how the calculation of processes related to ozone chemistry changes with model resolution, instead of on comparing with observational data to assess the improvement on model performance. The region around Hong Kong and the ambient Pearl River Delta is selected as a study target due to its complex topography and intense emission, at conditions which increasing model resolution was shown to cause a significant difference in modelled concentrations (e. g. Tan et al. (2015)).

The structure of the chapter is as the following. The background information about the simulated domain is first introduced in Section 2.1. The model configuration, input datasets and set-up are then described in Section 2.2. The results from the runs at different resolutions are then presented and compared in Section 2.3 regarding the distributions and statistics of the variables, their total sum, ozone production and loss rate, and the segregation and correlation between ozone and its precursors. The effect on vertical mixing of the species is evaluated from their vertical profiles. The modelled results are then compared with observational data in Section 2.4. The effect of the resolution of the emission inventory is also evaluated as an additional consideration in Section 2.5. Finally, conclusions and discussions are provided in Section 2.6.

2.1.2 Background information about the simulation domain

The study in this chapter focuses on the area around Hong Kong and the ambient Pearl River Delta region. Hong Kong is located in Southern China at the mouth of Pearl River Delta, bordering the city of Shenzhen in mainland China. There are three major geographical regions in the city of Hong Kong - Hong Kong Island, Kowloon and New Territories (including the outlying islands)(refer to Figure 2.1). The geography of Hong Kong is highly varied, with 60% of the total area being natural terrains, and 260 islands in the territory. The major mountain ranges are Tai Mo Shan in the centre of the New Territories (at elevation of 957 m), Lantau Peak on the Lantau Island (at elevation of 934 m), Ma On Shan (702 m) and Pat Sin Leng (Wong Leng at 639 m) in East New Territories. The flatlands are mainly located in the northern New Territories, Kowloon and the circumference of Hong Kong Island. The abundance of islands also provides Hong Kong with a number of harbour channels, such as the Victoria Harbour between Hong Kong Island and Kowloon, and the West Lamma Channel between Cheung Chau and Lamma Island. The complex geographic topography of Hong Kong complicates the

wind flows in the region.

With a total population of 7.45 millions[1], Hong Kong is an intensely-urbanised city. It is the city with the most skyscrapers (buildings taller than 150 m) in the world, and around 8,500 high-rising buildings (100 m or higher), among which include many for residential purpose. More than half the population are living on the 15^{th} floors or higher, making Hong Kong the highest urban agglomeration in the world[2]. The intense urbanisation further complicates the topography of Hong Kong. Due to its abundance of mountains and islands, only less than 25% of the areas in Hong Kong are of urban use (the areas in brown and orange on Figure 2.2), which are concentrated in the north of Hong Kong Island, Kowloon, and the new towns[3] located mainly in the eastern and the northwestern New Territories. Nowadays most of the urban lands in Hong Kong are used as commercial and residential purposes, as most of the factories moved to the mainland China before the 1990s. 40% of the other areas, which are mainly located around the terrains, are reserved as country parks (the areas in green on Figure 2.2).

Hong Kong suffers from serious air pollution. For example, only 4 out of the 16 air quality monitoring stations recorded an annual average NO_2 level within the compliance of the World Health Organisation Air Quality Guidelines in 2018[4]. The problem of air pollution in Hong Kong are mainly from two issues, local street-level pollution and regional smog (HKEPD Air Science Group 2016). Local street-level pollution is contributed from the pollutants from road transport, while the regional smog problem is a combination effect of emissions from road transport, shipping, industry and power plants in both Hong Kong and the ambient Pearl River Delta region. The main emission point sources in the city are the power plants in the Castle Peak and on the Lamma Island, and the port in Kwai Chung (Figure 2.3). A huge amount of pollutants are transported from the ambient Pearl River Delta region. The transport is most intense during the wintertime due to the prevailing northeasterly winds in the South Asia monsoon system. Some major ambient point sources ambient to Hong Kong are the She Kou ports and the Mawan power plant (Figure 2.3).

[1]According to the mid-2018 statistics released by the Census and Statistics Department, HKSAR government

[2]From the Global Tall Building Database of the Council on Tall Buildings and Urban Habitat (`http://www.skyscrapercenter.com/`)

[3]A planned urban centre created in an undeveloped or rural area to accommodate the booming population in Hong Kong after the Second World War. Similar to the "satellite town" in the United Kingdom.

[4]The compliance of the annual average NO_2 concentration in the World Health Organisation Air Quality Guidelines is 40 $\mu g/m^3$ (Organization et al. 2005).

Figure 2.1: Elevation map of Hong Kong, showing the three major territories in Hong Kong (Hong Kong Island, Kowloon, and New Territories, labelled in brown) and some part of Shenzhen (in white). It also shows the geological topography such as the major terrains and mountain peaks (marked in triangle), and the water channels concerned in later discussion.

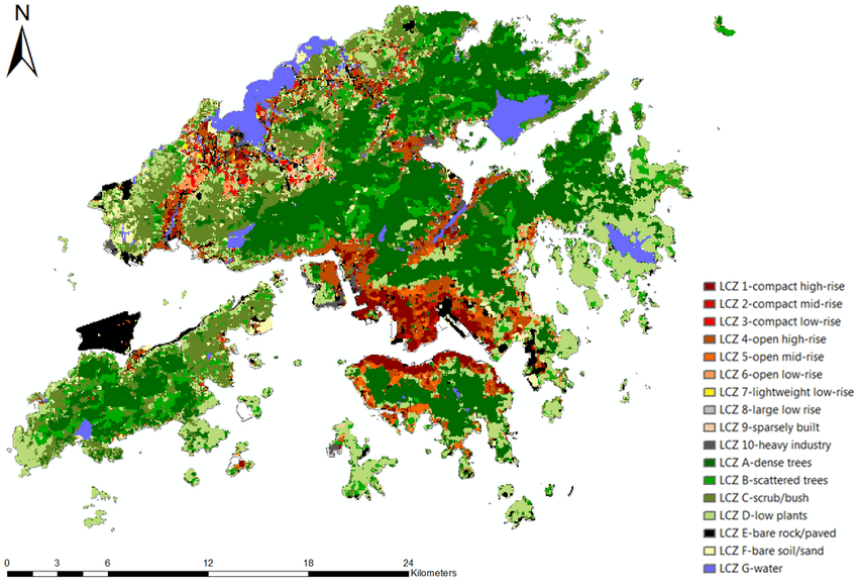

Figure 2.2: Landuse map of Hong Kong. The black/brown areas refer to the developed land, among which most of them are of urban landuse. The green areas are vegetated, mainly located around the terrains and reserved as country parks.

Figure 2.3: Map showing the point sources in and around Hong Kong. The main point sources inside the territory of Hong Kong are the power plants in Castle Peak and on Lamma Island, and the port in Kwai Chung. Ma Wan port and power station and the She Kou port in Shenzhen also pose serious influences on the air quality in Hong Kong.

Figure 2.4: Locations of the 16 observation stations of the Air Quality Monitoring Network operated by the HKEPD. The stations are classified into 4 categories - Roadside (marked in red solid), Urban (red circle), New Town (blue solid) and Rural (green solid).

2.1.3 Observation stations in Hong Kong

The air quality in Hong Kong is monitored by the Environmental Protection Department of the Hong Kong SAR Government (HKEPD). There are in total 16 observation stations in the Air Quality Monitoring Network operated by the HKEPD around the city of Hong Kong. The locations of the stations are shown on the map in Figure 2.4. Each of these stations contains equipments to measure the concentrations of carbon monoxide, nitrogen oxides, sulphur dioxide, ozone, PM 10 and PM 2.5. The hourly data are available online from the year 1990 to present on the HKEPD online archive (`https://cd.epic.epd.gov.hk/EPICDI/air/station/`), from which the observational data are collected for model validation.

Name	Code	Latitude	Longitude	Height (m)	Type
Central	CL	22.2818	114.1581	4.5	Roadside
Causeway Bay	CB	22.2802	114.1851	3	Roadside
Mong Kok	MK	22.3227	114.1683	3	Roadside
CentralWestern	CW	22.2849	114.1444	16	Urban
Eastern	EN	22.2829	114.2194	15	Urban
Kwai Chung	KC	22.3571	114.1296	13	Urban
Kwun Tong	KT	22.3134	114.2248	25	Urban
Sham Shui Po	SSP	22.3303	114.1591	17	Urban
Tseung Kwan O	TKO	22.3177	114.2696	16	Urban
Tsuen Wan	TW	22.3718	114.1145	17	Urban
Shatin	ST	22.3763	114.1845	25	New Town
Tai Po	TP	22.4510	114.1646	28	New Town
Tuen Mun	TMC	22.3912	113.9767	27	New Town
Tung Chung	TC	22.2889	113.9437	27.5	New Town
Yuen Long	YL	22.4452	114.0227	25	New Town
Tap Mun	TM	22.4714	114.3607	11	Rural

Table 2.1: List of observational stations in the HKEPD Air Quality Monitoring Network, showing the name, the abbreviated code, the location in latitude and longitude and the corresponding category of the individual stations.

The 16 stations are classified into 4 categories, Roadside, Urban, New Town and Rural, based on their surrounding environments. Table 2.1 lists the location, height and classification of the stations. The 3 Roadside stations (Mong Kok, Causeway Bay, and Central) are located right next to a road in the busiest urban areas in Hong Kong (3-5 m above the ground), with mixed residential and commercial landuse with heavy transport and tall buildings in the surrounding (refer to Figure 2.5). Other stations are located on buildings (10-30 m above ground). The Urban stations are located in the densely populated areas mixed with commercial and industrial landuse in Kowloon and the north of the Hong Kong Island. The New Town stations are located in the new towns in the New Territories with mainly residential purposes. The Rural station is located in the rural area of Tap Mun. It is far away from the local sources and is often treated as a background station. Figure 2.6 shows the surroundings of a station from each of these station categories.

Figure 2.5: The Roadside observation station in Central (left panel) and its surrounding (right panel). The measurement equipments of the Roadside stations are located on the side of a road. Photos from the website of HKEPD.

Figure 2.6: The general observation stations in Sham Shui Po (Urban, left panel), Shatin (New Town, middle panel), and Tap Mun (Rural, right panel). The degree of urbanisation diminishes from the left to the right. Photos from the website of HKEPD.

2.2 Methods

2.2.1 Model configuration

The simulations conducted in this chapter adopt similar model configurations as in Bouarar et al. (2017). The Weather Research and Forecasting model (Skamarock et al. 2008) version 3.6.1 coupled with chemistry and aerosols (Grell et al. (2005); Fast et al. (2006); hereafter the WRF-Chem model) is employed to simulate the meteorology and chemistry in Hong Kong and the ambient Pearl River Delta region. Four model domains centred around Hong Kong are constructed in our WRF-Chem simulations (refer to Figure 2.8). Domain d01, the largest domain at grid resolution of 27 km $\times$ 27 km, extends from South-East China to the north of Vietnam and the Philippines to cover most of the the polluted areas in Southern China. Domain d02 encompasses the Guangdong and Guangxi Provinces, the two south-most provinces in mainland China, at grid resolution of 9 km $\times$ 9 km. Domain d03 covers the Pearl River Delta, including also the megacity Guangzhou, at grid resolution of 3 km $\times$ 3 km. Domain d04, the smallest domain,

includes the whole city of Hong Kong and part of southern Shenzhen, at grid resolution of 1 km $\times$ 1 km. The four domains are nested one-way by the program NDOWN, such that the initial and boundary conditions of the 3 smaller domains (Domain d02, d03 and d04) are generated consecutively from the runs of the larger mother domain. The model consists of 51 vertical levels from the surface to 10 hPa (around 30 km). The altitude of the first model layer is at approximately 30 m above the ground, with a vertical spacing of about 40-50 m at the first 1 km, of 200-450 m for altitudes of 1-3 km and of 500-700 m for altitudes between 4 and 14 km. There are usually 9-10 levels within the first 1 km in the model, around the height of the top of the boundary layer when the boundary layer is fully grown.

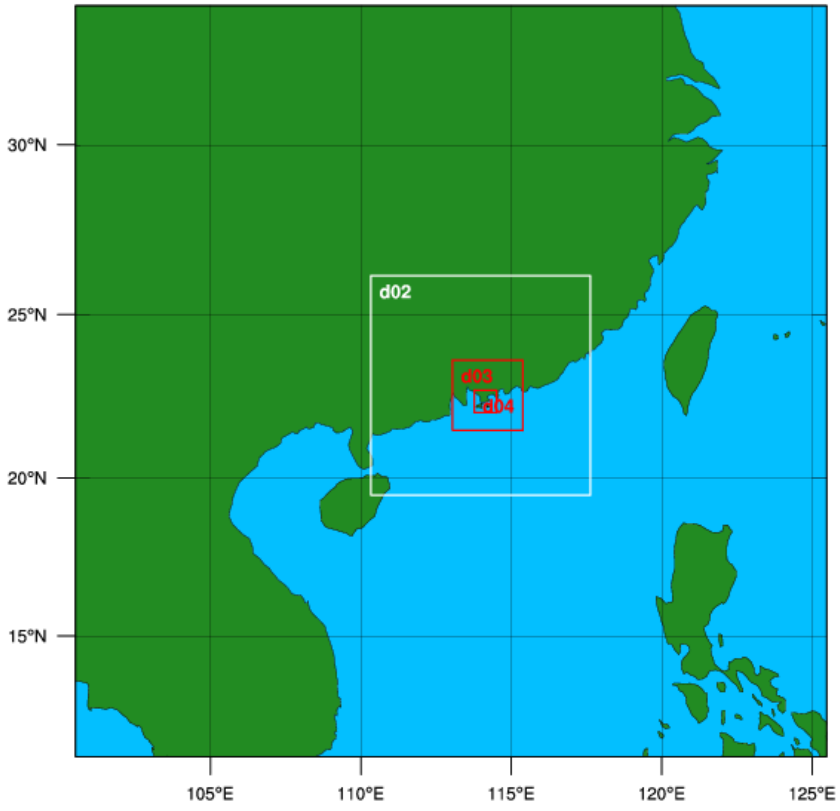

Figure 2.7: Simulation domains of the WRF-Chem simulations. Domain d01, d02, d03 and d04 are at resolutions of 27, 9, 3 and 1 km respectively. They are nested one-way. The innermost domain d04 is the main simulation domain in interest.

The options in the WRF runs are briefly described here. One can also refer to Bouarar et al. (2017) for more details. For the physics options, the resolved scale cloud physics is represented by the Thompson microphysics scheme (Thompson et al. 2004, 2008) . The sub-grid scale effects of convective and shallow clouds are parametrised as in Grell and Freitas (2013). The Goddard scheme (Chou et al. 1998) and the Rapid

Radiative Transfer Model (RRTM) (Mlawer et al. 1997) are employed to represent the short- and long-wave radiative transfer in the atmosphere respectively. The NOAH land-surface model (Chen and Dudhia 2001) and the revised MM5 Monin-Obukhov surface layer scheme are used to calculate the surface processes. The Yonsei University (YSU) boundary layer scheme (Hong et al. 2006) is applied to parametrise the vertical sub-grid scale fluxes due to eddy transport in the lower troposphere. It is a first-order nonlocal scheme consisting of a countergradient term and an explicit entrainment term in the turbulence flux equation.

Among the options in the chemistry module, the gas-phase chemistry in the simulation is calculated by the Model for Ozone and Related Chemical Tracers (MOZART-4) chemical scheme (Emmons et al. 2010). The aerosol processes are simulated by coupling MOZART with the Goddard Chemistry Aerosol Radiation and Transport (GOCART) aerosol module, which is a bulk aerosol model providing total mass information on sulphate, organic and black carbon, PM2.5 and PM10, and includes a sectional scheme for dust (5 bins) and sea salt (4 bins)(Chin et al. 2002; Ginoux et al. 2001). Subgrid convective parametrisation is applied on the chemical species to avoid underestimation of transport out of the boundary layer. A WRF-Chem model with similar configuration, with the exception of replacing the GOCART aerosol scheme by the MOSAIC scheme (Zaveri et al. 2008), has been successfully operated since 2016 to forecast air quality in China in the Marco Polo-Panda project[5].

2.2.2 Model input datasets

For the meteorology, the dataset of the corresponding time from the National Center for Environmental Prediction Global Forecast System (NCEP GFS) 0.25 Degree Global Forecast Grids Historical Archive is taken as the initial and lateral boundary conditions, which is at a horizontal resolution of $0.25^\circ \times 0.25^\circ$, with temporal resolution of 6 hours[6] (NCEP GFS 2015). The data are interpolated to the model grid using the standard WRF preprocessing system (WPS).

For the chemical and aerosol species, the initial and lateral boundary conditions are provided by the global operational forecasting system implemented within the EU MACC project[7] (Flemming et al. 2009, 2015). The MACC products are based on the MOZART model and are constrained by assimilation of CO, O_3 and NO_2 observations from several satellite instruments in the ECMWF 4D-Var assimilation system (Inness et al. 2015). Since the MOZART model consists of detailed formulations of VOC speciation and aerosol concentrations, the missing species in the MACC datasets required by MOZART, such as some VOC species, are provided by the MOZART-4 global model

[5]Online forecasts available on `http://www.marcopolo-panda.eu`

[6]One can download the datasets from `https://rda.ucar.edu/datasets/ds084.1/`

[7]Now is called CAMS (https://atmosphere.copernicus.eu)

forecasts from the National Center for Atmospheric Research (NCAR)[8] (Emmons et al. 2010). The emissions of trace species from biomass burning are taken from the Fire Inventory from NCAR version 1.5 (FINN v1.5) (Wiedinmyer et al. 2014), and are then distributed vertically in the model following the online plume-rise module (Freitas et al. 2011). Biogenic emissions of trace species from terrestrial ecosystems are obtained online from the Model of Emissions of Gases and Aerosols from Nature (MEGAN) version 2.04 (Guenther et al. 2006). Dust and seas salt are calculated using the GOCART emission scheme (Ginoux et al. 2001).

For anthropogenic emission, the MarcoPolo emission inventory is adopted in this study. The MarcoPolo emission inventory provides monthly emissions in East and Central China for the year 2014 (Hooyberghs et al. 2016). It contains several pollutant species including NO_X, $PM_{2.5}$, PM_{10}, BC, SO_2, VOCs, NH_3 and CO, categorised in six different sectors, namely industry, residential, energy, transport, agriculture and international shipping. The dataset includes a standard resolution inventory and a high resolution inventory. The standard resolution inventory, at a resolution of $0.25° \times 0.25°$, covers most part of China containing most major Chinese cities, the Korean peninsula, and part of Mongolia. It is mainly based on top-down emission estimates from satellite data (Stavrakou et al. 2016). The source sector information is based on the 2010 MIX- (Li et al. 2017) and the 2012 MEIC-inventory. The high resolution inventory, at a resolution of $0.01° \times 0.01°$, is available for three selected regions in China, the Beijing-Tianjin area, the Yangtze River Delta and the Pearl River Delta (green boxes in Figure 2.8 left panel). It is compiled by downscaling the standard resolution inventory . The downscaling techniques include using open source proxy data containing road maps (Open Street Maps), locations of power plants (Enipedia), population density (WorldPop) and landuse/land cover data (GlobCover). In this study the MarcoPolo high resolution inventory for the Pearl River Delta is used within the available domain, which is shown in Figure 2.8.

[8]can be obtained online from `http://www.acom.ucar.edu/wrf-chem/mozart.shtml`

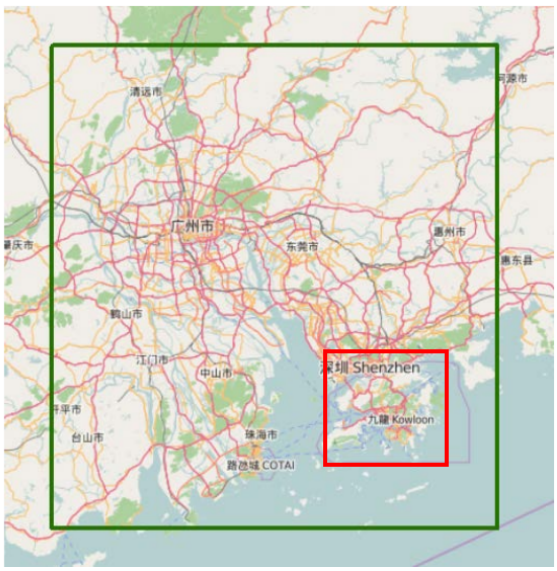

Figure 2.8: Domain of the high-resolution Marco Polo emission inventory in the Pearl River Delta region at a resolution of 0.01° × 0.01° (equivalent to a resolution of 1 km). The red box shows the innermost simulation domain d04.

The MarcoPolo datasets do not provide a VOC speciation scheme suitable for the MOZART scheme. The VOC emissions in MarcoPolo dataset are speciated according to the VOC speciation in the HTAPv2 emission inventory, which is adopted in Bouarar et al. (2017). The HTAPv2 emission inventory consists of gridmaps at the resolution of 0.1° × 0.1° containing several species including a list of non-methane VOCs for the years 2008 and 2010 (Janssens-Maenhout et al. 2015). The dataset is available on the ECCAD data portal[9]. Table A.1 lists the percentage of each VOC species in each sector over the total amount of VOC emissions in the HTAPv2 dataset in Domain d04. The VOC speciation of the MarcoPolo dataset is calculated according to the corresponding portion of each species in each sector. The HTAPv2 is also adopted for the regions outside the available domain of the high-resolution MarcoPolo emission inventory.

2.2.3 Model simulations

The WRF-Chem simulations are run in the two 11-day periods of 21st -31th July 2016 (Summer) and 19th -29th January 2017 (Winter). The simulations are conducted in both Summer and Winter time period to investigate the difference in the characteristic of pollution episodes in Hong Kong in the two seasons mainly due to the change in the prevailing wind direction. In Winter, the pressure difference between the cold mainland China and the warm South China sea gives rise to the northeast monsoon, bringing the pollutants from the mainland China to Hong Kong. On the other hand, in Summer,

[9]Dataset downloaded from http://eccad.aeris-data.fr

the sea breeze from the South China Sea brings relatively clean air to the territory. Therefore, air pollution is usually more severe during winter in Hong Kong.

The two specific 11-day periods are chosen such that there is no rainfall among most of the days simulated, according to the weather record from the Hong Kong Observatory[10]. There are long sunshine hours during those days, which favours ozone photochemistry. This also satisfies the clear-sky condition, which fits the conditions in the simulations in Chapter 3.

2.3 Results

2.3.1 Showcase on 27$^{\text{th}}$ January 2017

To illustrate the general effect of increasing resolution on model results related to the transport and chemistry of pollutants, the meteorological, emission and chemical model outputs from the simulations at the 4 different horizontal resolutions (27, 9, 3 and 1 km) on the day of 27$^{\text{th}}$ January 2017 (winter time) at 11 am (the morning case) and at 11 pm (the night case) are presented in colour maps in this section. Data at the first vertical level within in the innermost simulation domain, Domain d04 (Figure 2.8) are displayed in this section.

Figure 2.9 shows the maps of the contours of temperature at 2 m (in °C) and the vectors of horizontal winds (in m s^{-1}) at the first vertical layer at 11 am. For the temperature, at the lower resolutions (27 and 9 km), the model shows a general pattern that the inland areas (in the north) are warmer than the coastal areas (in the south). However, they show no local temperature variations, as it fails to resolve the local topographies. On the other hand, at the higher resolutions, especially at 1 km, the model can show substantial drops in temperature around the major mountain ranges such as the Pat Sin Leng, Tai Mo Shan and the Lantau Peak mountain ranges, and higher temperatures on the flatlands. For the winds, at a resolution higher than 27 km, the model shows a general trend of the northeasterly winds, which matches with the HKO record. But only beyond the resolution of 3 km can the model show the impact of mountain ranges (particularly around Tai Mo Shan and Lantau Peak) and the harbour channels (across the Victoria Harbour and the West Lamma Channel).

[10]Past weather records available from https://www.hko.gov.hk/wxinfo/pastwx/past.htm

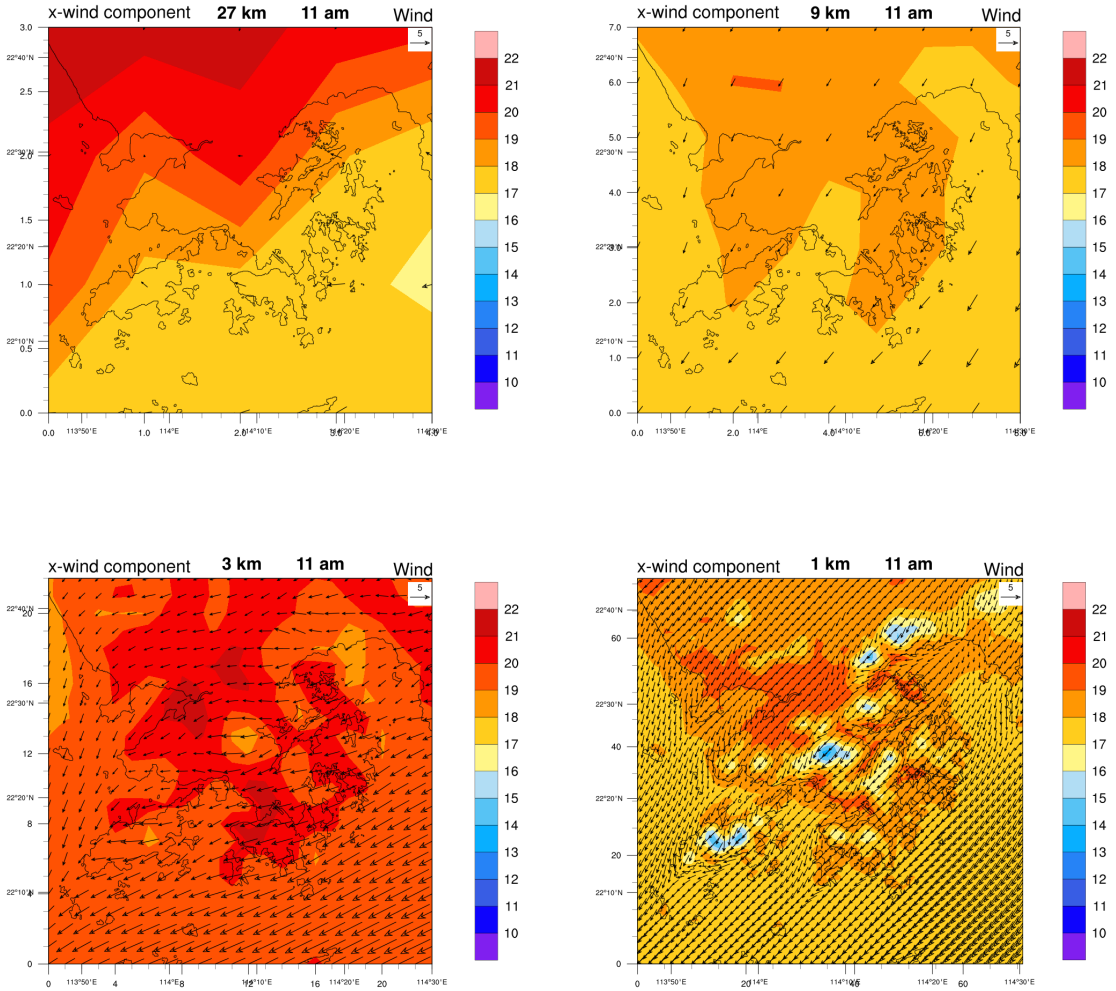

Figure 2.9: Temperature colour maps with surface wind vectors at resolution of 27 km (top-left) 9 km (top right), 3 km (bottom-left) and 1 km (bottom-right) in Domain d04 on 27-01-2017 at 11 AM. The coloured contour refers to the temperature at 2 m. The vectors refer to the horizontal winds at the surface. The scale of the wind vector is shown at the top-right corner of the bottom-right panel.

Figure 2.10 shows the same maps at 11 pm on 27th January 2017. One can see that except at the resolution of 27 km, the model shows a lower temperature over the landmass, but only at the resolutions of 3 and 1 km can the model show the lower temperatures around the mountain ranges. Again, at the resolutions of 9, 3 and 1 km, the model can show the trend of the easterly winds in the east and the southeasterly winds in the north of the domain, but only at the resolution of 1 km can the model show clear enough the effect of mountain ranges and harbour channels on the winds. Therefore, it is advised to adopt a resolution of at least 3 km, and even higher resolution at nighttime, to account for the effect of local geographical topography on the meteorology in Hong

Kong.

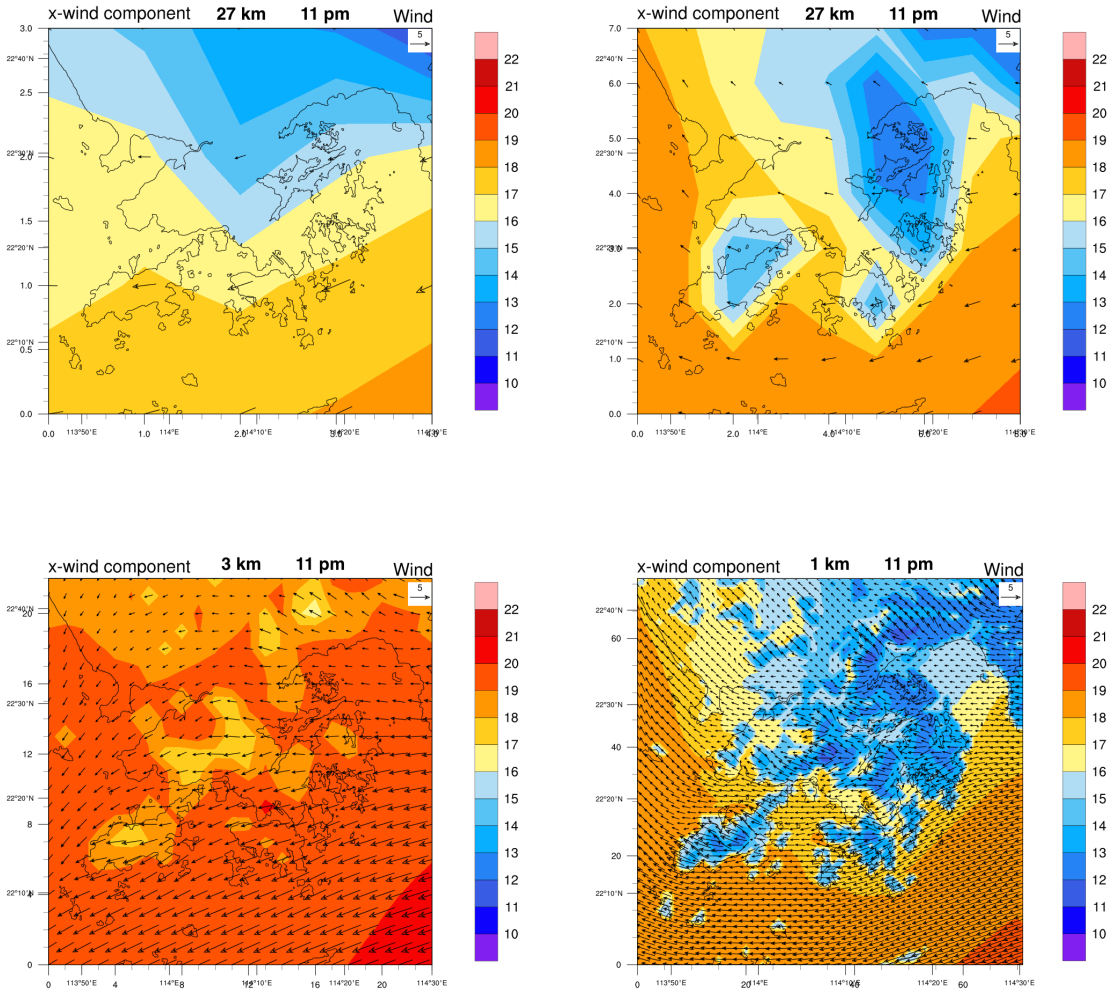

Figure 2.10: Temperature colour maps with surface wind vectors at resolution of 27 km (top-left) 9 km (top right), 3 km (bottom-left) and 1 km (bottom-right) in Domain d04 on 27-01-2017 at 11 PM. Similar description as in Figure 2.9.

Second, the emission fluxes of CO and NO_X (in unit of mol km^{-2} hr^{-1}) at different grid resolutions are inspected. Since the emissions do not vary diurnally in the model, only the colour maps of the emissions at 11 am on 27th January 2017 are shown here.

Figure 2.11 shows the spatial distribution of the CO emission flux. The main sources of CO in the region are vehicle exhausts and fuel combustion (HKEPD Air Science Group 2016). At the resolutions of 27 km and 9 km, the model can only show the higher emissions at the north because the model fails to resolve the exact location of the landmass (source areas) and the sea (relatively clean areas). As the resolution increases, the model can show a higher emission around the urban regions in the domain. At the

resolution of 1 km, it can even show clearly the emission hotspots at the power plants, around the highway network in Shenzhen, and the highly-populated regions in Hong Kong (e. g. Kowloon and north of Hong Kong Island, and new towns such as Shatin and Tai Po in the East, and Tuen Mun and Yuen Long in the West of New Territories).

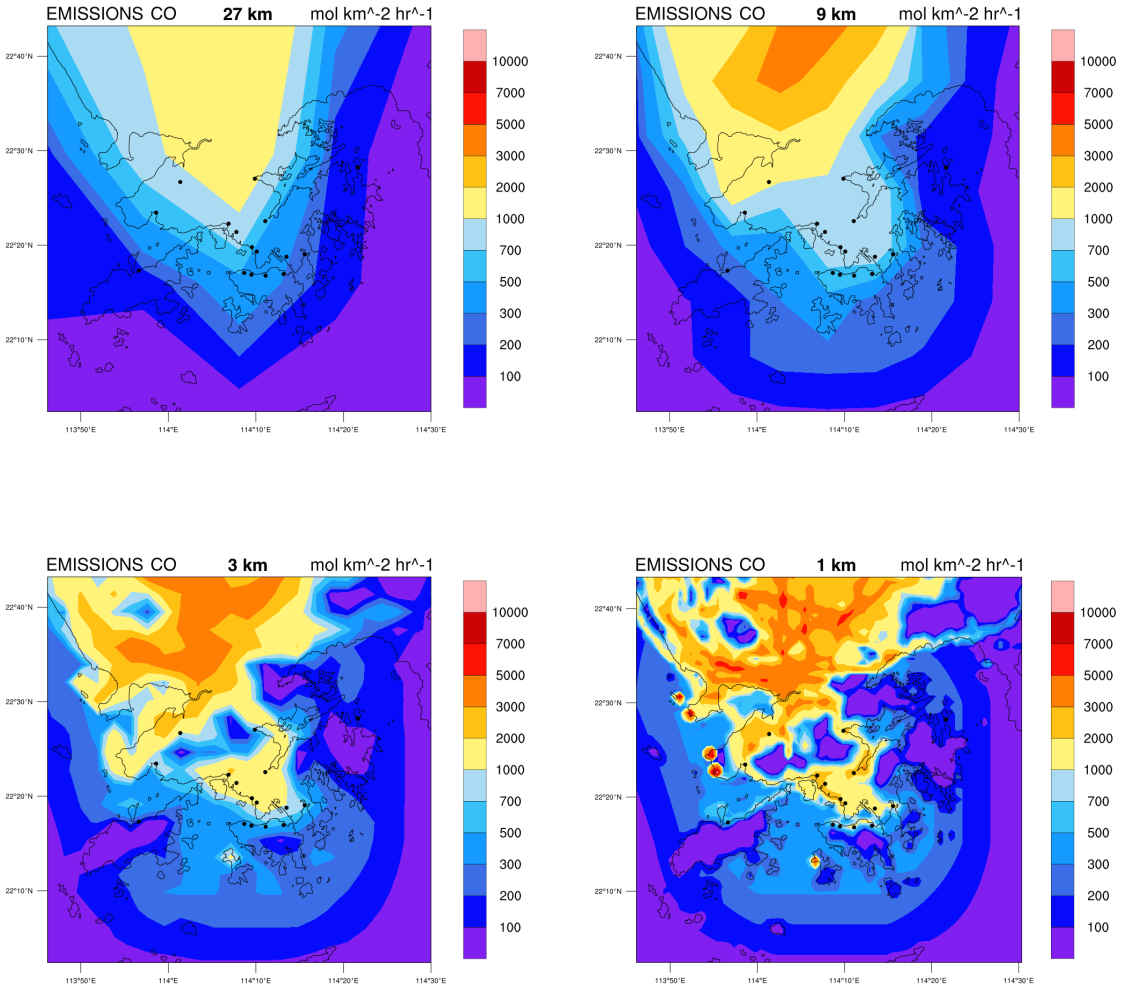

Figure 2.11: Spatial distribution of CO emission fluxes in mol km^{-2} hr^{-1} at resolution of 27 km (top-left), 9 km (top-right), 3 km (bottom-left) and 1 km (bottom-right) in Domain d04. The data at 11 am on 27^{th} January 2017 are shown here.

Figure 2.12 shows the same colour maps for NO_X emission. The emissions of NO and NO_2 are calculated from the total emission of NO_X at a fixed ratio of 9:1. Therefore, the distribution of NO_X emissions sufficiently represents those of NO and NO_2. The main sources of NO_X emission in the region are power plants and vehicles and marine vessels (HKEPD Air Science Group 2016). The change in spatial distribution of the NO_X emission fluxes with increasing resolution is very similar to that of CO, except

that the highway network in Shenzhen contributes less to NO_X than to CO emissions. So most of the NO_X emission hotspots are from the power plants and Shekou ports. The inventory also does not show the emissions from ships and vessels.

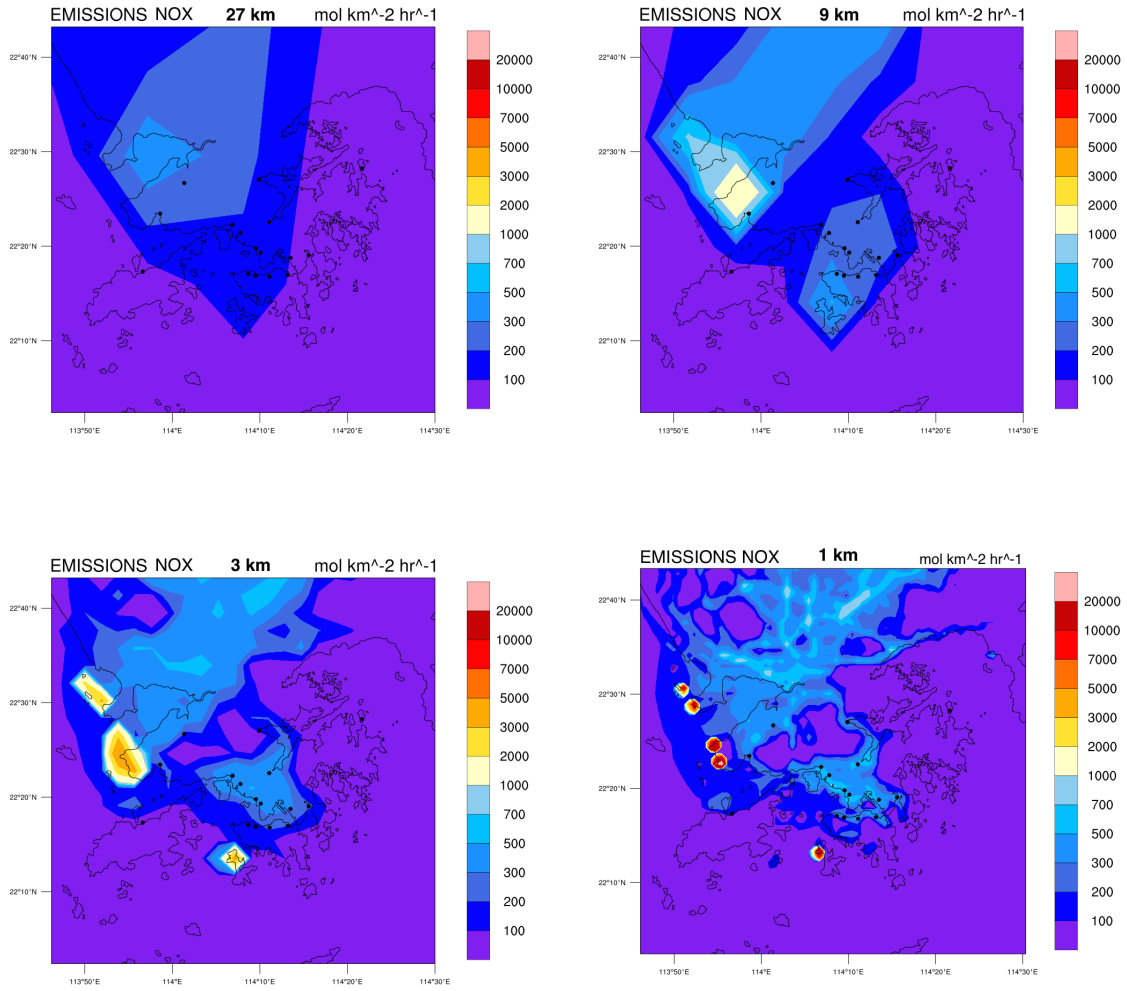

Figure 2.12: Spatial distribution of NO_X emission fluxes in mol km^{-2} hr^{-1} at resolution of 27 km (top-left), 9 km (top-right), 3 km (bottom-left) and 1 km (bottom-right) in Domain d04. The data at 11 am on 27th January 2017 are shown here. Note that the contours of NO_X emission flux are in logarithmic scale.

With the insights of how resolution affects the meteorology and emissions, the effect of increasing grid resolution on the modelled chemical concentrations is now investigated. Here the discussion focuses on the pollutants CO, NO, NO_2 and O_3. CO is a pollutant with long chemical lifetime (in weeks). Its distribution therefore mainly depends on transport. On the other hand, NO, NO_2 and O_3 are chemically active and inter-dependent by the titration of O_3 by NO_X with the chemical cycle of Reaction 1.14

and 1.15 (refer to Section 1.2 for more detailed information).

Figure 2.13 - 2.16 show the contours of the surface mixing ratios of CO, NO, NO_2 and O_3 respectively in the domain d04 at 11 am on 27 January 2017. For CO (Figure 2.13), at all resolutions, the model shows a peak of CO mixing ratio near the She Kou ports. Only at resolution of 1 km can the model resolve the peak near the Castle Peak power plants. In the meanwhile, it is relatively clean in other areas. Ignoring the intensity of the peak(s), the model shows similar pattern across the 4 resolutions in general, that the north-west part of the domain is more polluted with CO.

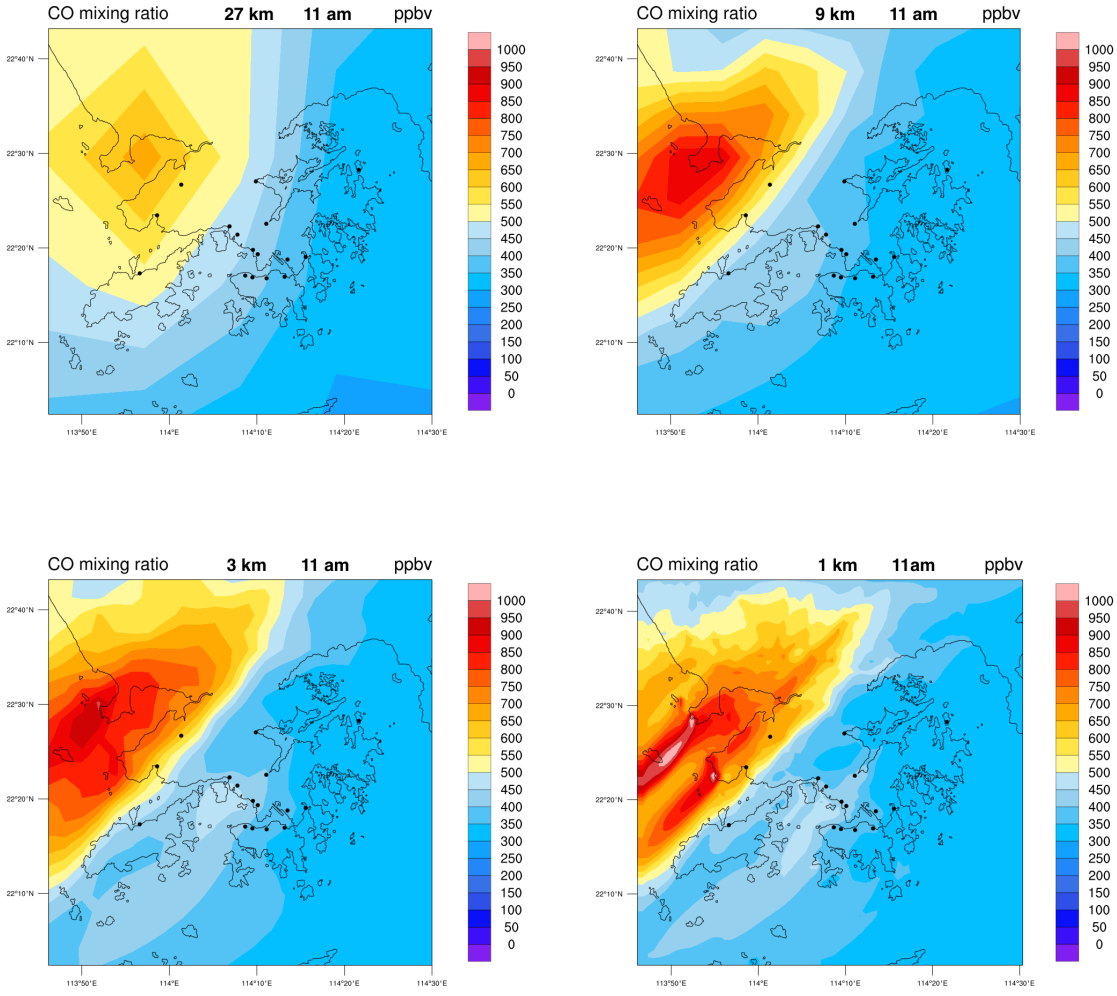

Figure 2.13: Colour maps of CO surface mixing ratio at resolution of 27 km (top-left), 9 km (top-right), 3 km (bottom-left) and 1 km (bottom-right) in Domain d04 at 11 am on 27th January 2017.

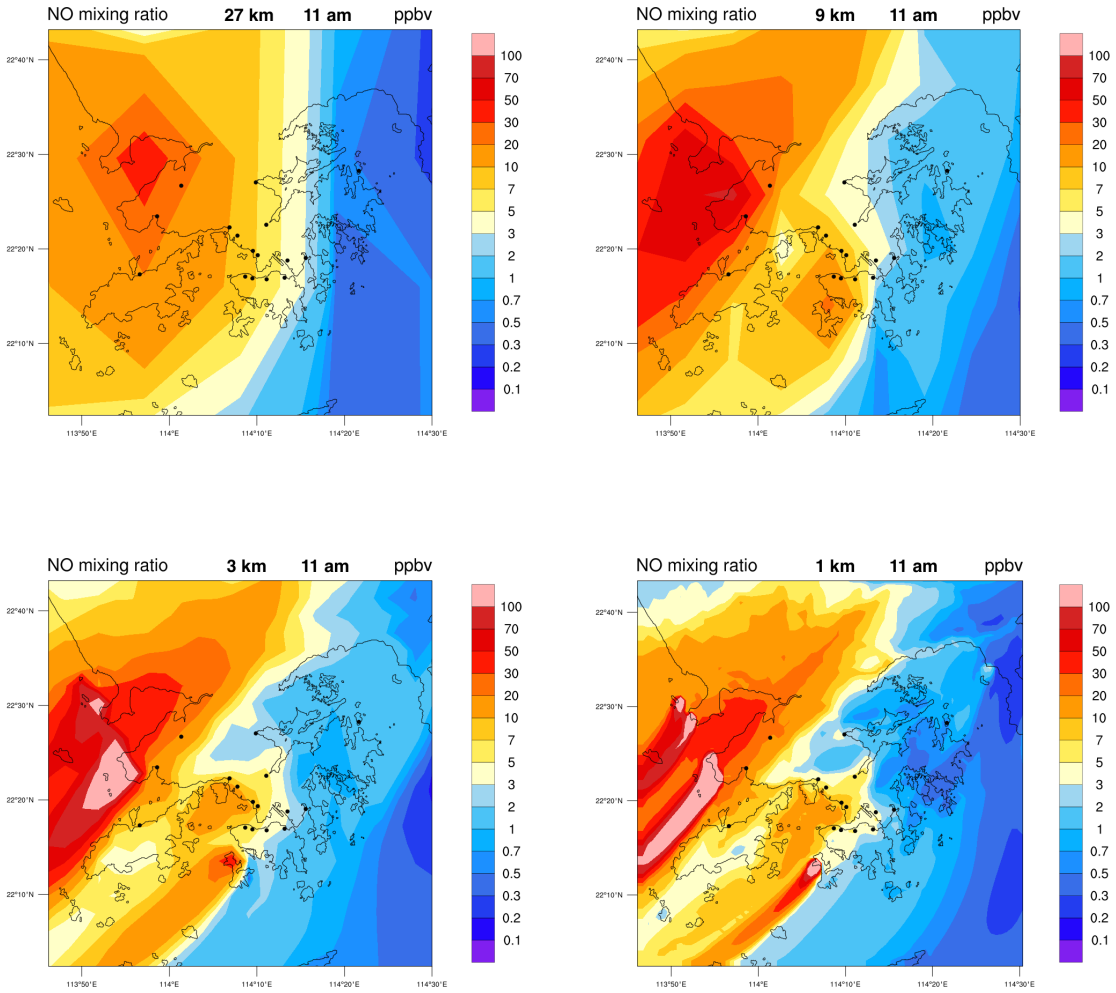

Figure 2.14: Colour maps of NO surface mixing ratio at resolution of 27 km (top-left), 9 km (top-right), 3 km (bottom-left) and 1 km (bottom-right) in Domain d04 at 11 am on 27$^{\text{th}}$ January 2017. Note that the contours of the NO mixing ratio are in logarithmic scale.

Similar situation also applies for NO (Figure 2.14). For all resolutions, the west half of the simulation domain is more polluted with NO due to the presence of the point sources in the west. The high-concentration areas of NO is more extended than that of CO because the Lamma power plant contributes more NO than CO emissions. Only at resolution up to 3 km can the model resolve the individual high-NO maxima at She Kou and Castle Peak (as the two locations are only 6 km away) and relatively high values in the areas west of Kowloon and along the West Lamma Channel (due to the Kwai Chung port). At the resolution of 3 km, the model starts to show drops in concentration from the ambient values only around Tai Mo Shan and downwind of the Lautau Peaks (the mountains block the advection of NO from the urban areas) . But at resolution of 1 km, the model shows drops also around other terrains. This is because at low

resolution, the height of a mountain is averaged out and the elevation of the terrains are underestimated. Therefore, the NO concentrations on the mountains are closer to the high values on ground level. Also, only at the resolution of 1 km can the model show higher values in the north of Hong Kong island and around the new towns (especially in Shatin and Tai Po), where traffic is heavy, and sharper high concentration areas in the downwind tails of the power plants. With higher resolution, the model also gives more extended high-concentration tails of NO downwind of the point sources due to less dilution in finer-size grid cells.

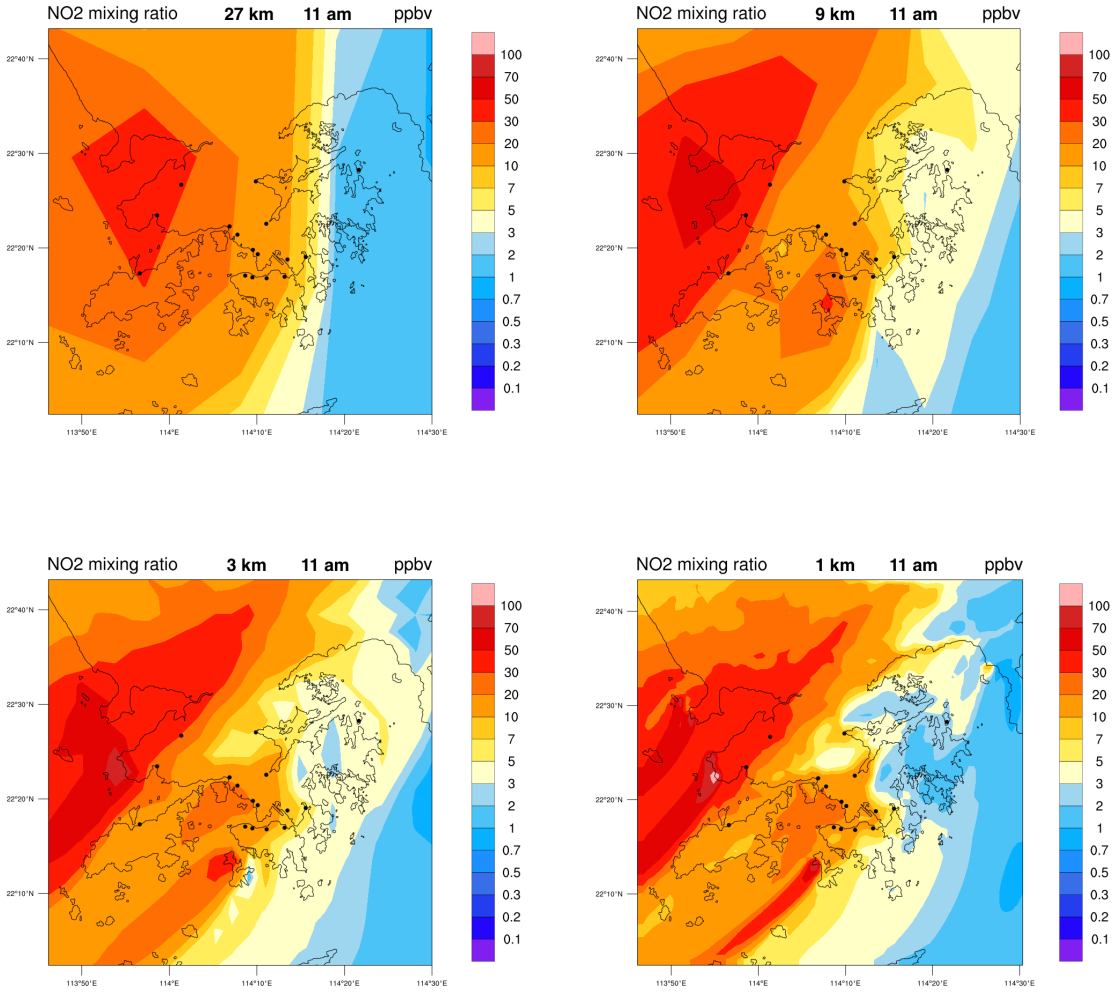

Figure 2.15: Colour maps of NO_2 surface mixing ratio at resolution of 27 km (top-left), 9 km (top-right), 3 km (bottom-left) and 1 km (bottom-right) in Domain d04 at 11 am on 27th January 2017. Note that the contours of the NO_2 mixing ratio are in logarithmic scale.

The NO_2 mixing ratio (Figure 2.15) follows similar distribution and pattern but with shallower concentration gradient than in the NO maps. Note that the high-NO_2 areas are

more extended than those for NO (compare the spatial coverage of the 5 ppbv contours of Figure 2.14 and 2.15). This is because NO_2 is mostly formed chemically (because the emission of NO and NO_2 is in a 9:1 ratio), and it takes time for the secondary NO_2 to form downwind of the point sources, prolonging the lifetime of NO_2.

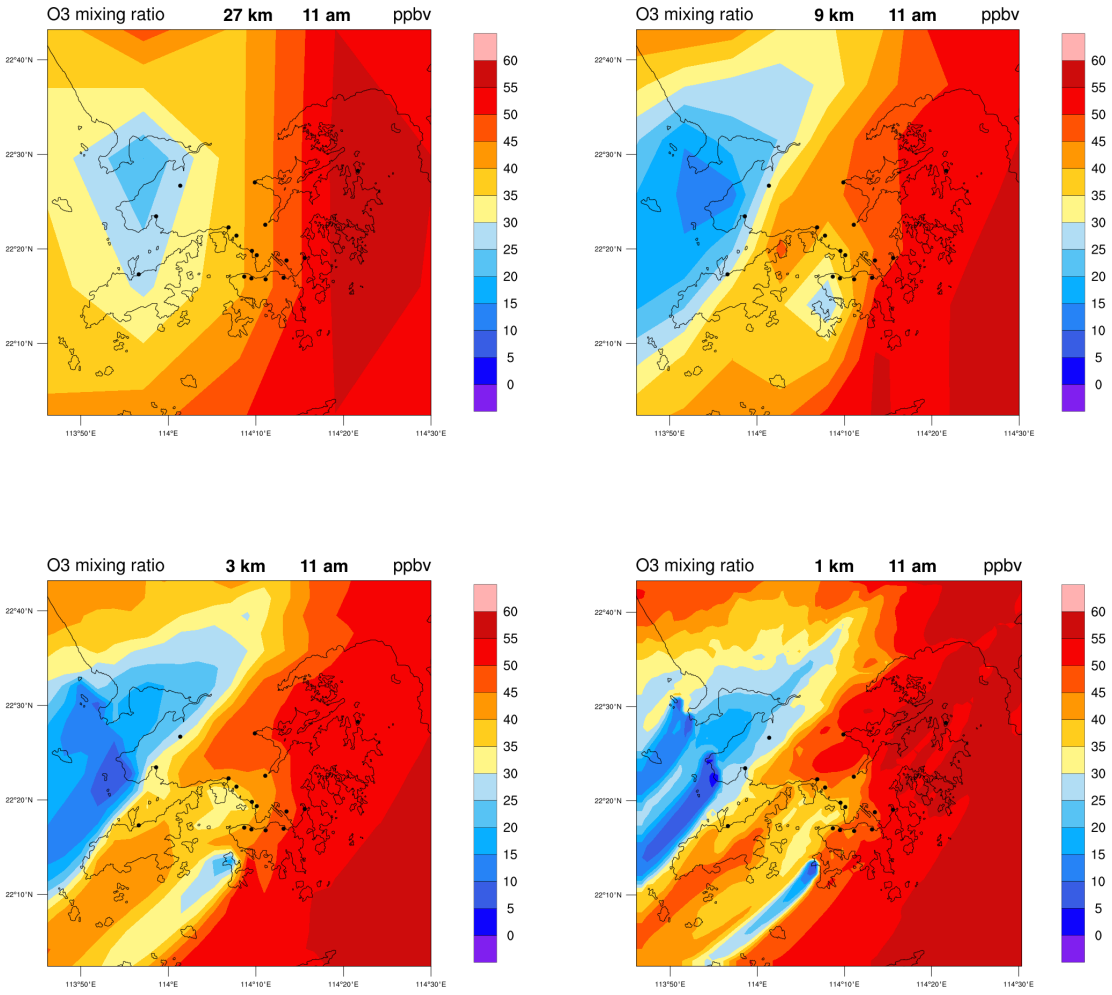

Figure 2.16: Colour maps of O_3 surface mixing ratio at resolution of 27 km (top-left), 9 km (top-right), 3 km (bottom-left) and 1 km (bottom-right) in Domain d04 at 11 am on 27th January 2017.

Due to the heavy NO_X titration of O_3 by NO_X, the resultant O_3 mixing ratio (Figure 2.16) follows an opposite pattern from those of NO and NO_2. In general, the concentration of O_3 is higher in the east half of the domain than in the west at all resolutions, as most of the local sources are located in the west and NO_X is more abundant there to titrate O_3. At the resolution of 27 km, there is only one local minima of the O_3 mixing ratio in the whole domain, located near the She Kou port. At the resolution of 9 km, the areas with low ozone values extend to the downwind regions of She Kou and Castle Peak, and there is another minima around the Lamma power plant. At the resolution of 3 km, the lower-value region also extends to the downwind region of the Lamma power plant, and a high-value region is visible downwind of the Lantau Peaks (due to the lower NO_X concentrations there). At the resolution of 1 km, the model shows sharper tails of low ozone-value areas at the downwind of the power plants, and higher values around the mountain ranges and downwind of the Lantau Peaks.

Figure A.1 - A.4 in Appendix A show the same maps as the previous ones but at 11 pm. For CO (Figure A.1), the peak of mixing ratio shifts from She Kou to the mainland of Shenzhen, where the highway network is located at. Only up to the resolution of 1 km can the model shows the peaks around the power plants at Castle Peak and the Kwai Chung port. It also reveals some high values in the new town of Shatin, Tai Po, Tuen Mun and Yuen Long. which are mainly contributed from transport. It is interesting to see the level of CO is higher in general at 11 pm than at 11 am. For NO (Figure A.2), unlike at 11 am, we can see a more extended area of high-value areas at the resolution of 27 km than higher resolutions. As the resolution increases, one can see more clearly the maxima around and at the downwind regions of the sources, around the highway network in Shenzhen and the new towns in the New Territories. The maxima of the NO mixing ratio at 11 pm is also in general higher than those at 11 pm. As the boundary layer height shrinks at night, the pollutants are trapped within a lower altitude. The continued emissions at night (from transport for example) further intensify the pollutant concentrations in the high-value areas at night. The mixing ratio of NO_2 (Figure A.3) shows similar variations as NO. For O_3 (Figure A.4), the areas with low values extend to the whole northwest quarter of the domain, but the mixing ratios around the mountains remain high, and some are even higher than the values at daytime.

In general, we can see that with higher resolution (in this case at the resolutions of 3 and 1 km), the model shows more significant influence of local topography (mainly terrains) and the heterogeneity in emissions to the mixing ratio values, and sharper and more extended tails of minima/maxima at the downwind areas of the emission point sources and in urbanised areas. It is because at higher resolutions, the model can resolve the local topography, and hence the wind motion around the mountains and harbour channel, and the emissions from local point sources.

2.3.2 General statistics

The showcase on 27th January 2017 gives a general description on how the grid resolution of a model affects the meteorology, emission and chemical calculations of the model, and its effect at daytime and nighttime. In this session, the model results at the 4 resolutions of 27, 9, 3 and 1 km are analysed statistically for a quantitative investigation. Here, the data of the first 72 hours are discarded as the spin-up time of the model. The remaining data are used as statistical analysis. It is also noted that only the data at the first vertical level are considered. The statistical analysis are performed over the data points covered by the domain D04 at the 4 respective resolutions (refer to Figure 2.17). The sample size at higher resolution is therefore larger. For instance, the numbers of grids in Domain d04 are 5×4, 9×9, 25×25 and 72×72 at the resolutions of 27, 9, 3 and 1 km respectively.

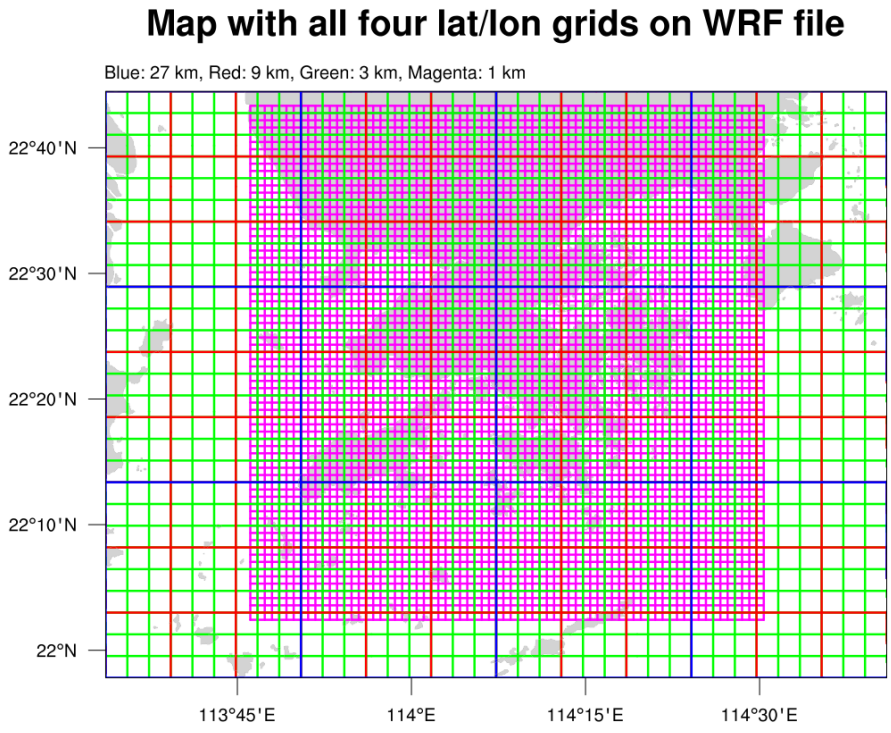

Figure 2.17: Grids of the WRF-Chem simulations cover the domain d04. The blue grids refer to the grids at the resolution of 27 km, the red grids at 9 km, the green grids at 3 km and the magenta grids at 1 km. The domain d04 refers to area covered by the magenta grids.

Figure 2.18 shows the statistics for horizontal winds varying with grid resolution. The mean magnitude of the horizontal winds reduces with increasing resolution. For

example, the mean wind magnitude drops by 13.8% when the resolution increases from 27 km to 1 km for the simulation in January 2017 (see Table A.2 in Appendix A). This can be explained by the cumulative distribution function (CDF) of the wind magnitude in January 2017 at the 4 resolutions (left panel). At higher resolution, the model tends to return lower values of wind magnitude. For instance, 18% of the winds calculated is weaker than 2 m s^{-1} (which is about the convective velocity in the convective boundary layer) at the resolution of 1 km, but it drops to 13% at the resolution of 27 km. During daytime[11], the magnitude of the horizontal winds are 20% higher at the resolution of 27 km than at 1 km (see Table A.3). The range of the wind direction also increases with resolution. The right panel shows the probability density function (PDF) of the wind direction in degree at different resolutions during the nighttime of the simulation days in July 2016[12]. One can see that the simulated wind direction span from 0.6° to 359.9° at the resolution of 1 km, and gradually shrinking with decreasing resolution to the range of 59.7° − 312.2° at resolution of 27 km (refer to Table A.6). This also hints that the winds are more sensitive to grid resolution at nighttime, as the atmospheric condition at nighttime is more stable than at daytime. The lower wind magnitudes and large range in wind directions with increasing resolution indicates that the variability of local transport are better reproduced in high-resolution models.

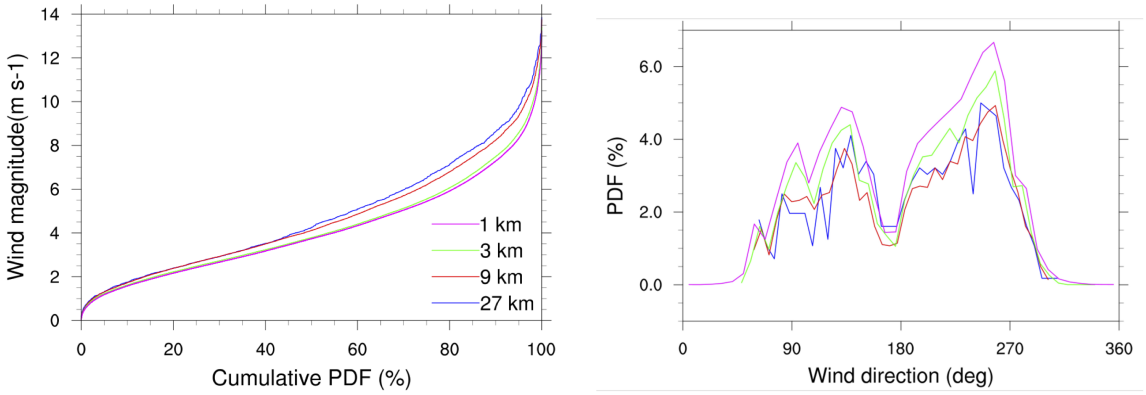

Figure 2.18: Left panel: Cumulative probability function of the wind magnitudes of the whole simulation period in January 2017. Right panel:Probability density function of the nighttime wind direction in July 2016.

The left panel of Figure 2.19 shows the variation of the mean planetary boundary layer (PBL) height in both January 2017 and July 2016. The PBL height decreases with increasing resolution in general. However, during Winter, the PBL height decreases systematically from the resolution at 27 km to 1 km. In Winter, the temperature at the altitude of 2 m also decreases with resolution both at daytime and nighttime (refer to Table A.3 to A.4). The colour maps of the showcase indicate the lower mean temperature

[11]at the hours at 8 am, 11 am, 2 pm and 5 pm
[12]at the hours at 8 pm, 11 pm, 2 am and 5 am

at higher resolutions is due to its ability to resolve local topography in the domain. During daytime (refer to Figure 2.9), the model at higher resolution is more capable to resolve the mountain ranges at high altitude, where the surface temperature is lower than on the flatlands. During nighttime (Figure 2.10), the model can capture better the exact location of the landmass, which are cooler than the sea, at higher resolution. Both factors decrease the mean temperature over the whole domain. This is also noticeable from the longer tail at low temperatures in the PDF of the temperature at 2 m (right panel of Figure 2.19), implying that the model is more capable of capturing extreme temperature values due to variation in local topography at higher resolution.

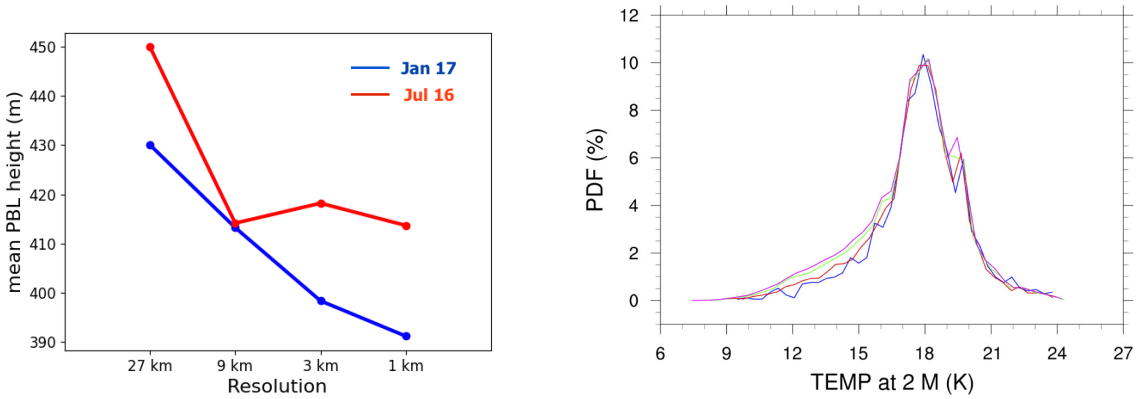

Figure 2.19: Left: Mean PBL height with different resolution in January 2017 (blue) and July 2016 (red). Right: Probability density function of the mean surface temperature in January 2017.

Emission fluxes

Figure 2.20 shows the statistics of the emission fluxes of CO and NO_X ($NO + NO_2$) at different resolution. The results in January 2017 and July 2016 are plotted in blue and red respectively. In general, the mean emission fluxes (top panels) of both CO and NO_X increase with resolution (the top-left panels). The deviation is most significant between the resolution of 27 km and the other resolutions. The mean emission fluxes at the resolution of 1 km almost double the means at 27 km for both species. This shows that even the mean emission fluxes within the same simulation can be diluted by using a lower-resolution model, as some part of the grids at lower resolution at the edge of the domain d04 actually lie outside of the domain (Figure 2.17). Most of these areas are located over the ocean where the emission is very low.

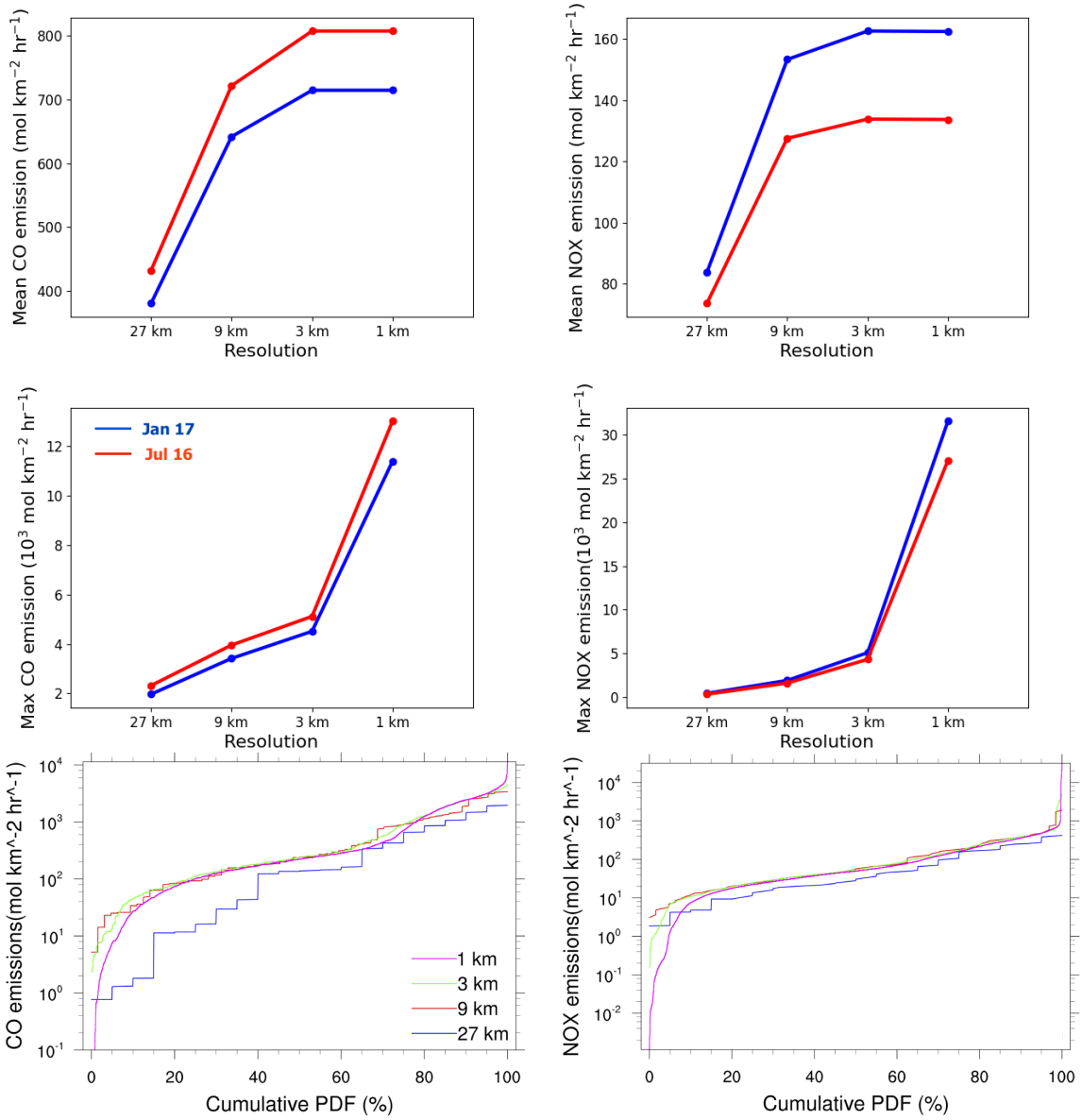

Figure 2.20: Plots showing the mean (top panels) and the maximum values (middle panels) the emission fluxes of CO (left panels) and NO_X in the domain d04 at 4 different resolutions in January 2017 (blue) and July 2016 (red). Bottom panels: Cumulative probability function of the emission fluxes of CO (left) and NO_X (right) in January 2017.

By comparing the maximum values of the emissions (middle panels), it illustrates that the model is better at capturing extreme emission signals at higher resolutions. The maximum values of the emissions of CO and NO_X at the resolution of 1 km are 2 orders of magnitude higher than that at 27 km, and 7-8 times higher than that at the resolution of 3 km. It is speculated that the maximum emission at 1 km are due to point-source emissions. The resolution of the emission inventory employed here is at 0.01°, i. e. around 1 km. In the inventory, a point source occupies a 1 km × 1 km grid,

which can be well captured by the model at the resolution of 1 km, but is diluted over a coarser grid at 3 km to $\sim 1/9$ of its original value. This can also be illustrated from the CDFs of the emissions (the bottom panels). For instance, at the resolution of 1 km, the values of CO emission fluxes range over 5 orders of magnitudes (0.1- 10^4), and 7 orders of magnitudes for NO_X (10^{-3} - 10^4). However, the ranges decreases drastically at the resolution of 27 km to 3 orders of magnitudes for CO (1 - 10^3), and 2 orders of magnitudes for NO_X (1 - 10^2). This clearly illustrate that low-resolution models tend to dilute high-emission values. In this case the effect is particularly sensitive to NO_X, hinting that the emission sources of NO_X is more localised.

Chemical calculations

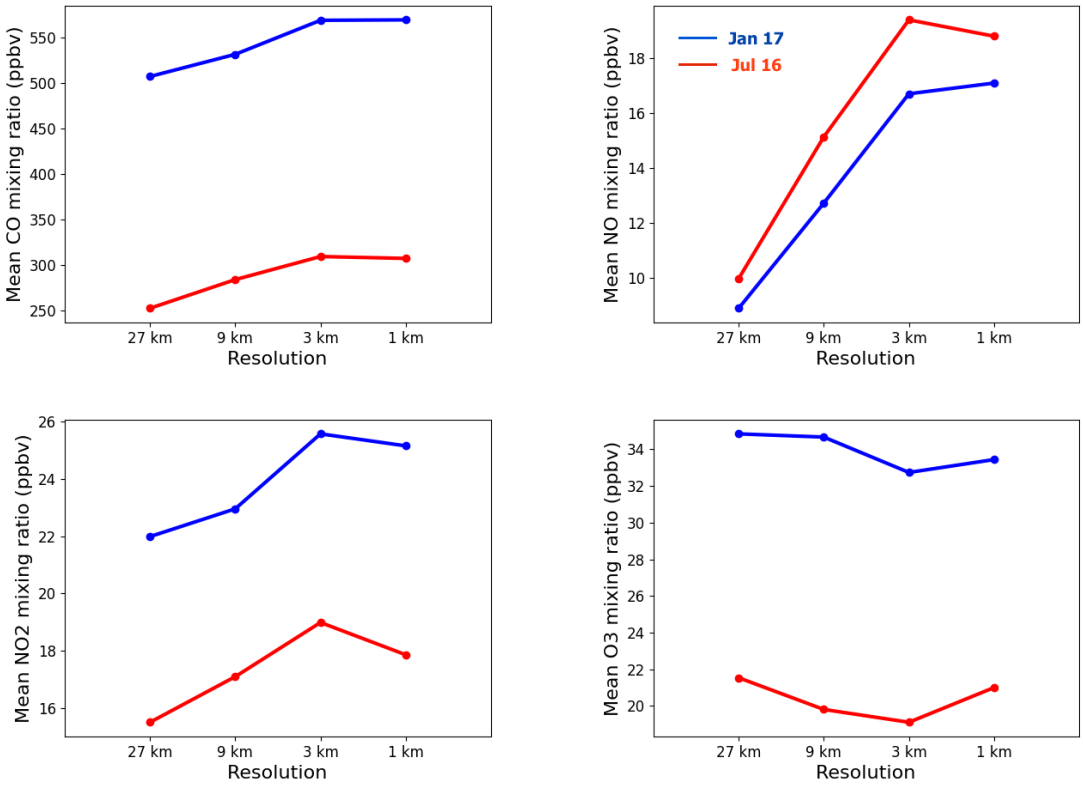

Figure 2.21: Plot showing the mean surface mixing ratio of CO (top-left), NO (top-right), NO_2 (bottom-left) and O_3 (bottom-right) in the domain d04 at 4 different resolutions over the whole simulation time in January 2017 (blue) and July 2016 (red).

Figure 2.21 shows the variation of statistics for the calculated surface mixing ratios of CO, NO, NO_2 and O_3 with increasing resolution in January 2017 (plotted in blue) and July 2016 (plotted in red). The mean surface mixing ratios of CO, NO and NO_2 increase with resolution in both summer and winter. The increase is most noticeable for NO, except when the resolution increases from 3 km to 1 km. These trends follow the trend of

the emission fluxes. Note that despite the lower emissions of CO, the mean mixing ratio of CO is higher in the winter. The main reason of the discrepancy is speculated to be due to regional transport. During winter, the northeasterly winds prevail, bringing more CO to the domain concerned. As CO is chemically inactive, its mixing ratio is prone to be affected by long-distance transport from the north of the domain in Shenzhen, at which the CO emission is higher associated with the highway network (refer to Figure 2.11).

Despite that the emission of NO_X is 20% higher in the winter than in the summer, the mean mixing ratio of NO is slightly higher in the summer. It is also noticeable that the NO/NO_X ratio is typically 10% higher in July 2016 than in January 2017 (refer to Table 2.2). During summer, the photochemical reaction converting NO_2 to NO and O_3 (Reaction 1.6) is more active due to the stronger solar irradiance, resulting in a higher NO/NO_X ratio. The NO/NO_X ratio also increases with resolution, implying photochemistry is more active at higher resolution. The relation of mean mixing ratio of O_3 with resolution is less clear. The mean surface O_3 mixing ratios tend to decrease slightly with resolution in both summer and winter, but the means at the resolution of 1 km are always higher than that at 3 km.

NO/NO_X	27-km	9-km	3-km	1-km
Jan 2017	0.29	0.26	0.39	0.40
Jul 2016	0.39	0.47	0.51	0.51

Table 2.2: Ratio between the all-time mean mixing ratio of NO and NO_X in January 2017 and July 2016.

One can see that from the CDFs of the mixing ratios (Figure 2.22) that, in general, the range and maximum value of the mixing ratios increase drastically with resolution for the primary pollutants. The effect is more substantial for NO and NO_2. These variation with resolution is similar to that in the emissions. For O_3, at the resolution of 1 and 3 km, there is a higher distribution at the low values. For example, 18% of the O_3 concentration is below 10 ppbv at the resolution of 27 km, and at resolution of 3 km it rises from 5% to 23%. The maximum O_3 concentration is also higher at higher resolution, but not as much as in the cases of NO and NO_2.

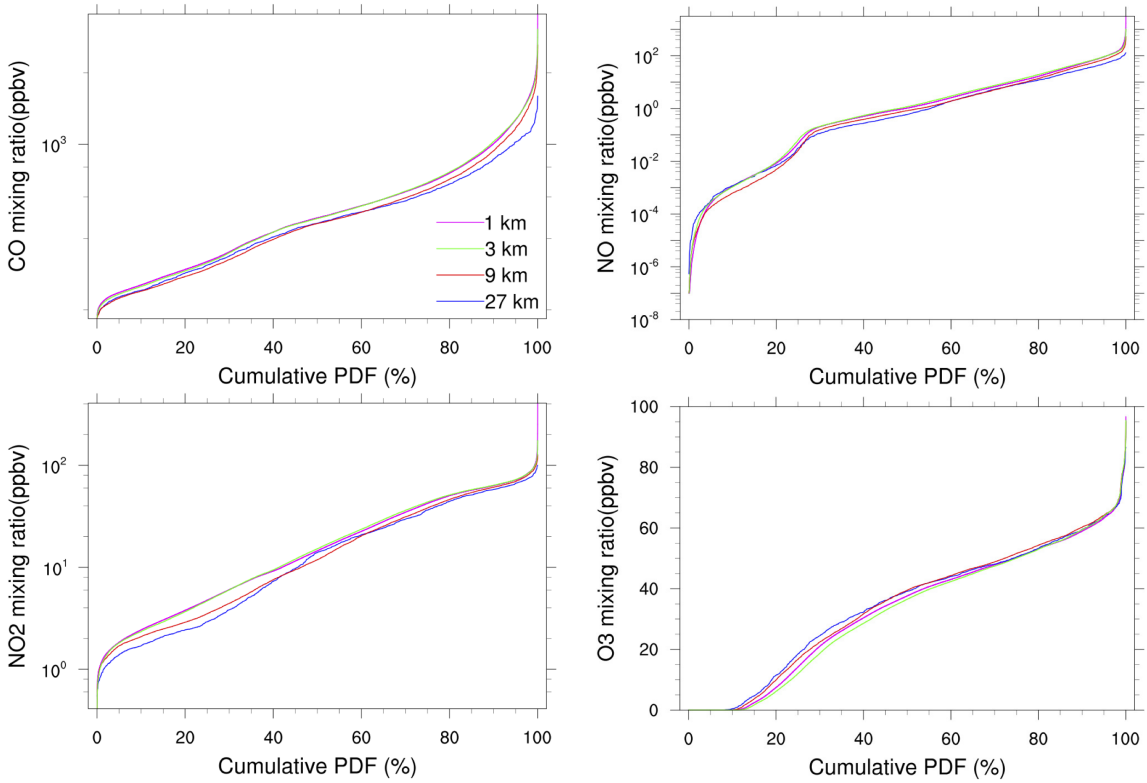

Figure 2.22: Cumulative probability functions of the mixing ratio of CO, NO, NO_2 and O_3 in the domain d04 at 4 different resolutions over the whole simulation time in January 2017.

Figure 2.23 shows the averaged diurnal cycle of the mixing ratios of CO, NO_X and O_3 over the 8 simulation days in January 2017. The diurnal cycle of the mixing ratio of CO (top-right panel) and NO_X (bottom-left panel) are highly influenced by the cycle of the PBL height (top-left panel). At all resolutions, the mixing ratios of CO and NO_X start decreasing at 08:00, when the PBL height starts increasing. This is because without implementing a diurnal cycle on the emissions, CO and NO_X is diluted when the PBL grows. For NO_X, the mixing ratio is at its minima at around 14:00, when the PBL height is maximum. However, for CO, its minima are at 17:00 instead. The wind direction also plays a role on the diurnal cycle here. During the daytime, the north-westerly wind prevails and brings CO from Shenzhen (north of the domain d04) to the domain. However, as the evening approaches, the easterly and south-easterly wind prevails instead and the domain d04 is under less influence of the high CO emission in the north of the domain. The CO mixing ratio therefore keeps on decreasing despite the PBL starts shrinking at 14:00. For O_3, the mixing ratio starts to rise at 08:00, as photochemical production is possible after sunrise. Ozone can also be entrained from the top of PBL as the PBL grows. It attains its maximum value at around 14:00, and rapidly decreases from 17:00, due to the termination of photochemical production and titration by NO_X at nighttime.

It is noticeable that the maxima of O_3 mixing ratio is at 17:00 at the resolution of

27 km, instead of at 14:00 as at the other resolutions. This may be explained by the insignificantly increase in the NO_X mixing ratio at the resolution of 27 km compared to other resolution. It is speculated to be due to the less rapid decrease in the boundary layer height from 14:00 to 17:00 at the resolution of 27 km than at the other higher resolutions (compare the gradient in the change of boundary layer height against time between 14:00 and 17:00). This favours ozone transport from higher altitudes (as the influence of regional ozone transport is high in Winter). The thicker boundary layer at the resolution of 27 km also leads to a less rapid increase in NO_X concentration, which favours ozone production.

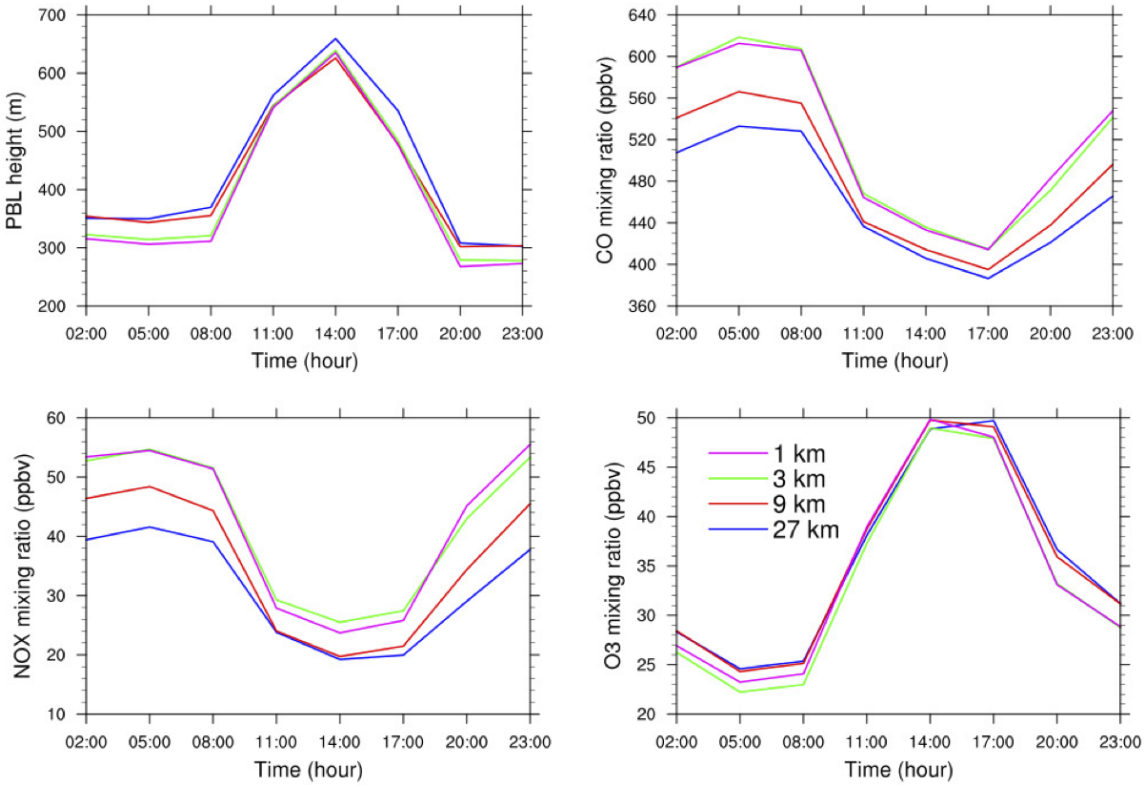

Figure 2.23: Averaged diurnal cycle of PBL height (top-left), CO (top-right), NO_X (bottom-left), and O_3 (bottom-right) in the domain d04 at 4 different resolutions in January 2017,

Total sum in the domain

The total sum of the amount of CO, NO, NO_2 and O_3 in the first 5 vertical levels[13] in the domain d04 is calculated in Mg in this session. The variation of its time-averaged values with resolution is explored here. Figure 2.24 shows the time-averaged total sums of the corresponding chemical species in January 2017 (blue curves) and July 2016 (red curves). For CO, NO and NO_2, the total sums are lowest at 27 km, as the emission at 27 km is also the lowest. However, the total sums decrease with increasing resolution from

[13]so that the whole column is always within the boundary layer in a day

9 km to 1 km. The decreasing trend of the total sum from 9 km to 1 km is opposite to the increasing trend of emissions. For CO, the decrease of total sum with increasing resolution is presumably due to the reduced regional transport from outside the domain d04 (especially from Shenzhen where the CO emission is very high). For NO and NO_2, the decrease is speculated to a combination effect of the reduced regional transport and the increase in chemical loss of NO_2 with increasing resolution[14] (See Section 2.3.2). For O_3, the total sum decreases with model resolution starting from 27 km. This decrease is speculated to be due to the reduced regional transport and the decreasing net ozone production rate with increasing resolution (See Section 2.3.2).

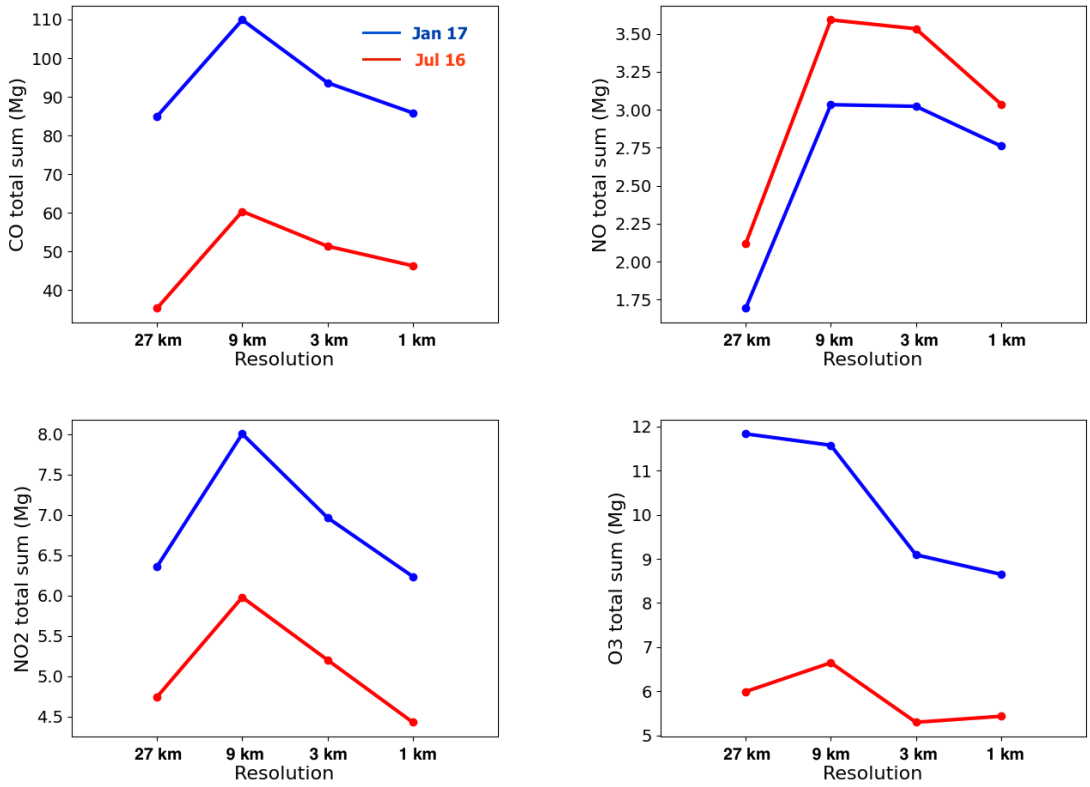

Figure 2.24: Plot showing the time-averages of the total sum of the amount of CO (top-left), NO (top-right), NO_2 (bottom-left) and O_3 (bottom-right) in the first 5 vertical levels in Domain d04 at 4 different resolutions in January 2017 (blue) and July 2016 (red).

The total sum in July 2016 in general follow similar trends, but the total sums of CO, NO_2 and O_3 in January 2017 almost double the sums in July 2016. The total sum of NO is, however, slightly lower in January 2017 than in July 2016. These disagree with the seasonal trend of the emissions between the two periods. The discrepancy in CO is due to the change in direction of regional transport, while that in NO is due to

[14]This reduces the amount of NO_2 available to by cycled back to NO by Reaction 1.15, despite the increase of photochemical activity with increasing resolution, and hence also reduces the amount of NO.

the more active photochemistry in the summer (Table 2.2). Note that the decreasing trend of the total sum of O_3 is more distinctive in the winter.

Ozone production and loss rates

The ozone production rate $P(O_3)$ and loss rate $L(O_3)$ are calculated from the results at the 4 different resolutions. For more background information about the ozone production and loss, one can refer to Section 1.2.

Figure 2.25 shows the average ozone production (solid) and loss (dashed) rate over the domain d04 at the 4 different resolutions in January 2017 (blue) and July 2016 (red). The ozone production rate is calculated from Equation 1.9 and the peroxyl radicals considered in the calculation here are listed in Table A.8. Only the daytime data is used for the calculation of Figure 2.25 as ozone production is most efficient during daytime when photochemistry can take place. The ozone production rate has a general increasing trend with increasing resolution, except in July 2016 that the average rate at the resolution of 27 km is exceptionally high. The increasing trend is presumably due to the higher emission of NO_X with increasing resolution (refer to top-left panel of Figure 2.12). It is also noticeable that the ozone production rate in July 2016 is almost double of the rates in January 2017, due to more active photochemistry in the summer time.

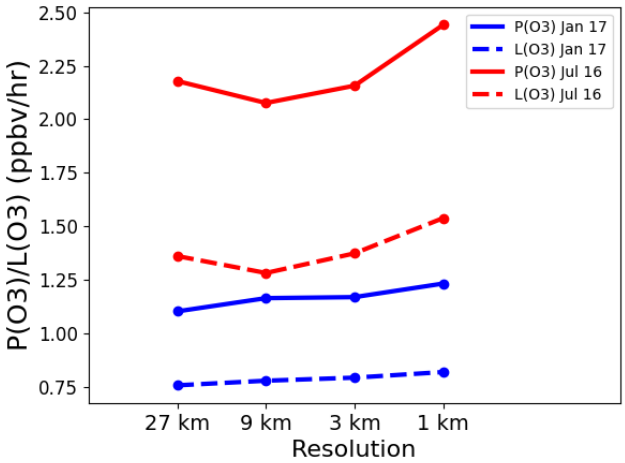

Figure 2.25: Average ozone production rate (dashed lines) and ozone loss rate (dashed line) over Domain d04 at different resolutions. The blue curves refers to the time-averaged results in January 2017, while the red curves refers to those in July 2016.

The average ozone loss rate is calculated from Equation 1.21 (refer to Table A.10, A.11 and A.13 for the VOCs and peroxyl radicals involved). The ozone loss rate tends to increase with resolution in both January 2017 and July 2016 (except the exceptionally high value at the resolution of 27 km in July 2016). This is because there exist more

NO_2 hotspots at higher resolutions (refer to Figure A.3), which encourage the loss of NO_X by converting NO_2 to nitric acid and organic nitrates. The ozone loss rate is again higher in Summer.

The net ozone production rate (net $P(O_3)$) is given by the difference between the ozone production and loss rate ($P(O_3)$-$L(O_3)$). The left panel of Figure 2.26 gives the net ozone production rate over the whole simulation time at the 4 different resolutions in January 2017 and July 2016. For July 2016, one can see that the net ozone production rate decreases when the resolution increases from 27 km to 3 km. Since the NO_X concentration increases with resolution, the non-linearity of ozone chemistry causes the net ozone production rate to decrease (see Figure 1.4). However, when the resolution increases to 1 km, the net rate increases again. That is anticipated from the fact that the increase in ozone loss rate from 3 km- to 1 km-resolution is less than the increase in ozone production rate. The higher net ozone production rate at the resolution of 1 km may be due to the slightly drop of mean NO mixing ratio when the resolution increases from 3 km to 1 km (see Figure 2.21). In addition, from the table showing the individual terms contributing to the ozone production and loss rate (Table A.9 and A.12), one can see a substantial increase in the contribution of VOCs to ozone production, hinting the unexpectedly high net ozone production rate may be due to the higher concentrations of VOCs at the resolution of 1 km. In January 2017, the net production rate is mildly increasing with the increasing resolution. However, when one refers to the corresponding ozone production rate per NO_X molecules (right panel of Figure 2.26), the value tends to decrease with increasing resolution, consistent with Figure 1.1.

Note that despite the net ozone production rate is higher in July 2016 than in January 2017, both the mean concentration (bottom-right panel of Figure 2.21) and the total sum (bottom-right panel of Figure 2.24) of ozone are higher in January 2017, indicating that a large amount of ozone in the simulated domain in January 2017 is actually contributed from regional transport. While the mean concentrations share similar pattern with the net ozone production rate, the total sum has a very different shape. The more systematic decrease in the ozone total sum in both the simulation period when the resolution increases from 9 to 3 km is probably due to less amount of ozone mixed into the simulation domain from the edge of the domain.

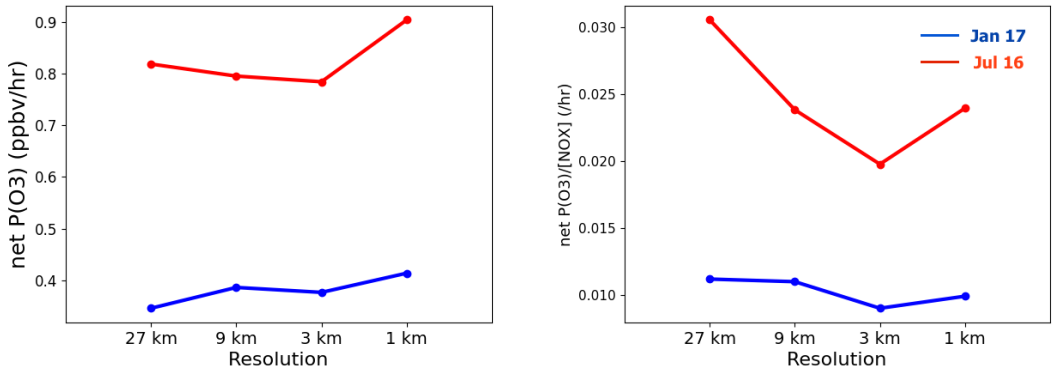

Figure 2.26: Net ozone production rate.

Figure 2.27: Average net ozone production rate (left panel) and the net rate over NO_X concentration during the whole simulation time over the whole domain d04. The blue curves refers to the results in January 2017, while the red curves refers to those in July 2016.

2.3.3 Segregations and correlations

After exploring the statistics of individual chemical species, the statistics showing the relations between the NO_X species and O_3 are examined here. The segregation of the chemical species is correlated to how well the two corresponding species are mixed in a given domain. The heterogeneity of the emission sources, transport and local mixing of the species are some main factors accounting for their segregation of pollutants. This also includes the chemical reactions involving the two concerned species if the species are chemically active. To quantify such segregation, the segregation coefficients between the surface concentrations of species A and B are calculated by

$$I_{AB} = \frac{\overline{(A - \overline{A}) \cdot (B - \overline{B})}}{\overline{A}\,\overline{B}},$$

in which the barred variables refer to the horizontal-mean values.

Figure 2.28 shows the segregation coefficients of betweenNO and O_3 (top panels), between NO_2 and O_3 (middle panels) and between NO and NO_2 (bottom panels) in January 2017 (left panels) and July 2016 (right panels). The solid lines refer to the time-average coefficient over the whole simulation time, while the dashed lines refer to the time average over daytime and the dotted lines refer to that over nighttime. In January 2017, the magnitude of the segregation coefficient between NO and O_3 increases with resolution from -0.28 to -0.38 at daytime, but decreases from -0.81 to -0.65 at nighttime. The change is most significant when the resolution increases from 27 km to 9 km. This difference in the relation with resolution between day and night is due to the difference in chemical process in the cycle between NO_X and O_3. In daytime the photochemical production of O_3 is possible, and with increasing resolution, the location producing

ozone should be separated away from the emission sources of NO. While at night, the cycle is dominated by the titration of O_3 by NO_X. As the O_3 titration increases with resolution (suggested by the increasing ozone loss rate), the segregation between NO and O_3 decreases during the O_3 titration, as the concentrations of both O_3 and NO decrease almost at same time during titration.

The segregation coefficient of NO_2-O_3 becomes more negative with increasing reaction, with all-time averages ranging from -0.26 to -0.29. However, the variation of the coefficients among the resolutions of 9, 3 and 1 km is less than 1%. These coefficients for daytime and nighttime also follow similar relations with resolution. But the segregation coefficient at night is typically 20% higher at nighttime than at daytime. This is as expected, as the atmosphere is more convective during daytime, it facilitates mixing of pollutants in the boundary layer, and hence reduces pollutants segregation.

The segregation coefficients between NO and NO_2 are always greater than one, showing that the two concentrations are positively correlated to each other. The coefficient between NO and NO_2 is also opposite in their relations with resolution between daytime and nighttime values, with daytime values increasing with resolution, and the nighttime value decreasing at night. This is probably also due to the change of dominant process in the cycle between NO_X and O_3.

The patterns of the coefficients in July 2016 are in general similar to those in January 2017, except the exceptionally low values at the resolution of 3 km. The coefficient magnitude between NO and O_3 also increases with resolution at nighttime, contrary to the decreasing trend in January 2017. This may be due to a prolonged day time in the summer. The discrepancy between the daytime and nighttime values of the coefficient between NO and O_3 and between NO_2 and O_3 are also 10% greater than that in the winter. It is speculated to be due to the more convective boundary layer in the summer, increasing mixing (less segregation) in the daytime. On the other hand, the pollutants are more segregation during the nighttime in July 2016 than in January 2017 due to a more shallow (and hence less convective) boundary layer in July 2016 (see TableA.4 and A.6).

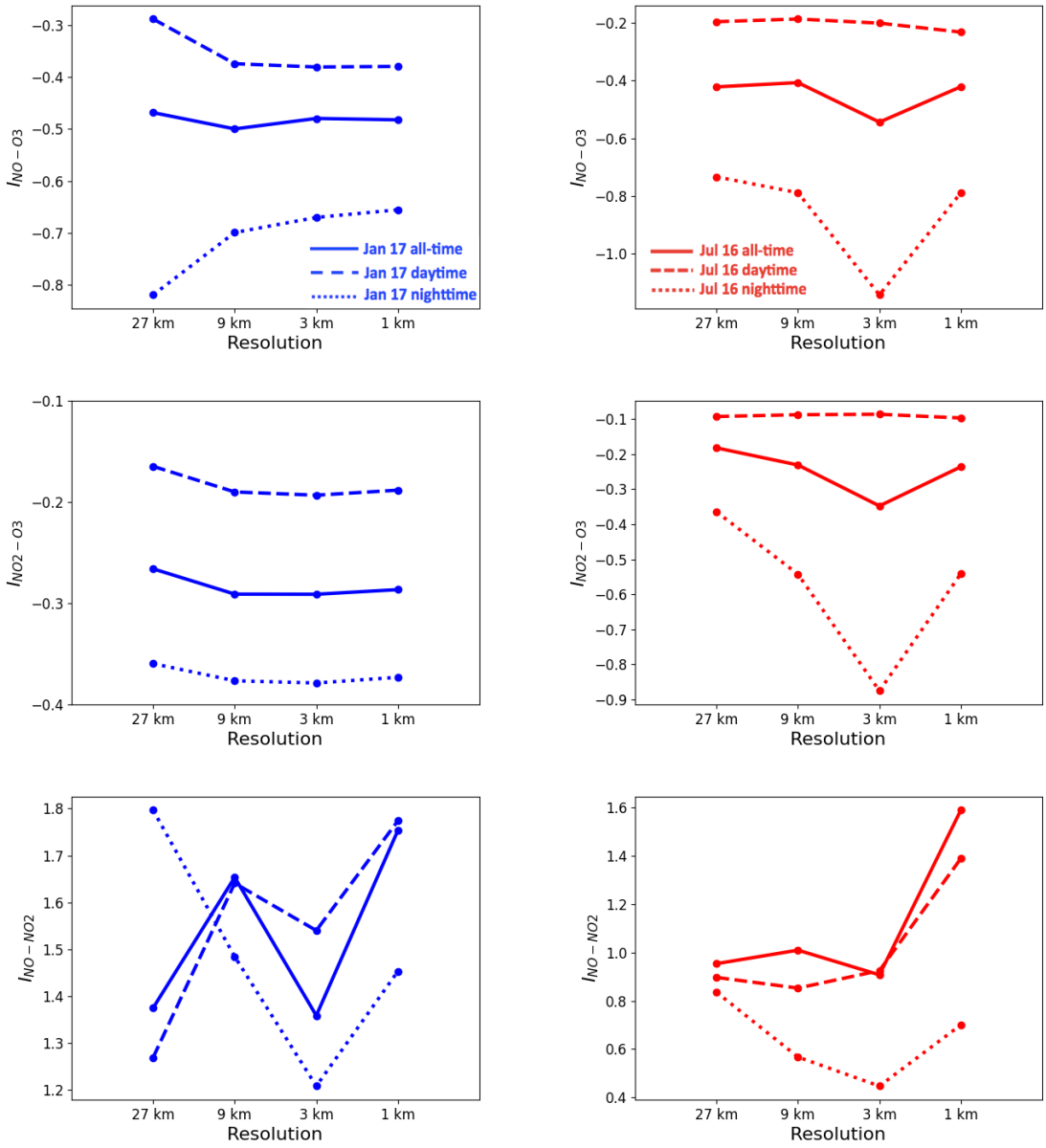

Figure 2.28: Plot showing the segregation coefficients between O_3 and NO (top panels), between O_3 and NO_2 (middle panels), and between NO and NO_2 (bottom panels) in Domain d04 at 4 different resolutions in January 2017 (left panels) and July 2016 (right panels). The solid line shows the all-time values, while the daytime and the nighttime values are plotted in dashed and dotted lines respectively.

In order to look into the correlations between the NO_X species and O_3, the mixing ratios of O_3, O_X (NO_2 + O_3) and NO_2 are plotted against the mixing ratios of NO_X in Figure 2.29 for the data inside the domain d04. O_X refers to the oxidants in the ozone chemistry, i. e. the sum of O_3 and NO_2. One can refer to Section 1.2 for more information on ozone chemistry. Only the daytime results in July 2016 is shown as the photochemistry is only possible during daytime, and more active during summer.

The top-left panel of Figure 2.29 shows a plot of mixing ratio of NO_X against that of O_3 at the 4 resolutions. From the negative slopes, one can see in general the mixing ratio of O_3 decreases with increasing NO_X. However, the slope becomes less negative with increasing resolution. The Pearson's coefficients between the mixing ratio of $\log(NO_X)$ and O_3 are -0.61, -0.45, -0.42 and -0.36 at the resolution of 27, 9, 3 and 1 km respectively. The negative correlation between NO and O_3 indicates that the simulation domain is in the VOC-limited regime (Seinfeld and Pandis 2012), and the lower negative effect of NO_X to O_3 may hint a more active effect of VOC on ozone chemistry with increasing resolution (Song et al. 2011).

The top-right panel of Figure 2.29 shows a plot of mixing ratio of NO_X against that of O_X. Under the ozone chemistry between O_3 and NO_X, the mixing ratio of the oxidant O_X against NO_X usually follows a linear relationship. The result of the linear regression - the slope, the intercept and the R-squared values are shown in Table 2.9. The distributions at the 4 resolutions are in similar pattern, with a more diverse distribution at low values of NO_X (< 100 ppbv) and a more distinctive linear trend at higher values of NO_X (> 100 ppbv). The slope of the linear fit is 0.0501, 0.0667, 0.06830 and 0.0796 at the resolution of 27, 9, 3 and 1 km respectively. According to the quantitative analysis on chemistry of NO and O_3 (Clapp and Jenkin 2001), the slope in this plot represents the local contribution to O_X in levels of NO_X. This means the local distribution to O_X is around 7% of the NO_X level, which is comparable with the other previous studies (e. g. Clapp and Jenkin (2001); Xie et al. (2016)). This local contribution increases by 3% when the resolution increases from 27 km to 1 km. The intercept of the linear fit corresponds to the regional contribution to O_X, i. e. the background O_X. The intercept is at a similar level of around 35 ppbv at all resolutions.

The bottom-left panel of Figure 2.29 shows a plot of mixing ratio of NO_X against that of NO_2. By comparing the plot with that between NO_X and O_X, one can see at high NO_X concentrations, the main component of O_X is in fact NO_2. This can be explained by the low value of O_3 at high NO_X value in the plot between NO_X and O_3 . The relation between NO_X and NO_2 follows a very distinctive linear trend. The slope decreases as the resolution increases, from 0.41 at 27 km to 0.25 at 1 km, meaning that the local contribution to NO_2 drops by $\sim 16\%$ of NO_X level as the resolution increases from 27 km to 1 km, consistent with the increasing NO/NO_X ratio with increasing resolution (Table 2.2). Along with the increase local contribution to O_X, this implies the local contribution to O_3 increases with resolution, as O_X is the sum of NO_2 and O_3. The intercept, showing the background NO_2 level, is 2-6 ppbv, showing a small regional contribution to the mixing ratio of NO_2 to the domain d04.

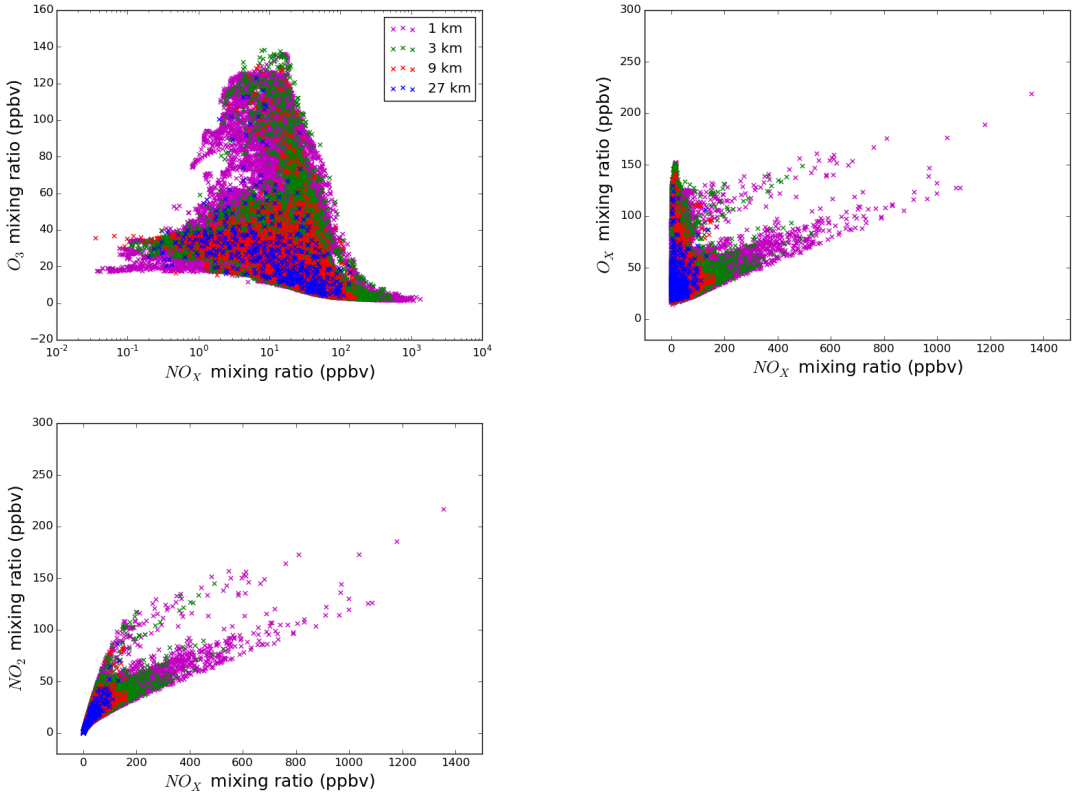

Figure 2.29: Scatter plots showing the relations between the NO_X species and O_3 (top-left panel), between NO_X and O_X (top-left panel), and between NO_X and NO_2 (bottom-left panel) at different resolution during the daytime in July 2016.

$\log(NO_X)-O_3$	27-km	9-km	3-km	1-km
Pearson's coefficient	-0.4475	-0.4283	-0.4161	-0.3595
NO_X-O_X	27-km	9-km	3-km	1-km
Slope	0.0501	0.0667	0.0683	0.0796
Intercept	36.8	35.3	36.4	37.3
R^2	0.0668	0.1043	0.1273	0.1605
NO_X-NO_2	27-km	9-km	3-km	1-km
Slope	0.4128	0.3508	0.2764	0.2458
Intercept	2.1	3.6	5.7	6.3
R^2	0.9261	0.8852	0.8541	0.8383

Table 2.3: The linear regression results of the relations between the NO_X and O_X mixing ratios shown in Figure 2.29.

2.3.4 Vertical profiles at different resolutions

The physical and chemical quantities in boundary layer vary with height due to the vertical structure and the dynamics of the boundary layer. Although the spatial

resolution only changes the size of the model grid meshes horizontally but not vertically, increasing model resolution also changes the vertical profiles of the calculated physical and chemical quantities. In this section, the vertical profiles of the horizontal mean, the variance and the vertical flux of the physical and chemical quantities discussed in the previous sections are presented. One should also refer to Section 1.1 for more information about the structure and dynamics of the boundary layer.

The vertical profiles at the hour 2 pm averaged over the 8 simulation days in January 2017 (the first 3 days are discarded as spin-up time) are shown here as the boundary layer attains its full height around 1400. The growth of the boundary layer is buoyancy-driven, hence one can understand the vertical structure of the convective boundary layer (CBL) from the buoyancy profile. Figure 2.30 shows the horizontal-mean of buoyancy against height (left panel) and its variance (right panel). The buoyancy b is calculated from Equation 1.1, and $\theta_{v,0} = 273$ K. In the buoyancy variance profile ($\overline{b'b'}$) (right panel), one can still see a clear maximum at around 1100 m at all resolutions. Therefore, the averaged boundary layer height at 1400 is assumed to be 1100 m.

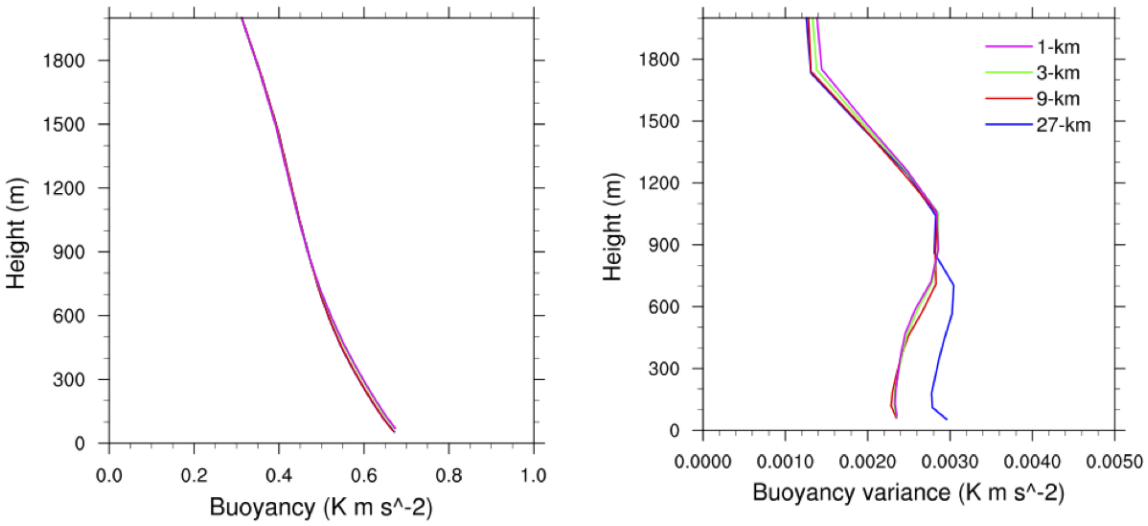

Figure 2.30: Vertical profiles of horizontal-mean buoyancy $\bar{b}$ and buoyancy variance $\overline{b'b'}$ at different resolutions at 2 pm averaged over the 8 simulation days in January.

Figure 2.31 shows the plots of the horizontal-mean of the meteorological variables, the potential temperature ($\bar{\theta}$, top-left panel), magnitude of the horizontal winds ($\overline{\sqrt{U^2+V^2}}$, top-right panel) and the vertical wind ($\bar{W}$, bottom-left panel) against height. Model resolution does not have a significant effect on the vertical profile of the potential temperature, but has substantial effect on both the horizontal and vertical winds. Within the CBL, the magnitude of the horizontal winds decreases for altitude with increasing resolution. The magnitude of the horizontal winds at the resolution of 27 km is the highest, and is around 1.5 times larger than that at 1 km at the surface level. The lower horizontal wind magnitude at high resolution hints a larger contribution of local

transport (which is with lower wind speed). Among the different resolutions, there is an increasing tendency of the horizontal winds with height in the CBL, and a decreasing tendency above it in the entrainment zone, and increasing again in the free troposphere.

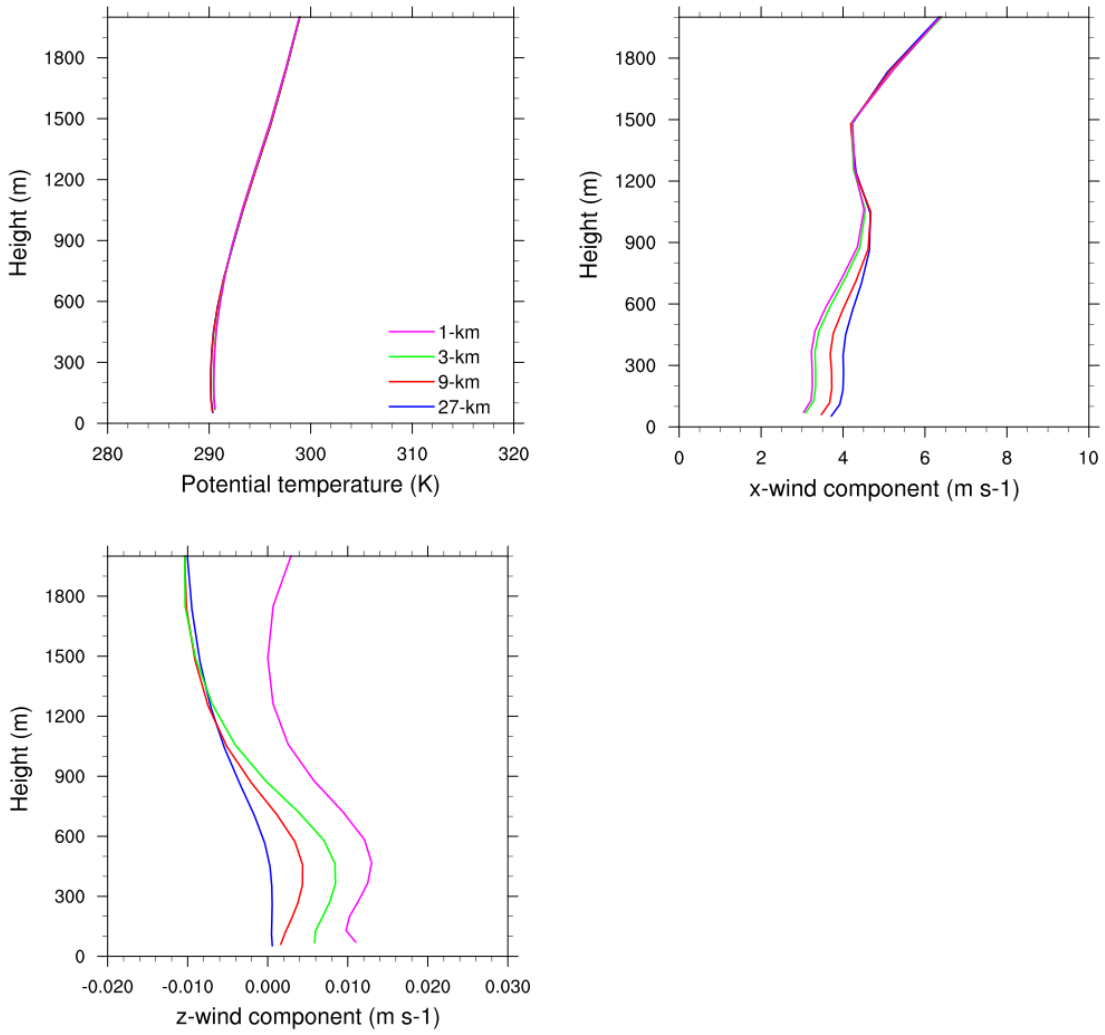

Figure 2.31: Vertical profiles of horizontal-mean potential temperature $\bar{\theta}$ (top-left panel) and horizontal wind speed $\overline{\sqrt{U^2+V^2}}$ (top-right panel) and vertical wind $\bar{W}$ at different resolutions at 2 pm averaged over the 8 simulation days in January.

The magnitude of the vertical winds, on the other hand, increases significantly with increasing resolution, indicating more vertical transport is available at higher resolution. At the resolution of 3 km and 1 km, one can observe a change of sign in the gradient of the vertical profile at around 100 m, which corresponds to the transition from the surface layer to the mixed layer in a boundary layer (refer to 1.1). However, this feature cannot be observed at the resolution of 9 km and 27 km. There is also a change of sign in the

vertical winds at the resolution of 27, 9 and 3 km from positive (upward) to negative (downward) at an altitude of 500-1000 m (this altitude increases with resolution). Above that altitude, the mean vertical transport is downward at these resolutions. However, the vertical winds at the resolution of 1 km stay positive, indicating a mean upward transport.

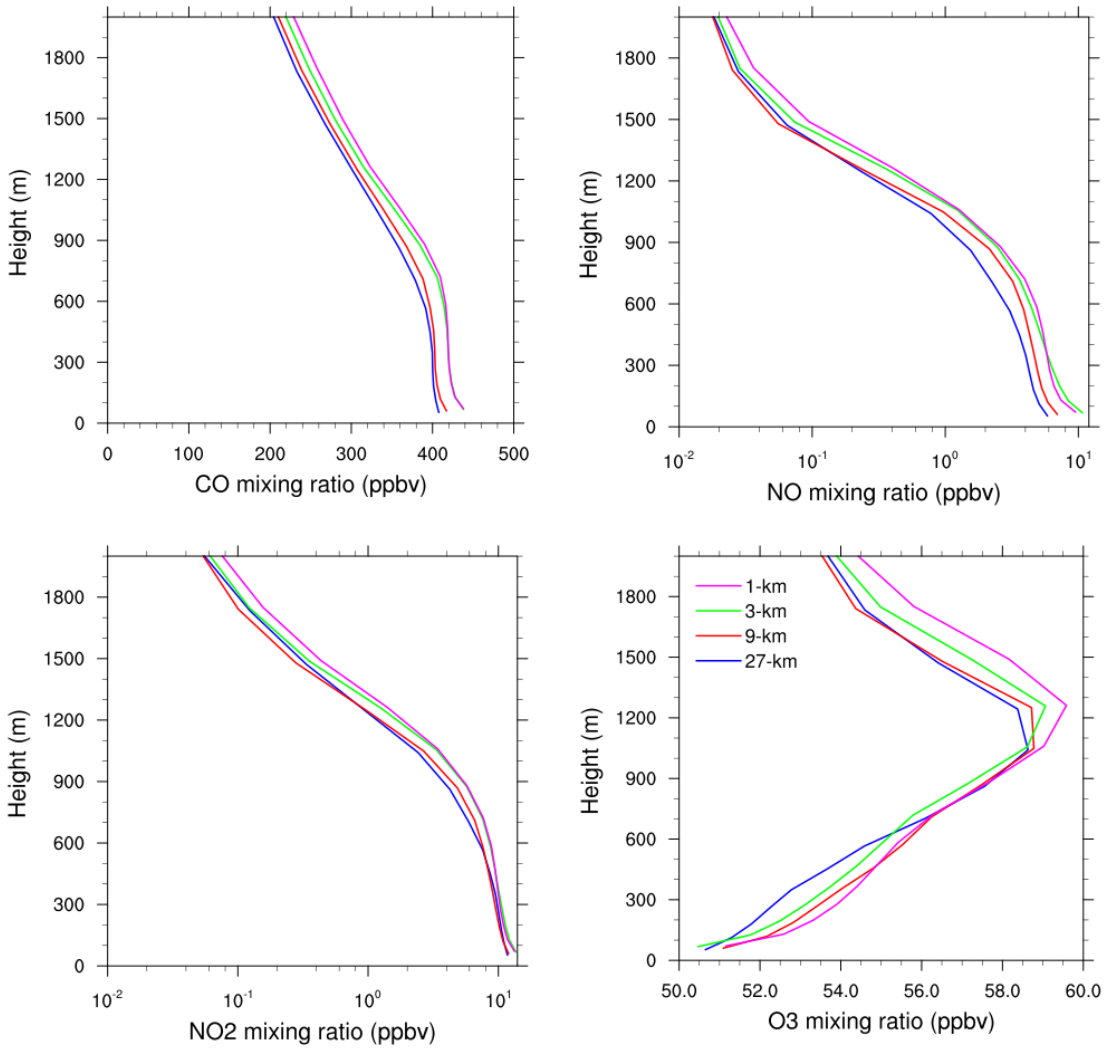

Figure 2.32: Vertical profiles of horizontal-mean concentrations of CO (top-left panel), NO (top-right panel), NO_2 (bottom-left panel) and O_3 (bottom-right) at different resolutions at 2 pm averaged over the 8 simulation days in January.

Figure 2.32 shows the plots of the horizontal-mean concentrations of CO (top-left panel), NO (top-right), NO_2 (bottom-left) and O_3 (bottom-right) against height. For CO, NO and NO_2, the concentrations decrease with height at all resolution, as these species are mainly emitted from the surface. The surface values at resolutions of 3 km

and 1 km are significantly higher than those at 9 km and 27 km. However, if we look at the gradient of the concentration, that is the decrease of concentration per altitude increase, the gradients are larger at the resolutions of 27 km and 3 km, especially for NO and NO_2. A smaller gradient indicates that the species are more well-mixed vertically. For O_3, the concentration increases with height for altitudes within the boundary layer, but decreases again above 1000 m. The surface concentration is around 51.0 ppbv for all resolutions. It is noticeable that the gradient of ozone concentration is larger with increasing resolution at the first 300 m, meaning that ozone is more vertically segregated with increasing resolution.

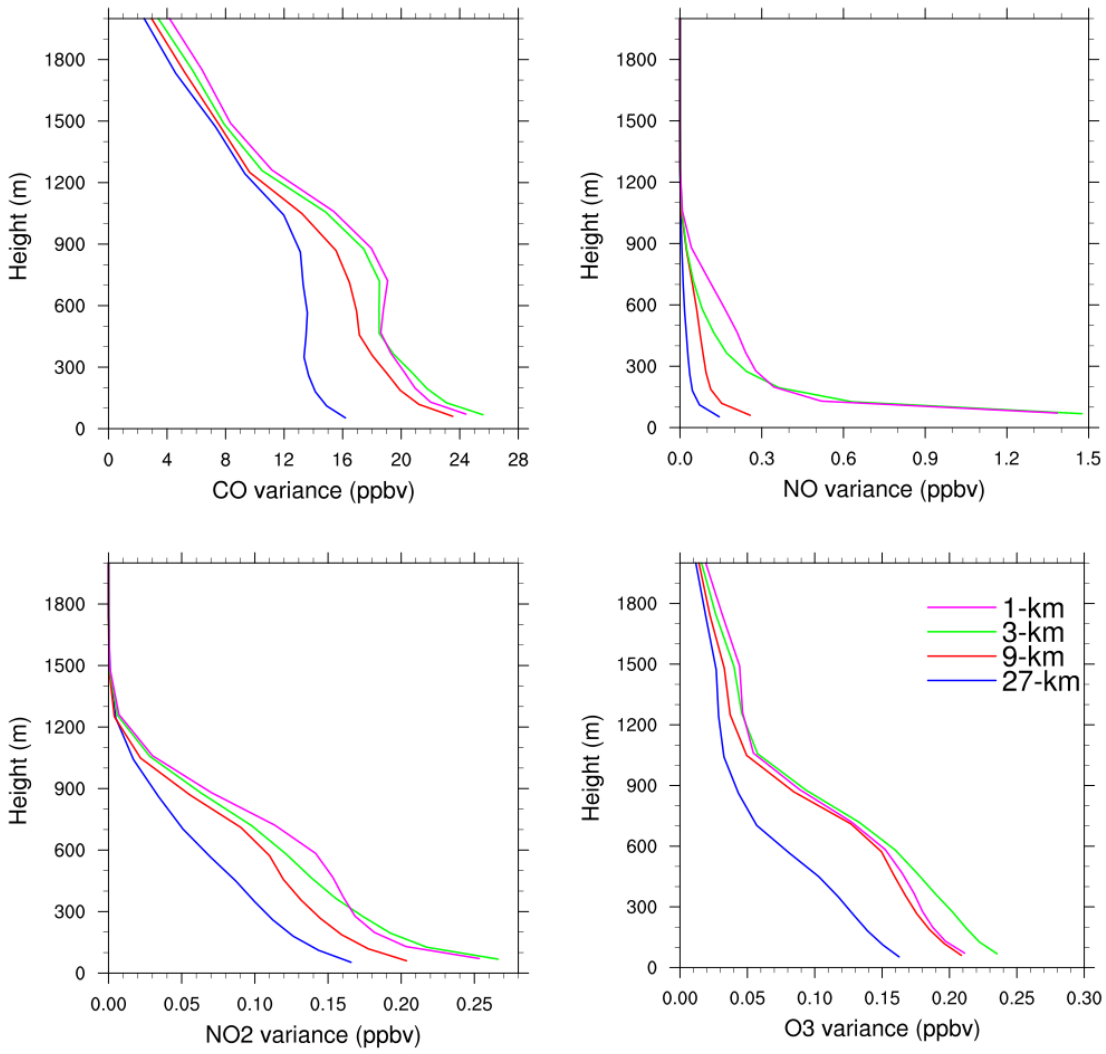

Figure 2.33: Vertical profiles of horizontal-mean concentration variances of CO (top-left panel), NO (top-right panel), NO_2 (bottom-left panel) and O_3 (bottom-right) at different resolutions at 2 pm averaged over the 8 simulation days in January.

Figure 2.33 shows the plots of the horizontal-mean variances of the concentrations of CO ($\overline{CO"CO"}$, top-left panel), NO ($\overline{NO"NO"}$, top-right), NO_2 ($\overline{NO2"NO2"}$, bottom-left) and O_3 ($\overline{O3"O3"}$, bottom-right) against height. Note that all concentration variances decrease with height for all resolutions. For CO, NO and NO_2, the variance at the surface is largest at the resolution of 3 km, but still very close to those at the resolution of 1 km. Otherwise, the concentration variance generally increases with increasing resolution. However, for altitudes higher than 300 m, the variance at the resolution of 1 km becomes greater than that at 3 km. For O_3, the variance is largest at the resolution of 3 km for all altitudes within the boundary layer. The profile at the resolution of 1 km is similar to that at 9 km, and the variance has its lowest value again at the resolution of 27 km.

Figure 2.34 shows the plots of the horizontal-mean vertical fluxes of the concentrations of CO ($\overline{CO"W"}$, top-left panel), NO ($\overline{NO"W"}$, top-right), NO_2 ($\overline{NO2"W"}$, bottom-left) and O_3 ($\overline{O3"W"}$, bottom-right) against height. In general, the magnitude of the flux increases with increasing resolution for all species. For CO, NO and NO_2, the flux is positive at most of the altitudes, except for altitudes at the first 200 m for resolution of 3 km, 9 km and 27 km. Here, a positive flux means upward transport of the species while the negative flux refers to downward transport. Also, for the species of NO and NO_2, the altitude at which the flux is at its maximum value at the resolution of 1 km, which is around 350 m, is a bit lower than those at the resolution of 9 and 3 km, which are at 500 m. This maxima indicates the altitude at which the vertical mixing of the corresponding chemical species is most efficient. For O_3, the shape of the vertical profile of the concentration flux is quite different at different resolutions. At the resolution of 1 km, the flux is negative for altitudes below 750 m, with a peak of flux magnitude at around 350 m. Above 750 m, the flux becomes positive for the rest of the boundary. The profiles at resolutions of 9 and 3 km follow similar tendency. At the first 200 m, the flux is positive, but above that height, the flux becomes negative in the rest of the boundary layer, with a peak in the flux magnitude at around 500 m. At the resolution of 27 km, there is a weak positive flux for altitudes below 600 m, and a weak negative flux above that height. One can see from the variation of vertical profile of the ozone vertical flux at different resolution that, the transport of ozone is particularly sensitive to model resolution. Similar to the profiles of NO and NO_2, the altitude of the maxima of the vertical flux tends to decrease with increasing resolution.

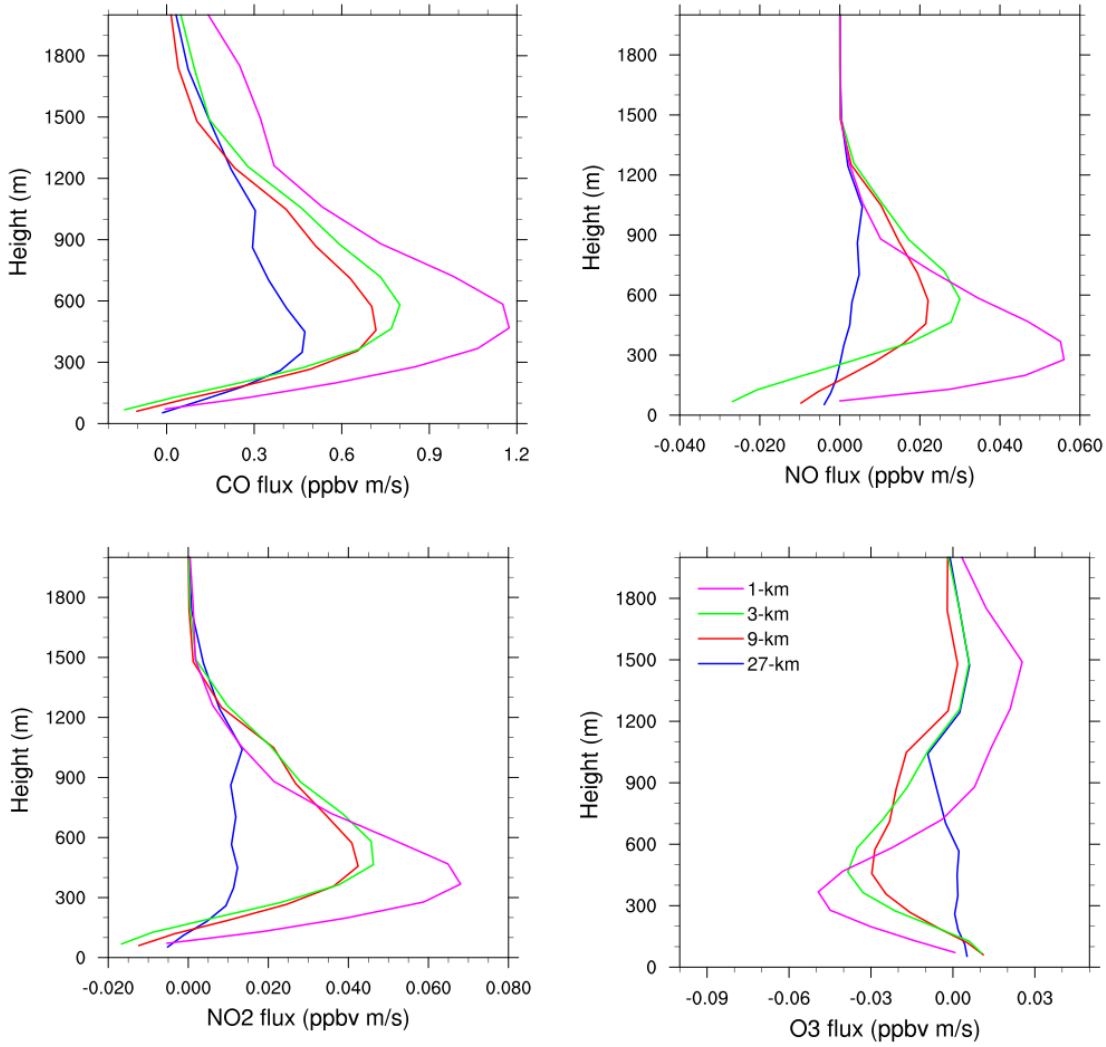

Figure 2.34: Vertical profiles of horizontal-mean vertical concentration fluxes of CO (top-left panel), NO (top-right panel), NO_2 (bottom-left panel) and O_3 (bottom-right) at different resolutions at 2 pm averaged over the 8 simulation days in January.

2.4 Model comparison with observational data

To assess the performance of the model at different resolution, the modelled data at the 4 different resolutions are compared with observational data form the monitoring stations of HKEPD using statistical metrics. One can refer to Session 2.1.3 for further details of the HKEPD monitoring stations. The daytime data in January 2017 are evaluated with the following statistical metrics.

Given that there are N pairs of modelled and observed quantities of M_i and O_i, the

modelled mean $\bar{M}$ and the observed mean $\bar{O}$ can be respectively expressed as

$$\bar{M} = \frac{1}{N}\sum_{i=1}^{n} M_i$$

and

$$\bar{O} = \frac{1}{N}\sum_{i=1}^{n} O_i,$$

while the modelled and observed standard deviations σ_M and σ_O are

$$\sigma_M = \left[\frac{1}{N}\sum_{i=1}^{n}\left(M_i - \bar{M}\right)^2\right]^{\frac{1}{2}}$$

and

$$\sigma_O = \left[\frac{1}{N}\sum_{i=1}^{n}\left(O_i - \bar{O}\right)^2\right]^{\frac{1}{2}}$$

The ensemble N includes the data collected or modelled at the daytime of the simulation period at a specific station.

To quantify the difference between the modelled and observed datasets, we calculate the mean bias

$$MB = \frac{1}{N}\sum_{i=1}^{n}\left(M_i - O_i\right).$$

The mean fractional bias

$$MFB = \frac{2}{N}\sum_{i=1}^{n}\left(\frac{M_i - O_i}{M_i + O_i}\right)$$

is also calculated as another reference metric to avoid overemphasising the high tail of the distribution, which is more suitable for data covering an extended range of values (mostly likely for NO and NO_2) (Brasseur and Jacob 2017). The range of the MFB is between -2 and +2. However, MFB may overemphasise low values of which relative errors may be large but of little interest to the problem. To compensate the effect, the normalised mean bias (NMB) is also employed

$$NMB = \frac{\sum_{i=1}^{n}\left(M_i - O_i\right)}{\sum_{i=1}^{n} O_i}$$

as a more robust metric, by taking the ratios of the sums instead of the sums of the

ratios (Brasseur and Jacob 2017). The Pearson's correlation coefficient

$$r = \frac{\sum_{i=1}^{n} \left(M_i - \bar{M}\right)\left(O_i - \bar{O}\right)}{\left[\sum_{i=1}^{n} \left(M_i - \bar{M}\right)\right]^{\frac{1}{2}} \left[\sum_{i=1}^{n} \left(O_i - \bar{O}\right)\right]^{\frac{1}{2}}}$$

is adopted to characterise the correlation between the modelled and observed datasets. A value of +1 indicates a perfect linear correlation between the model and observation. A value close to zero implies that the variability in the observed data is controlled by processes that the model fails to capture. In that case, even a model can capture the observed mean, it may get the mean correctly for a wrong reason if r is non-significant. A negative value hints that the modelled data do not match with the observed data.

To evaluate the model performance at stations located in areas with different landuse and emission characteristics, the comparison between the modelled and observed data at the following 4 individual/groups of stations are discussed: (1) the Roadside stations (Central, Causeway Bay and Mong Kok), (2) Tap Mun station, (3) Tuen Mun station, and (4) New Town East stations.

First of all, the overall performance at the Roadside stations is evaluated. The averages of the statistical metrics of the 3 Roadside stations are listed on Table A.20. The time series of the modelled and observed mixing ratios of CO, NO_X and O_3 at one of these stations, Central, are plotted in Figure 2.35. CO, NO_X are largely underestimated in the model at all resolutions. The model biases decrease slightly ($\sim$ 5-9 %) when the resolution increases from 27 km to 9 km. But beyond 9 km, the model performance does not improve with increasing resolution. The model undercasts the observed mixing ratios of CO, NO and NO_2 by 41%, 87% and 57% respectively at the resolutions of 9 km, at which the biases are at their minimal values. With increasing resolution, the biases of these species also increase by 1-10%. On the other hand, the concentration of O_3 is largely overestimated due to the underestimated NO concentrations (hence less deposition by NO). Again the biases are at their minimal values at the resolution of 9 km, with the NMB equal to 150%. With all species, the Pearson's correlation coefficients between the modelled and observed data decrease with resolution. All these indicate that beyond the resolution of 9 km, increasing model resolution does not have a significant impact on the modelled results at these Roadside stations, which is characterised by their intense urbanisation and strong local emissions (mainly vehicle exhausts). Increasing model resolution does not necessarily improve the model performance either. The first possible explanation is due to the overly low emissions in the urban area. Despite of its high resolution, the emission inventory still underestimates the emission from vehicles in these urban areas of Hong Kong. Using NO_X as an example, from the NO_X emission colour map in Figure 2.12, although the emission of NO is noticeably elevated in the

urban areas, the increment is not significant. While the observed NO mean of the Roadside stations is 884 times higher than that of the New Town East stations (in Table A.23), the NO emissions at all these stations are comparable. Another reason is that with intense urbanisation, merely increasing model resolution still cannot capture the processes occurring in the complex urban topography (such as the flows across street canyons). Other adaptations, such as urban canopy, or even turbulent flow-resolving models like LES or CFD, may be necessary for further model improvement[15].

Being a rural site, Tap Mun station is another station where increasing resolution shows little impact on model performance. One can refer to the time series on Figure 2.36 and the metrics listed on Table A.21) for the evaluation at Tap Mun station. Again, the models undercasts the observed mixing ratios of CO and NO_X, and the biases are at their minimal values at the resolution of 9 km. The modelled CO mixing ratio underestimated the observed values by more than 300 ppb, or by more than 40%. Despite of the comparable NMB values, the mean biases of the NO and NO_2 concentrations are within 2 ppb, which is actually insignificant. Due to the small mean bias of NO and NO_2, the modelled ozone values are accurate, which only underestimate the observations by 2 - 4 %. The large underestimation of CO at Tap Mun station is most likely due to the overly low emissions from the inventory. Unlike the Roadside stations, at Tap Mun station, which is located in the rural area and is usually used as a background station, the emission source is likely to be regional or from shipping (as the station is also by the sea). Increasing model resolution has little impact on the model calculation, because there are not much small-scale features around this rural site. The result is also consistent with previous studies (Schaap et al. 2015).

[15]Actually the setting of this WRF model may not be adequate for the concentrations at the Roadside stations as (1) the height of the Roadside station is 3-5 m above the surface, but the first vertical level in the WRF model starts at $\sim$ 20 m; (2) the pollutant concentration at the road depends highly on the peak hours of traffic, which is not taken into consideration in the emission inventory.

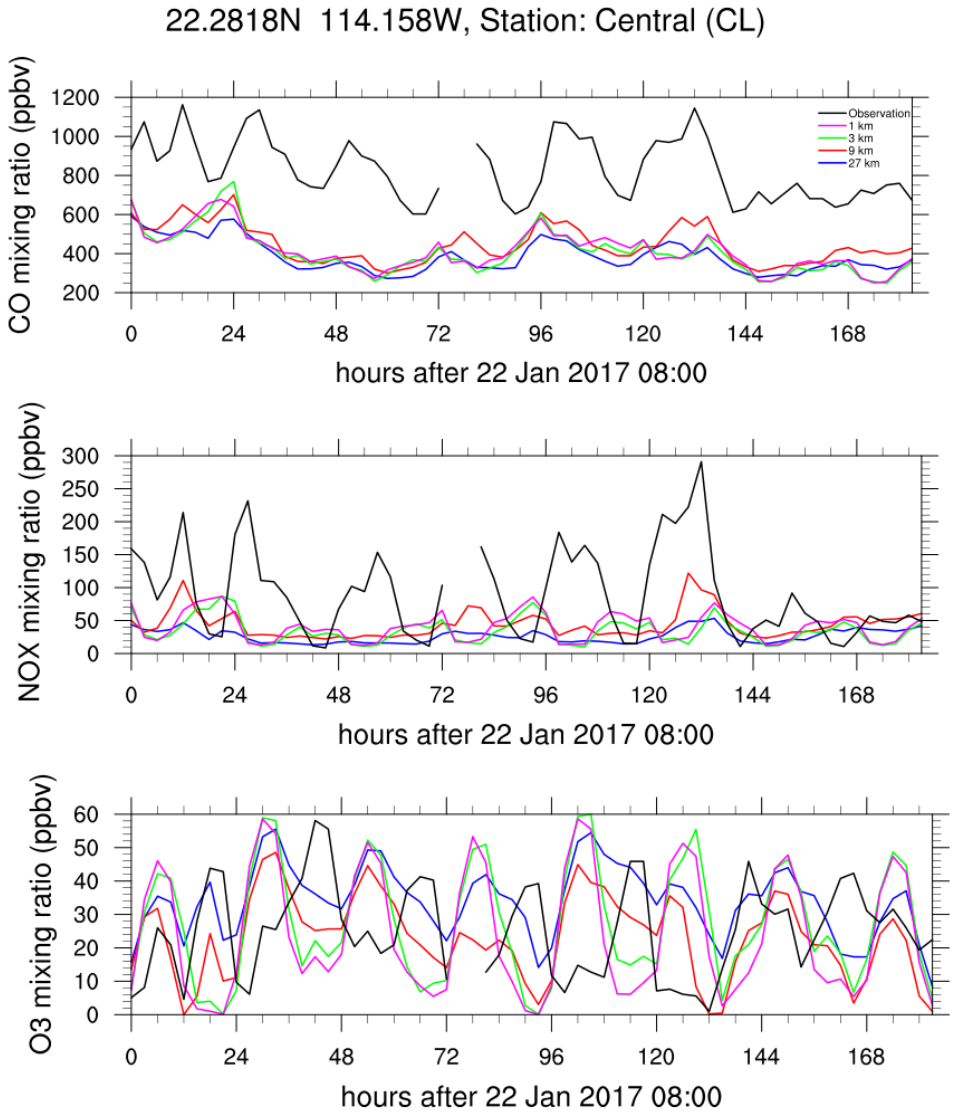

Figure 2.35: Time series of the observed and modelled mixing ratios of CO (top), NO_X (middle) and O_3 (bottom) at the 4 different resolutions from 22nd January 2017 8 am at Central station. The modelled data are plotted with blue, red, green and magenta at the resolution of 27, 9, 3 and 1 km respectively. The observed data are plotted in black. The data presented here are averaged every 3 hours.

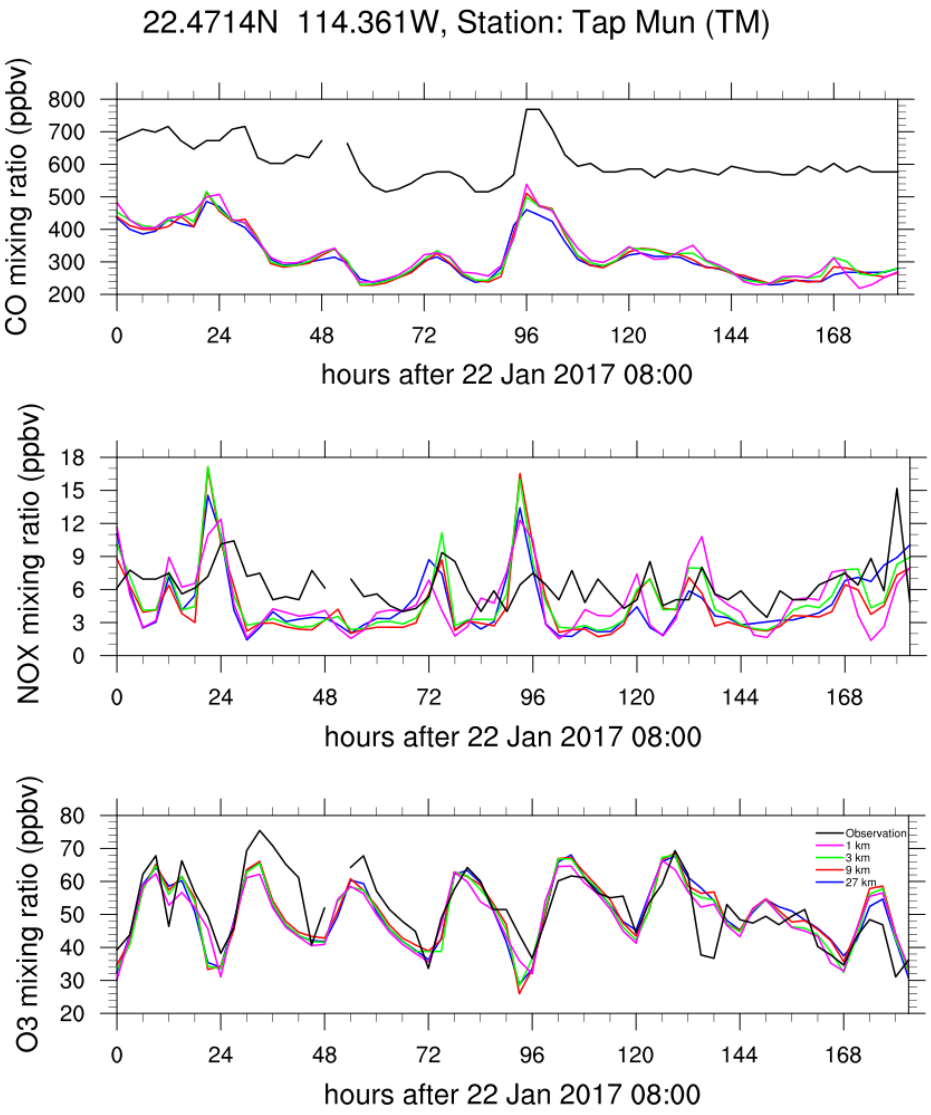

Figure 2.36: Time series of the observed and modelled mixing ratios of CO (top), NO_X (middle) and O_3 (bottom) at the 4 different resolutions from 22nd January 2017 8 am at Tap Mun station. The modelled data are plotted with blue, red, green and magenta at the resolution of 27, 9, 3 and 1 km respectively. The observed data are plotted in black. The data presented here are averaged every 3 hours.

The next station to explore is the Tuen Mun station, which is the closest station to the Castle Peak power plants. The statistical metrics of the station is listed on Table A.22 and the time series of the mixing ratios from the model and observation are plotted on Figure 2.37. The model gives a relatively accurate estimation of the CO concentration, with bias of +2 - +8% at all resolutions. However, the concentrations of NO and NO_2 are largely overestimated in the model. The model overcasts the observed NO concentration by 322%, 856%, 274% and 200% at the resolution of 27, 9, 3 and 1 km respectively, and by 88%, 126%, 47% and 40% for NO_2. The overcasting is most

significant at the resolution of 9 km. It is because both the Tuen Mun station and the Castle Peak power plants fall into the same model grid at the resolution of 9 km, as their distance is only 7 km, less than the grid spacing. The emitted chemicals are hence overmixed in that model grid. Although the Tuen Mun station and the power plants are also located in the same model grid at resolution of 27 km, the coarser grid dilutes the emission of the power plant, compensating the effect of overmixing. At higher resolutions of 3 and 1 km, the finer grids differentiate the power plants with the station, further diminishing the overcasting. However, the emission inventory used probably overestimates the emission of NO_X from the power plants, as the concentration of NO is still overestimated by 200% at the resolution of 1 km. The concentration of O_3, on the other hand, is underestimated by 28 - 71%. The bias is largest at the resolution of 9 km, and smallest at 1 km. From the example of Tuen Mun station, one can see that increasing resolution has a significant impact and improvement on the model performance when the station is close to a point source by preventing overmixing of pollutants in coarse model grid.

The model performs best at the New Town East stations. The averaged statistical metrics of the two stations are listed on Table A.23 and the time series of the mixing ratios from the model and observation at the Shatin station are plotted on Figure 2.38. At the resolution of 27, 9, 3 and 1 km, the NMB are +39%, -31% , -21% and -12% respectively for NO, +34%, -16%, -1% and +3% for NO_2, and -22% -6%, -9% and -6% for O_3. The Pearson's correlation coefficient also has an increasing trend with resolution for all the 3 species. The New Town East stations are relatively far from the point sources and there is a relatively low level of local emissions (less vehicles). Under these conditions, the model can perform relatively well. Since these two stations are in new towns that are moderately urbanised, increasing model resolution has an impact on the calculated results and can improve model performance.

At last the overall performance of the model at the 4 different resolutions is evaluated with the observational data from all the 16 stations. The Index of Agreement (IOA) is also introduced here

$$IOA = \begin{cases} 1 - \dfrac{\sum_{i=1}^{n} |M_i - O_i|}{2\sum_{i=1}^{n} \left|O_i - \bar{O}\right|} & \text{if } \sum_{i=1}^{n} |M_i - O_i| \leq 2\sum_{i=1}^{n} \left|O_i - \bar{O}\right| \\ \dfrac{2\sum_{i=1}^{n} \left|O_i - \bar{O}\right|}{\sum_{i=1}^{n} |M_i - O_i|} - 1 & \text{if } \sum_{i=1}^{n} |M_i - O_i| > 2\sum_{i=1}^{n} \left|O_i - \bar{O}\right| \end{cases} \tag{2.1}$$

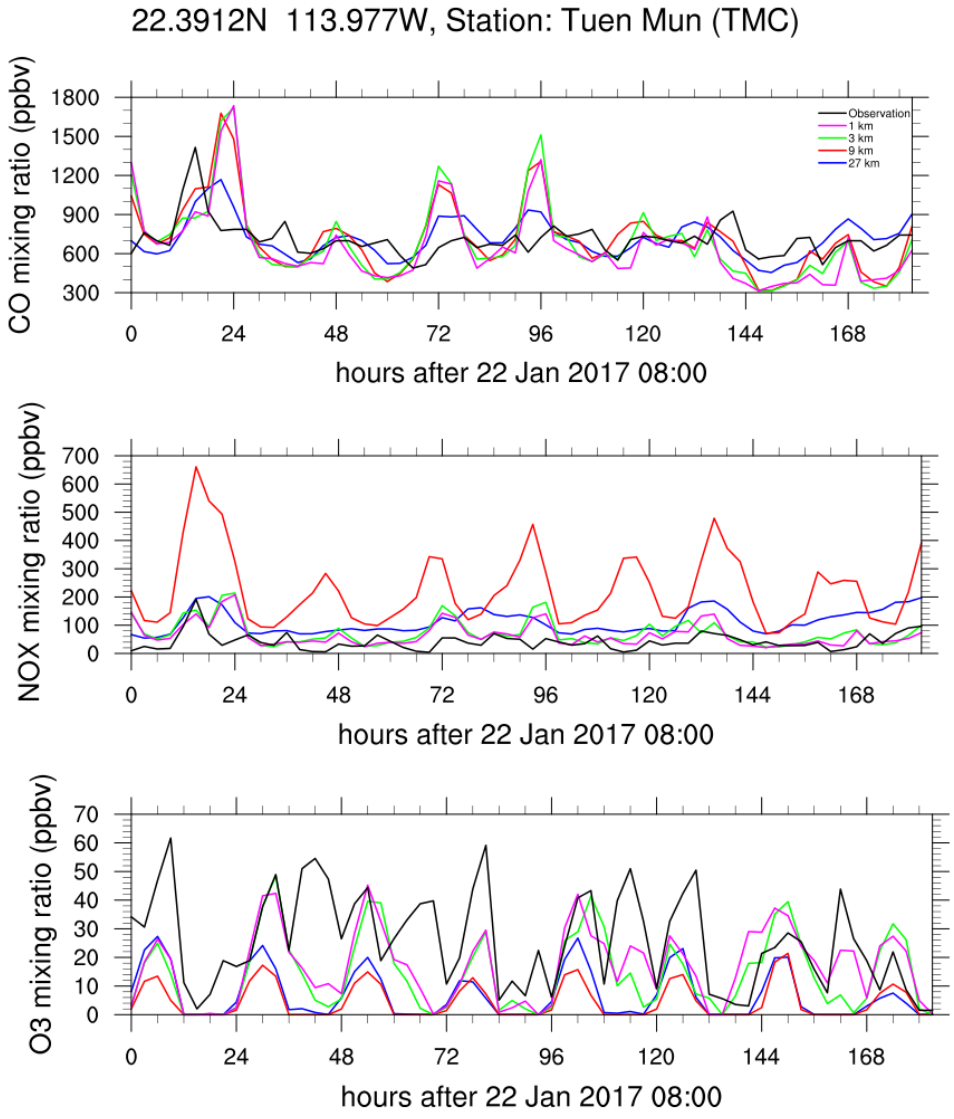

Figure 2.37: Time series of the observed and modelled mixing ratios of CO (top), NO_X (middle) and O_3 (bottom) at the 4 different resolutions from 22nd January 2017 8 am at Tuen Mun station. The modelled data are plotted with blue, red, green and magenta at the resolution of 27, 9, 3 and 1 km respectively. The observed data are plotted in black. The data presented here are averaged every 3 hours.

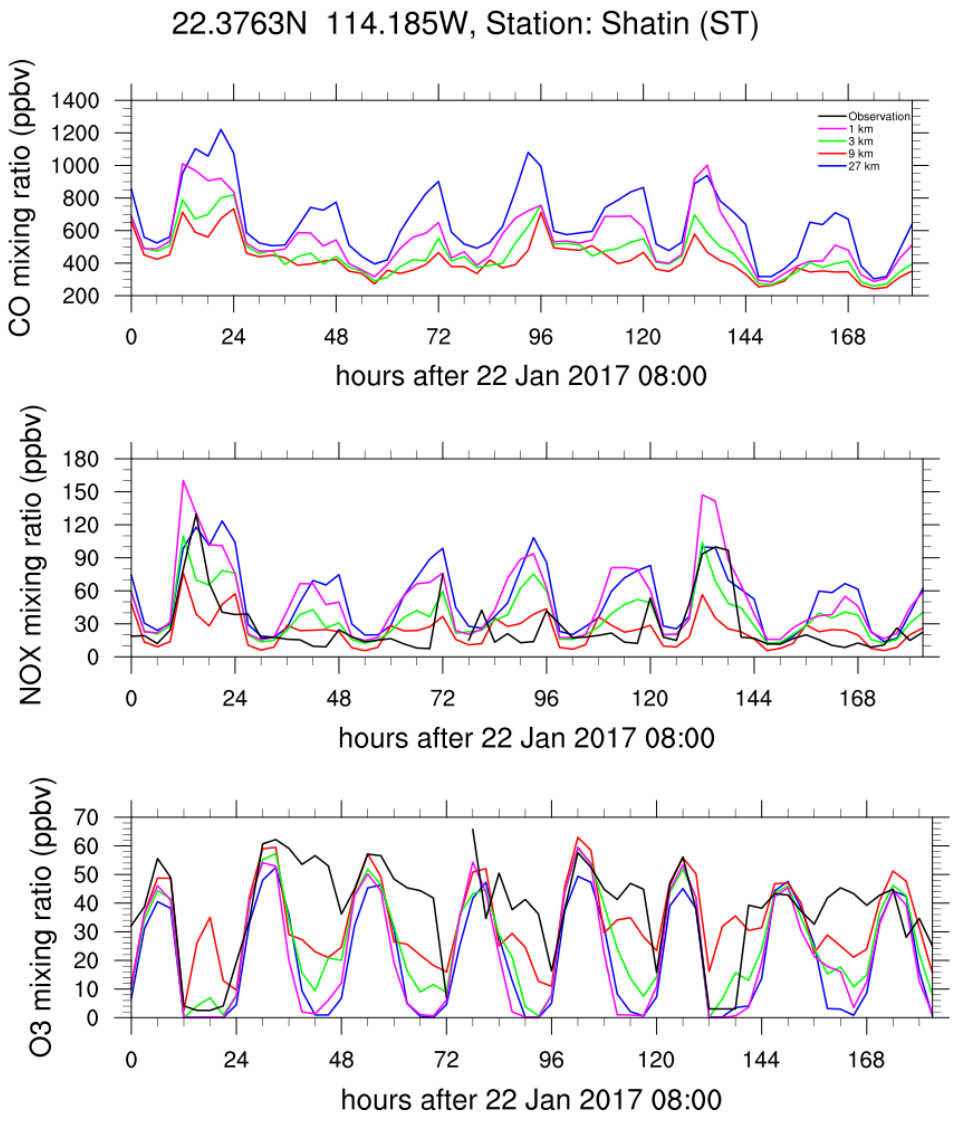

Figure 2.38: Time series of the observed and modelled mixing ratios of CO (top), NO_X (middle) and O_3 (bottom) at the 4 different resolutions from 22nd January 2017 8 am at Shatin station. The modelled data are plotted with blue, red, green and magenta at the resolution of 27, 9, 3 and 1 km respectively. The observed data are plotted in black. The data presented here are averaged every 3 hours.

for the evaluation of the overall performance (Willmott et al.)[16]. The value is bounded by -1 and 1. A value of 1 indicates a perfect match, and -1 indicates no agreement with the observation at all. The mean mixing ratios, mean bias, normalised mean bias and the index of agreement (Equation 2.1) are calculated for the daily mean mixing ratios. One can see in general, the model undercasts CO, NO and O_3 mixing ratios, and overcasts NO_2 mixing ratio. From the biases, it is not obvious that at which resolution the model is performed the best. However, if one refers to the index of agreement, which also consider the trend of the time series, one can see that the model performs significantly better at the resolutions of 1 and 3 km than the lower resolutions with a significantly higher IOA (except in CO). The improvement is more significant for NO and NO_2. However, when the resolution increases from 3 km to 1 km, the improvement is not so significant. This is consistent with the other studies on other big cities (e. g. Tie et al. (2010); Kuik et al. (2016)).

Overall performance

CO	obs	27-km	9-km	3-km	1-km
Mean (ppbv)	639.27	434.93	431.94	430.14	440.37
MB (ppbv)	-	-87.62	-70.62	-79.72	-72.53
NMB (%)	-	-6.12	-4.93	-5.57	-5.07
IOA	-	-0.0989	-0.1302	-0.1458	-0.1149
NO	obs	27-km	9-km	3-km	1-km
Mean (ppbv)	34.08	15.66	24.60	21.23	21.80
MB (ppbv)	-	-0.79	0.09	-0.79	-0.70
NMB (%)	-	-11.37	1.30	-11.40	-10.17
IOA	-	0.4827	0.1853	0.4982	0.5153
NO_2	obs	27-km	9-km	3-km	1-km
Mean (ppbv)	25.72	28.77	30.41	28.95	29.18
MB (ppbv)	-	0.30	0.59	0.38	0.50
NMB (%)	-	3.00	5.85	3.80	4.94
IOA	-	0.3257	0.3626	0.4929	0.4890
O_3	obs	27-km	9-km	3-km	1-km
Mean (ppbv)	21.62	20.47	19.40	20.59	21.24
MB (ppbv)	-	-0.42	-0.67	-0.57	-0.62
NMB (%)	-	-3.44	-5.46	-4.65	-5.07
IOA	-	0.3463	0.4033	0.4634	0.4694

Table 2.4: Averaged Statistical metrics between the observed and modelled data over all stations. The means of the modelled and observed data, the standard deviation of the modelled and observed data (σ) and the mean biases between the modelled and observed data (MB) are in units of ppbv. The normalised mean biases (NMB), the mean fractional biases (MFB), and the Pearson's correlation coefficients (r) are dimensionless.

[16]There are multiple versions of the index of agreement from a number of authors. Here the version used in (Bouarar et al. 2017) is adopted.

2.5 Effect of emission resolution

In this section the effect of emission resolution on the chemical calculation of the WRF-Chem model is evaluated. The MarcoPolo emission at the original resolution of $0.01° \times 0.01°$ is degraded into a coarser resolution of $0.1° \times 0.1°$ by lumping every 10×10 of the original grid to one coarser grid. The emission inventory at both resolutions are then used in the WRF-Chem model at the model resolution of 1 km. The runs with the emission at the original resolution of 0.01° is named MarcoPolo, and the one with emission at resolution of 0.1° is named MPlores in this section.

The colour maps of the NO emission on 27$^{\text{th}}$ January 2017 at 11 am in the MarcoPolo and MPlores runs are shown on the left and right panels of Figure 2.39 respectively. One can see with the lower resolution, the point sources are diluted in the map of the MPlores run. It also fails to show the high-emission regions around Tuen Mun and around Lamma island around the power plants. From the statistics of the emission data (Table 2.5), despite the slightly lower mean emission fluxes of the CO and NO_X emission in MPlores, the maximum emission fluxes of CO and NO_X in the MPlores run are 3.56 and 56.23 times lower than the MarcoPolo run respectively.

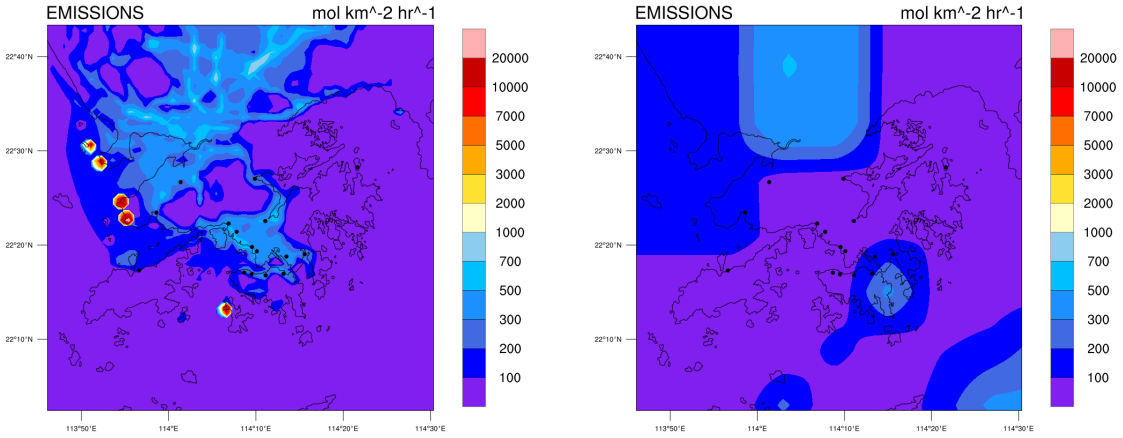

Figure 2.39: Left: NO emission flux of MarcoPolo (top-left) on 27$^{\text{th}}$ January 2017 at 11 am with the original MarcoPolo emission inventory at 1 km resolution. Right: NO emission flux of MPlores (top-right) with the MarcoPolo emission inventory at 10 km at the same time.

CO	MarcoPolo	MPlores
Mean	714.24	642.96
Standard deviation	1109.19	816.04
Maximum	11382.20	3195.61

NO_X	MarcoPolo	MPlores
Mean	162.52	134.04
Standard deviation	852.30	128.20
Maximum	31569.35	561.43

Table 2.5: General statistics of the emissions of CO, NO_X (mol km^{-2} hr^{-1}) of the MarcoPolo and degraded 10 km-resolution emission inventory MPlores over all the simulation time in January 2017.

Figure 2.40 shows the colour maps of the ozone concentrations from the MarcoPolo (left panel) and MPlores (right panel) runs on 27th January 2017 at 11 am. The map of the MPlores run fails to show the distinct low ozone-concentration regions downwind of the point sources as in the map of the MarcoPolo run (in the south-west direction of Tuen Mun, She Kou and Lamma Island), as it also fails to show the NO_X emission hotspots from the point sources. From the statistics of the concentrations of CO, NO, NO_2 and O_3 (Table 2.6), the mean concentrations of these species are similar in the two runs, except that the mean NO concentration in the MPlores run is 36% lower. Consistent with the emission statistics, the maximum concentrations in the MPlores run are also lower for CO and NO_X, with the maximum NO concentration 10.6 times lower than that in the MarcoPolo run. However, the maximum O_3 concentration in MPlores is slightly higher than in the MarcoPolo run by 3%.

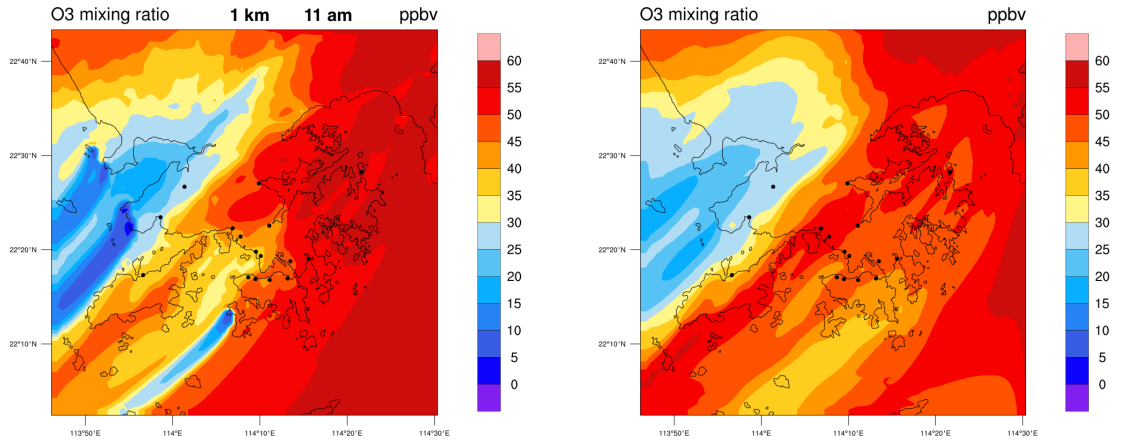

Figure 2.40: Colour maps of O_3 mixing ratio MarcoPolo (left) and MPlores (right) emission inventory. In both cases the model resolution is 1 km.

CO	MarcoPolo	MPlores
Mean (ppbv)	569.01	545.33
Standard deviation (ppbv)	335.85	297.52
Maximum (ppbv)	3540.02	2722.63
Total sum (Mg)	85.86	82.28
NO	MarcoPolo	MPlores
Mean (ppbv)	17.08	10.98
Standard deviation (ppbv)	52.07	25.86
Maximum (ppbv)	3115.62	294.07
Total sum (Mg)	2.76	1.78
NO_2	MarcoPolo	MPlores
Mean (ppbv)	25.15	25.25
Standard deviation (ppbv)	25.09	20.76
Maximum (ppbv)	406.73	117.39
Total sum (Mg)	6.24	6.28
O_3	MarcoPolo	MPlores
Mean (ppbv)	33.44	32.42
Standard deviation (ppbv)	21.30	18.97
Maximum (ppbv)	96.70	99.50
Total sum (Mg)	8.65	8.39

Table 2.6: General statistics of the mixing ratios of CO, NO, NO_2 and O_3 using the MarcoPolo and MPlores inventory over all the simulation time in January 2017.

When one compares the total amount of CO, NO, NO_2 and O_3 in the whole domain d04 (the bottom rows of the specific species in Table 2.6), the differences of the sums of CO, NO_2 and O_3 between the two runs are less than 5%, but the total sum of NO in the MPlores run is 35.6% lower than that in the MarcoPolo run. As shown in Table 2.7, the average ozone production rate ($P(O_3)$) in the MPlores run is slightly less than in the MarcoPolo run by 3.4%, presumably due to the lower mean NO concentration in the MPlores run. The average loss rate ($L(O_3)$) is 4.6% lower in the MPlores run, consistent with its higher NO_2 mean concentration. As a results, the net ozone production rate in the MPlores run 19.7% less than that in the MarcoPolo runs. This net ozone production rate is a bit lower than expected from just a 3.0% decrease in ozone total sum in the MPlores run.

	MarcoPolo	MPlores
$P(O_3)$	1.2316	1.1898
$L(O_3)$	0.8179	0.8574
net $P(O_3)$	0.4137	0.3323

Table 2.7: Ozone production and loss rate of the MarcoPolo and MPlores runs over all the simulation time in January 2017.

Table 2.8 shows the segregation coefficients in the MarcoPolo and MPlores runs. The segregation coefficients between NO and O_3 are similar in the two runs, with the coefficient in the MPlores run only 1% less negative than in the MarcoPolo run. However, the segregation coefficient between NO_2 and O_3 in the MPlores run is 31% less negative than in the MarcoPolo runs, meaning that in the MPlores run the NO_2 and O_3 are less

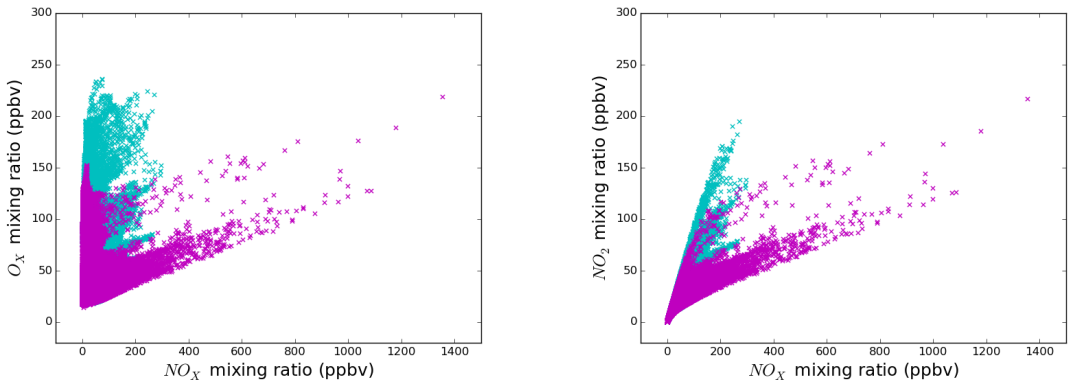

H

Figure 2.41: Scatter plots showing the relations between O_X and NO_X, between NO_2 and NO_X using MPlores (cyan) and MarcoPolo (magenta) emission inventory during the daytime in July 2016.

segregated. The coefficient between NO and NO_2 also drops by 22.8% in the MPlores run, hinting that NO and NO_2 are less correlated.

Segregation coefficient	MarcoPolo	MPlores
NO-O_3	-0.4824	-0.4755
NO_2-O_3	-0.2865	-0.1967
NO-NO_2	1.7531	1.3529

Table 2.8: Coefficients of segregation between O_3 and NO, between O_3 and NO2, between NO and NO_2 using MarcoPolo and MPlores emission inventory over all the simulation time in January 2017 at all time.

We then look the correlations between NO_X and O_X, and between NO_X and NO_2, where their scatter plots between the two species pairs are shown on Figure 2.41. The corresponding results of their linear regression are shown in Table 2.9. From the slope of the plots of the concentration of O_X against that of NO_X, one can see that the local contribution of NO_X to O_X is 3.7% higher in the MPlores run. From the intercept, the background O_X concentration in the MPlores run is also slightly higher by 6.1 ppb. The local contribution may be due to the wider coverage of low-NO_X concentration areas which produces more ozone. The higher regional contributions may be due to the dilution of the precursor emission that mix more O_X from the neighbouring region to the simulated domain. However, when one compares the correlation between NO_X and NO_2 concentrations, the slope in the MPlores run increases by 14.1%, hinting that either more of the NO_X content is constituent of NO_2, or more NO is converted to NO_2 in the MPlores run. This is also consistent with the exceptionally low total amount of NO in the whole domain in the MPlores run.

NO_X−O_X	MarcoPolo	MPlores
Slope	0.0796	0.1162
Intercept	37.36	43.50
R^2	0.0257	0.0176
NO_X−NO_2	MarcoPolo	MPlores
Slope	0.2457	0.3866
Intercept	6.29	4.33
R^2	0.8383	0.8552

Table 2.9: Results of the linear regression of the relations between mixing ratios shown in Figure 2.41.

At last the model comparison between the simulated results from the two runs and the observation data is evaluated. Data at two observation stations, Tuen Mun and Shatin, are illustrated to compare the model performance between the MarcoPolo and MPlores run. Figure 2.42 shows the time series of the results from the two runs and the observational data on 22th January 2017 8 am to 29th January 2017 5 am at Tuen Mun station, and Table A.24 shows the corresponding time-averaged statistical metrics. At the Tuen Mun station, which is close to the point sources of the Castle Peak power plants, the CO concentration is relatively high. The MPlores run gives an underestimated value of CO concentration by 130% due to the dilution effect of its low-resolution emission. However, the MPlores run actually has better results for the concentrations of NO, NO_2 and O_3. It overestimates the NO concentration by 98%, improved from the 200% overestimation by the MarcoPolo run. The MPlores run also gives a less overestimated value of NO_2 concentration, improved by 8.24% from the MarcoPolo run. Due to the less overestimated NO_X concentrations, the model also gives a less underestimated O_3 concentration, improved by 6.19% from the MarcoPolo run. It illustrates here, that the dilution effect of the low-resolution emission inventory compensates the overestimation of NO emission from the point sources in the original inventory. Also note that the temporal variation of the MPlores run actually highly resembles that in the MarcoPolo run.

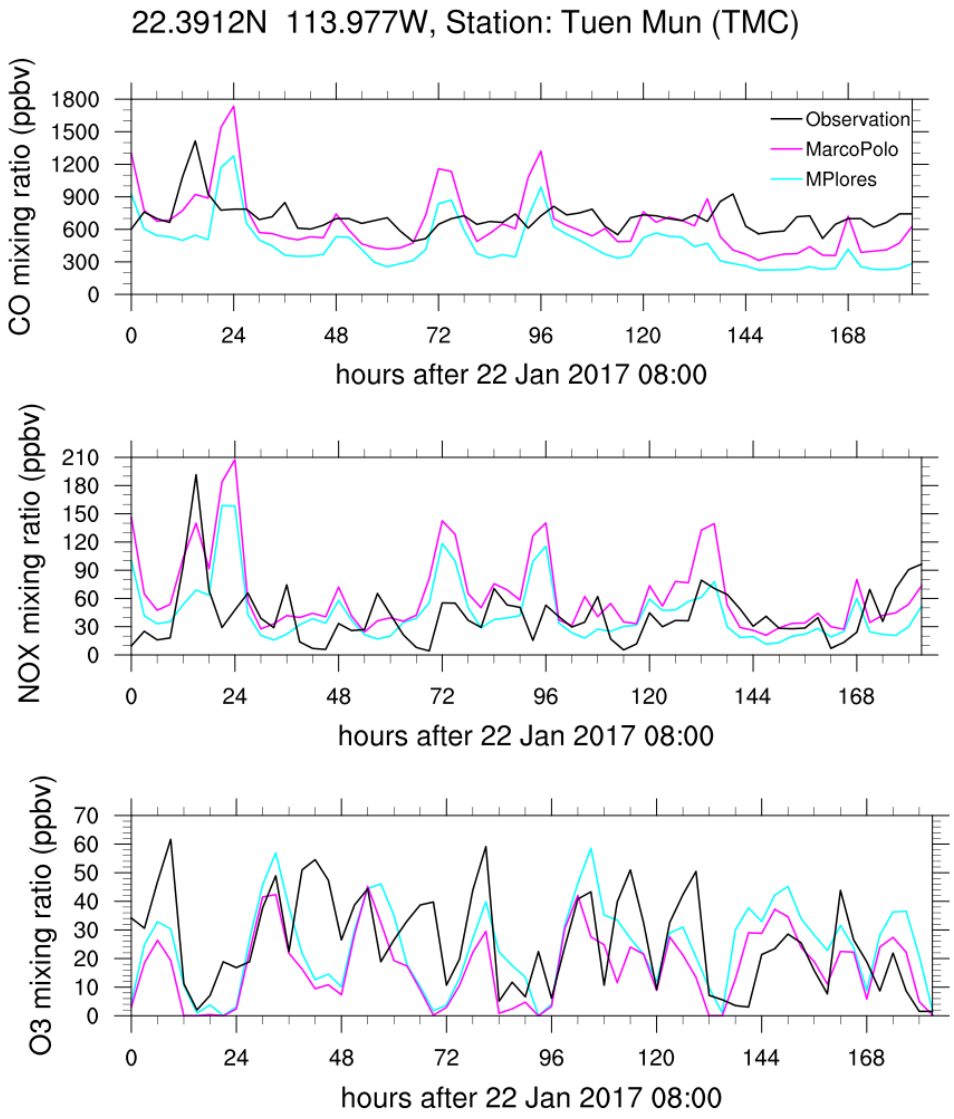

Figure 2.42: Time series of the observed and modelled mixing ratios of CO (top), NO_X (middle) and O_3 (bottom) in the MarcoPolo (magenta) and MPlores (cyan) runs from 22nd January 2017 8 am at Tuen Mun station. Similar description as Figure 2.35.

Then the performance at the Shatin station, located in a suburb area and relatively far away from the point sources, is evaluated. The MPlores run again gives a lower CO concentration, 22% less than that from the MarcoPolo run. It also underestimates the concentrations of NO and NO_2 by 66% and 32% respectively, in contrary to the 7% and 22% respective overestimation in the MarcoPolo run. The time series in Figure 2.43, the MPlores run fails to capture some of the high-emission peaks of NO_X (see the peaks at around 15 and 132 hour). However, the MPlores run only slightly overestimates the O_3 concentration by 8%, which have a comparable performance as in the MarcoPolo run, which underestimates O_3 concentration by 12%. From the time series, the MPlores run actually gives are more accurate O_3 calculation on the daily maximum value in the

period of 0 to 84 hours. It also does not deplete O_3 completely like in the MarcoPolo run, which better fit with the observations when O_3 nighttime values are not zero. From the two examples, one can see that using emission inventory at low resolution does not necessary gives a worse concentration results, as its dilution effect may compensate other errors from a high-resolution emission inventory.

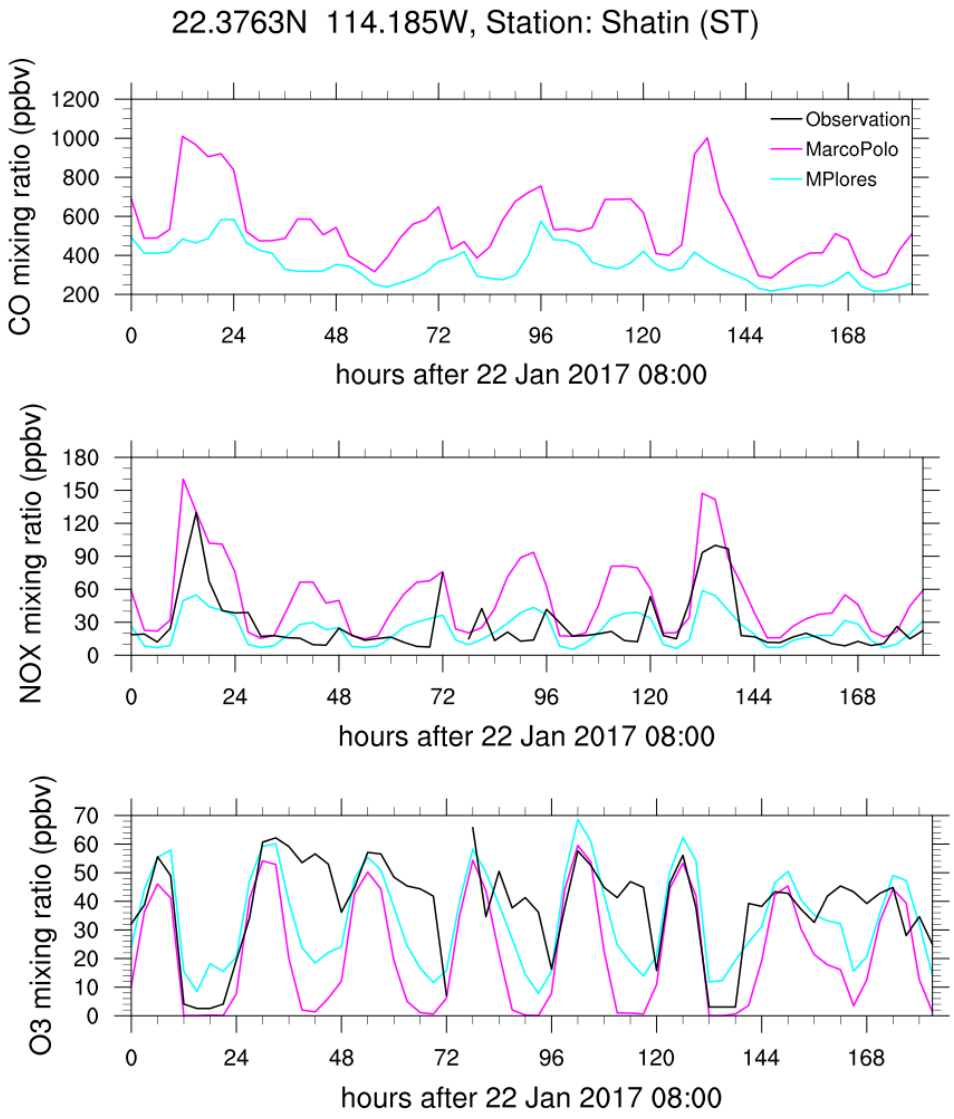

Figure 2.43: Time series of the observed and modelled mixing ratios of CO (top), NO_X (middle) and O_3 (bottom) in the MarcoPolo (magenta) and MPlores (cyan) runs from 22nd January 2017 8 am at Shatin station. Similar description as Figure 2.35.

Overall performance			
CO	obs	MarcoPolo	MPlores
Mean (ppbv)	639.27	440.37	386.71
MB (ppbv)	-	-134.75	-72.53
NMB (%)	-	-18.82	-10.13
IOA	-	-0.26	-0.11
NO	obs	MarcoPolo	MPlores
Mean (ppbv)	34.08	21.80	14.52
MB (ppbv)	-	-13.55	-7.03
NMB (%)	-	-39.18	-20.35
IOA	-	0.49	0.52
NO_2	obs	MarcoPolo	MPlores
Mean (ppbv)	25.72	29.18	25.07
MB (ppbv)	-	-0.20	0.50
NMB (%)	-	-4.01	9.89
IOA	-	0.47	0.48
O_3	obs	MarcoPolo	MPlores
Mean (ppbv)	20.84	20.47	24.73
MB (ppbv)	-	-0.14	-0.62
NMB (%)	-	-2.23	10.15
IOA	-	0.49	0.47

Table 2.10: Averaged statistical metrics between the observed and modelled data in the MarcoPolo and MPlores runs of all stations of the chemical species CO, NO, NO_2 and O_3. Similar description as Table A.20.

At last the overall performance of the MPlores and MarcoPolo runs are evaluated by calculating the statistical metrics on the daily mean mixing ratios as in Section 2.4. The MarcoPolo run have both smaller bias and a higher scores in the IOA for CO and NO. For NO_2, the MarcoPolo run has a higher bias than the MPlores run but a slightly higher score in IOA, possibly due to better correlation with the observation data. However, for O_3, the MarcoPolo run has both a higher bias and a lower score in the IOA, implicating it gives a worse match with the observation than the MPlores run. This may be explained by the less underestimation of ozone at nighttime in the MPlores run.

From the two station examples and the overall statistics, one can see that using emission inventory at low resolution tends to underestimates the precursor concentrations. However, its dilution effect may compensate the overestimated emission values a high-resolution emission inventory, and reduce the underestimation of ozone values at night.

2.6 Conclusions and Discussions

Calculation on ozone chemistry and production is particularly sensitive to model resolution due to the non-linear chemistry of ozone. To investigate the problem, a sensitivity study on ozone chemistry to model resolution is conducted in this chapter. The study targets at the region around Hong Kong and the ambient Pearl River Delta

due to its intense emission sources, dense urbanisation and complex topography.

For this purpose, a WRF-Chem model is set up using similar configuration as in Bouarar et al. (2017) with 4 nested domains at 4 different resolutions of 27, 9, 3 and 1 km. The $0.01^\circ \times 0.01^\circ$ emission inventory around the Pearl River Delta region from the Marco Polo-Panda project is used (Hooyberghs et al. 2016). The results within the smallest domain (d04) from the runs at the 4 different resolutions are analysed and inter-compared to quantitatively evaluate the effect of increasing model resolution. We focus on the change in model calculation of processes related to ozone chemistry, instead of on model performance improvement as in the previous studies (e. g. Schaap et al. (2015)). Two 11-day periods in January 2017 and July 2016 are simulated as the Summer and Winter data.

The effect of model resolution is very distinguished when compared the colour maps at different resolutions. Only at the resolutions of 1 and 3 km can the model show the impact of geographic topography on temperature and wind variations. With increasing resolution, the mean horizontal winds decrease and the range of the wind direction increases. The mean boundary layer height also decreases. There is a longer tail of low temperature in the probability density function of the surface temperature, which corresponds to the lower temperature at the higher elevation on the terrains. Increasing model resolution also better resolves the emission hotspots of precursors. Only at the resolution of 1 km can the model identify the highway network in Shenzhen and highly-populated regions in Hong Kong as high-emission areas. The mean emission fluxes of CO and NO_X increase with increasing resolution. In particular, the maximum CO and NO_X emission fluxes increase in 1-2 orders of magnitude as the resolution increases from 27 km to 1 km. The effect is more sensitive for NO_X emission.

For the calculated mixing ratios, the model also shows sharper and more extended tails of high-concentration regions for CO and NO_X and low-concentration regions for O_3 at the downwind areas of the point sources as the resolution increases. Only at the higher resolutions can the model give minima values of CO and NO_X and the maxima of O_3 at the high-elevation areas around the terrains. The mean mixing ratios of CO and NO_X tend to increase with resolution, while that of O_3 decreases with resolution. However, the relations of the mean mixing ratios with resolution are not so clear between the resolution of 1 and 3 km. NO/NO_X ratio also increases with resolution, hinting more active photochemistry with increasing model resolution. The diurnal cycle of CO and NO_X varies mainly dynamically with the evolution of the boundary layer height, and O_3 varies diurnally accordingly and also with the availability of daylight. However, the diurnal cycle between NO_X and O_3 is delayed at the resolution of 27 km, presumably because the boundary layer shrinks less rapidly than in the runs at the higher resolutions, which prolongs the transport of regional ozone from higher altitudes.

The time-averaged total amounts of CO and NO_X decrease as the resolution increases

from 9 km to 1 km. The total amount of O_3 decreases systematically from 27 km to 1 km in Winter. The tendency is however not so clear during Summer. The ozone production rate increases with increasing resolution, consistent with the increasing NO/NO_X ratio. The ozone loss rate also increases with resolution, presumably because more NO_2 hotspots are resolved at higher resolutions, encouraging the loss of NO_X by converting NO_2 to nitric acid and organic nitrates. The net ozone production rate per NO_X concentration decreases when the resolution increases from 27 km to 3 km, as expected from the non-linearity of ozone chemistry and the increase in NO_X mixing ratios. However, the rate increases again when the resolution increases from 3 km to 1 km. It is presumably due to a combination effect of the slight drop of mean NO and NO_2 mixing ratios and a substantial increase in the contribution of VOCs to ozone production.

Despite the net ozone production rate is higher in Summer, both the mean concentration and the total sum of O_3 are higher in Winter, indicating a large contribution of O_3 from regional transport in Winter. The prominent decrease in modelled O_3 total sum is speculated to be a combined effect of the decreasing regional influence and the decreasing net ozone production rate with increasing resolution.

As the distribution of the calculated mixing ratios changes with increasing resolution, it also changes the segregation and correlation between the NO_X species and O_3. The segregation between NO and O_3 increases with resolution during daytime in Summer and Winter, and decreases during nighttime in Winter. The deviation is most significant when the resolution increases from 27 km to 9 km. Similar pattern also occurs to the segregation coefficient between NO and NO_2, suggesting the change in processes in the $NO-NO_2-O_3$ chemical cycle between day and night. The correlations between the NO_X and O_X species are calculated for the daytime data in Summer due to the more active photochemistry at that period of time. With increasing model resolution, the relation between NO_X and OX becomes more positive, indicating that the local contribution to O_X in levels of NO_X increases by 3% as the resolution increases from 27 km to 1 km.

Although only the horizontal grid resolution changes among the 4 runs, it also affects the vertical profiles of the physical and chemical variables. In particular, both the mean and variance of the vertical wind increase significantly with increased resolution. The change of grid resolution can even change the direction of the mean vertical transport in some altitudes. Increasing grid resolution also increases the magnitude of fluxes of CO, NO, NO_2 and O_3. The vertical profile of ozone flux is particularly sensitive to grid resolution. Both of its magnitude and sign change with different resolutions. For example, at the resolutions of 9, 3 and 1 km, the O_3 flux is negative in the lower part of the boundary layer, indicating mean downward transport; but the flux becomes positive when the resolution decreases to 27 km.

The model performance at the 4 resolutions is then evaluated with observational data. The observational data are obtained from 16 ground stations in Hong Kong, covering

4 types of areas in different urbanisation levels. In particular, the model improves its performance with increasing resolution more significantly when it is close to a point source or in a moderately urbanised area. The improvement is less significant in rural areas, similar to previous findings (e. g. Tie et al. (2010)). The model shows almost no improvement with increasing resolution on street-level observation in highly-urbanised areas. Overall, the model gives a smaller bias (except for CO) and a higher score in the index of agreement with increasing resolution. The improvement, however, is not so significant when the resolution increases from 3 km to 1 km.

At last a simulation is performed with the grid resolution of 1 km but with a resolution degraded emission inventory at the resolution of $0.1^\circ \times 0.1^\circ$, i. e. 10 times coarser than the original emission data. With the coarser emission inventory, the net ozone production rate decreases by $\sim 20\%$. The segregation between NO_2 and O_3 drops by 31%. The local contribution by NO_X to O_3 increases by 3.7%, and by 14.1% to NO_2, hinting more NO is converted to NO_2. Although the new run tends to underestimate precursor concentrations and does not match the peak concentrations as good as in the high-resolution emission run, the diluted emission in the coarser emission inventory compensates the overestimation in the original inventory near a point source. It also gives a less underestimation on ozone nighttime values.

The statistics analysed in this chapter focus mainly on the mixing ratios of CO, NO_X and O_3 concerning ozone chemistry. However, VOCs, such as isoprene, are also known to play an important role in ozone chemistry, especially in this case that the simulated domain is in the VOC-limited regime. The study stays the focus on the species CO, NO_X and O_3 for the purpose of comparison with the results in the later chapter. Therefore an analysis involving VOCs is limited in this Chapter. However, due to the abundance of vegetative areas (48% of the total landmass[17]) in between urban areas in Hong Kong, similar approaches including the effect of isoprene and other VOCs would be useful for further study.

During the nighttime, the model usually gives substantial overestimations in CO and NO_X concentrations and underestimations in O_3. This is speculated to be due to the underestimated vertical mixing during nighttime in the model. Excess residual heat from the building surfaces often induce more vertical mixing than normal ground surface, making the urban nighttime boundary layer less stable. The model may not take this effect into account as it does not include any special treatment related to urban structures. This scenario is also reported in many other studies (Bouarar et al. 2017; Kuik et al. 2016).

The significant overestimated modelled concentration at the Tuen Mun observation station also raised the concern on the accuracy of emission data from point sources in

[17]including the areas of woodland and shrubland, from the land utilisation data in Hong Kong 2017 from the HKSAR Planning Department (`https://www.pland.gov.hk/pland_en/info_serv/statistic/landu.html`).

the emission inventory used (in this case this is the Castle Peak power plants). Liu et al. (2016) reported a decreasing trend of NO_X emission in China after the year 2011, despite in many emission inventory an increasing trend is assumed. As the Marco Polo emission inventory is released in 2014, it may not be updated enough to account for the emission in 2016 and 2017. Hence there is a chance that the emission data in 2016 and 2017 are overestimated. It is also noted that the potential error induced from the emission inventory is substantially large. For instance, if we assume that the overestimation of the modelled concentrations in the Tuen Mun station is solely due to the overestimated emission from the Castle Peak power stations, the mean bias for NO is $\sim 200\%$ even at the resolution of 1 km. Compared with the effect from the change in model resolution, that increasing the model resolution from 27 km to 1 km decreases ozone production efficiency by $\sim 35\%$, increases the segregation between NO and O_3 by 35% and increases the local contribution of NO_X to O_3 for 3%, the error from emission inventory is more prominent. However, this great influence may only apply to areas which are close to the point sources with overestimated emissions.

From the underestimation of CO and NO_X concentrations in the model at the roadside and urban stations, one may also speculate that the emission inventory underestimates the emission from local transport. In fact, the local transport accounts for $\sim 30\%$ of the NO_X emission in Hong Kong (Environment Bureau 2013), and therefore an accurate emission of local transport is crucial in the simulated domain. However, an accurate local transport emission requires an extensive survey on the local transport data from local organisations, which are not covered by the downscaling procedures in the Marco Polo emission inventory. Also, the model does not include a diurnal variation of the emissions, which is significant in transport emission due to the prominent traffic peak hours in big cities. Future improvement on modelling in the area may take these points regarding local transport emission into account.

The relative large biases in the roadside stations also raise the question that whether regional models similar to the adopted model is adequate to model roadside air quality. First, the first vertical layer in the model is with a vertical spacing of ~ 20 m, which is higher than the roadside stations at an altitude of 3-5 m. The modelled data may not be suitable to be compared to observation data obtained from such stations. Second, as these stations are well inside the urban canopy, in which the turbulent flow structure is complex, the resolution at 1 km fails to resolve such turbulent motions. Extra techniques such as urban canopy model or even coupled large-eddy simulations are necessary to tackle with such situations.

It is also noted that the meteorological data are missing in the observation stations. This makes model validation on local wind transport difficult in this study. Also there are only observation data at the surface layer from the stations. An observation of pollutant concentrations at multiple vertical level is most valuable when accounting for

the vertical mixing of pollutants (Wang et al. 2001). With the potential installation of LIDAR[18] system in observation stations[19], vertical profiles of modelled concentrations can be validated in the near future.

Despite the above-mentioned limitations in the study of this chapter, this study still successfully serves its purpose to illustrate the substantial effect of model resolution on calculating ozone chemistry and production in aspects of concentration statistics, ozone production rates, segregation between ozone and its precursors, and local contributions of NO_X to ozone. In the next chapter we shall look into the problem in a finer scale which resolves turbulence explicitly.

[18]The LIDAR (LIght Detection And Ranging) is a remote sensing instrument operating in the optical range. Depending on the desired measurement, lidar systems use various light-matter interactions such as Rayleigh, Mie and Raman scattering or fluorescence, to measure the ozone vertical distribution (Harris et al. 1998).

[19]For example in Hong Kong, such LIDAR system has been planned by the Environmental Protection Department and a proposal has been handed to the Legislative Council for financing the system in December 2018.

Chapter 3

Chemical-turbulence Interaction in Planetary Boundary Layer

3.1 Introduction

3.1.1 Chapter objective and outline

From Chapter 2, we have learnt that at different resolution of model grid and emission inventory, chemical transport models (CTMs) calculate chemistry differently. At higher resolution, the model is more capable to resolve meteorological conditions with varied topography (e. g. wind patterns) and locations of source and sink of segregated pollutants. With these increasing resolving capacities, the ozone production efficiency (net ozone production rate per NO_X concentration) decreases due to the non-linearity of ozone chemistry. The daytime segregation between NO_X and O_3 and the local contribution of NO_X to O_3 also increase. The model at high resolution gives better agreements with observations in moderately urbanised area and near point sources. However, the deviation in statistics of model results is not so significant when the resolution increases from 3 km to 1 km. One of the possible reasons causing such "bottleneck" in model improvement with increasing resolution in a relatively high resolution range is the misrepresentation of subgrid processes in the CTMs. For example, even a CTM at the resolution of 1 km fails to resolve turbulent motions in the atmosphere. The typical turbulent length scale in urban environment is $\sim O(10)$ m, but a resolution at such length is not practical in operational CTMs. Therefore, in this chapter, a turbulent-resolving tool, direct numerical simulations (DNS), is employed to explicitly calculate the effect of turbulent motions on chemical reactions in the boundary layer.

Several past studies have investigated the topic in a convective boundary layer with initially-segregated sources , mainly by mean of large-eddy simulations (LES) (e. g. Schumann (1989); Krol et al. (2000); Vinuesa and de Arellano (2003, 2005), etc.). The

Damköher number is used to classify the turbulent and chemical regimes in which turbulent mixing significantly affects chemical reactions in atmospheric flows (Damköhler 1940; Danckwerts 1952; Toor 1969; Donaldson and Hilst 1972). For fast reactions with $Da \geq 1$, where the chemical timescale of the reactant is comparable to or shorter than the turbulent timescale of the atmosphere, the reactants are not well mixed by turbulence before chemical reaction takes place. Such inefficient turbulent mixing of the chemicals causes the chemical reaction to undergo a significantly different rate from its imposed value. Vinuesa and de Arellano (2003) suggested the use of the effective chemical reaction rate to quantitatively describe such effect of inefficient turbulent mixing on the rate of chemical reaction. Their study also showed that in the fast chemistry regime ($Da = 0.8 - 1.9$), the effective chemical reaction rate is only $\sim 85\%$ of the imposed rate.

Some studies (Krol et al. 2000; Auger and Legras 2007; Ouwersloot et al. 2011) also accounted for the impact of source heterogeneity on such chemical-turbulence interaction, and illustrated that heterogeneous emission increases the segregation of the precursors and further decreases the actual reaction rates under a range of emission configurations. The investigation also extended to more realistic chemical schemes and environments. In particular, Kim et al. (2016) investigated the impact of turbulent mixing on isoprene-OH reactivity by LES with a comprehensive chemistry scheme, and showed that the segregation of isoprene and OH causes $\sim 20\%$ decrease to $\sim 10\%$ increase in the horizontally-averaged chemical reaction rate, depending on the emission flux of nitrogen oxides. Brosse et al. (2017) conducted a similar study focusing on the atmosphere in southern West Africa, and found a reduction of up to 8% in the mean chemical rate between the OH radical and C>2 aldehydes in their urban case. All these studies point to a direction that the inefficient turbulent mixing of the chemicals in the atmosphere would alter the reaction rate from its imposed value substantially in urban conditions, in which the emission sources are particularly intense and heterogeneous.

In this chapter, DNS simulations are conducted to investigate the impact of inefficient turbulent mixing on chemical reactions in a convective boundary layer, first in a similar configuration as in the previously-mentioned studies. In contrast to the previous LES works, our DNS simulations can explicitly resolve the convective turbulent motions in the boundary layer without uncertainties from subgrid turbulent parametrisations. While previous studies focus on agricultural and rural conditions where the emission fluxes are relatively low ($\sim O$ (0.01) ppb m s^{-1}), the simulations here extend to strong emission fluxes in typical urban values ($\sim O$ (0.1-1.0) ppb m s^{-1}) to re-examine the effect in urban environment. With strong emission fluxes, subgrid turbulent parametrisation in LES simulations may induce significant error near the surface where the tracer is emitted (Vinuesa and Porté-Agel 2005, 2008).

The results from DNS are then degraded into lower resolution to mimic the calculation from regional models. Previous work always compared their LES results with a

complete-mixing model, which assumes tracers to be completely mixed within the whole boundary layer in the simulation domain (or in other words, assumes the whole boundary layer to be in the same model grid). This attempt is however unsuitable for the comparison with CTMs, as regional CTMs nowadays are usually at resolutions of a few kilometres, and consist of multiple vertical levels within the boundary layer.

At last, a parametrisation scheme based on physical and chemical variables easily obtainable from the simulation is then formulated for purpose of implementation into a regional model. There have been previous attempts to parametrise this subgrid chemical-turbulence interaction (Vinuesa and de Arellano 2005; Petersen and Holtslag 1999), but these schemes involved a lot of parameters such as the entrainment fluxes and the covariance of the concentrations, which are too complicated to be derived within an operational CTMs.

The structure of the chapter is as follows. The problem of misrepresenting subgrid chemical-turbulence interaction is first illustrated by simulations with tracer advecting in turbulent wind field in a box mimicking a grid in a large-scale model right after this section.The DNS model with a bottom-top emitted and a top-bottom entrained tracers reacting in a second-order chemical scheme is first described, and its results are then presented. Based on these results, the mechanism of how turbulence affect chemical reactions is discussed. The impact of degrading the model resolution on chemical calculation is then assessed. This is then followed by extending the investigation to simulations with NO_X-O_3 chemistry and heterogeneous surface emission. At last the parametrisation of the effect of turbulence on chemistry is then formulated and its implication in chemical-transport modelling in urban environments in a CTM is speculated.

3.1.2 Interaction between turbulent mixing and chemical reactions: Fundamental representation

Chemical-turbulence interaction is considered to be a sub-grid process, and is unresolved in large-scale models. To preview this problem in a fundamental representation, tracer advection simulations in turbulent wind field within a model grid in a large-scale model with the simulation domain mimicking a grid in a large-scale model. Possible errors can also be induced from the adopted advection scheme, the dimension and the resolution of the simulations. In this section, we will explore how the numerical schemes in a model may introduce errors to the calculation of tracer advection in a turbulent flow, and how subgrid turbulent motion affects chemical reactions with varied Reynolds number, the chemical reaction rate coefficient and the initial separation between the reactant tracers.

Numerical schemes for tracer advection

Different numerical methods have been developed to solve equations in atmospheric flows. There are a number of numerical schemes to solve the simple advection equation in general to adapt with different simulation settings (see Brasseur and Jacob (2017) and Dullemond and Wang (2009) for overview, and Durran (2010) in details). In this session different numerical schemes are explored to search for a suitable scheme to solve the problem addressed in this session.

To illustrate the variety of numerical schemes, a range of schemes are employed to solve the one-dimensional advection equation:

$$\frac{\partial \Psi}{\partial t} + u\frac{\partial \Psi}{\partial x} = 0$$

for a step-function Ψ advecting with a constant velocity of u along the x-direction. The analytical results of the tested schemes and the exact solution are plotted in the left panel of Figure 3.1. Despite of the simplicity of the problem, the employed schemes all give a range of different solutions. To address the problem studied in this thesis, a good numerical scheme should fulfil the following criteria. First, it should be mass-conserving in order to prevent artificial loss of the chemicals. Second, it should be sign-preserving. Otherwise negative concentration may produced in the analytical solution, which results in error in the calculation of chemical reactions. Last, the scheme should be non-diffusive, since the numerical diffusion of the scheme produces spurious reactions.

According to these criteria, the upwind-class schemes are better performed in the setting of this scenario (plotted in details on the right panel of Figure 3.1). The upstream scheme is a first-order scheme which gives the solution

$$\Psi_i^{n+1} = \Psi_i^n - \frac{u\Delta t}{\Delta x}\left(\Psi_i^n - \Psi_{i-1}^n\right)$$

at $x = x_i$ and $t = t_n$. The solution is mass-conserved and sign-preserved. However, it is also highly diffusive, which generates excessive numerical mixing, and thus is not desirable. The second-order Fromm scheme is a piecewise linear scheme, which is expressed as

$$\Psi_i^{n+1} = \Psi_i^n - \frac{u\Delta t}{\Delta x}\left(\Psi_i^n - \Psi_{i-1}^n\right) - \frac{1}{2}\frac{u\Delta t}{\Delta x}\left(\sigma_i^n - \sigma_{i-1}^n\right)(\Delta x - u\Delta t).$$

The piecewise slope σ_i^n at $x = x_i$ and $t = t_n$ is then

$$\sigma_i^n = \frac{\Psi_{i+1}^n - \Psi_{i-1}^n}{2\Delta x}.$$

The Fromm scheme is less diffusive, but produces overshooting and undershooting at points where the slope is large. Undershooting results in negative concentrations, and therefore should be avoided. The remaining two schemes, MPDATA and van Leer,

are advanced upwind scheme. The advanced schemes are less diffusive and do not generate overshooting or undershooting results, and therefore are considered to be good candidates.

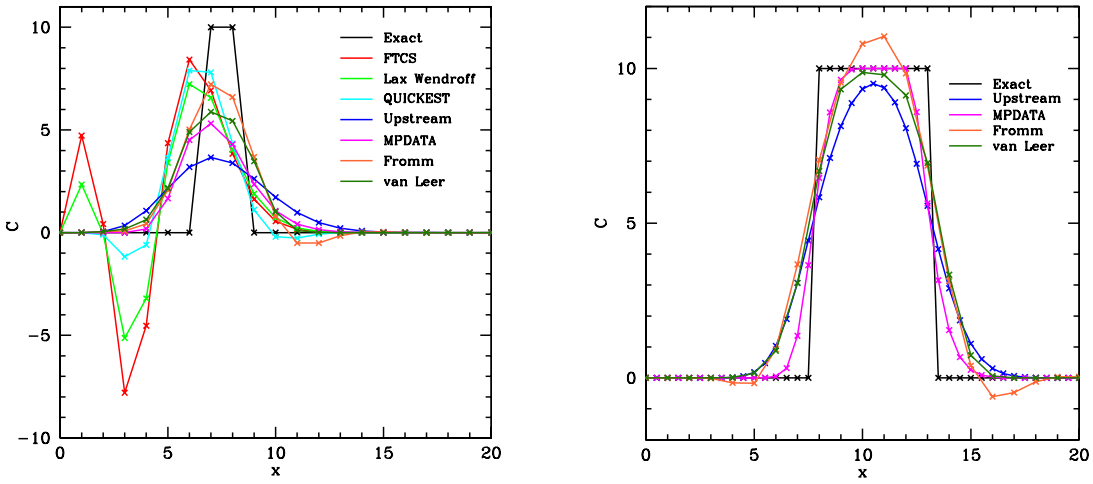

Figure 3.1: *Left panel:* Plots of solutions of a variety of Eulerian schemes. *Right panel:* Plots of solutions of the first-order upstream scheme, the second-order Fromm scheme, an advanced scheme with anti-diffusion steps (MPDATA) and with flux limiter (van Leer). In both panels, the exact solutions are plotted in black, and the solutions are plotted after 500 timesteps.

After the analysis in one dimension, we move to tracer advection in two dimensions. Two tracers A and B are advected parallelly in a diagonal constant wind with $(u, v) = (1, 1)$, where u and v are the x and y component of the wind field. A simple chemistry scheme ($A + B \rightarrow C$, by solving $dn_C/dt = n_A n_B$, where n_A, n_B and n_C are the concentration of Tracer A, B and C respectively) is employed to check for spurious production of the third tracer C, which is solely due to numerical diffusion of the schemes. The upstream, MPDATA and van Leer scheme are adopted. Figure 3.2 shows contour maps of the tracer concentrations after 500 steps and the production of Tracer C in simulations using different schemes. Both the upstream scheme and the MPDATA scheme produce some amount of Tracer C at the end of the simulation, which are solely artificial. However, in the van Leer scheme, the solution stops diffusing further after certain timesteps, and eventually results in no production of Tracer C at the end of the simulation. With its relatively limited numerical diffusion, the van Leer scheme is a suitable scheme for tracer advection in this context, and is therefore adopted in the later simulations of the section.

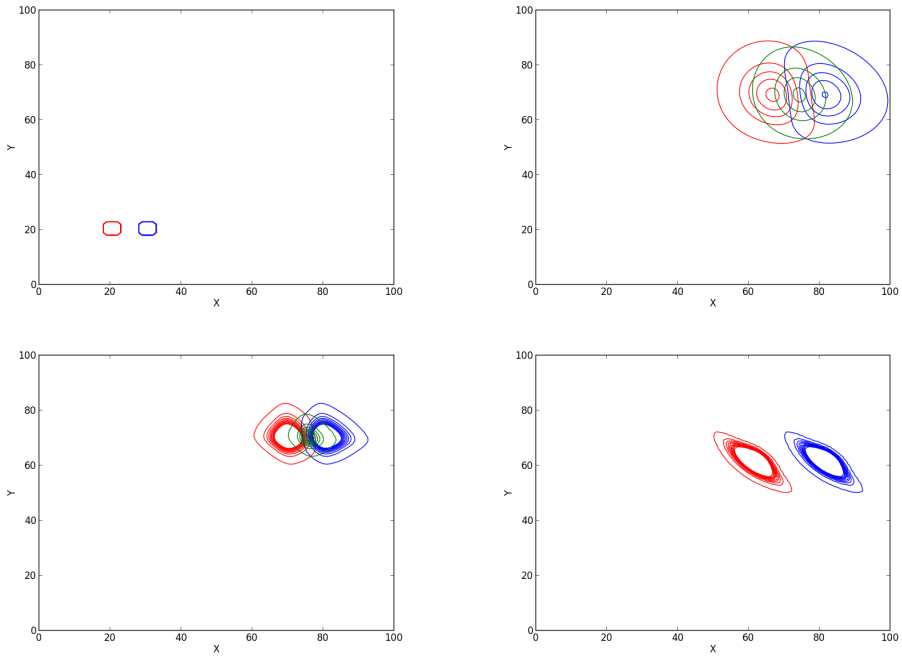

Figure 3.2: Concentration contour plots from the 2D tracer advection simulations with different numerical schemes. *Top left:* Initial condition of the simulation. A southwesterly constant wind field is applied. The red contours refer to Tracer A and the blue contours refer to Tracer B. One contour level is equivalent to 0.1. *Top right:* Solutions of the first-order upstream scheme after 500 timesteps. The green contours refer to Tracer C, which is produced by reaction between Tracer A and B. *Bottom left:* Solutions of MPDATA scheme after 500 timesteps. *Bottom right:* Solutions of the van Leer scheme after 500 timesteps. Note that no Tracer C is formed.

Tracer advection with turbulent mixing

Eddy diffusion Simulations with tracers advecting in a 3D turbulent wind field with simple chemistry are conducted to evaluate the interaction between turbulent motions and chemical reactions within a model grid cell. At first, a turbulent wind field is generated by adding a randomly generated streamfunction to that of a constant wind field. The turbulent intensity of the wind field, defined by $\sigma_u/\overline{u}$, where σ_u and $\overline{u}$ are the root-mean-square and the mean of the component of the field respectively, can be varied between the magnitude of the turbulent and constant component of the streamline. A tracer was advected in such a field with the van Leer scheme (refer to the left panel of Figure 3.3). This is then compared to a simulation with the tracer advecting in a constant wind field with an eddy diffusion term $K_D\nabla^2 x$, where K_D is the diffusion coefficient (refer to the right panel of Figure 3.3). This is a common technique used in large-scale models to account for turbulent mixing. One can see the simulation with eddy diffusion cannot represent the inhomogeneous distribution of the tracer advecting in a turbulent field.

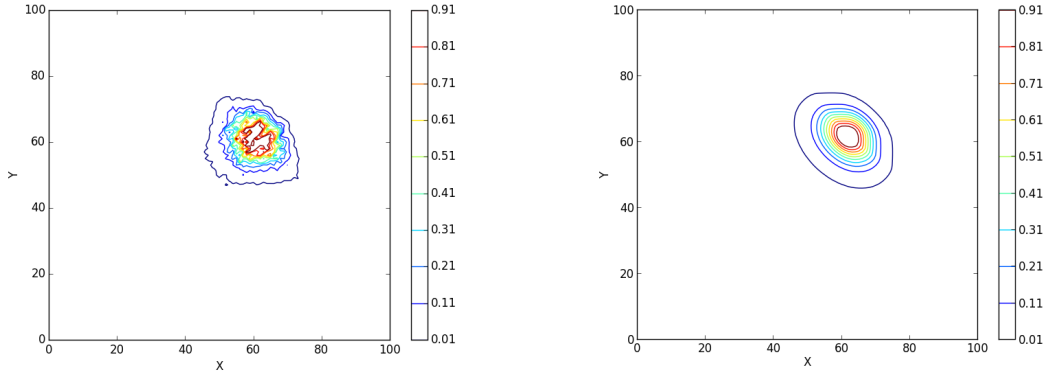

Figure 3.3: Concentration contour plots from 2D tracer advection simulations with turbulent mixing. *Left panel:* Tracer advection in a turbulent wind field. *Right panel:* Tracer advection in a constant wind field with artificial eddy diffusion.

Methodology

Simulations with tracer advecting in a 3D turbulent wind field with simple chemistry are conducted to evaluate the subgrid chemical-turbulence interaction, in which the simulation domain represents a single grid cell in a large-scale model. The results were then compared to a reference complete-mixing model, depicting a large-scale model which neglects the subgrid effect.

Simulation settings A 3D decaying isotropic turbulent field was generated by a code adopted from Orlandi (2012). Here the choices of initial conditions in the code are summarised. One should refer to Orlandi (2012) for the detailed description of the code.

To compute a decaying isotropic turbulent field, the Navier-Stokes equations for an incompressible flow

$$\nabla \cdot \mathbf{u} = 0$$
$$\frac{\partial \mathbf{u}}{\partial t} + (\mathbf{u} \cdot \nabla)\mathbf{u} = -\nabla p + \frac{1}{Re}\nabla^2 \mathbf{u},$$

where $\mathbf{u}$ are the velocity components, t is time, p is pressure and $Re = LU/\nu$ is the Reynolds number with the characteristic length L and velocity U over the viscosity ν, are solved with the initial energy spectrum (Mansour and Wray 1994)

$$E(\kappa, 0) = \frac{q^2}{2A} \frac{1}{\kappa_p^{\sigma+1} + \kappa^\sigma} \exp\left[-\frac{\sigma}{2}\left(\frac{\kappa}{\kappa_p}\right)^2\right],$$

where κ is the wavenumber, κ_p is the wavenumber at which $E(\kappa, 0)$ is maximum, $q^2/2$ is the turbulent kinetic energy, σ is a parameter, and $A = \int_0^\infty \kappa^\sigma \exp(-\sigma\kappa^2/2)d\kappa$. The

energy spectra is related to the amplitude the Fourier models of the velocity components

$$\hat{\mathbf{u}}(\kappa) = \alpha e_i^1 + \beta e_i^2,$$

where e_i^1, e_i^2 are mutually orthogonal unit vectors in the plane orthogonal to the wave mentor, and α and β are complex coefficients given by

$$\alpha = \left(\frac{E(\kappa,0)}{4\pi\kappa^2}\right)\exp(i\theta_1)\cos(\phi),$$

and

$$\beta = \left(\frac{E(\kappa,0)}{4\pi\kappa^2}\right)\exp(i\theta_2)\sin(\phi),$$

where θ_1, θ_2 and ϕ are uniformly distributed random number between 0 and 2π. A second-order Runge-Kutta scheme is used to advance in time.

Ten repetitive runs with different additional phase to the wavenumber k are performed for each set of variables in the simulation. Periodic boundaries are set in all dimensions. The simulation is run in a domain of $L_x \times L_y \times L_z$, and $L_x = L_y = L_z = 2\pi$ with number of nodes of $64 \times 64 \times 64$ for all 3D runs. The velocity fields $\mathbf{u} = (u, v, w)$ are then calculated from the streamfunction ψ with the relation

$$\mathbf{u} = \nabla \times \psi.$$

The advection of tracers are calculated by using the van Leer scheme.

Two reactant tracers, Tracer A and B, advect in the turbulent wind field, and react to form Tracer C ($A + B \rightarrow C$). Tracer chemistry are calculated after the advection by solving the following equations:

$$\begin{aligned}
\frac{\mathrm{D}\mathbf{A}}{\mathrm{D}t} &= -k_c\mathbf{A}\mathbf{B} + s_A \\
\frac{\mathrm{D}\mathbf{B}}{\mathrm{D}t} &= -k_c\mathbf{A}\mathbf{B} + s_B \\
\frac{\mathrm{D}\mathbf{C}}{\mathrm{D}t} &= k_c\mathbf{A}\mathbf{B},
\end{aligned}$$

where $\mathbf{A}, \mathbf{B}$ and $\mathbf{C}$ are the concentration fields of Tracer A, B and C respectively, k_c is the prescribed chemical reaction rate, and s_A and s_B are the source function of Tracer A and B, which will be explained in the later part of this section.

To conserve the scalar fields, an implicit-explicit averaged scheme is used to analytically calculate the tracer concentration fields as the following:

$$\begin{aligned}
\mathbf{A}^{t+1} &= \mathbf{A}^{adv} - \frac{1}{2}k_c \mathrm{d}t \left(\mathbf{A}^{t+1}\mathbf{B}^{adv} + \mathbf{A}^{adv}\mathbf{B}^{t+1}\right) \\
\mathbf{B}^{t+1} &= \mathbf{B}^{adv} - \frac{1}{2}k_c \mathrm{d}t \left(\mathbf{A}^{adv}\mathbf{B}^{t+1} + \mathbf{A}^{t+1}\mathbf{B}^{adv}\right) \\
\mathbf{C}^{t+1} &= \mathbf{C}^{adv} - k_c \mathrm{d}t \mathbf{A}^{t+1}\mathbf{B}^{t+1},
\end{aligned}$$

where the terms with superscript adv refer to quantities calculated at time t after the advection step and the terms with subscript $t+1$ refer to the quantities at timestep $t+1$.

Tracer A is emitted in a $\pi/8 \times \pi/8 \times \pi/8$ cube at the middle of the simulation domain at a constant rate of s_A, i.e.

$$s_A(x,y,z) = \begin{cases} 1 & \text{if } \frac{L_x}{2} \le x \le \frac{L_x}{2} + \frac{\pi}{8} \text{ and } \frac{L_y}{2} \le y \le \frac{L_y}{2} + \frac{\pi}{8} \text{ and } \frac{L_z}{2} \le z \le \frac{L_z}{2} + \frac{\pi}{8} \\ 0 & \text{elsewhere ,} \end{cases}$$

so that the total emission of Tracer A over the whole simulation domain is

$$S_A = \int_{domain} s_A \mathrm{d}x\mathrm{d}y\mathrm{d}z = 64.$$

Tracer B is emitted uniformly over the whole simulation so that

$$s_B = \frac{S_B}{L_x L_y L_z}$$

and

$$S_B = \int_{domain} s_B \mathrm{d}x\mathrm{d}y\mathrm{d}z = S_A.$$

As Tracer B is emitted at the background, this emission configuration is called "background source" (BS). The initial configuration is depicted in the schematic diagram shown on the left panel of Figure 3.9. The streamlines at $t = 0$ and $t = 5000$ in the simulation are illustrated on the right panels of Figure 3.4.

The simulations are conducted in sets of two variables, the Reynolds number Re and the chemical reaction rate coefficient k_c. The Reynolds number represents the turbulent intensity of the wind field. With the chemical reaction rate coefficient k_c, one can get the Damköhler number

$$Da = \frac{t_{turb}}{t_{chem}} \sim \frac{k_c}{Re},$$

where t_{turb} and t_{chem} are the timescales of turbulence and chemical reaction respectively. For reactions with $Da \ll 1$, the chemicals are well-mixed. For the reactions with $Da \geq 1$,

the chemicals are not mixed well by turbulence before they react, and the chemical-turbulence interaction becomes important.

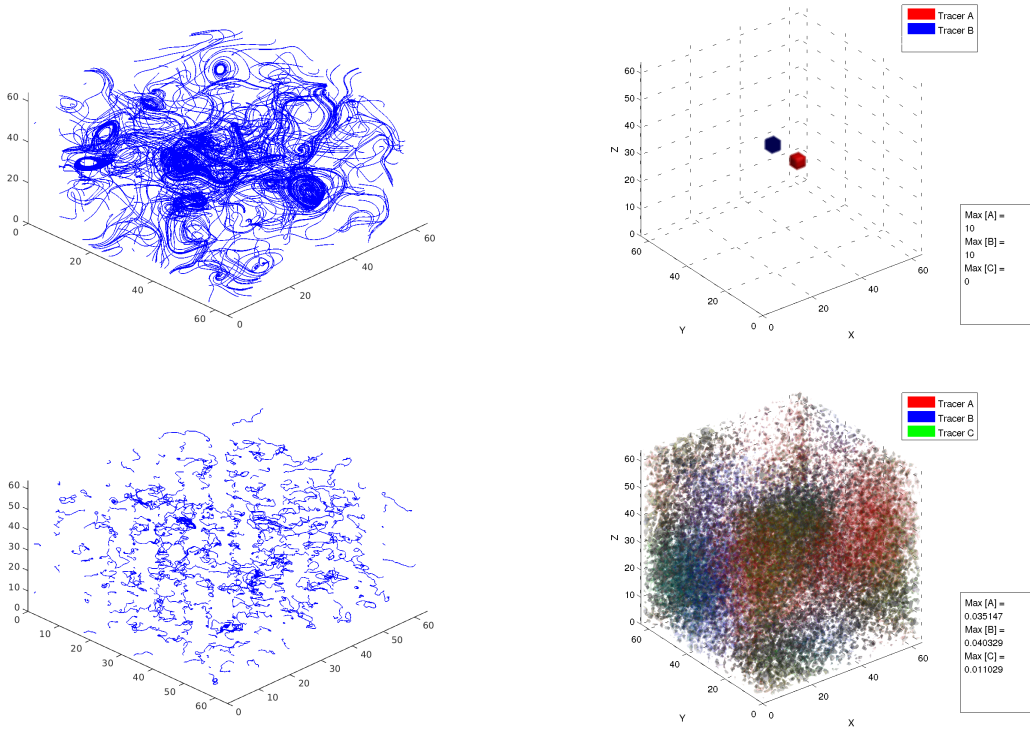

Figure 3.4: Tracer advection simulation with simple chemistry in a 3D turbulent field, with instant plumes (Case I) with $Re = 10^6$, $K_c = 1.0$ and $ds = 20$.
Top left: Streamline of the initial turbulent wind field *Bottom left:* Streamline plot after 5000 timesteps.
Top right: Initial condition of the simulation with the *LS* configuration. Tracer A and B are plotted in red and blue respectively. *Bottom right:* Isosurface plots of the tracer concentrations after 5000 timesteps. The green isosurface refer to Tracer C.

Analysis parameters The subgrid chemical-turbulence interaction is unresolved in a large-scale model, so that the tracers are assumed to be completely mixed in a grid. A complete-mixing model, which represents such calculation in a large-scale model, is used as a reference to account for the significance of the subgrid chemical-turbulence interaction. The results of the aforementioned simulations are compared with the values from the complete-mixing model. In the complete-mixing model, Tracer A and B are assumed to be well-mixed inside the grid box throughout the calculation, so that the

tracer concentration fields can be calculated analytically without the advection from

$$\frac{\mathrm{d}\mathbf{A}_{ref}}{\mathrm{d}t} = -k_c\mathbf{A}_{ref}\mathbf{B}_{ref} + s_{A,0}$$
$$\frac{\mathrm{d}\mathbf{B}_{ref}}{\mathrm{d}t} = -k_c\mathbf{A}_{ref}\mathbf{B}_{ref} + s_{B,0}$$
$$\frac{\mathrm{d}\mathbf{C}_{ref}}{\mathrm{d}t} = k_c\mathbf{A}_{ref}\mathbf{B}_{ref},$$

and the source terms of the reactant tracers are

$$s_{A,0} = \frac{S_A}{L_xL_yL_z}$$

and

$$s_{B,0} = \frac{S_B}{L_xL_yL_z}.$$

The corresponding reference amount of Tracer C produced is therefore

$$N_{C,ref} = \iint \mathbf{C}_{ref}\mathrm{d}x\mathrm{d}y\mathrm{d}z.$$

This quantity is then used to normalise the amount of Tracer C produced in the simulations

$$N_C = \iiint \mathbf{C}\mathrm{d}x\mathrm{d}y\mathrm{d}z.$$

So that the normalised amount of Tracer C produced $N_C/N_{C,ref}$ is the first parameter for the simulation analysis. In the complete-mixing model, $N_C/N_{C,ref} = 1$.

The second parameter for analysis is the segregation coefficient between the reactant tracers $I_{S,AB}$. The tracers are initially segregated in the simulations, according to the prescribed emission configurations. Turbulence mixes the tracers and changes the segregation between the tracers. Performing Reynolds averaging to the concentration field, the field can be decomposed into the mean term (with angle-brackets) and the perturbed term (primed term)

$$\mathrm{A} = \langle\mathbf{A}\rangle + \mathbf{A}'$$

and

$$\mathrm{B} = \langle\mathbf{B}\rangle + \mathbf{B}'.$$

The segregation coefficient between Tracer A and B is expressed here as

$$I_{S,AB} = \frac{\langle(\mathbf{A} - \langle\mathbf{A}\rangle)(\mathbf{B} - \langle\mathbf{B}\rangle)\rangle}{\langle\mathbf{A}\rangle\langle\mathbf{B}\rangle} = \frac{\langle\mathbf{A}'\mathbf{B}'\rangle}{\langle\mathbf{A}\rangle\langle\mathbf{B}\rangle}.$$

The effective chemical reaction rate k_{eff} can be related to the tracer segregation.

Taking the volume average of the production of Tracer C, one can get

$$\begin{aligned}\langle\frac{\mathrm{d}\mathbf{C}}{\mathrm{d}t}\rangle &= k_c\langle\mathbf{AB}\rangle \\ &= k_c(\langle\mathbf{A}\rangle\langle\mathbf{B}\rangle - \langle\mathbf{A}'\mathbf{B}'\rangle) \\ &= k_{eff}\langle\mathbf{A}\rangle\langle\mathbf{B}\rangle.\end{aligned}$$

Therefore, the effective chemical reaction rate can be calculated from

$$\begin{aligned}k_{eff} &= k_c\left(1+\frac{\langle\mathbf{A}'\mathbf{B}'\rangle}{\langle\mathbf{A}\rangle\langle\mathbf{B}\rangle}\right) \\ &= k_c\left(1+\langle I_{S,AB}\rangle\right).\end{aligned}$$

In the complete-mixing model, $k_{eff} = k_c$.

Results

Dependency on Reynolds number Re First, the dependency of the subgrid chemical-turbulence interaction on the Reynolds number is evaluated. Figure 3.5 shows the cases with different Reynolds number Re with the chemical reaction rate $k_c = 1.0$. As illustrated the left panel of Figure 3.5, the amount of Tracer C produced increases with the Reynolds number. This is due to the increased turbulent mixing with higher Reynolds number. The amount of Tracer C produced is initially higher than the reference value (dashed line) in all case because of the more concentrated source of Tracer B in the central region of the simulation domain than a completely-mixed situation at the early stage of the simulations. However, this effect is level off as the tracers accumulate. The amount of Tracer C produced approaches to some certain values dependent on the given Reynolds number, with the case with $Re = 10000$ corresponds closest to the complete-mixing model. However, the amount of Tracer C produced is still only $\sim 45\%$ of reference value. Note that when the Reynolds number is high enough (compare the case with $Re = 3000$ & $Re = 10000$), the Reynolds-number similarity is attained, at which the resultant statistical quantities no longer depend on the Reynolds number. We have checked the cases with $Re = 3000$ and $Re = 10000$ with simulations of doubled number of nodes to make sure the similarity is not due to resolution issue (See Section 3.1.2).

The intensity of segregation between Tracer A and B $I_{S,AB}$ is plotted in the right panel of Figure 3.5. Initially when the concentrations of both Tracer A and B are low, the reactants are mixed more easily. But as the tracers accumulate, the mixing of the tracers relies on turbulent mixing. In the cases of $Re = 100$ and $Re = 500$, the turbulent mixing is weak, so that $I_{S,AB}$ drops exponentially to -1, which a longer e-folding time for larger Reynolds numbers. For the cases of $Re = 3000$ and $Re = 10000$, the effect

of turbulent mixing is significant, and there exists a quasi-equilibrium value for $I_{S,AB}$ when the effect of turbulent mixing is comparable to the chemical reaction. This quasi-equilibrium state is reached at a later time and for a longer period of time when the Reynolds number is higher, as the corresponding turbulent mixing is more prominent. However this system leaves this quasi-equilibrium after a short while because of the dissipating turbulence and the accumulating tracers, and $I_{S,AB}$ converges to -1 at the end of the simulation.

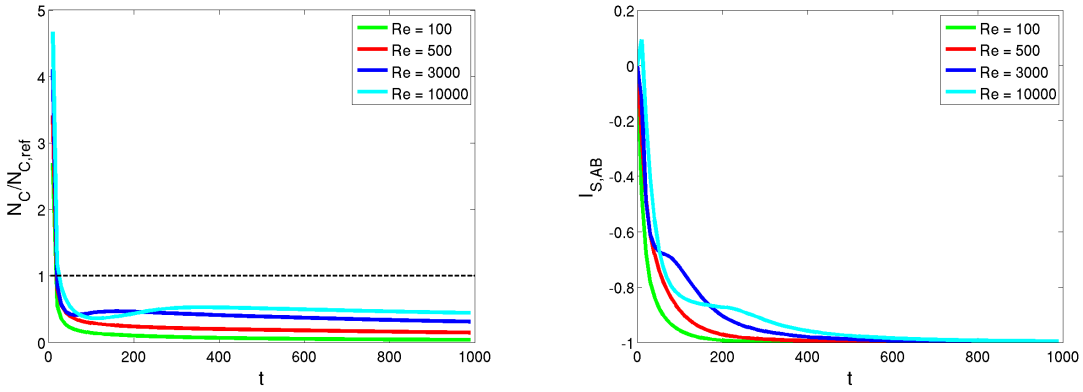

Figure 3.5: Tracer advection simulation with simple chemistry in a 3D turbulent field, with the configuration of BS with varied Reynolds number Re and $k_c = 1.0$.
Top panel: Normalised production of Tracer C $N_C/N_{C,ref}$. *Bottom panel:* Segregation between Tracer A and B $I_{S,AB}$.

Dependency on chemical reaction rate k_c Figure 3.6 shows the cases with different chemical reaction rate k_c with $Re = 3000$. With a smaller chemical reaction rate k_c, the amount of Tracer C produced in the simulations approaches to the reference value (refer to the left panel). This is because a smaller k_c with a given Reynolds number corresponds to a smaller Damköhler number, allowing more time for the tracers to be mixed before they react chemically. One can see that with sufficiently low k_c (referring to the case with $k_c = 10^{-4}$), the simulation results correspond closely to the reference value. This can also be illustrated with the segregation between Tracer A and B. The reactants are less segregated when the chemical reaction is slow, since the tracers are mixed more before they react.

There is a practical implication of this investigation to the real-life problem of chemistry in the atmosphere. The Reynolds number in the atmosphere is so high that it reaches the criteria of Reynolds number similarity. The rate of the chemical reaction concerned becomes the dominating factor of the problem. As the range of chemical rates for reactions in the atmospheric is vast, one may expect varied dependency on chemical-turbulence interaction for different reactions.

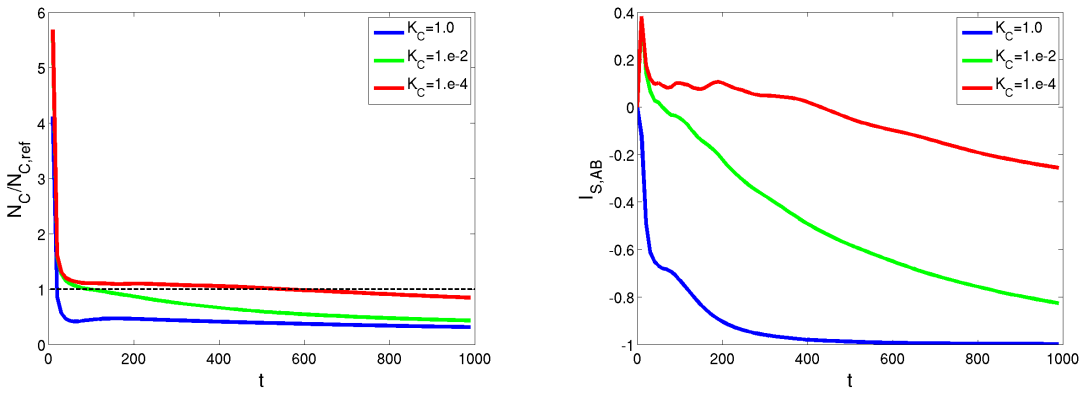

Figure 3.6: Tracer advection simulation with simple chemistry in a 3D turbulent field, with the configuration of BS with varied chemical reaction rate k_c and $Re = 3000$.
Top panel: Normalised production of Tracer C $N_C/N_{C,ref}$. *Middle panel:* Subgrid influence parameter Δ. *Bottom panel:* Segregation between Tracer A and B $I_{S,AB}$.

Dependency on source configuration To investigate the influence of source configuration on the problem, a second emission configuration is examined. Tracer A is emitted as the same configuration in the *BS* cases, while Tracer B is emitted in another $4 \times 4 \times 4$ cube, which is separated from the source of Tracer A by a distance of ds., i. e.

$$s_B = \begin{cases} 1 & \text{if } \frac{L_x}{2} + ds \leq x \leq \frac{L_x}{2} + ds + 3 \text{ and } \frac{L_y}{2} \leq y \leq \frac{L_y}{2} + 3 \text{ and } \frac{L_z}{2} \leq z \leq \frac{L_z}{2} + 3 \\ 0 & \text{elsewhere} \end{cases}.$$

Again, $S_A = S_B = 64$. This second configuration is called "localised source" (LS).

Figure 3.7 show the cases with source emission configuration BS, LS with $ds = 10$ and LS $ds = 30$, with $Re = 3000$ and $k_c = 1.0$. One can see that the BS case produces the largest amount of Tracer C, followed by the LS $ds = 10$ case, when the tracer sources are closely located to each other. However, the effect of source inhomogeneity is not significant in this setting of the simulations, especially when the tracers are accumulated. We shall investigate again the effect of inhomogeneous emission sources in the later chapters of this thesis.

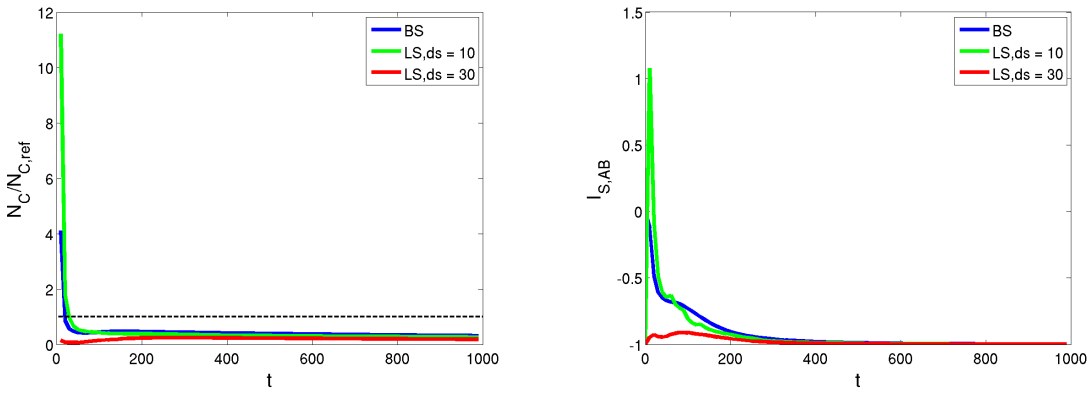

Figure 3.7: Tracer advection simulation with simple chemistry in a 3D turbulent field, with the configuration of BS and LS with tracer separation $ds = 10$ or 30, with $Re = 3000$ and $k_c = 1.0$.
Top panel: Normalised production of Tracer C $N_C/N_{C,ref}$. *Bottom panel:* Segregation between Tracer A and B $I_{S,AB}$.

2D vs 3D Mixing

To save computational costs, models are sometimes run in two dimensions instead of three dimensions. 2D simulations also allow the model to be run in a higher resolution. In this session, the simulations conducted in 2D fields will be conducted with the ones in 3D fields. Figure 3.8 shows the streamlines and the tracer concentrations of one of the performed 2D simulations. Here two sets of 2D simulations with different resolution were performed, one with higher resolutions with grids of 256×256 (2DHR), another with the same resolution of the 3D simulations (64×64, here referred as 2DLR). The configuration of the 2D simulations is set as a 2D projection of the 3D simulations, and the source configuration is adopted as in the BS configuration. The emission is set so that the total emission of Tracer A and B are equal to that in the 3D simulation, so that Tracer A is emitted in a $\pi/8 \times \pi/8$ box in the middle of the simulation domain:

$$s_A(x,y) = \begin{cases} 4 & \text{if } \frac{L_x}{2} \le x \le \frac{L_x}{2} + \frac{\pi}{8} \text{ and } \frac{L_y}{2} \le y \le \frac{L_y}{2} + \frac{\pi}{8} \\ 0 & \text{elsewhere} \end{cases}$$

$$s_B = \frac{S_B}{L_x L_y L_z},$$

so that $S_A = S_B = 64$.

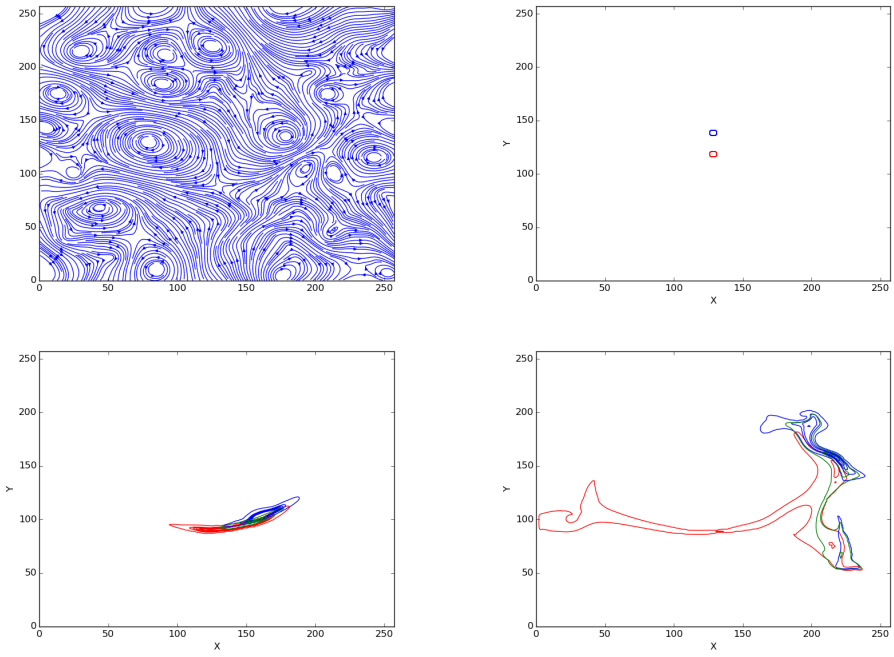

Figure 3.8: Tracer advection simulation with simple chemistry in a turbulent field *Top left:* Streamline of the turbulent wind field adopted. *Top right:* Initial condition of the simulation. Tracer A and B are plotted in red and blue respectively. *Bottom left:* Snapshot of simulation after 2000 timesteps. The green contours refer to Tracer C. *Bottom right:* Snapshot of simulation after 5000 timesteps.
We assume here that the domain represents a grid cell of a coarse model, and we show the sub-grid behaviour of reactive species in a turbulent flow.

Figure 3.10 shows the simulations with $Re = 3000$ and $k_c = 1.0$ for the 2DLR, 2DHR and 3D runs. One can see from the left panel, that the 2D simulations always produce a larger amount of Tracer C than in the 3D runs. This is due to the fact that in the 2D simulations, the emission region is projected as a cuboid instead of a cube as in the 3D simulations (refer to Figure 3.9). It allows a larger surface area for mixing between Tracer A and Tracer B in the 2D simulations. The 2DLR and the 2DHR cases produce almost the same amount of Tracer C, indicating that the resolution in the 2DLR runs is high enough to resolve the turbulent dissipation for $Re = 3000$. However, in all cases the amount of Tracer C produced is still less than the reference value in the complete-mixing model.

The right panel shows the segregation of the reactant tracers. The tracers are mostly segregated in the 2DHR runs. This is because the high resolution in the model can provide more information about the distribution of the tracer concentrations, hence segregation between the tracers is more well-resolved. This is followed by the 3D runs. As there is one additional free dimension in the 3D runs, the 3D simulations are better resolved than the 2DLR runs despite of the same number of nodes in one dimension.

Another point to note is that the architecture of a 2D and 3D turbulent field is

different. By studying the velocity fields of the 2D and 3D simulations (refer to the left panels of Figure 3.8 and 3.4), one can notice that vortex stretching is only present in the 3D field but not the 2D field. When we look at the vorticity transport equation for incompressible fluid

$$\frac{\mathrm{D}\vec{\omega}}{\mathrm{D}t} = (\vec{\omega}\cdot\nabla)\vec{u} + \nu\nabla^2\vec{\omega},$$

the vortex stretching term, which is the first term on the right hand side of the above equation, is zero in two-dimensional flow. Therefore, in two-dimensional flow, the vortices combine to form larger vortices as time evolves, while the vortices cascade to smaller vortices in the three-dimensional flow, corresponding to the turbulence properties in real-life observations.

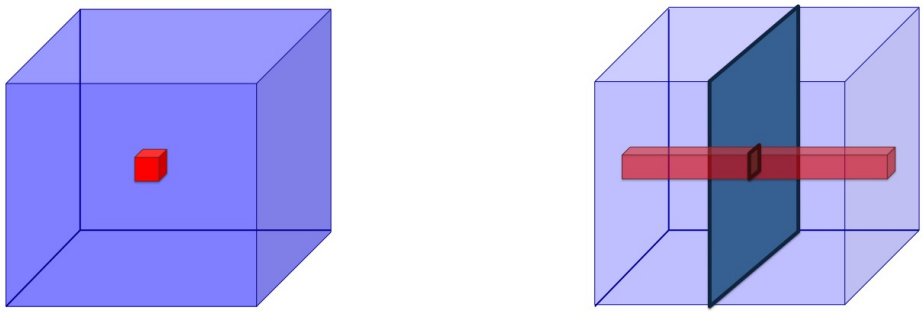

Figure 3.9: 3D projection of the 2D simulation. *Left panel:* Initial setting of Tracer A (in red) and B (in blue) in the 3D simulations. *Right panel:* 3D projection of the corresponding 2D simulations. The cross section refers to the simulation domain. The square with the source of Tracer A is projected as a cuboid instead of the cube in the 3D simulation. This produces additional mixing.

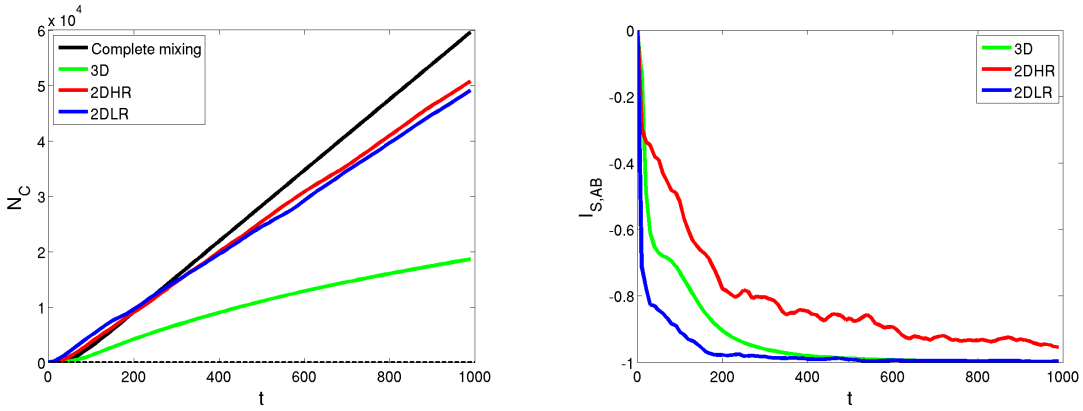

Figure 3.10: Tracer advection simulation with in a 2DLR, 2DHR and 3D turbulent field, with the configuration of BS, $Re = 3000$ and $k_c = 1.0$.

Resolution issues

The resolution affects the simulations in different extent with different Reynolds number and chemical reaction rates. Here we illustrate the importance of resolution when the Reynolds number is higher and when the chemical reaction rate is low.

High Reynolds number Now we would look at the importance of resolution in the simulations with high Reynolds numbers. Figure 3.11 shows the results of the runs of 2DLR, 2DHR and 3D runs with $Re = 10000$ and $k_c = 1.0$. Unlike the case with $Re = 3000$ (Figure 3.10), one can see that the amount of Tracer C produced in the 2DHR runs is significantly more than the 2DLR runs. This is because the resolution in the 2DLR case is not high enough to resolve the Kolmogorov length scale at $Re = 10000$. The Kolmogorov length scale η is related to the Reynolds number Re and the characteristic length scale L, corresponding to the size of the domain, by

$$\frac{L}{\eta} \sim Re^{3/4}.$$

Therefore the number of nodes required to resolve the Komogorov length scale $N \sim L/\eta$.

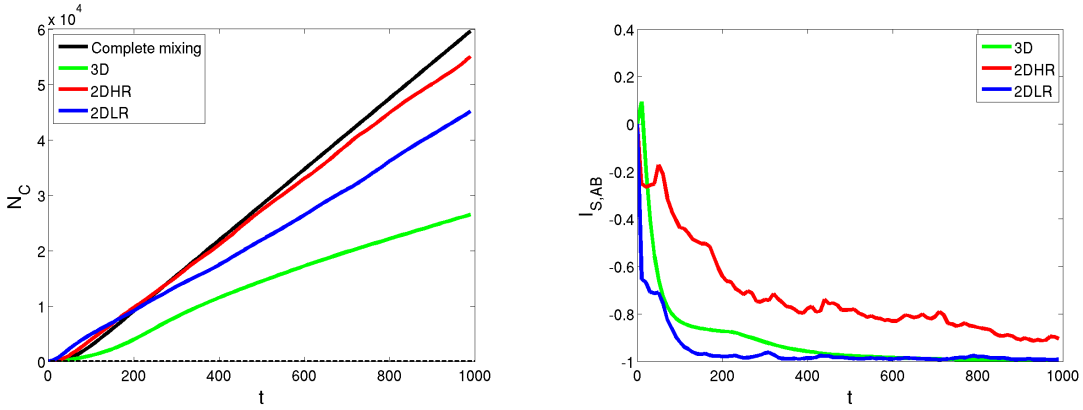

Figure 3.11: Tracer advection simulation with in a 2DLR, 2DHR and 3D turbulent field, with the configuration of BS, $Re = 10000$ and $k_c = 1.0$.

Unresolving the Kolmogorov length scale can possibly lead to an underestimation of turbulent mixing, as illustrated in Figure 3.12. The left panel shows a high-resolution model, that can resolve the Kolmogorov length scale at a given Reynolds number Re, and the right panel shows another model with a lower resolution that cannot resolve the Kolmogorov length scale. The red squares indicate the location of the tracer source. In the high-resolution model (left panel), the tracer dissipates due to turbulent mixing, and spreads to the areas of pink and orange boxes. However, in the low-resolution model (right panel), the tracer can only dissipate to the pink squares as the resolution of the

model cannot resolve the size of the orange boxes on the left panel (i.e. the smallest-scale eddies in the turbulent field). Therefore, the orange boxes indicate the neglected dissipation of the tracer due to insufficient turbulent mixing.

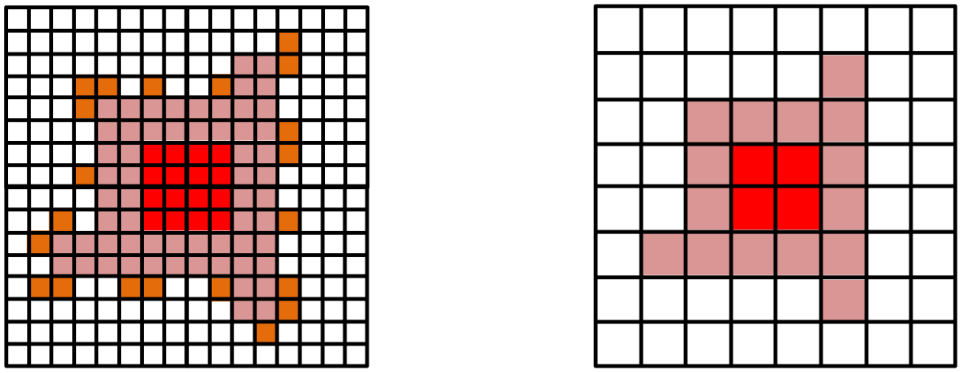

Figure 3.12: Underestimated turbulent mixing in a model with insufficient resolution.

Low chemical reaction rate Next the importance of simulation resolution is investigated in slow-chemistry cases. Figure 3.13 shows the results of runs of 2DHR, 2DLR and 3D runs with $Re = 3000$ and $k_c = 10^{-4}$. As aforementioned, the resolution in both the 2DLR and 2DHR runs is high enough to resolve the turbulent mixing in the flow at $Re = 3000$ (the dynamical aspect). However, when the chemistry is slow ($k_c = 10^{-4}$), much more amount of Tracer C is produced in the 2DLR runs than in the 2DHR runs (refer to the left panel in Figure 3.13). This is due to the fact that the low resolution produces more artificial mixing in an unresolved grid. Note that in this case both 2D runs produce more amount of Tracer C than in the complete-mixing model (black line).

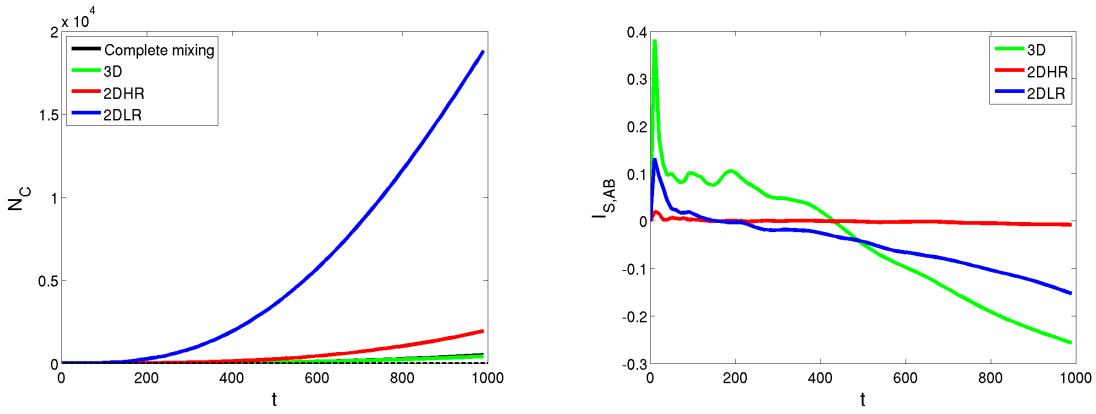

Figure 3.13: Tracer advection simulation with in a 2DLR, 2DHR and 3D turbulent field, with the configuration of BS, $Re = 3000$ and $k_c = 10^{-4}$.

The effect of over-mixing can be illustrated by Figure 3.14. Figure 3.14 shows (1) a complete-mixing model, (2) a higher-resolution model and (3) a lower-resolution model.

In a situation with a low Damköhler number (i.e. with a low chemical reaction rate at a given Reynolds number Re, slow chemistry), one can assume that the reactant tracers, Tracer A and B, with a total amount of N_A and N_B over the whole simulation domain, are well mixed. In the complete-mixing model, the total amount of Tracer C produced is

$$\begin{aligned} N_{C,ref} &= \iint \mathbf{C}\mathrm{d}x\mathrm{d}y \\ &= \iint k_c \mathbf{A}\mathbf{B}\mathrm{d}x\mathrm{d}y \\ &= \iint k_c \frac{N_A}{L_X L_Y}\frac{N_B}{L_X L_Y}\mathrm{d}x\mathrm{d}y \\ &= k_c \frac{N_A}{L_X L_Y}\frac{N_B}{L_X L_Y}\cdot L_X \cdot L_Y \\ &= k_c \frac{N_A N_B}{L_X L_Y}. \end{aligned}$$

L_X and L_Y are the size of the simulation domain in the x- and y- direction respectively.

In the first model, the simulation domain is then simulated in a model with a resolution of $\delta x_1 \times \delta y_1$ (size of the grid, $\delta x_1 > 1$, $\delta y_1 > 1$), or with nodes of $q_{X,1} \times q_{Y,1}$, and $q_{X,1} = L_X/\delta x_1$ and $q_{Y,1} = L_Y/\delta y_1$. Therefore, in each of the grid, the amount of Tracer A and B are $n_{A,1} = N_A/q_{X,1}q_{Y,1}$ and $n_{B,1} = N_B/q_{X,1}q_{Y,1}$ respectively. The amount of Tracer C produced is

$$\begin{aligned} n_{C,1} &= k_c n_{A,1} n_{B,1} \\ &= k_c \frac{N_A}{q_{X,1}q_{Y,1}}\frac{N_B}{q_{X,1}q_{Y,1}}. \end{aligned}$$

And the total amount of Tracer C produced would be

$$\begin{aligned} N_{C,1} &= n_{C,1} \cdot q_{X,1} \cdot q_{Y,1} \\ &= k_c \frac{N_A N_B}{q_{X,1}q_{Y,1}} \\ &= k_c \frac{N_A N_B}{L_X L_Y} \cdot \delta x_1 \cdot \delta y_1 \\ &= N_{C,ref} \cdot \delta x_1 \cdot \delta y_1. \end{aligned}$$

In the second model with lower resolution with nodes of $q_{X,2} \times q_{Y,2}$ (size of the grid),

or with grid size of $\delta x_2 \times \delta y_2$, the amount of Tracer C produced is then

$$\begin{aligned} N_{C,2} &= \frac{N_A}{q_{X,2}q_{Y,2}} \frac{N_B}{q_{X,2}q_{Y,2}} \cdot q_{X,2} \cdot q_{Y,2} \\ &= k_c \frac{N_A N_B}{L_X L_Y} \cdot \delta x_2 \cdot \delta y_2 \\ &= N_{C,ref} \cdot \delta x_2 \cdot \delta y_2. \end{aligned}$$

Since $\delta x_2 > \delta x_1$ and $\delta y_2 > \delta y_1$, $N_{C,2} > N_{C,1} > N_{C,ref}$. However, this excess in production of Tracer C is purely due to the artificial mixing from the model.

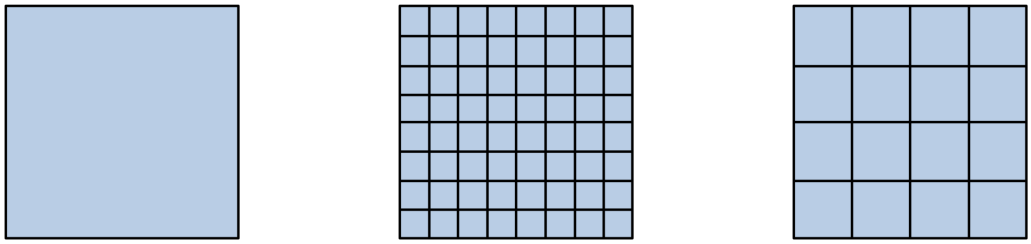

Figure 3.14: Artificial mixing due to insufficient resolution.

3.2 DNS model in a convective boundary layer

After exploring in a fundamental representation how subgrid chemical-turbulence interaction can affect the calculation of chemical reactions, the investigation is moved to a more realistic scenario - in a convective boundary layer.

3.2.1 Dynamical settings

The relations between turbulence and chemistry in a convective boundary layer is investigated in this chapter by means of direct numerical simulations (DNS). Contrary to previous studies that always addressed this issue based on data from large-eddy simulations (LES), DNS is adopted here to remove the uncertainties introduced by subgrid-scale turbulence model and numerical artifacts possibly induced by different LES models (Mellado et al. 2018). In LES, the Navier-Stokes equations are solved with filtered parameters and closed with subgrid-scale parametrisation which represent the effects in the unresolved scales. Therefore, results from LES depend on the adopted subgrid-scale parametrisations, numerical schemes and grid/filter properties of the corresponding LES models. Uncertainties associated with subgrid turbulence models in LES have been reported in its applications near the surface (e. g. Zilitinkevich et al. (1998)), and in the entrainment zone (e. g. Sullivan and Patton (2011)). On the other hand, in DNS, the

Navier-Stokes equations are solved explicitly with all exact atmospheric parameters except for the Reynolds number (Re). Conducting DNS with Re in typical atmospheric condition ($\sim 10^7 - 10^8$) is computationally impossible. However, with Reynolds number similarity, one can perform DNS with moderate values, which still allows certain extrapolation of the DNS results to corresponding atmospheric conditions (Dimotakis 2000; Monin). Reynolds number similarity is an experimental observation of which properties of turbulent flows become practically independent of Re once Re reaches a critical value ($\sim 10^4$) (Tennekes et al. 1972; Monin). The clarity and universality of the governing equations of DNS (the Navier-Stokes equations) make the DNS results easier to be interpreted and their numerical uncertainties more clearly quantified through grid convergence studies (Mellado et al. 2018). Therefore, DNS provides an alternative for studying the topic as a test for the subgrid models in LES and as an intercomparison study of the LES results (Moin and Mahesh 1998; Mellado et al. 2018).

The dynamical part of the simulations performed in this chapter follows similar settings in Garcia and Mellado (2014) and Van Heerwaarden et al. (2014). In the model, the Navier-Stokes equations of incompressible fluids in the Boussinesq approximation[1] are solved to calculate the buoyancy and the velocity fields:

$$\nabla \cdot \mathbf{u} = 0, \tag{3.1}$$

$$\frac{\partial \mathbf{u}}{\partial t} + \nabla \cdot (\mathbf{u} \otimes \mathbf{u}) = -\nabla p + \nu \nabla^2 \mathbf{u} + b\mathbf{k}, \tag{3.2}$$

$$\frac{\partial b}{\partial t} + \nabla \cdot (\mathbf{u} b) = \kappa \nabla^2 b, \tag{3.3}$$

where $\mathbf{u}(\mathbf{x}, t)$ is the velocity vector with components (u, v, w) along the directions $\mathbf{x} = (x, y, z)$ at time t, respectively, p is the modified pressure divided by the constant reference density, and $b(\mathbf{x}, t)$ is the buoyancy expressed in Equation 1.1. The background buoyancy profile is set as $b_0(z) = N^2 z$, where N^2 is the Brunt-Väisälä frequency. The parameters ν and κ are the kinematic viscosity and the molecular diffusivity respectively. $\mathbf{k}$ is the unit vector along the dimension z. The system is statistically homogeneous in the horizontal direction, such that its statistics depend only on z and t.

A no-penetration, no-slip boundary condition is imposed at the surface and a no-penetration, free-slip boundary condition is imposed on the top boundary. Neumann boundary conditions are imposed for the buoyancy and velocity fields at both the top and the surface to maintain fixed constant fluxes. Inside the sponge layer, which occupies the upper region of the computational domain, the velocity and buoyancy fields are relaxed towards zero and $N^2 z$ respectively. The height of the top boundary is adjusted so that the turbulent region is far enough from the top to avoid significant interaction. Periodic boundary condition is implemented in lateral directions.

[1]The density of the fluid is assumed to be constant except in the buoyancy term.

The results of the chapter are based on the data in the fully developed turbulent regime in the simulation that is established after the initial transient phrase. In that regime, the initial conditions have been sufficiently forgotten, and the parameters $\{\nu, \kappa, B_0, N\}$ define the system completely (where B_0 is the surface buoyancy flux). N and B_0 are chosen to non-dimensionalise the equations (Fedorovich et al. 2004; Garcia and Mellado 2014), such that the system yields a reference time scale T_0 as N^{-1}, a reference length scale L_0 as $(B_0/N^3)^{\frac{1}{2}}$ and a reference velocity scale U_0 as $(L_0 B_0)^{\frac{1}{3}}$. With the Prandtl number ($Pr = \nu/\kappa$) set to 1, the system only depends on the reference buoyancy Reynolds number

$$Re_0 = \frac{B_0}{\nu N^2},$$

which is set to be 15000 in all simulations. Re_0 refers to the Reynolds number in the entrainment zone (Garcia and Mellado 2014), and with an equivalent Reynolds number of $\sim$ 1000 in the mixed layer. With these values, the Reynolds number in the whole boundary layer lie within the range where the Reynolds number similarity applies.

The size of the computational grid is $720 \times 720 \times 512$ for all the simulations (the number of vertical layer is 512). Stretching is applied vertically to increase the resolution near the surface in order to resolve the surface layer, and to stretch the grid size in the upper portion of the domain end to further separate the top boundary from the turbulent region. The total simulation domain size is $120L_0 \times 120L_0 \times 34.4L_0$. With the typical atmospheric parameter that $L_0 \sim 100$ m and $U_0 \sim 1$ m s^{-1}, the horizontal resolution of the model in use is equivalent to 15 m $\times$ 15 m with a total domain size of 12 km $\times$ 12 km. Along the vertical dimension, the vertical grids are stretched from a grid spacing of $\Delta z = 6.72$ m at the surface to $\Delta z = 266.28$ m at the top of the domain at 16 km. The simulations are terminated after a total simulation time equivalent to 4.5 hours in default, representing the hours from sunrise to midday, during which the boundary layer grows convectively and the convective boundary layer is well developed.

The boundary layer height z_i is calculated by searching for the height where the buoyancy variance $[b'b']$ [2] is maximum away from the surface layer (refer to the definition in Section 1.1). For example, the top-left panel of Figure 3.15 shows the vertical profile of $[b'b']$ at the end of the simulation, indicating that $z_i = 2300$ m at the end of the simulation. The top-right panel of Figure 3.15 shows the evolution of the boundary layer height throughout the simulation. As the boundary layer grows in depth, the corresponding convective velocity and turbulent timescale[3] evolve in time. With the definitions in Equation 1.3 and 1.2, their evolutions are shown on the bottom-left and bottom-right panels of Figure 3.15 respectively. The turbulent timescale t_{turb} will be used to calculate the Damköhler number Da in later sections.

[2]The quantity with squared brackets [] refer to the horizontal mean of the corresponding quantity hereafter.

[3]The turbulent timescale refers to the convective timescale as discussed in Section 1.1.

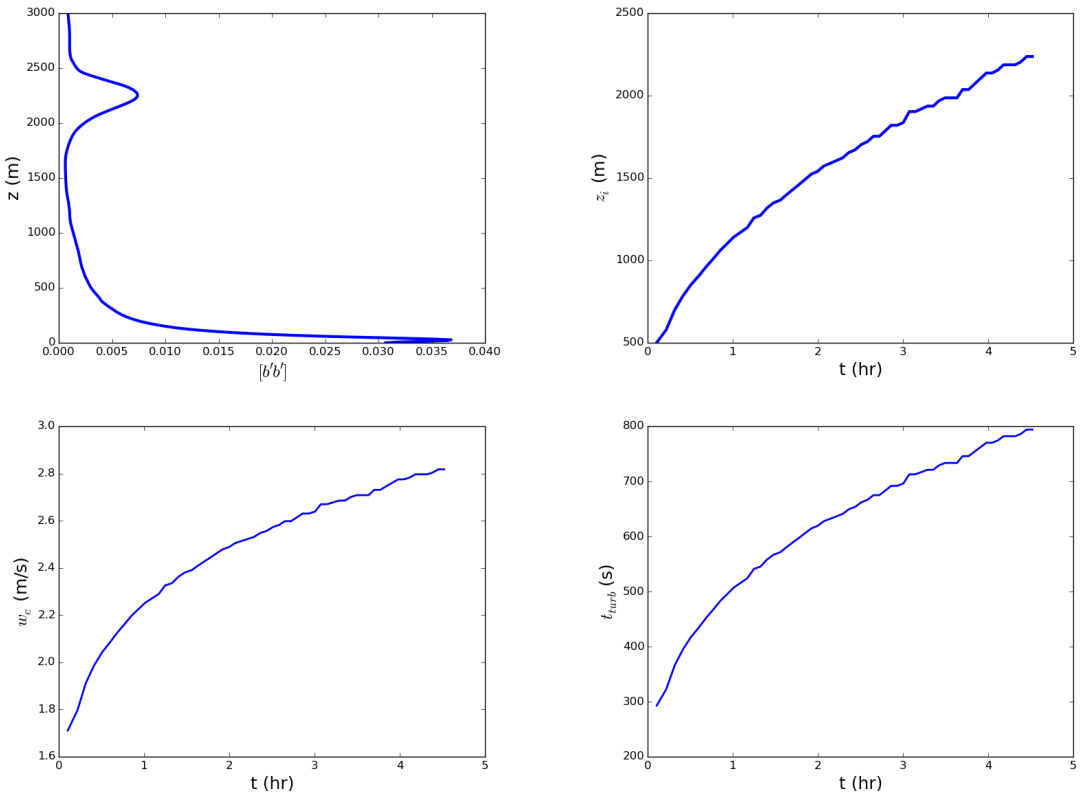

Figure 3.15: *top-left panel*: Vertical profile of the variance of the horizontally averaged buoyancy at the end of the simulation. Since the boundary layer height z_i is defined as the height with the maximum variance away from the surface layer, the boundary layer height is 2,250 m in this case; *top-right panel*: Evolution of the boundary layer height z_i with time; *bottom-left panel*: Evolution of the convective velocity w_c with time; *bottom-right panel*: Evolution of the convective timescale, i. e. the turbulent timescale t_{turb} with time.

3.2.2 Chemical settings

In the first part of our study, a top-bottom entrainment-emission configuration is adopted in our DNS simulation as in Vinuesa and de Arellano (2005). Figure 3.16 shows the set-up configuration of the simulation. The bottom-top tracer, from here is called Tracer A, is emitted from the surface at a constant flux F_A at 0.05 ppb m s^{-1}. The top-bottom tracer, Tracer B hereafter, is entrained from the free troposphere, in where the mixing ratio of Tracer B ($\langle B \rangle_0$) is fixed at 2 ppb. Tracer A and B react in a second-order chemistry scheme to form Tracer C:

$$k\text{: A} + \text{B} \longrightarrow \text{C} \ .$$

And k is the imposed chemical reaction rate. Therefore, the mixing ratios of the three species A, B and C vary with time with their rates equal to [4]

$$\frac{d\langle C\rangle}{dt} = -\frac{d\langle A\rangle}{dt} = -\frac{d\langle B\rangle}{dt} = k\langle A\rangle\langle B\rangle$$

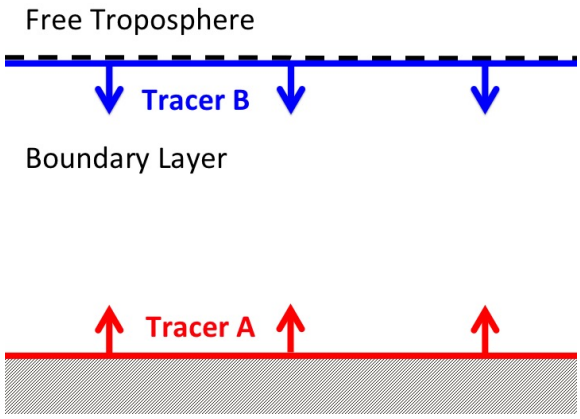

Figure 3.16: Schematic diagram of the configuration of the DNS simulations.

Neumann boundary conditions are imposed at the boundaries on the mixing ratios of the tracers so that the surface flux of Tracer A is constant at F_A, and the surface fluxes of B and C are zero. In the free troposphere, the mixing ratios of A and C are zero, and the mixing ratio of B is fixed constantly and homogeneously at $\langle B\rangle_0$. The mixing ratio of Tracer B is relaxed down the boundary layer to zero on the surface. Initial and boundary conditions of the simulation are listed in Table 3.1.

Variables	Initial conditions
F_A	0.05 ppb m s^{-1} at the surface
$\langle B\rangle_0$	2 ppb in Free Troposphere
$L_X \times L_Y \times L_Z$	12 km $\times$ 16 km $\times$ 12 km
$N_X \times N_Y \times N_Z$	720 $\times$ 512 $\times$ 720

Table 3.1: Initial and boundary conditions for the DNS simulation with the second-order chemistry scheme ($A + B \rightarrow C$). F_A is the constant flux of Tracer A at the surface, and $\langle B\rangle_0$ is the fixed mixing ratio of Tracer B in the free troposphere. $L_X \times L_Y \times L_Z$ refers to the size of the simulation domain, and $N_X \times N_Y \times N_Z$ refers to the number of nodes used in the simulations.

The rate equations of the species are non-dimensionalised by introducing the characteristic scales for the mixing ratios. The characteristic scale for Tracer A is derived from F_A, with $\langle A\rangle_0 = F_A U_0^{-1}$. For Tracer B, the characteristic scale is $\langle B\rangle_0$. For Tracer C, it is

[4]The quantity with angled brackets $\langle\rangle$ refers to the volumetric mean of the corresponding quantity hereafter.

defined as $\langle C\rangle_0 = L_0 U_0^{-1} k \langle A\rangle_0 \langle B\rangle_0$. The mixing ratio of the tracers are then normalised with these scales so that the normalised mixing ratios are defined as $c_A = \langle A\rangle/\langle A\rangle_0$, $c_B = \langle B\rangle/\langle B\rangle_0$ and $c_C = \langle C\rangle/\langle C\rangle_0$. With these, the rates of the three tracers are expressed as the following equations:

$$L_0 U_0^{-1} \frac{dc_A}{dt} = -K_A c_A c_B$$
$$L_0 U_0^{-1} \frac{dc_B}{dt} = -K_B c_A c_B$$
$$L_0 U_0^{-1} \frac{dc_C}{dt} = -c_A c_B,$$

where the dimensionless rate constants $K_A = L_0 U_0^{-1} k \langle B\rangle_0$ and $K_B = L_0 U_0^{-1} k \langle A\rangle_0$.

Five chemistry cases with four different imposed chemical reaction rate k, namely very slow, slow, fast and very fast chemistry, are considered, and a set of simulation with two inert tracers, i. e. with no chemistry, is conducted as a reference. The chemical reaction rates for the cases with very slow, slow, fast and very fast chemistry are 4.75×10^{-5}, 4.75×10^{-4}, 4.75×10^{-3} and 4.75×10^{-2} ppb^{-1} s^{-1} respectively. As a reference, the rate of chemical reaction between nitrogen monoxide and ozone is 4.75×10^{-4} ppb^{-1} s^{-1}, corresponding to the case with slow chemistry. The imposed chemical reaction rate k and initial Damköhler numbers Da_0 of the five cases are list in Table 3.2. The cases here with slow and fast chemistry are in the same settings as the two cases presented in Vinuesa and de Arellano (2005). Using our DNS model, we can test the sensitivity of their LES studies.

Cases	Chemical reaction rate (k)	Initial Damköhler number (Da_0)
No chemistry	0	-
Very slow	4.75×10^{-5}	0.01
Slow	4.75×10^{-4}	0.1
Fast	4.75×10^{-3}	1
Very fast	4.75×10^{-2}	10

Table 3.2: Corresponding imposed chemical reaction rate k in ppb^{-1} s^{-1} and the initial Damköhler numbers Da_0 of the five chemistry cases.

3.3 Results

3.3.1 General statistics

Time series

To analyse the results from the DNS simulation, we first look at the time series of the volumetrically averaged means and standard deviations of the mixing ratios of Tracer

A, B and C.

In most cases except with no chemistry and very slow chemistry, the mixing ratios of Tracer A and B drop over the simulation (refer to left panels in Figure 3.17), with increasing depletion with faster chemical reaction rate. Tracer A is almost depleted in the very fast-chemistry case. Due to the depletion of Tracer A, the amount of Tracer C produced and Tracer B depleted is similar in the fast- and very fast-chemistry case, despite an increase of chemical reaction rate by a factor of 10 for the latter case. The chemical reaction between Tracer A and B is Tracer A-limiting in these two cases.

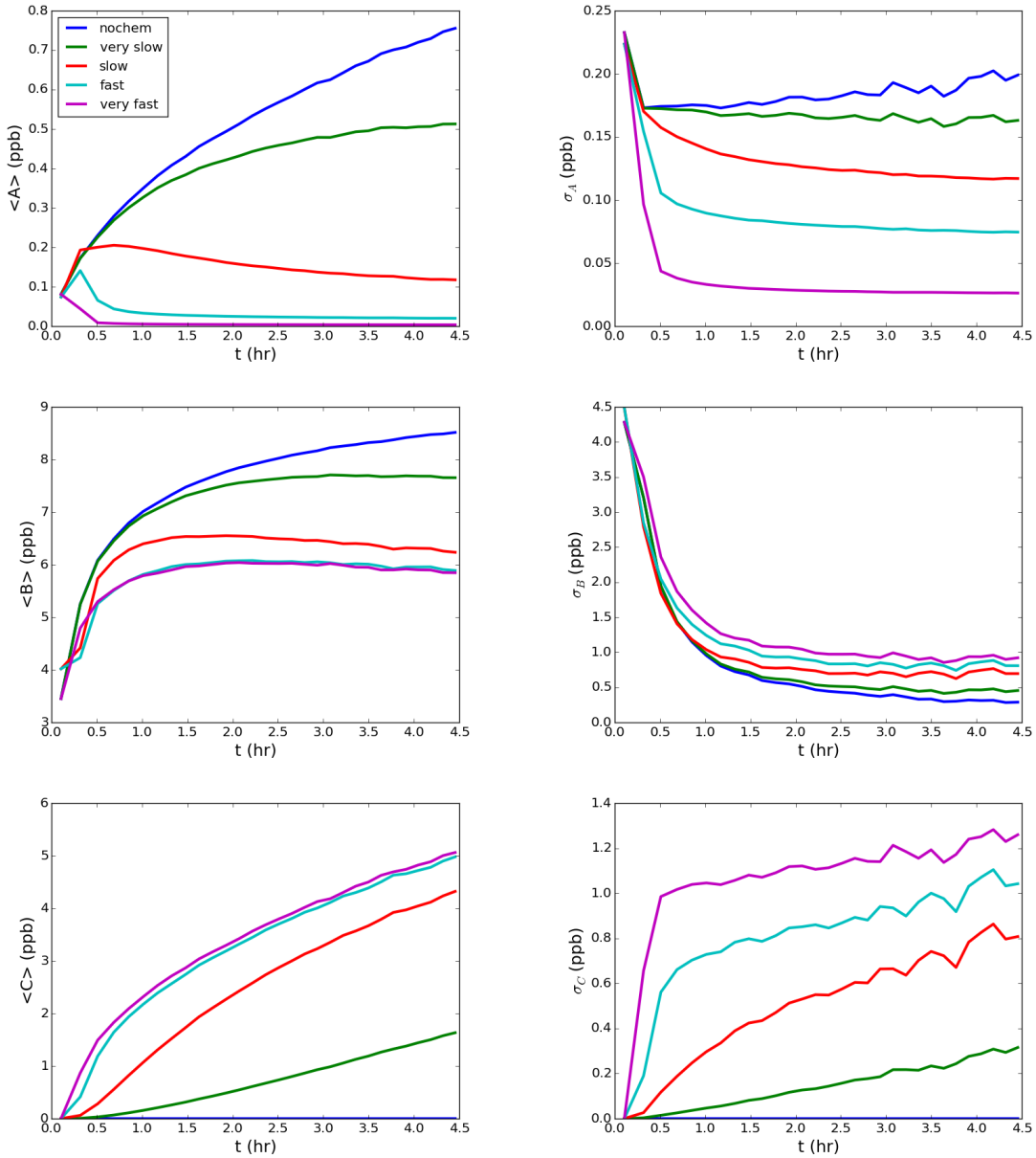

Figure 3.17: Evolution of volumetrically averaged mean (*left panel*) and standard deviation (*right panels*) of the mixing ratio of Tracer A (*top*), B (*middle*) and C (*bottom*) with time, in the five chemistry cases.

In the right panels of Figure 3.17, the standard deviations of the three tracers are shown. The standard deviation of the mixing ratio of Tracer A decreases with increasing chemical reaction rate due to increase depletion of Tracer A when the chemistry is fast. Yet with the also decreasing amount of Tracer B with increasing chemical reaction rate, the standard deviation of the mixing ratio of Tracer B increases slightly. Since Tracer B is always in surplus, the chemical consumption of Tracer B is relatively unimportant. The standard deviation in the no-chemistry case (the blue line) gives the value when Tracer B can be most efficiently mixed in the CBL (hence the least standard deviation). The introduction of chemistry decreases the efficiency of turbulence mixing. This effect amplifies as the chemical reaction rate increases, resulting in the increase in standard deviation. The standard deviation of Tracer C increases with increasing chemical reaction rate due to its increased amount produced. Note that here at the end of the simulation, both the standard deviations of the mixing ratios for Tracer A and B attain equilibrium, i. e. the system attains statistical equilibrium. The standard deviations of Tracer C mixing ratio do not attain equilibrium as there is no depletion of Tracer C in the chemistry scheme.

Vertical profiles

We then look at the vertical profiles of the horizontally averaged statistics concerned at the end of the simulation, at the time when statistical equilibrium is attained.

Figure 3.18 shows the horizontally averaged means of the mixing ratios against height. One can see that all tracers are well-mixed in the mixed layer, indicated by the small gradient of the mixing ratio against height (inverse of the gradient of the plots). For Tracer A (top-panel in Figure 3.18), the gradient of mixing ratio against height increases with the imposed chemical reaction rate, implying that turbulence mixes Tracer A less efficiently with faster chemistry. However, Tracer A is almost depleted in the mixed layer for fast- and very fast-chemistry cases. The high amount of Tracer A in the surface layer is due to the constant emission of Tracer A from the surface. This amount decreases with increasing chemical reaction rate as more Tracer A is consumed with faster chemistry.

Tracer B is well-mixed in the boundary layer even in the surface layer for the very slow- and slow-chemistry cases (refer to the middle panel of Figure 3.18, but its mixing ratio significantly drops in the surface layer for the fast- and very fast-chemistry cases. It is because Tracer B consumes Tracer A mostly in the surface layer in both the fast chemistry cases. Note that Tracer B is even more well-mixed in the mixed layer than Tracer A (by comparing the gradient of mixing ratio against height between that of Tracer A and of Tracer B, refer to the red line for the slow-chemistry case, for example), because Tracer B is in surplus.

Tracer C is generally well-mixed in the mixed layer except in the very fast-chemistry case. The substantially high mixing ratio of Tracer C in the surface layer indicates

that most Tracer C is formed in the surface layer. For the very fast-chemistry case, a significant gradient of mixing ratio against height is observed even in the mixed layer. This is because the production of Tracer C is faster than the transfer of Tracer C by turbulent mixing throughout the mixed layer.

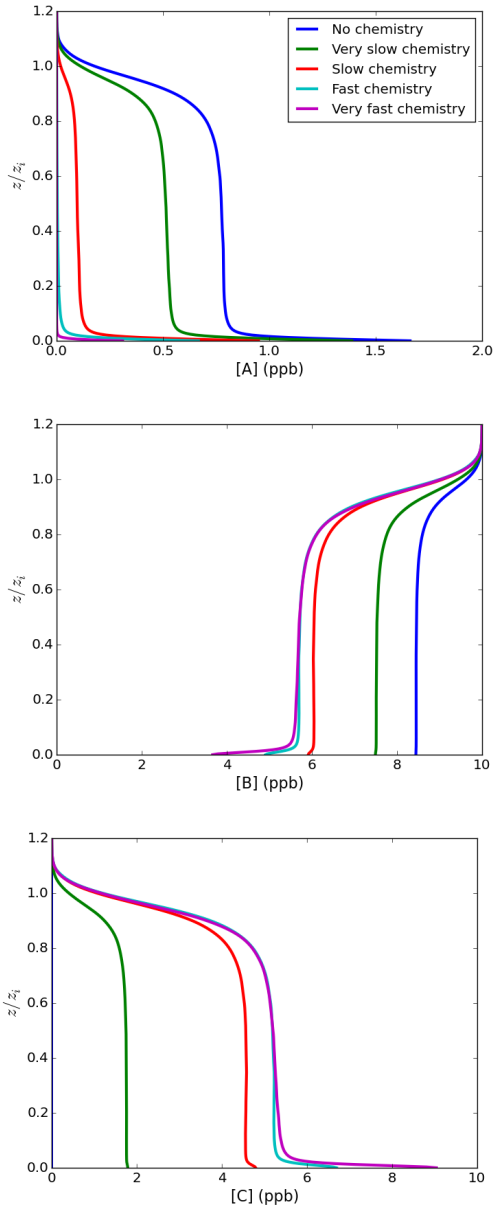

Figure 3.18: Vertical profiles of mixing ratio of Tracer A (*top*), B (*middle*)and C (*bottom*) at the end of the simulation in the five chemistry cases.

The left panels of Figure 3.19 show the variance of the mixing ratio of the three tracers. For Tracer A (top-left panel), one can see the variance is largest at the top of the surface layer, except in the no- and very slow-chemistry cases, where the variance is largest at the top of the whole boundary layer. The large variance in the surface layer is

induced by the constant emission of Tracer A at the surface. The variance decreases as the chemical reaction rate increases due to the increased consumption of Tracer A. The decrease in variance is more rapid at the top of the surface layer, as Tracer A is highly depleted at the top of the boundary layer when chemistry is fast.

For Tracer B (middle-left panel), the variance is largest at the top of the boundary layer in all cases, where Tracer B is entrained from the free troposphere to the mixed layer. There is a smaller peak at the top of the surface layer due to its high consumption on Tracer A in the surface layer. The variance increases with the chemical reaction rate, except at the top of the boundary layer in the very fast-chemistry case. In that case, the mixing ratio of Tracer A is almost zero at the top of the boundary layer, so that the contribution of Tracer B's consumption on Tracer A to the variance vanishes.

The variance profiles of Tracer C (bottom-left panel) highly reconcile with those of Tracer B, except having higher values in the surface layer. In principle, the variances of Tracer A and B both contribute to that of Tracer C, as Tracer C is the product of the two tracers. However, since Tracer B is always in surplus, its influence to the statistics of Tracer C is higher.

The right panels of Figure 3.19 show the vertical fluxes of the tracers (the covariance between the mixing ratio of the tracers and the vertical velocity). From the positive values of the fluxes, both Tracer A and C are highly correlated with the updraft of air in the boundary layer. The exception at the location near the top of the boundary layer in the no- and very-slow chemistry cases hints a different transport mechanism in the encroachment zone. On the other hand, Tracer B is highly correlated with the downdrifting air.

For Tracer A, the flux decreases with chemical reaction rate. As the chemistry becomes faster, more Tracer A is consumed, and the role of turbulent mixing diminishes. The flux is always largest at the top of the surface layer, again due to the surface emission of Tracer A. In contrary, the flux increases with increasing chemical reaction rate for Tracer B and C. The height with maximum flux is transiting from near the top of the boundary layer with slow chemistry, to near the surface with fast chemistry. This is due to the increasing lifetime of Tracer B with an increasing chemical reaction rate because Tracer A is depleting. More Tracer B can flow down the boundary layer without being consumed, and more Tracer C is produced at a lower altitude in the boundary layer, from where they are carried away by the updrifting air.

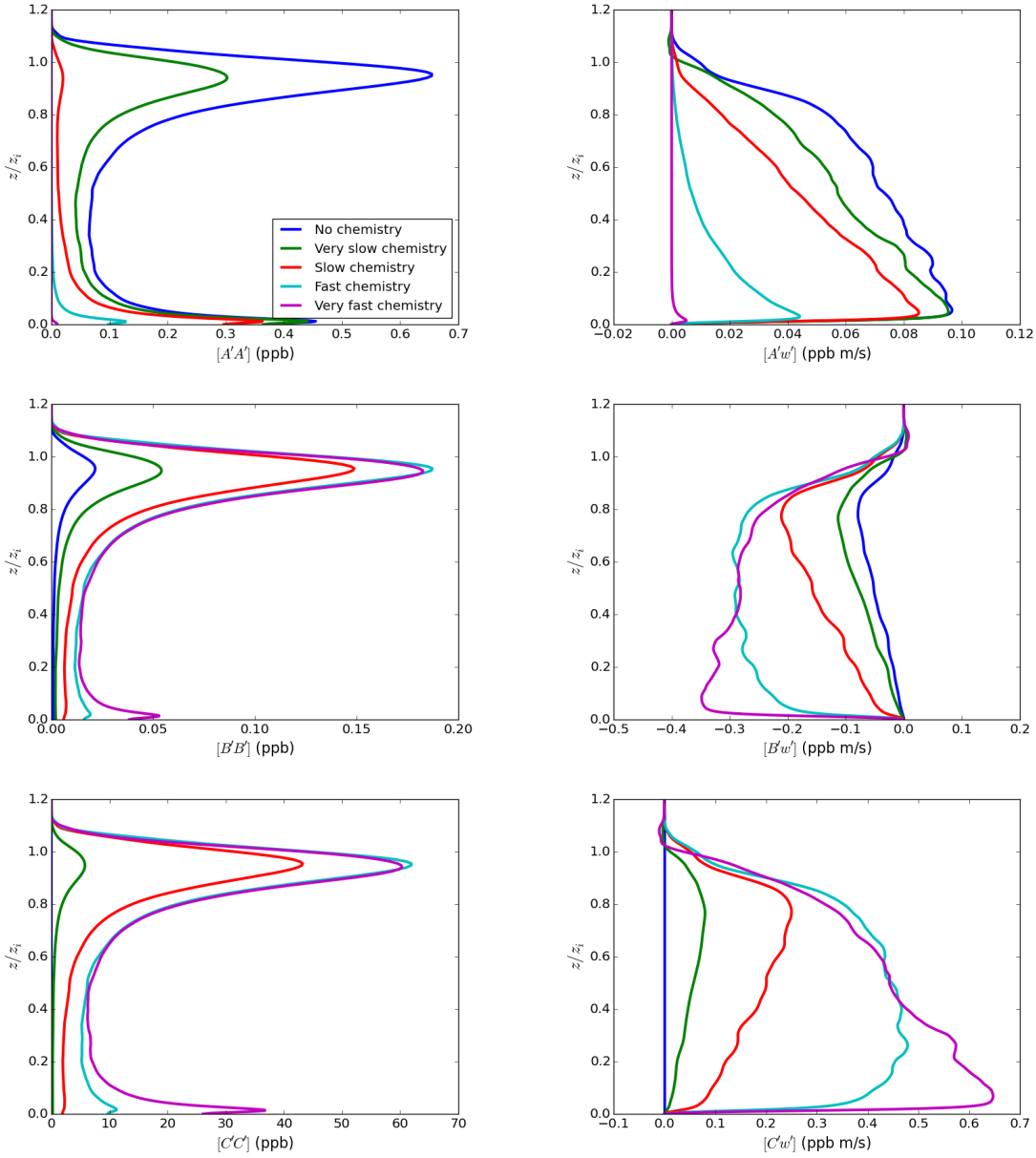

Figure 3.19: Vertical profiles of the variance of mixing ratio (*left panel*) and the vertical fluxesof Tracer A (*top*), B (*middle*) and C (*bottom*) at the end of the simulation with the 5 chemistry cases.

3.3.2 Tracer Segregation and effective chemical reaction rate

The importance of chemical-turbulence interaction can be estimated from the Damköhler number. The Damköhler numbers of Tracer A and B are expressed in Equations 1.23 and 1.24 respectively. The initial Damköhler number Da mentioned previously refers to the initial Damköhler number of Tracer A. As the boundary layer grows, the Damköhler numbers evolve with the dynamical variables and the mean mixing ratios, inspite of the

fixed imposed chemical reaction rate k. Figure 3.20 shows the evolution of the Damköhler numbers of Tracer A and B with time. Note that the difference of the Damköhler number of Tracer B among the four chemistry cases is less than an order at the end of the simulation, unlike that of Tracer A.

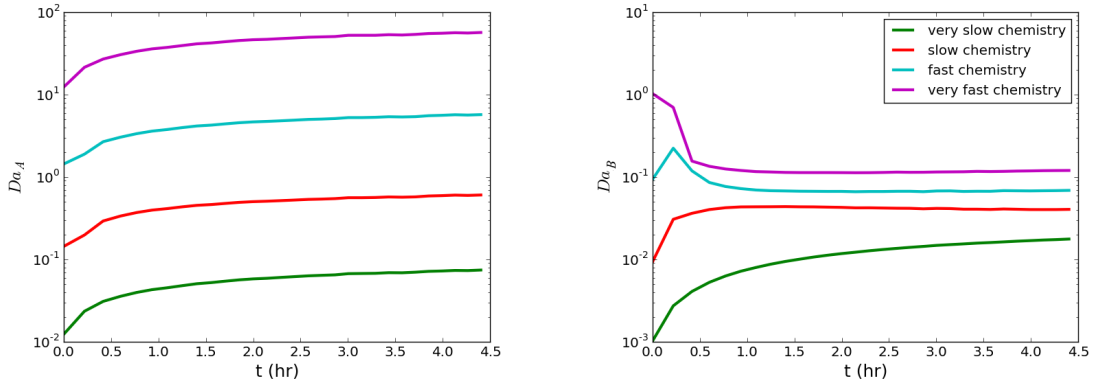

Figure 3.20: Evolution of the Damköhler number of Tracer A (*left*) and B (*right*) with time in the 4 chemistry cases.

The effective chemical reaction rate k_{eff}, which measures the actual chemical reaction rate under the influence of turbulent motions, is calculated from the segregation between the concentrations of Tracer A and B as in Equations 1.25. The evolution of the normalised effective chemical reaction rate k_{eff}/k of the four chemistry cases is plotted in Figure 3.21. We take the time-averaged value of the effective chemical reaction rate k_{eff}/k over the last 1.5 hours in the simulation, when statistical equilibrium is attained. In the four chemistry cases, the effective chemical reaction rate k_{eff} is 98.7%, 96.5%, 86.9% and 64.9% of the imposed chemical reaction rate k from very slow to very fast chemistry respectively. This implies that a complete-mixing model overestimates the reaction rate from 1.3 - 35.1 %, depending on the imposed chemical reaction rate k.

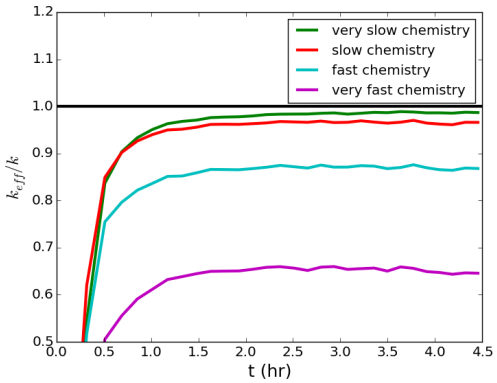

Figure 3.21: Evolution of the normalised effective chemical reaction rate k_{eff}/k with time for the 4 chemistry cases.

To illustrate the effect of tracer segregation on chemical production, we look at the colour maps of production term (kAB) in the slow- and fast-chemistry cases in Figure 3.22. These colour maps are plotted at the end of the simulation. Although the production term is generally smaller in the slow-chemistry case (due to its small k, refer to the left panel), Tracer C is produced throughout the boundary layer. In the fast-chemistry case (right panel), Tracer C is dominantly produced near the surface layer. In the mixed layer, Tracer C is produced only in some regions.

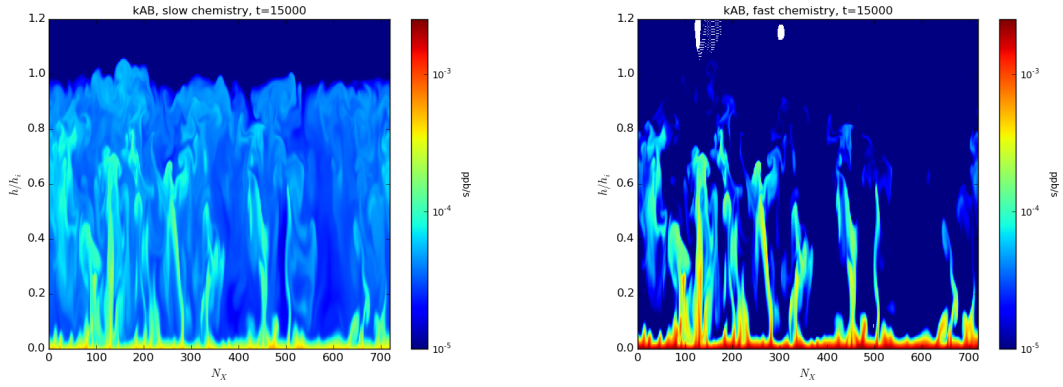

Figure 3.22: Colour maps of the production term (kAB) at the end of the simulation in the slow- (*left*) and fast- (*right*) chemistry cases.

The effective chemical reaction rate also varies with height. The effective chemical reaction rate can be written as a function of height z:

$$[k_{eff}](z) = (1 + \frac{[A'B']}{[A][B]})k \tag{3.4}$$

$$= (1 + [I_S](z))k. \tag{3.5}$$

The height-dependent effective chemical reaction rate $k_{eff}(z)$ can show us the over/underestimation of the calculated chemical reaction rate from the actual value by a model that assumes Tracer A and B are well-mixed horizontally within a layer at a specific height z. Figure 3.23 shows the effective chemical reaction rate as a function of the normalised height with the boundary layer height (z/z_i) for the four chemistry cases. The effective chemical reaction rate k_{eff} is minimum just below the top of the boundary layer, and is 92%, 83%, 62% and 55% of the imposed value from very slow to very fast chemistry respectively. It means that if the model assumes Tracer A and B are completely mixed within the layer at the height just below the top of the boundary, it overestimates the chemical reaction rate by 8-45% at that particular height.

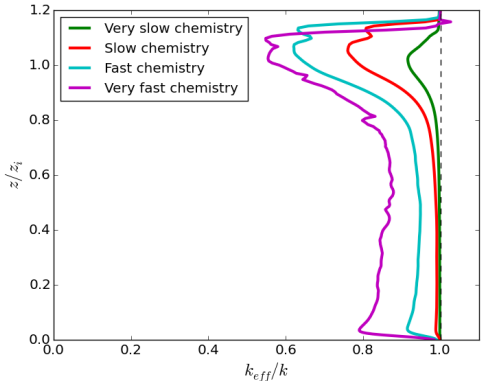

Figure 3.23: Vertical profile of the segregation coefficient $I_S(z)$ and the effective chemical reaction rate $k_{eff}(z)/k$ at the end of the simulation for the 4 chemistry cases.

3.3.3 Mechanism of chemical-turbulence interaction

Budget analysis

To explain the mechanism of the chemical-turbulence interaction, we look into the budget equation of the mixing ratio of the tracers, following the method in Li et al. (2009). A tracer with concentration field ϕ_i evolves with the continuity equation:

$$\frac{\partial \phi_i}{\partial t} + u_i \frac{\partial \phi_i}{\partial x_i} = \kappa \frac{\partial^2 \phi_i}{\partial x_i^2} - k\phi_i\phi_j,$$

in which the tracer advecting in a wind field $u_i = (u, v, w)$ reacts with another tracer with concentration field ϕ_j at a chemical reaction rate k. The parameter κ refers to the molecular diffusivity. The concentration fields ϕ_i and ϕ_j and the velocity field u_i are then disseminated into mean and turbulent components, i. e. $\phi_i = \bar{\phi}_i + \phi_i$", $\phi_j = \bar{\phi}_j + \phi_j$", $u_i = \bar{u}_i + u_i$". Consider only the vertical dimension z and take the horizontal average of the equations, one can get the following five terms:

$$-\frac{\partial [\phi_i]}{\partial t} - \frac{\partial [\phi_i" w"]}{\partial z} + \kappa \frac{\partial^2 [\phi_i]}{\partial z^2} - k\left([\phi_i][\phi_j] + [\phi_i" \phi_j"]\right) = 0,$$

where the dashed parameters refer to the turbulent variables. We name these five terms from the left to the right time derivative, turbulent diffusion, molecular diffusion, chemistry (mean) and chemistry (turbulent). The budgets of these terms of the three tracers in the no-, slow- and fast-chemistry cases are presented here and plotted in Figure 3.24, 3.25 and 3.26 respectively. In general (except the time derivative term), a negative term contributes to the loss of the tracer, and a positive term contributes to the gain of the tracer.

We first look at the budget of Tracer A from the surface up the boundary layer (top

panels in Figure 3.24, 3.25 and 3.26). In the surface layer, one can see observe a very positive molecular diffusion term and very negative turbulent diffusion term in all chemistry cases. The largely positive molecular diffusion term is due to the shear near the surface. The large negative turbulent diffusion term indicates that turbulence is responsible for transferring the emitted Tracer A away from the surface layer. However, as the chemistry becomes fast (refer to Figure 3.26 to the fast-chemistry case), the chemistry mean term has more contribution to the loss of Tracer A in the surface layer, and grows even larger than the turbulent diffusion term. In the mixed layer, the turbulent diffusion term becomes positive, reflecting that turbulence mixing is transporting Tracer A into the mixed layer (from the surface layer). In the no-chemistry cases, the turbulent diffusion term is compensated by the negative molecular diffusion and time derivative terms. In the two other chemistry cases, the turbulent diffusion term is mainly compensated by the chemical mean term. As the chemical reaction transits from slow to fast chemistry, the turbulent diffusion term decreases with height, meaning turbulence transports less Tracer A up the mixed layer. This is because the chemistry is too fast that Tracer A reacts chemically before turbulence brings it up to the mixed layer. This results in a decrease in the mixing ratio of Tracer A (also see the first panel of figure 3.18 for the vertical profile of Tracer A), and hence a decrease of the chemical mean term with height.

We then explore the budget of Tracer B from the encroachment zone down the boundary layer (second-top panels in Figure 3.24, 3.25 and 3.26). In the encroachment ozone, one can see observe a very negative turbulent diffusion term. This is because turbulence is carrying Tracer B away from the encroachment zone. There is always a transition of molecular diffusion term from negative to positive down the encroachment zone. This is a result of the mechanical transport in the encroachment zone. Just above the top of the boundary layer, shear takes Tracer B away from the free troposphere (to the boundary layer), resulting a loss in the region. On the other side, just below the top of the boundary layer, shear brings Tracer B from the free troposphere, resulting in a gain of the mixing ratio of Tracer B. As Tracer B flows down the boundary layer, the turbulent diffusion term is transiting from negative to positive at a certain height. Below this height, turbulence is responsible to supply Tracer B, and to compensate the chemical mean term in the slow- and fast-chemistry cases. This transiting height, also the same height with maximum vertical flux of Tracer B and (refer to its vertical profile in the middle-right panel of Figure 3.19) is lower when the chemistry is fast. This is because with faster chemistry, the chemical lifetime of Tracer A is shorter, and Tracer A is almost depleted in certain height. It in turn prolongs the chemical lifetime of Trace B, allowing turbulence to bring Tracer B further down in the mixed layer. The chemical mean term is always negative, as Tracer B is a reactant, and its magnitude increases down the boundary layer. The largely negative chemical term in the surface layer indicates that Tracer B is chemically destroyed by the surface-emitted Tracer A.

The positive turbulent diffusion term also increases, as turbulence mixing is supplying Tracer B for its chemical reaction with Tracer A.

Lastly we go through the budget of Tracer C in the direction up the boundary layer (bottom panels in Figure 3.24, 3.25 and 3.26). In the surface layer, a largely positive chemical mean term can be observed, as Tracer C is largely produced in the surface layer. The term increases with faster chemistry. It is compensated by the negative turbulent diffusion term, meaning turbulence is taking the produced Tracer C away from the surface layer. As Tracer C flows up the boundary layer, the turbulent diffusion term is transiting from negative to positive at a certain height. This transitional height is identical to that described in Tracer B. Turbulent diffusion results in an accumulation of Tracer C just below the top of the boundary layer. This is probably because turbulence cannot bring Tracer C further up to the free troposphere across the top of the boundary layer.

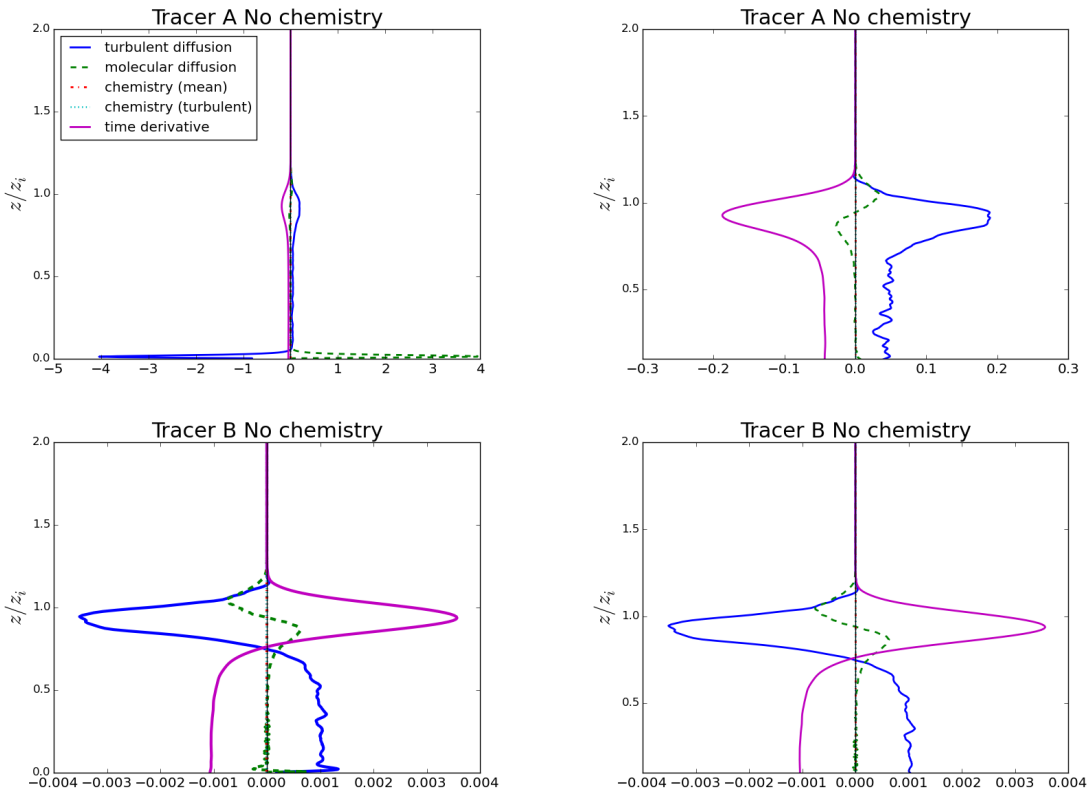

Figure 3.24: Different terms in the budget equation for the no chemistry case for Tracer A (*top*) and B (*bottom*). The left panels show the budget profiles throughout the whole boundary layer, and the right panels show the zoomed profiles above the surface layer.

In all the cases the chemical turbulent term appears to be insignificant. Its largest contribution is usually in the region of the surface layer and encroachment zone. However, if you consider the ratio between the chemical turbulent and chemical mean term,

which is the segregation coefficient, the ratio becomes significant when the chemistry is fast. This is because the chemical mean term is relatively small in the mixed layer for all tracers, bringing the segregation coefficient to a large value.

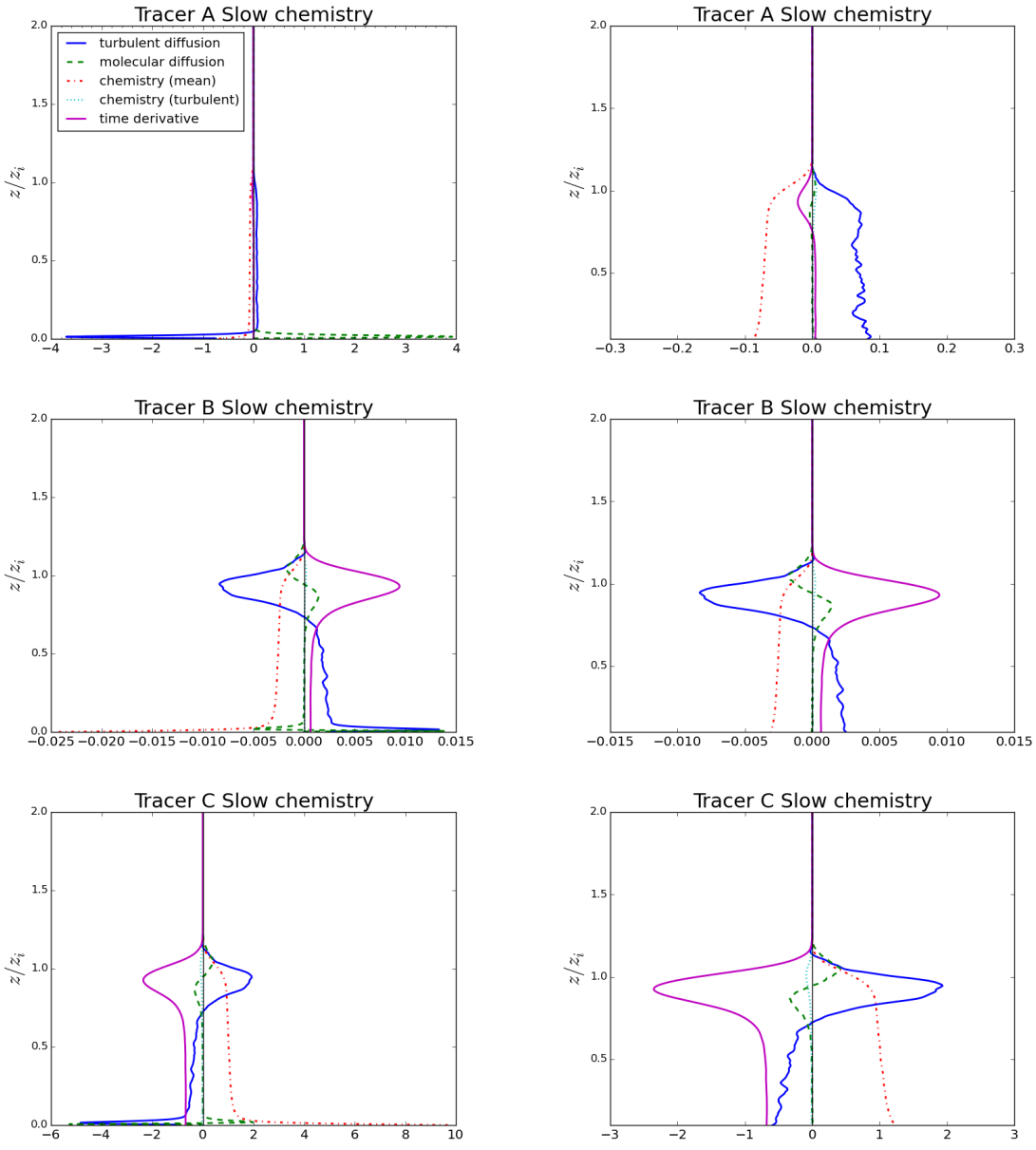

Figure 3.25: Different terms in the budget equation for the slow chemistry case for Tracer A (*top*), B (*middle*) and C (*bottom*). The left panels show the budget profiles throughout the whole boundary layer, and the right panels show the zoomed profiles above the surface layer.

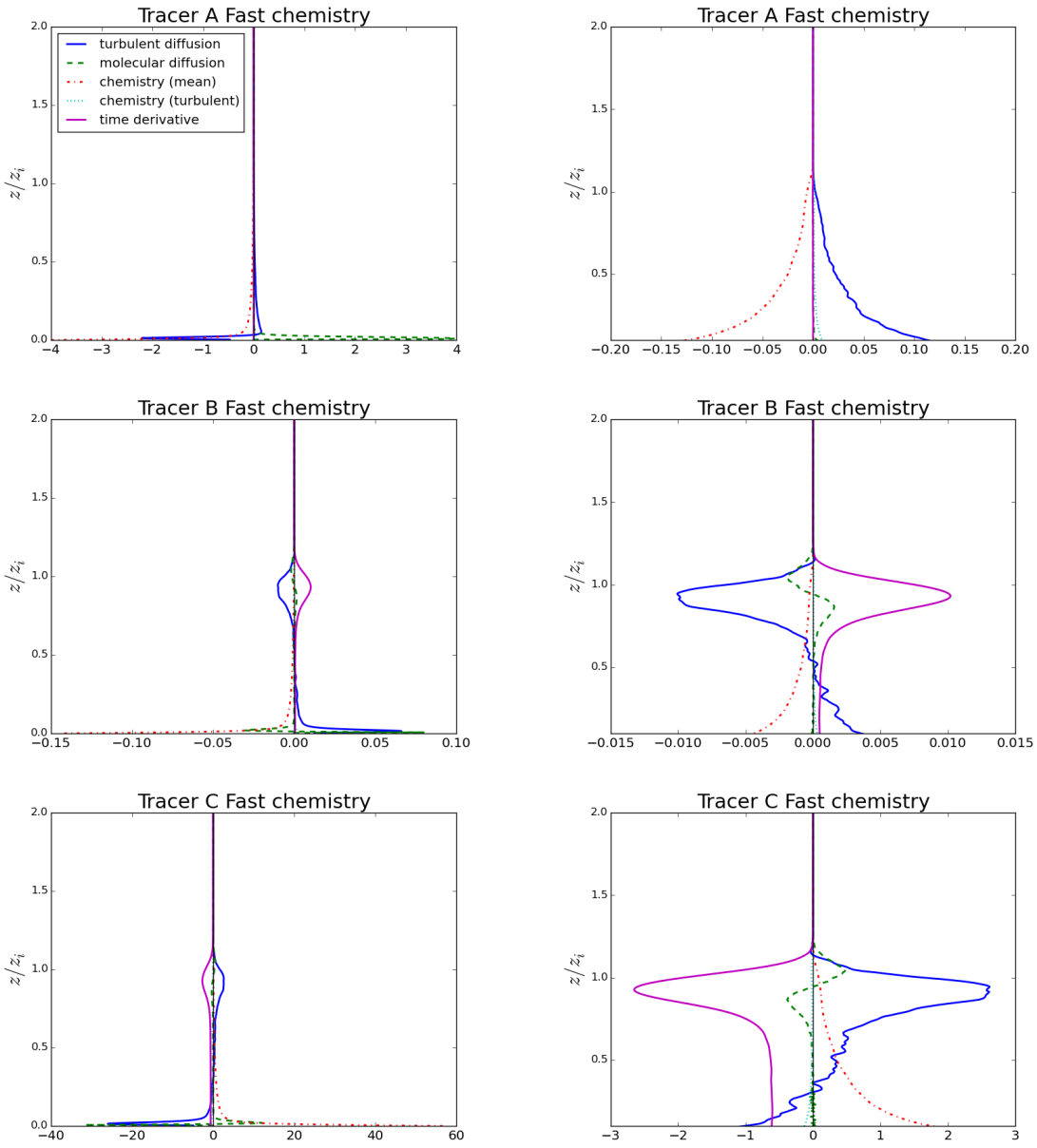

Figure 3.26: Different terms in the budget equation for the fast chemistry case for Tracer A (*top*), B (*middle*) and C (*bottom*). The left panels show the budget profiles throughout the whole boundary layer, and the right panels show the zoomed profiles above the surface layer.

Eddy diffusion coefficient

Another way to examine the mechanism of the interaction between turbulent motion and chemical reaction is to examine how the eddy diffusion coefficient κ_{eddy} changes with the imposed chemical reaction rate. Here, the eddy diffusion coefficient is defined as

$$\kappa_{eddy} = -\frac{\frac{\partial \phi_i w}{\partial z}}{\frac{\partial^2 \phi_i}{\partial z^2}}, \tag{3.6}$$

which is also a parametrisation coefficient commonly employed in large-scale transport models to account for turbulent mixing. From the continuity equation, one can see that at equilibrium state,

$$-u_i \frac{\partial \phi_i}{\partial x_i} + \kappa \frac{\partial^2 \phi_i}{\partial x_i^2} - k\phi_i\phi_j = 0.$$

Dividing both sides by the gradient of the fluxes, and substituting Equation 3.6, we get

$$\kappa\kappa_{eddy} + k\phi_i\phi_j \left(\frac{\partial \phi_i w}{\partial z} \right)^{-1} = 0.$$

Hence, one can speculate that, as the chemical term (the second term on the left hand side of the above equation) increases with increasing k, the turbulent term (the first term), which is the product of the molecular diffusion coefficient, and the eddy diffusion coefficient, decreases. This implies with faster chemistry, the eddy diffusion coefficient decreases.

Figure 3.27 shows the eddy diffusion coefficient of Tracer A normalised with the product of the convective velocity w_c and the boundary layer height z_i as a function of height at the end of the simulation. It shows that with faster chemical, the average eddy diffusion coefficient is smaller, which agrees with our speculation. It is also noted that the height with maximum κ_{eddy} also increases with faster chemistry. That is inherited from the shape of the fluxes ($\phi_i w$).

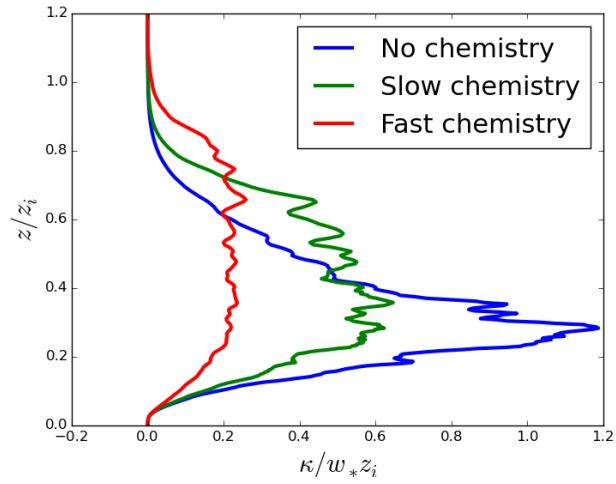

Figure 3.27: Normalised eddy diffusion coefficient of Tracer A at the end of the simulation with the 3 chemistry cases.

Figure 3.28 shows the eddy diffusion coefficient of Tracer B. it shows some discontinuity in the middle of the mixing layer. This is because Tracer B is mixed well in the mixing layer due to its surplus, which gives a close to zero value to the gradient of the mixing ratio. Apart from those regions, once can see that values of the eddy diffusion

coefficient of Tracer B are generally smaller that that of Tracer A, but in general increase with increasing reaction rate.

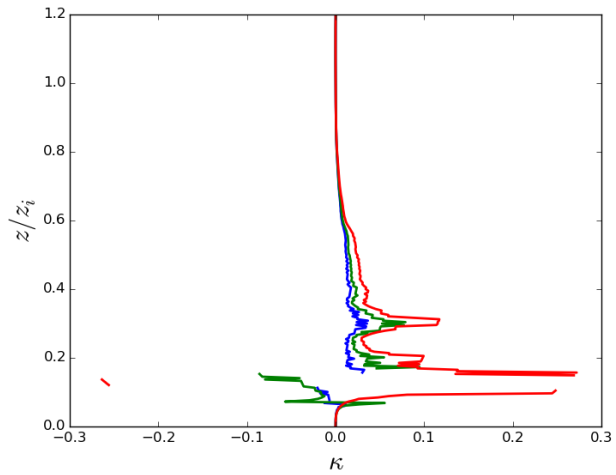

Figure 3.28: Normalised eddy diffusion coefficient of Tracer B at the end of the simulation with the 3 chemistry cases.

3.3.4 Model resolution degrading

Degrading model resolution artificially mixes tracers, and hence decreases the tracer segregation (or increases the effective chemical reaction rate). In the previous sessions, we always compare the effective chemical reaction rate with a model that assumes complete mixing in the whole boundary layer. However, the resolution in model chemical-transport models, especially those in regional-scale, is higher in order of a few kilometres. And there are usually multiple vertical levels within the boundary layer, instead of just one level. These high-resolution models are often employed in urban areas. To evaluate the importance of sub-grid chemical-turbulence interaction in these regional chemical-transport models, we degrade our model to 2 horizontal resolutions (1- and 3-km, with 12 and 4 nodes in the horizontal direction respectively) and 3 vertical resolutions (32-lev, 64-lev and 128-lev, with 32, 64 and 128 nodes in the vertical direction in the whole domain, and with on average 10, 20 and 40 levels within the boundary layer respectively), resulting in four coarse-grid models, namely 1 km-128 lev, 1 km-64 lev, 1 km-32 lev, 3 km-128 lev and 3 km-64 lev and 3 km-32 lev. The values are selected according to common grid sizes in regional chemical-transport models. The number of nodes and the resolutions of the models are listed in Table 3.3.

	DNS	1 km-128 lev	1 km-64 lev	1 km-32 lev	3 km-128 lev	3 km-64 lev	3 km-32 lev
$N_X \times N_Y \times N_Z$	720 × 512 × 720	12 × 128 × 12	12 × 64 × 12	12 × 32 × 12	4 × 128 × 4	4 × 64 × 4	4 × 32 × 4
Horizontal resolution (km)	0.017	1.005	1.005	1.005	3.016	3.016	3.016
Vertical resolution (km)*	0.032	0.126	0.253	0.506	0.126	0.253	0.506

Table 3.3: Corresponding horizontal and vertical resolutions of the original and coarser-grid models. ∗: The stated values are the averaged vertical resolutions of the models, as vertical grids stretch with height.

We then calculate the effective chemical reaction rate k_{eff} of the four models, and compare the values with our DNS model. Figure 3.29 shows the evolution of the segregation coefficient I_S with time of the four coarse-grid models in the slow-, fast- and very fast-chemistry cases. The solid lines refer to the DNS models. One can see that degrading the model resolution does not have a significant impact on the calculation of tracer segregation in the model in the slow-chemistry case. However, the effect is significant in the fast and very fast chemistry cases. The model with lower resolution tends to give a higher (or less negative) value of the segregation coefficient. They fail to resolve the segregation of the tracers, and assume that they are mixed inside a model grid, resulting in the underestimation of tracer segregation (a less negative segregation coefficient).

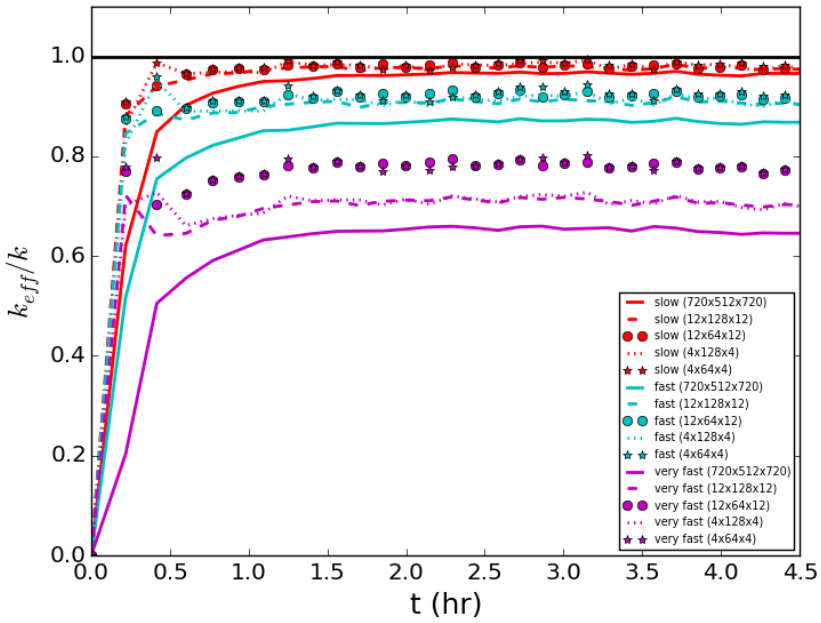

Figure 3.29: Evolution of segregation coefficient of the coarse-grid models in the 4 chemistry cases with time

One can also observe (most obviously from the very fast-chemistry case, the magenta lines) the segregation coefficient does not differ much between models with 1-km and 3-km horizontal resolution with the same vertical resolution, but varying the vertical

resolution greatly alters the calculation. The reduced vertical resolution is the more limiting factor in this case, as Tracer A and B are segregated along the vertical direction.

We then take the time-average of calculated normalised effective chemical reaction rate (k_{eff}/k) over the last 1.5 hours of the simulation of the four coarse-grid models. The results are listed in Table 3.4. The results from the DNS model are listed in the first column. By comparing the values with those from the DNS model, we can estimate how much the coarse-grid models over/underestimate the actual chemical reaction rate due to its degraded resolution. We record the deviation in percentage in brackets. The largest deviation is in the very fast-chemistry case, in which the effective chemical reaction rate is overestimated by ∼22% in both the models with 32 vertical levels. From these results, we can observe significant improvement in model performance when the model horizontal grid refines from the whole simulation domain (∼ 12 km) to 3 km, indicated by the reduced overestimation of the chemical reaction rate from 15-35% to 4-22% for both fast-chemistry cases. However the improvement is insignificant when the model horizontal resolution increases from 3 km ot 1 km (both lie in the range of 4-22%). This is consistent with the findings in Chapter 2. The improvement is more significant with increasing vertical resolution. The overestimation drops from 15-35% to 8.0-22.4% from a one vertical layer-model to a 32 vertical-layer model, and further decreases to 5.3-12.9% and 3.9-5.6% with a 64 and 128 vertical-layer model respectively in both fast-chemistry cases.

Cases	DNS	1 km-128 lev	1 km-64 lev	1 km-32 lev	3 km-128 lev	3 km-64 lev	3 km-32 lev
Very slow	0.9870	0.9913 (+0.43%)	0.9928 (+0.58%)	0.9959 (+0.89%)	0.9922 (+0.52 %)	0.9934 (+0.64%)	0.9986 (+1.16%)
Slow	0.9652	0.9762 (+1.10%)	0.9795 (+1.43%)	0.9870 (+2.18%)	0.9798 (+1.46%)	0.9825 (+1.73%)	0.9946 (+2.94%)
Fast	0.8687	0.9075 (+3.88%)	0.9213 (+5.26%)	0.9484 (+7.97%)	0.9102 (+4.15%)	0.9231 (+5.44%)	0.9585 (+8.98%)
Very fast	0.6492	0.7055 (+5.63%)	0.7777 (+12.85%)	0.8669 (+21.77)	0.7053 (+5.61%)	0.7765 (+12.73%)	0.8735 (+22.43%)

Table 3.4: Normalised effective chemical reaction rate coefficient (k_{eff}/k) of models with different resolutions with the 4 chemistry cases. The values in the brackets show the deviation of the coefficients from the coarser-grid models from the DNS simulation.

Figure 3.30 shows the horizontally-averaged segregation coefficient ($I_S(z)$) against height of the four coarse-grid model in the slow-, fast-, and very fast-chemistry cases. Now the coefficient varies with the horizontal resolution, as the height-dependent segregation coefficient compares the segregation within the same vertical layer. One can see that all coarse-grid models fail to show the local minimum at the top of the surface layer, as the surface layer is too thin for these models to resolve. They also show a less prominent minimum at the top of the boundary layer, as have fewer grids around the encroachment zone, and the segregation functions are therefore smoothed.

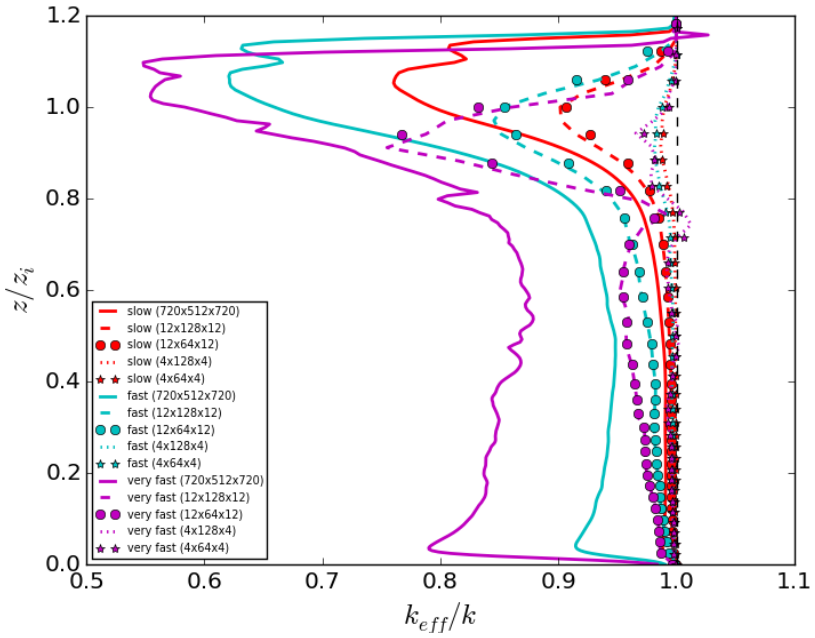

Figure 3.30: Vertical profile of segregation coefficient of the coarse-grid models in the 4 chemistry cases at the end of the simulation

3.3.5 Strong emission flux

The above DNS simulations are then extended to scenarios with stronger emission fluxes of Tracer A. Tracer A is emitted at a fluxes of 0.5 ppb m s^{-1} and 1.4 ppb m s^{-1}. The mixing ratio of Tracer B is fixed at 2 ppb. Only the slow- and fast-chemistry cases are repeated.

The left panels of Figure 3.31 show the vertical profiles of the mixing ratio of Tracer A (top panel), B (middle) and C (bottom) at the end of the simulation. As a reference, the results from the previous simulations with emission flux of Tracer A at 0.05 ppb m s^{-1} with the slow- and fast-chemistry cases in blue and green respectively. One can see that with the increased emission flux, Tracer A accumulates in the boundary layer. On the other hand, Tracer B is almost completely depleted. As the emission flux of Tracer A increases and/or the chemistry becomes faster, the depth that Tracer B can be replenished from the free troposphere becomes narrower, and Tracer B starts being depleted at a closer distance from the top of the boundary layer (or at a higher altitude). Tracer C is accumulated near the top of the boundary layer, at here most of the Tracer B is concentrated. Within the boundary layer, similar amount of Tracer C is produced, despite the different emission fluxes and imposed chemical reaction rates, since Tracer B is depleted in all scenarios.

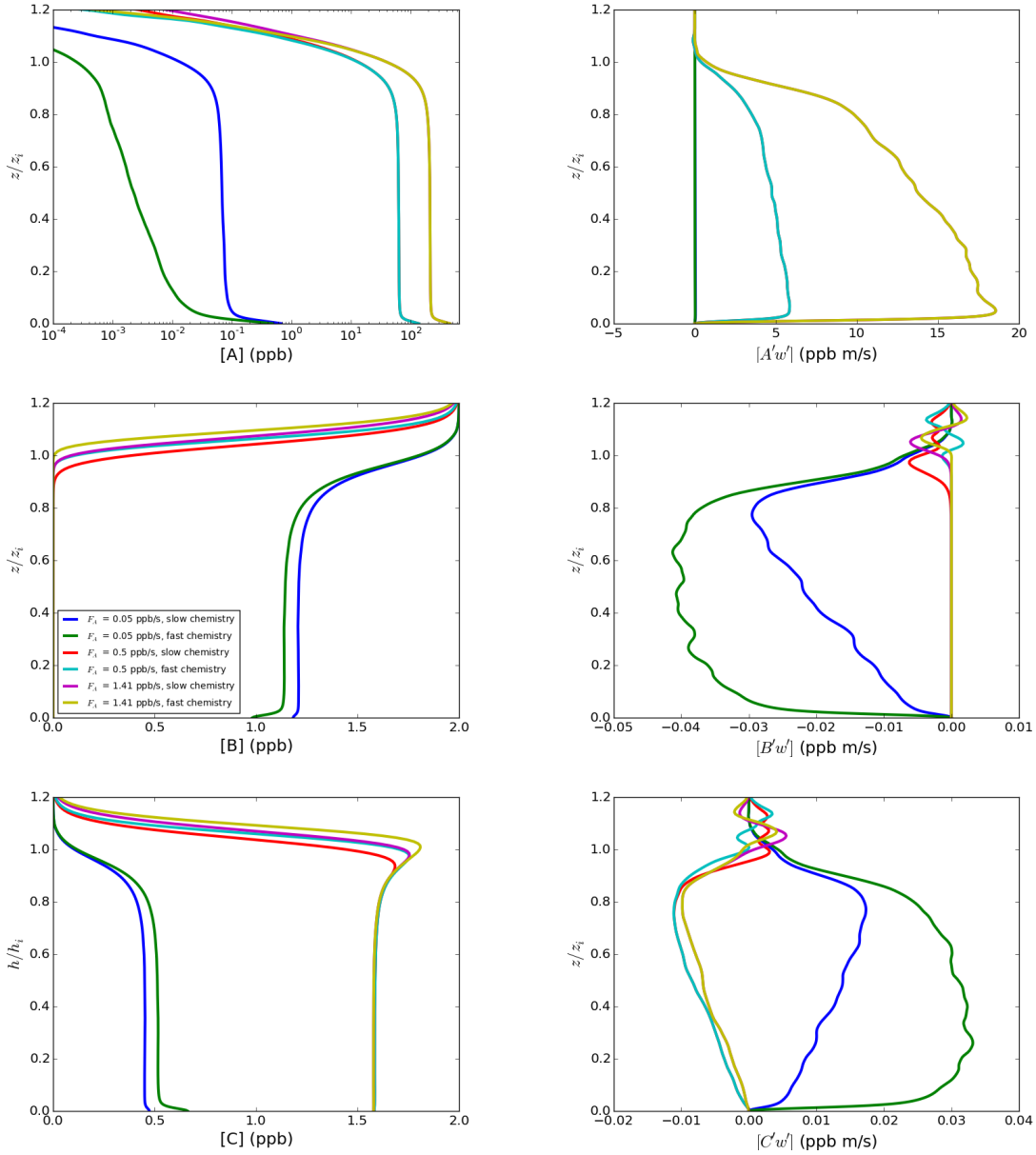

Figure 3.31: Vertical profiles of the horizontal mean of mixing ratio (*left panel*) and the covariance between the mixing ratio and the vertical velocity (*right panel*) of Tracer A (*top*), B (*middle*) and C (*bottom*) at the end of the simulation with the 5 chemistry cases.

The right panels of Figure 3.31 show the vertical profiles of the fluxes of the tracers. The fluxes of Tracer A are positive in the boundary layer, indicating that Tracer A is updraft-correlated, and is at its maximum at the top of the surface layer, similar as in the previous simulations. The fluxes of Tracer B are negative, indicating that Tracer B is downdraft-correlated, and is at its minimum at the height where its mixing ratio just turns zero (near the top of the boundary layer). The fluxes of Tracer B also turn zero at the location where its mixing ratio is zero. The fluxes of Tracer C show different behaviour as in the previous simulations. The fluxes of Tracer C become negative,

indicating that Tracer C is downdraft-correlated, same as Tracer B. This also implies that the chemistry here is Tracer B-limiting, contrary to the previous simulations. This can also be illustrated from the production term (plotted in Figure 3.32). The maximum of the production term shifts from the top of the surface layer to near the top of the boundary layer as the emission flux of Tracer A increases, shifting from near the source of Tracer A (emitted from the surface) to near the source of Tracer B (entrained from the free troposphere).

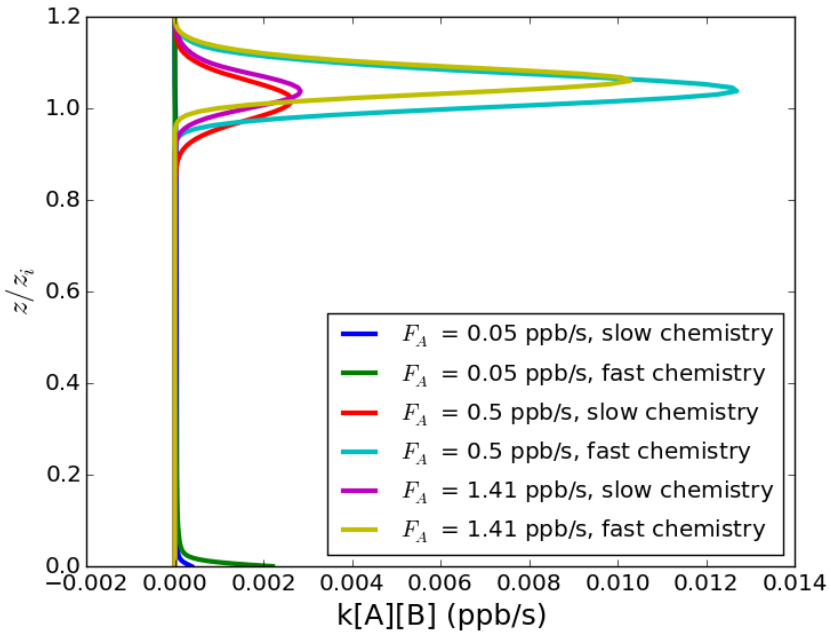

Figure 3.32: Vertical profile of the production term of C $k[A \cdot B]$ at the end of the simulation for the 5 cases with different emission fluxes.

The effective chemical reaction rates of the simulation with strong emission fluxes are then calculated. One can see that, with strong emission flux of Tracer A, the effective chemical reaction rate is very low even for the slow chemistry cases. For the slow-chemistry cases, the effective chemical reaction rate is only 12.25% and 8.19% of the imposed rate respectively with emission fluxes of Tracer A at 0.5 ppb m s^{-1} and 1.4 ppb m s^{-1}. For the fast-chemistry cases, the effective rate further drops to 3.04% and 2.26% respectively. This is because Tracer B is highly depleted in the boundary layer due to the high concentration of Tracer A. Tracer A and B are therefore highly segregated. Tracer B is only present near the top of the boundary layer, and this is where chemical reaction can take place (see Figure 3.32).

3.4 Heterogeneous emission

Chemical settings

The previous DNS simulations are further extended to heterogeneous surface emission of the two precursor Tracer A and B. Tracer A and B are emitted alternately both from the surface in a 2-km patch. Figure 3.33 shows a schematic diagram describing the simulation configuration. The emission fluxes adopted are doubled from the values adopted in the simulations with homogeneous emission in order to conserve the total fluxes. The same chemistry scheme (A+B $\rightarrow C$) and the same imposed chemical reaction rates k (refer to Table 3.2) are adopted as in the simulations with simple chemistry scheme. The simulation are run for 8 hours to capture the growth of the boundary layer from sunrise to the afternoon.

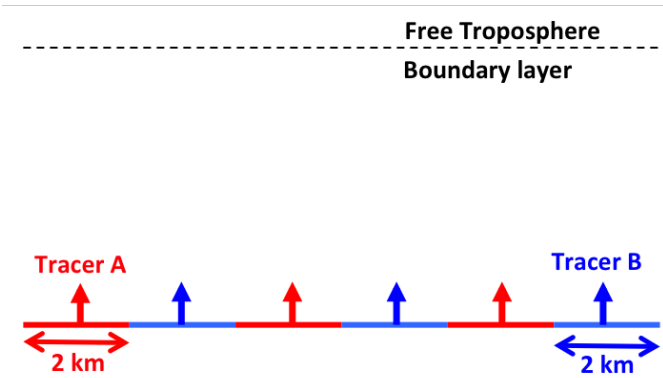

Figure 3.33: Schematic diagram for the configuration of the DNS simulations with heterogeneous surface emission of Tracer A and B.

Statistics

The time series of the volumetrically averaged mean and standard deviation of the mixing ratios of the tracers in the heterogeneous emission runs are shown in Figure 3.34. Only the statistics of Tracer A and C are shown here because the statistics of Tracer B follow similar trend as that of Tracer A. From the mean of the mixing ratio (left panels), Tracer A (and B) are depleting except in the very slow-chemistry (and no-chemistry) case. Note that the amount of Tracer C produced is only differed by around 10% between the fast- and very fast-chemistry cases at the end of the simulation, despite the difference in the imposed chemical reaction rate by a factor of 10. From the standard deviation (right panel), we can see that the system is approaching statistical equilibrium. The middle panels show the vertical profiles of the mixing ratio at the end of the simulations.

For Tracer A (and B), there is always a surplus in mixing ratio in the surface layer, as the tracer is emitted from the surface. The mixing ratio decreases with height, and the gradient of the mixing ratio increases with faster chemistry due to less efficient turbulent mixing. For Tracer C, there is always a surplus in the surface layer, and Tracer C starts accumulating in the boundary layer as the chemical reaction rate increases.

Figure 3.35 shows the vertical profiles of horizontally averaged mean and flux of the mixing ratio of Tracer A and C at the end of the simulation. Both the positive values of Tracer A and C show that both the reactants and the product are correlated to the updrifting air. The flux of Tracer A is always maximum at the top of the surface layer due to its surface emission. On the other hand, the location of the maximum flux of Tracer C decreases with faster chemistry due to the shortening chemical lifetime of the reactants.

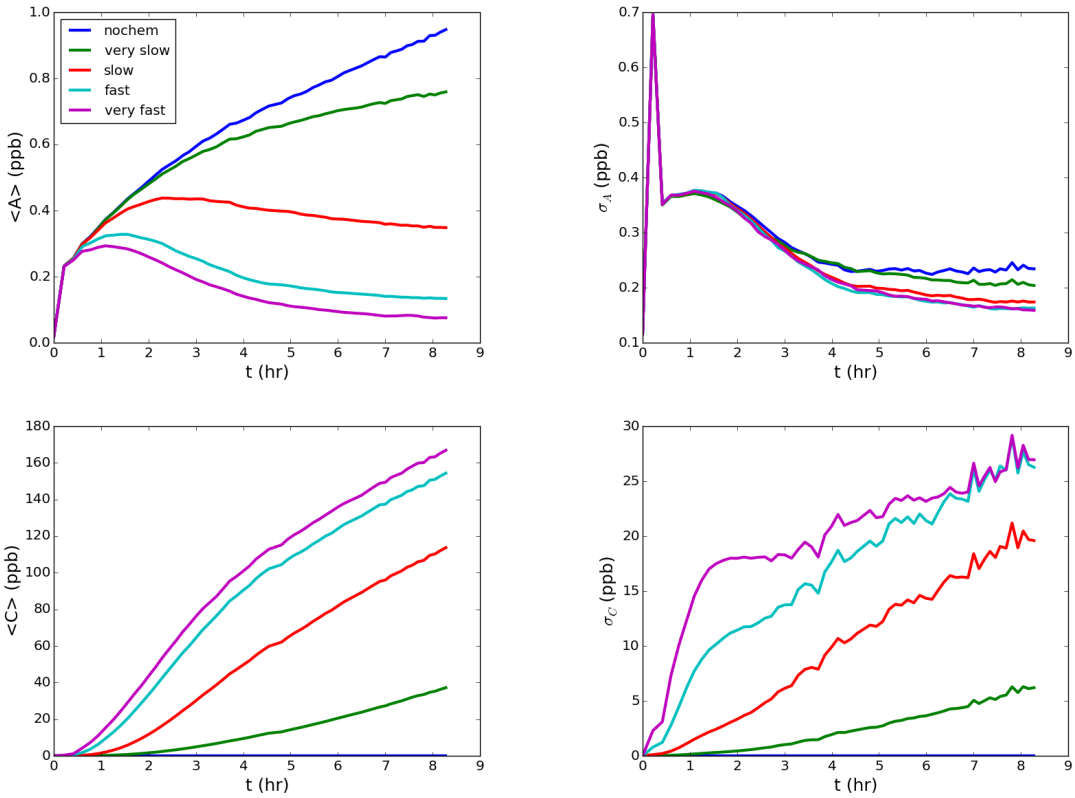

Figure 3.34: Evolution of volumetrically averaged mean (*left panel*) and standard deviation (*right panels*) of the mixing ratio of Tracer A (*top*) and C (*bottom*) with time, in the five chemistry cases.

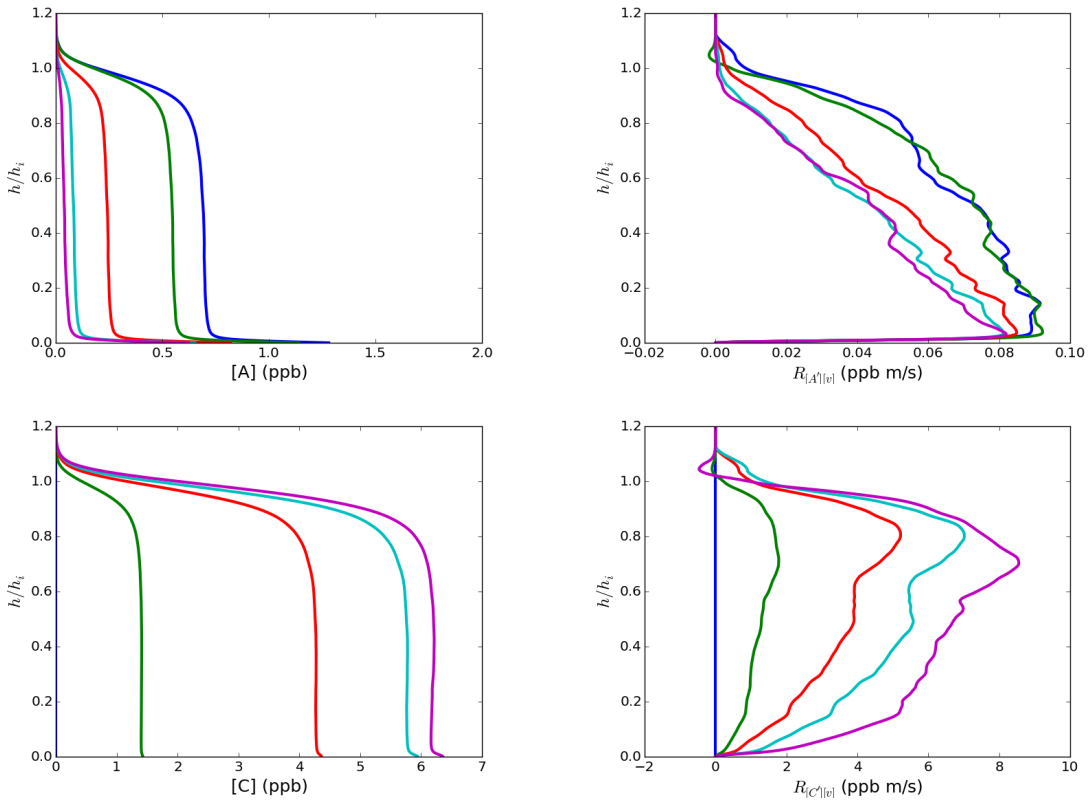

Figure 3.35: Vertical profiles of the variance of mixing ratio (*left panel*) and the covariance between the mixing ratio and the vertical velocity (*right panel*) of Tracer A (*top*) and C (*bottom*) at the end of the simulation with the 5 chemistry cases.

Segregation and effective chemical reaction rate

The effective chemical reaction rate k_{eff} is then calculated for the 4 chemistry cases. The evolution of the normalised effective chemical reaction rate k_{eff}/k is plotted in the left panel of Figure 3.36. One can see the actual chemical reaction rate is overestimated by a complete-mixing model by $\sim 25\%$ in the fast-chemistry case, and even by 75% in the very fast-chemistry case. On the other hand, the actual chemical reaction rate is underestimated when the chemistry is slow enough (for 2% in the very-slow chemistry case). The time-averaged values k_{eff}/k of the last 1.5 hour of the simulation are listed on the first column in Table 3.5. This can show that the effect of turbulent motion on chemical calculation is non-trivial when the surface emission is heterogeneous. The right panel of Figure 3.36 shows the vertical profile of the normalised height-dependent effective chemical reaction rate $k_{eff}(z)/k$ at the end of the simulation. One can see that the effective chemical reaction rate is minimum at the surface ranging from 0.0 in the very fast-chemistry case (does not mix at all) to 0.7 in the very slow-chemistry case. It is because the tracers are not allowed enough time to mix when they are just emitted from the surface. This means that if the model assumes the tracers to be completely mixed at

the first layer from the surface, it may have overestimated the reaction rate by as much as 100%. The effective chemical reaction rate increases with higher altitude. Except in the very fast chemistry case, the effective chemical reaction rate is even greater than the imposed rate at the region near the top of the boundary layer.

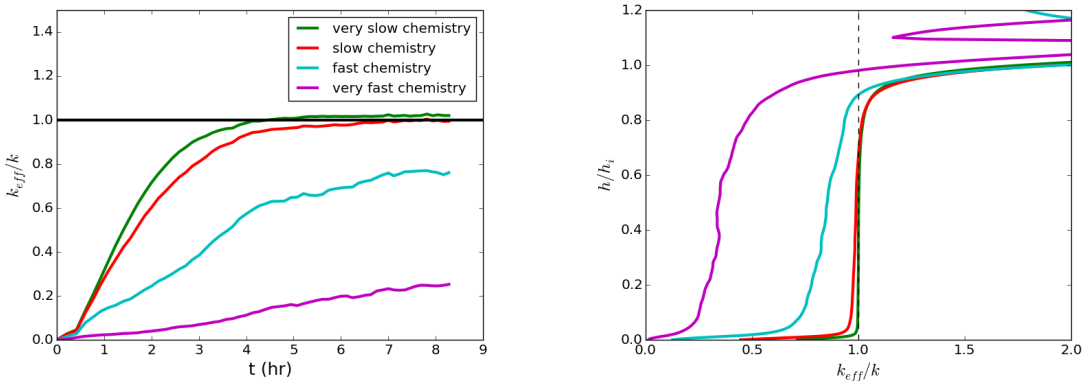

Figure 3.36: Vertical profile of the segregation coefficient $I_S(z)$ and the effective chemical reaction rate $k_{eff}(z)/k$ at the end of the simulation for the 4 cases with different chemical reaction rate k.

Model resolution degrading

The effect of model resolution degrading for the simulations with heterogeneous emission is then evaluated. The results of the 4 coarse-grid models are listed in Table 3.5. in the very slow- and slow-chemistry case, the effect of degrading model resolution is small, with the largest deviation from the DNS calculation of no more that 5%. However, it is worth noticing that in the very slow-chemistry case, some coarse-grid models underestimate the chemical reaction rate, instead of only overestimation in all the other DNS simulations. On the other hand, in the fast- and very fast-chemistry case, the effect of degrading model resolution is significant, with an overestimated rate of at least 10%. One can see that for models (i. e. the 3 km-horizontal resolution models) with resolution lower than the emission heterogeneity length scale (in this case it is 2 km), the coarse-grid model performs even worse than a complete-mixing model, indicated by an over-mixing of tracers with k_{eff}/k greater than 1. For example, in the very fast-chemistry case, the 3 km-125 m model overestimates the actual chemical reaction rate by 150%, while the complete-mixing model overestimates the rate by 75%. This is because the model grid fails to resolve the heterogeneity of the emission sources, and mixes the originally segregated tracers in the lower layers at a higher concentration than the complete-mixing model, which artificially mixes the tracers all over the whole boundary layer and dilutes the tracer concentration. The model with higher vertical resolution overestimates the reaction rate even more, as its first layers are thinner, and hence contain even higher concentration of the emitted tracers in the lower-level grids.

Cases	DNS	1 km-125 m	1 km-250 m	3 km-125 m	3 km-250 m
Very slow	1.0214	1.0168 (-0.46%)	1.0126 (-1.01%)	1.0250 (+0.36 %)	1.0195 (-0.19%)
Slow	0.9981	1.0041 (+0.60%)	0.9994 (+0.13%)	1.0601 (+6.20%)	1.0471 (+4.90%)
Fast	0.7640	0.8681 (+10.41%)	0.8663 (+10.23%)	1.2692 (+50.52%)	1.2092 (+44.52%)
Very fast	0.2425	0.5676 (+32.51%)	0.7777 (+53.52%)	1.7513 (+150.88%)	1.5808 (+133.83%)

Table 3.5: Normalised effective chemical reaction rate coefficient (k_{eff}/k) of models with different resolutions with the 4 chemistry cases with heterogeneous surface emission. The values in the brackets show the deviations of the coefficients from the coarser-grid models from the DNS simulation.

3.5 $NO-NO_2-O_3$ chemistry

Chemical settings

Our DNS simulations are then extended to a chemistry scheme involving nitrogen oxides (NO and NO_2) and ozone (O_3). This is a common chemical reaction involved in pollution episodes. The configuration of the simulations with the $NO-NO_2-O_3$ chemistry scheme follows similar physical settings as in our first set of DNS simulations. Nitrogen monoxide (NO) is emitted from the surface at a constant emission flux F_{NO} and ozone (O_3) is entrained from the free troposphere, in where the mixing ratio of ozone ($O_{3,0}$) is fixed at 40 ppb. Neumann boundary conditions are imposed at the boundaries on the mixing ratios of the species so that the surface flux of NO is constant at F_{NO}, and the surface fluxes of O_3 and NO_2 are zero. In the free troposphere, the mixing ratios of NO and NO_2 are zero, and the mixing ratio of O_3 is fixed constantly and homogeneously at $O_{3,0}$. The mixing ratio of O_3 is relaxed down the boundary layer to zero on the surface. Initial and boundary conditions of the simulation are listed in Table 3.6.

The simulation adopts the following chemistry scheme:

$$k\text{: } \mathrm{NO} + \mathrm{O_3} \longrightarrow \mathrm{NO_2} + \mathrm{O_2}$$
$$J_{NO_2}\text{: } \mathrm{NO_2} + h\nu \xrightarrow{+\mathrm{O_2}} \mathrm{NO} + \mathrm{O_3},$$

where the imposed chemical reaction rate is $k(T) = k_0 \exp[-T_{act}/T(K)]$ with $k_0 = 3.0 \times 10^{-12}$ cm^3 s^{-1} and $T_{act} = 1500$ K, and the photolysis rate of nitrogen dioxide (NO_2) is $J_{NO_2} = 0.798 \times 10^{-2}$ s^{-1}. The rate equations of O_3, NO and NO_2 are then non-dimensionalised following similar approaches as in the second-order chemistry scheme by introducing the characteristic scales for O_3 ($O_{3,0}$), NO ($NO_0 = F_{NO}U_0^{-1}$) and NO_2 ($NO_{2,0} = J_{NO_2}^{-1} k_0 NO_0 O_{3,0}$). With the normalised concentrations $c_{O_3} = \langle O_3 \rangle / O_{3,0}$, $c_{NO} =$

$\langle NO\rangle/NO_0$ and $c_{NO_2} = \langle NO_2\rangle/NO_{2,0}$, the rate equations are written as

$$\begin{aligned} L_0U_0^{-1}\frac{dc_{O_3}}{dt} &= -K_{O_3}\omega \\ L_0U_0^{-1}\frac{dc_{NO}}{dt} &= -K_{NO}\omega \\ L_0U_0^{-1}\frac{dc_{NO_2}}{dt} &= K_{NO_2}\left(\omega + \alpha_3 c_{NO_2}\right), \end{aligned}$$

where $\omega = c_{NO_2} - c_{O_3}c_{NO}\exp[-\alpha_1(1+\alpha_2 b/b_0)]$, and

$$\alpha_1 = T_{act}/T_0, \quad \alpha_2 = b_0/g, \quad \alpha_3 = k_1/J_{NO_2},$$

with $k_1 = 10^{-5}$ and the dimensionless rate constants are

$$K_{O_3} = L_0U_0^{-1}k_0NO_0, \quad K_{NO} = L_0U_0^{-1}k_0O_{3,0}, \quad K_{NO_2} = L_0U_0^{-1}J_{NO_2}.$$

O_3 and NO_2 are deposited at the surface level with constant deposition velocities w_{O_3} and w_{NO_2} of 0.3 and 0.2 cm s^{-1} respectively, based on common observed values. Therefore, relaxation terms are imposed near the surface for O_3 and NO_2:

$$\begin{aligned} \left.\frac{dc_{O_3}}{dt}\right|_{dep} &= -d_{O_3}c_{O_3} \\ \left.\frac{dc_{NO_2}}{dt}\right|_{dep} &= -d_{NO_2}c_{NO_2}, \end{aligned}$$

where

$$d_{O_3} = L_0U_0^{-1}w_{O_3}/h_{dep}, \quad d_{NO_2} = L_0U_0^{-1}w_{NO_2}/h_{dep},$$

and h_{dep} is the depth of the layer where the relaxation term is active, which are the bottom six vertical layers of the simulation domain, or 10 m equivalent to typical atmospheric conditions.

Five cases with different NO-fluxes (F_{NO}) are considered, at values of 10^{10}, 10^{11}, 10^{12}, 5×10^{12}, and 10^{13} molecules cm^{-2} s^{-1} respectively, equivalent to 0.004, 0.04, 0.4, 2.0 and 4.0 ppb m s^{-1}. The values are selected based on observations in areas ranged from rural to highly polluted environments (values adopted from Kim et al. (2016) and emission inventory at urban area regions in Pearl River Delta region from Hooyberghs et al. (2016)). Here we use the case with NO-flux of 10^{12} molecules cm^{-3} s^{-1} as a reference, and name the 5 scenarios with different NO-fluxes as 0.01F, 0.1F, 1F, 5F and 10F respectively from low to high NO emission fluxes.

Variables	Initial conditions
$\langle O \rangle_{3,0}$	40 ppb in PBL
F_{NO}	0.01-10 $\times 10^{12}$ molecules cm^{-2} s^{-1} at the surface
w_{O_3}	0.3 cm/s
w_{NO_2}	0.2 cm/s

Table 3.6: Initial and boundary conditions for the DNS simulation with the NO−NO_2−O_3 chemistry scheme, where $\langle O \rangle_{3,0}$ refers to the fixed mixing ratio of ozone in the free troposphere, F_{NO} is the emission flux of nitrogen monoxide at the surface (variable), w_{O_3} and w_{NO_2} are the deposition velocities of ozone and nitrogen dioxide on the surface, $L_X \times L_Y \times L_Z$ refers to the size of the simulation domain, and $N_X \times N_Y \times N_Z$ refer to the number of nodes used in the simulations.

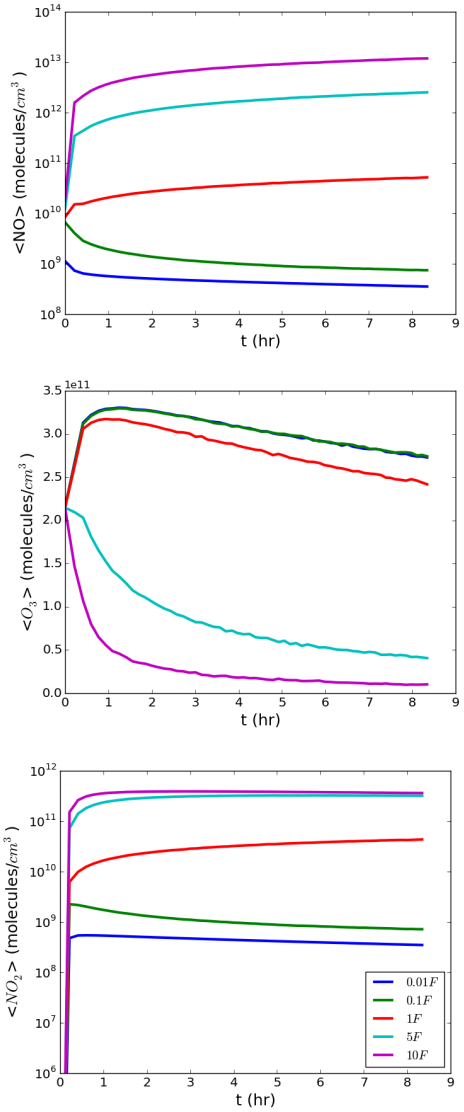

Figure 3.37: Evolution of volumetrically averaged mean of the number density of NO (*top*), O_3 (*middle*) and NO_2 (*bottom*) with time, in the five cases with different NO-emission fluxes.

Statistics

Figure 3.37 shows the time series of volumetrically averaged mean of the number density of NO (top panel), O_3 (middle panel) and NO_2 (bottom panel) in the boundary layer. In all the cases O_3 is consumed despite of the intensity of NO emission flux. NO is consumed for the 0.01 and 0.1F cases, where the emission fluxes are weak. Note that despite the emission flux of NO increases by a factor of 2 between the 5F and 10F cases, the amount of NO_2 produced in the two cases is not much different.

Figure 3.38 shows the vertical profiles of horizontally averaged mean of the number density (left panels) and the vertical fluxes (right panel) of NO (top panels), O_3 (middle panels) and NO_2 (bottom panels) at the end of the simulation. In most cases, all chemicals are vertically well-mixed in the boundary layer except in the surface layer, due to the emission of NO and the deposition of O_3 and NO_2 on the surface. In the 10F case, one can see that NO_2 is accumulated around the top of the boundary layer. This is because most of the NO_2 is produced around the top of the boundary layer, Due to its high emission flux, NO consumes most of the O_3 in the lower part of the boundary layer, and O_3 are replenished from the free troposphere just near the top of the boundary layer and an excess amount of NO_2 is formed. This can be illustrated by vertical profile of the production term of NO_2 ($k[NO \cdot O_3]$) in Figure 3.39, similar to the strong-emission cases. When the emission flux of NO is weak (the 0.01 and 0.1 cases), NO_2 is produced evenly in the boundary layer (except in the surface layer where O_3 is deposited). In the 1F case, there is a peak of NO_2 production just at the top of the surface layer due to the combined effect of the surface emission of NO and the deposition of O_3 in the surface layer. As the density of NO is low, it is consumed by O_3 once it is emitted from the surface layer. The chemistry is NO-limiting in this case. As the NO emission flux increases, the chemical lifetime of NO also increases, so that NO can flow all the way up and consume the O_3 in the boundary layer. Therefore, the location with maximum NO_2 production shifts from the top of the surface layer to the top of the boundary layer, where O_3 is entrained. The chemistry also shits to O_3-limiting with the increases NO emission flux.

The concentration of NO is highly correlated with the updraft of air in the boundary layer, except at the location near the top of the boundary layer where the updrifting air pushes the downdrifting air to bring air composed of only O_3 from the free troposphere. On the other hand, O_3 is highly correlated with the downdrifting air. The concentration of NO_2 is correlated with the updrafts when the emission flux of NO is low (in 0.01F, 0.1F and 1F cases), and is shifted to downdraft-correlated when the emission flux of NO is high. That is again due to the shift of the chemistry from NO-limiting to O_3-limiting.

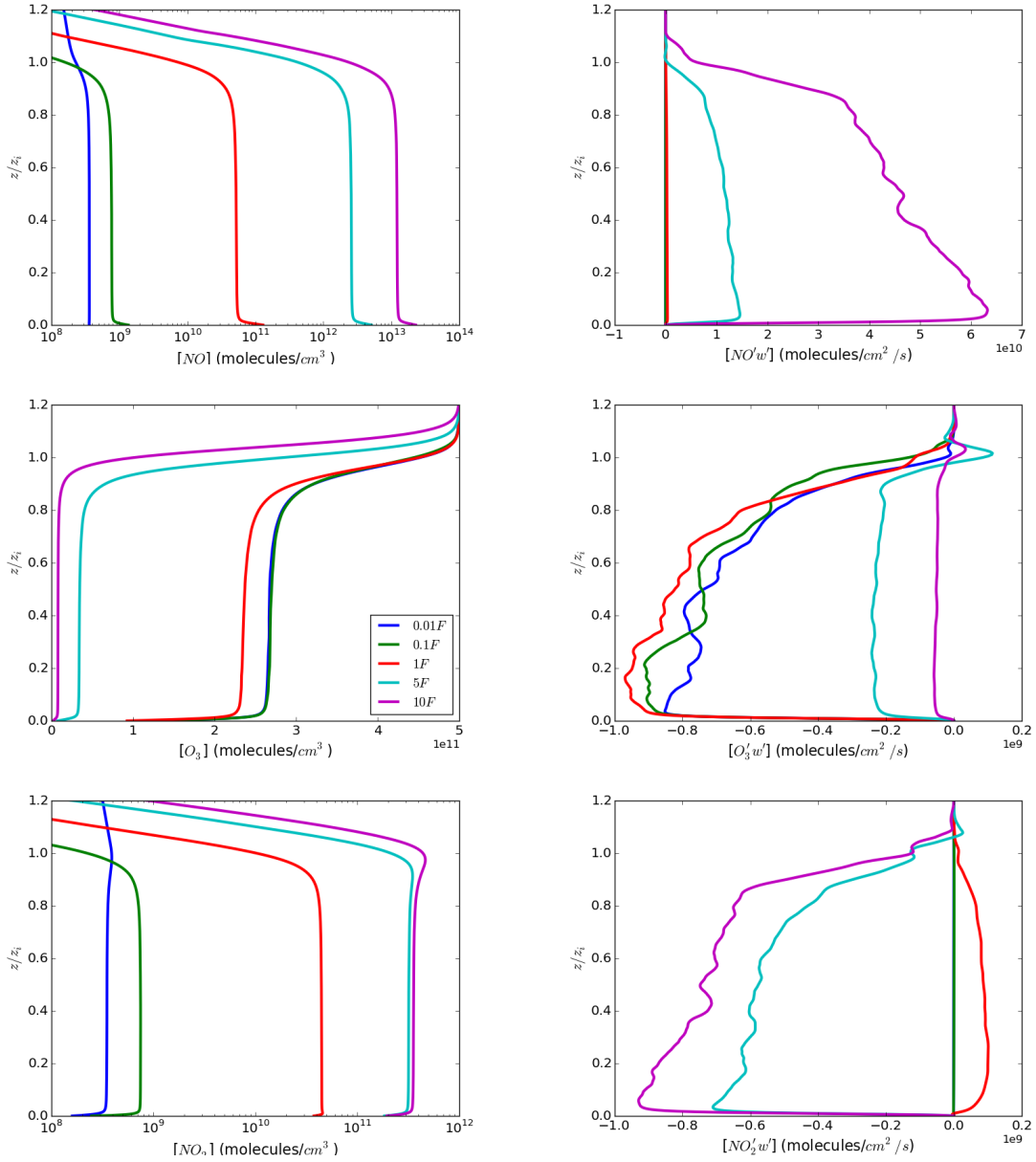

Figure 3.38: Vertical profiles of the horizontal mean of mixing ratio (*left panel*) and the covariance between the mixing ratio and the vertical velocity (*right panel*) of NO (*top*), O_3 (*middle*) and NO_2 (*bottom*) at the end of the simulation with the 5 cases with different NO-emission fluxes.

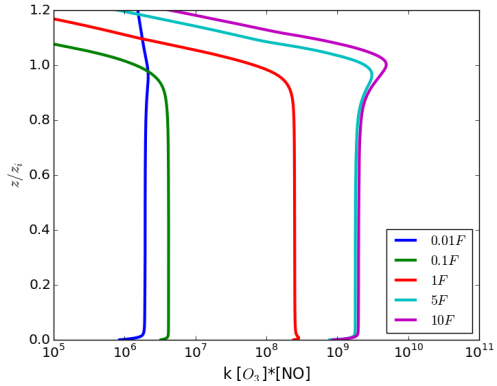

Figure 3.39: Vertical profile of the production term of NO_2 $k[NO \cdot O_3]$ at the end of the simulation for the 5 cases with different NO-emission fluxes.

Segregation and effective chemical reaction rate

Following Equation 1.23 and 1.24, the Damköhler numbers of O_3 and NO can be respectively expressed as:

$$Da_{O_3} = k\langle NO \rangle \left(\frac{z_i^2}{B_0} \right)^{\frac{1}{3}}$$

$$Da_{NO} = k\langle O_3 \rangle \left(\frac{z_i^2}{B_0} \right)^{\frac{1}{3}}.$$

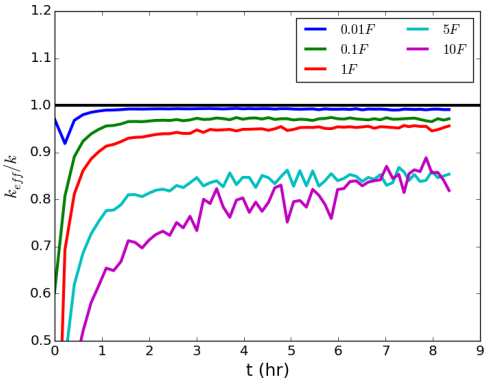

Figure 3.40: Evolution of the normalised effective chemical reaction rate k_{eff}/k with time for the 5 cases with different NO-emission fluxes.

We then evaluate the effective chemical reaction rate in the NO_x-O_3 cases. The evolution of the normalised effective chemical reaction rate (k_{eff}/k) of the 5 cases with different NO fluxes is plotted in Figure 3.40. We take the time-averaged value of the normalised effective chemical reaction rate over the last 1.5 hours in the simulation. In the 5 cases, the effective chemical reaction rate coefficient k_{eff} is 99.1%, 97.1%, 95.3%,

85.1% and 85.4% of the imposed chemical reaction rate k respectively from the lowest to the highest NO-fluxes. This implies that a complete-mixing model overestimates the reaction rate from 0.9% - 14.9%, depending on the NO emission flux F_{NO}. Note that the value of k_{eff}/k is almost the same for the 5F and 10 F cases.

Figure 3.41 shows the vertical profile of the normalised height-dependent effective chemical reaction rate $(k_{eff}(z)/k)$ at the end of the simulation. The effective chemical reaction rate is minimum just below the top of the boundary layer, similar as in the previous cases with the second-order chemistry scheme (refer to Figure 3.23). The effective chemical reaction rate is 98%, 83%, 82%, 49% and 44% of the imposed value from the lowest to the highest emission flux of NO. The deviation from the imposed value in the surface layer is smaller than the cases with the second-order chemistry scheme due to the deposition of O_3 on the surface.

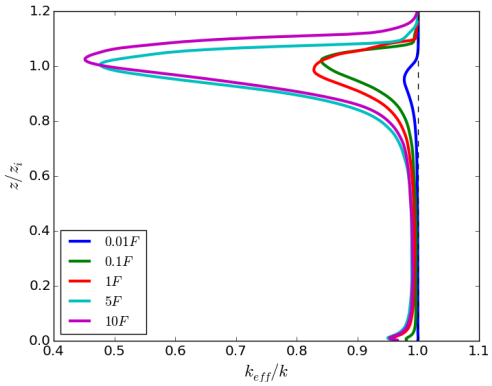

Figure 3.41: Vertical profile of the effective chemical reaction rate $k_{eff}(z)/k$ at the end of the simulation for the 5 cases with different NO-emission fluxes.

Model resolution degrading

These DNS simulations are then degraded into coarser-grid models following the same treatment as in the previous simulations. The resultant normalised effective chemical reaction rate k_{eff}/k is listed on Table 3.7. The values in brackets show the deviation in percentage of the calculated effective chemical reaction rate in the coarse-grid models from the DNS simulations. The influence of degrading the model on cases with low NO emission flux (0.01F, 0.1F and 1F cases) is generally small with an overestimation of actual chemical reaction rate of less than 3%. However, when the NO emission flux is high (the 5F and 10F cases), the influence is more significant, with the overestimation ranging from 5.7% to 12.7%.

F_{NO}	DNS	1 km-128 lev	1 km-64 lev	1 km-32 lev	3 km-128 lev	3 km-64 lev	3 km-32 lev
10^{10}	0.9914	0.9941 (+0.27%)	0.9956 (+0.42%)	0.9975 (+0.61%)	0.9967 (+0.53 %)	0.9976 (+0.62%)	0.9979 (+0.65%)
10^{11}	0.9701	0.9806 (+1.05%)	0.9852 (+1.51%)	0.9916 (+2.15%)	0.9872 (+1.71%)	0.9903 (+2.02%)	0.9936 (+2.35%)
10^{12}	0.9532	0.9677 (+1.45%)	0.9748 (+2.16%)	0.9858 (+3.26%)	0.9752 (+2.20%)	0.9804 (+2.72%)	0.9864 (+3.32%)
5×10^{12}	0.8507	0.9074 (+5.67%)	0.9367 (+8.60%)	0.9709 (+12.02%)	0.9394 (+8.87%)	0.9571 (+10.64%)	0.9854 (+13.47%)
10^{13}	0.8544	0.9192 (+6.48%)	0.9473 (+9.29%)	0.9771 (+12.27%)	0.9496 (+9.52%)	0.9655 (+11.11%)	0.9810 (+12.66%)

Table 3.7: Normalised effective chemical reaction rate coefficient (k_{eff}/k) of models with different resolutions with the 5 cases with different fluxes of NO (F_{NO} in molecules cm^{-2} s^{-1}. The values in the brackets show the deviation of the coefficients from the coarser-grid models from the DNS simulation.

3.6 Parametrisation of the effective chemical reaction rate

To explore the relations between the effective chemical reaction rate and other physical and chemical variables, the variables in all the simulations with the second-order chemical reaction in Section 3.3 and 3.4, together with the corresponding initial and final Damköhler numbers and the normalised effective chemical reaction rates are listed in Table 3.8. Here it is assumed that, since the Damköhler number of a tracer at a particular time actually involves information about the turbulent (the PBL height and the convective velocity) and the chemical properties (imposed reaction rate and the concentration of the other reacting tracer), the corresponding Damköhler number reflects the instantaneous state of turbulence and chemical reaction respectively, and therefore indicates their effects on the instantaneous effective chemical reaction rate. With that assumption, one can speculate that the effective chemical reaction rate is in fact related to the final Damköhler numbers, and significantly deviates from the imposed rate when (1) the Damköhler number of the limiting reactant (the reactant which is depleting) is approaching or greater than 1; (2) when the ratio between the final Damköhler numbers of the two tracers is particularly small or large (which indicates either Tracer A or B is depleting). This conclusion is consistent with what is reported in other studies (e. g. de Arellano et al. (2004)). However, here we propose that the determining variable should be the Damköhler number of the *limiting* reactant, instead of only the Damköhler number of the emitting reactant (Tracer A), in order to take the shift of chemical regime from Tracer A-limiting to Tracer B-limiting into account. This is newly found owing to our extension of exploration of the problem to cases with strong emissions. Therefore, it is speculated that the normalised effective chemical reaction rate (k_{eff}/k) is a function of the final Damköhler number of the limiting reactant (Da_{lim}) and the ratio of the final Damköhler numbers of the two reactants ($r_{Da} = Da_{A,f}/Da_{B,f}$).

To simplify the problem, the relation of the effective chemical reaction rate with Da_{lim} is first explored with the results of the simulations with heterogeneous emissions in Section 3.4. Since the boundary conditions of Tracer A and B are symmetrical, the statistics of Tracer A and B are similar, so that $Da_A \sim Da_B$ and r_{Da} is roughly equal to 1.

Therefore, for the cases with heterogeneous emission, k_{eff}/k is related to the geometric mean of the final Damköhler numbers of A and B ($\tilde{Da_f} = \sqrt{Da_{A,f}^2 + Da_{B,f}^2}$). The results from the best fit is plotted in Figure 3.42. From the best fit, $k_{eff}/k = exp[-0.5\tilde{Da_f}]$, indicating that k_{eff}/k follows an exponential distribution with Da_{lim}.

Homogeneous								
$\langle A_0 \rangle$ (ppb)	$\langle B_0 \rangle$ (ppb)	$F_{buoy,0}$	k	$Da_{A,i}$	$Da_{B,i}$	$Da_{A,f}$	$Da_{B,f}$	k_{eff}/k
0.071	2	1	0.01	0.0124	0.0010	0.0743	0.0177	0.9870
0.071	2	1	0.1	0.1438	0.0094	0.6051	0.0405	0.9652
0.071	2	1	1.0	1.4377	0.0938	5.7148	0.0688	0.8687
0.071	2	1	10.0	12.3520	1.0267	56.7361	0.1200	0.6492
0.071	2	0.5	0.1	0.1531	0.0100	0.3798	0.0558	0.9520
0.071	2	0.5	1.0	1.5306	0.0999	3.3438	0.1036	0.7989
2	2	1	0.1	0.1531	0.0560	0.0002	99.7068	0.0819
2	2	1	1.0	1.5306	0.5602	4.8058×10^{-5}	997.0659	0.0226
0.71	2	1	0.1	0.1531	0.0214	0.0028	29.8211	0.1225
0.71	2	1	1.0	1.5306	0.2142	0.0033	298.1865	0.0304
Heterogeneous								
0.071*2	0.071*2	1	0.01	0.0002	0.0002	0.0319	0.0318	1.0204
0.071*2	0.071*2	1	0.1	0.0024	0.0024	0.1496	0.1488	0.9952
0.071*2	0.071*2	1	1.0	0.0241	0.0241	0.5665	0.5578	0.7634
0.071*2	0.071*2	1	10.0	0.2406	0.2406	3.2605	3.1573	0.2522
0.71*2	0.71*2	1	0.1	0.0069	0.0069	1.9960	2.0482	0.3068
0.71*2	0.71*2	1	1.0	0.0686	0.0686	15.9511	16.4730	0.0487
2*2	2*2	1	0.1	0.0121	0.0121	3.1373	3.2651	0.2109
2*2	2*2	1	1.0	0.1211	0.1211	26.9289	28.2074	0.0285

Table 3.8: The initial conditions (characteristic concentrations$\langle A_0 \rangle$ and $\langle B_0 \rangle$, normalised buoyancy flux $F_{buoy,0}$, chemical reaction rate (imposed) k), the initial Damköhler numbers $Da_{A,i}$ and $Da_{B,i}$, and final Damköhler numbers $Da_{A,f}$ and $Da_{B,f}$ with the resultant normalised effective chemical reaction rate k_{eff}/k in the DNS simulations with the second-order chemistry scheme with homogeneous emission and heterogeneous emissions.

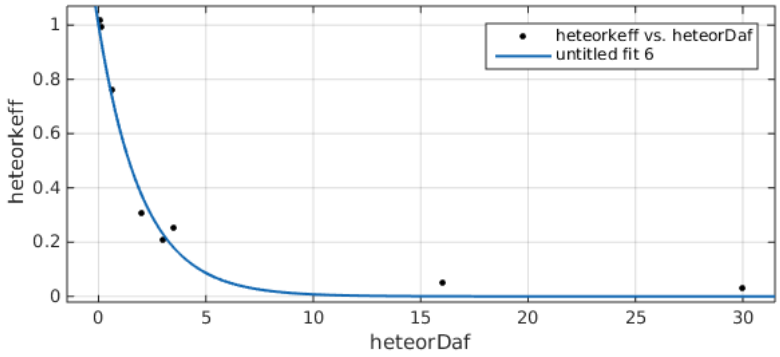

Figure 3.42: Fit with heterogeneous emission of the normalised effective chemical reaction rate against the geometric mean of the final Damköhler numbers $\tilde{Da_f}$. The function is $k_{eff}/k = exp[-0.5\tilde{Da_f}]$. The sum of squares due to error (SSE) is 0.0150. The R-square is 0.9873. The root mean squared error (RMSE) is 0.0463.

The next step is to explore the relation between k_{eff}/k and r_{Da}. Four data points with similar values of $\tilde{Da_f}$ ($\sim$ 0.15) are selected to derive k_{eff}/k as a function of r_{Da}, of which the result is plotted in the Figure 3.43. From the best fit, $k_{eff}/k = 0.9943exp[-((\log r_{Da} - 0.3367)/3.812)^2]$, indicating that k_{eff}/k follows a gaussian distribution with the logarithmic of r_{Da} ($\log r_{Da}$).

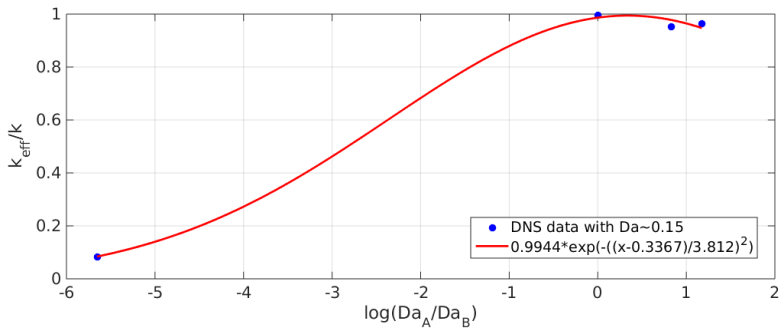

Figure 3.43: Fit with homogeneous emission of the normalised effective chemical reaction rate against $\log r_{Da}$ with similar $\tilde{Da_f}$. The function is $k_{eff}/k = 0.9943exp[-((\log r_{Da} - 0.3367)/3.812)^2]$. The SSE is 0.00149. The R-square is 0.9982 and the adjusted R-square is 0.9947. The RMSE is 0.03239.

The data from the cases with homogeneous emission are then fitted as a product of a Gaussian function of $\log r_{Da}$ and an exponential function of Da_{lim}. The result from the best fit is plotted in the Figure 3.44. From the best fit, $k_{eff}/k = 0.961 \exp[-((\log r_{Da} - 0.6268)/3.356)^2] \cdot \exp(-0.00055 Da_{lim})$.

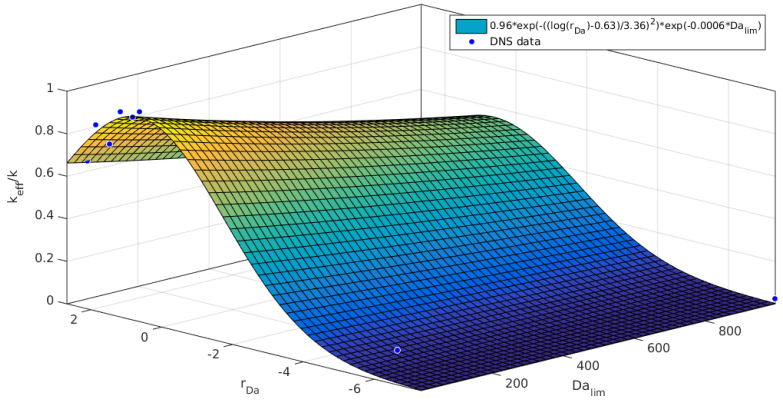

Figure 3.44: Fit with homogeneous emission of the normalised effective chemical reaction rate against the final Da ratio and the final Da_{lim}. The function is $k_{eff}/k = 0.961exp[-((\log r_{Da} - 0.6268)/3.356)^2] \cdot exp(-0.00055 Da_{lim})$. The SSE is 0.0168. The R-square is 0.9898 and the adjusted R-square is 0.9847. The RMSE is 0.0530.

From the relations obtained from the cases with the second-order chemical reaction, it is learnt that k_{eff}/k follows a Gaussian relation with $\log r_{Da}$ and an exponential

relation with Da_{lim}:

$$\frac{k_{eff}}{k} \propto \exp\left[-\left(\frac{\log r_{Da}+b}{c}\right)^2\right] \cdot \exp\left(dDa_{lim}\right),$$

where b, c, d are some fitting coefficients. It is known from the Taylor expansion that, when $[(\log r_{Da}+b)/c]^2 \ll 1$,

$$\exp\left[-\frac{(\log r_{Da}+b)^2}{c^2}\right] \approx 1-\left(\frac{\log r_{Da}+b}{c}\right)^2,$$

and when $Da_{lim} \ll 1$,

$$\exp(dDa_{lim}) \approx 1 - dDa_{lim}.$$

Therefore,

$$\begin{aligned}\exp\left[-\frac{(\log r_{Da}+b)^2}{c^2}\right] \cdot \exp(dDa_{lim}) &\approx 1-\left(\frac{\log r_{Da}+b}{c}\right)^2 \cdot dDa_{lim} \\ &\approx 1-\alpha(\log r_{Da}+b)^2 \cdot Da_{lim},\end{aligned}$$

where α is another fitting coefficient that $\alpha = d/c^2$. From this, one can write a correction factor F_{eff} to the chemical reaction rate from k_{eff}/k, such that

$$F_{eff} = 1 - \frac{k_{eff}}{k} \propto \alpha(\log r_{Da}+b)^2 \cdot Da_{lim}. \tag{3.7}$$

The parameter α is also named the impact factor from now as it indicates how significant Equation 3.7 is. With these, the analysis with the least-square fitting method is now extended to the cases with NO_X-O_3 chemistry. The related physical and chemical variables and parameters are listed in Table 3.9. In the cases with NO_X-O_3 chemistry, the final Damköhler number of O_3 (Da_{O_3}), the limiting species when $F_{NO} \geq 0.4$ ppb m s^{-1}) and the ratio between the Damköhler numbers of NO and O_3 ($r_{Da} = Da_{NO,f}/Da_{O3,f}$) are considered in the fitting. The best fit of F_{eff} against Da_{O3} and $\log r_{Da}$ with the function in Equation 3.7 is $F_{eff} = 0.004331(\log r_{Da}+2.637)^2 \cdot Da_{O_3}$ (shown in Figure 3.45). Therefore, the effective chemical reaction rate is given as

$$k_{eff}/k = 1 - 0.004331(\log r_{Da}+2.637)^2 \cdot Da_{O_3}. \tag{3.8}$$

F_{NO} (ppb m s^{-1})	$Da_{NO,i}$	$Da_{O3,i}$	$Da_{NO,f}$	$Da_{O3,f}$	k_{eff}/k
0.004	1.1591	0.0061	4.9676	0.0065	0.9914
0.04	1.1591	0.0360	4.9898	0.0137	0.9701
0.4	1.1591	0.0455	4.4408	0.8885	0.9554
2.0	1.1591	0.0662	0.7824	43.0598	0.8507
4.0	1.1591	0.0974	0.1858	204.9693	0.8544

Table 3.9: The initial conditions (NO emission flux F_{NO}), the initial Damköhler numbers$Da_{NO,i}$ and $Da_{O3,i}$, and final Damköhler numbers $Da_{NO,f}$ and $Da_{O3,f}$ with the normalised effective chemical reaction rate k_{eff}/k in the DNS simulations with the $NO-NO_2-O_3$ chemistry scheme.

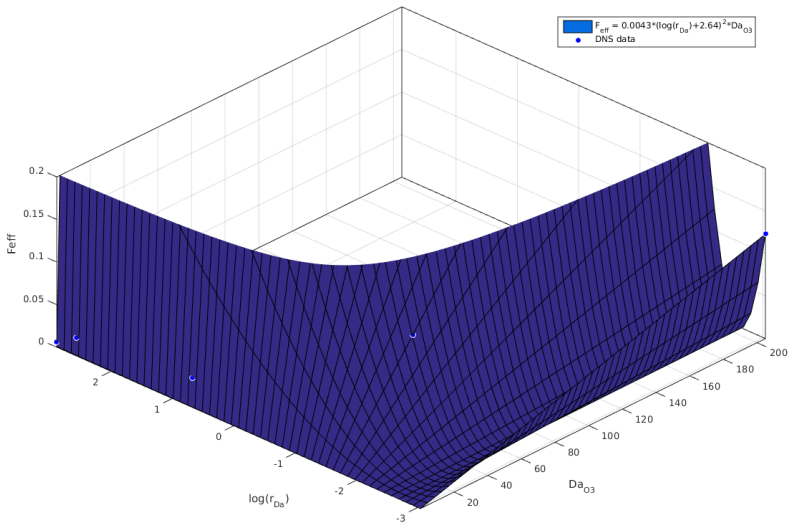

Figure 3.45: Fit with ozone chemistry of the normalised effective chemical reaction rate (k_{eff}/k) against Da_{O_3} and $\log r_{Da}$. The best-fit function is $F_{eff} = 0.004331(\log r_{Da} + 2.637)^2 \cdot Da_{O_3}$. The SSE is 0.0008643. The R-square is 0.9516 and the adjusted R-square is 0.9355. The RMSE is 0.01697.

Based on the results with the degraded model resolution, Equation 3.7 is fitted along with the results for the 1 km-32 lev model (refer to the bracketed values on the fifth column on Table 3.7). At that resolution, the fit gives a $\alpha = 0.003552$ (shown on Figure 3.46, and hence the effective chemical reaction rate is given as $k_{eff}/k = 1 - 0.003552(\log r_{Da} + 2.637)^2 \cdot Da_{O_3}$. Note that the lower value of α at the resolution of 1 km is due to the compensation from its higher resolving power.

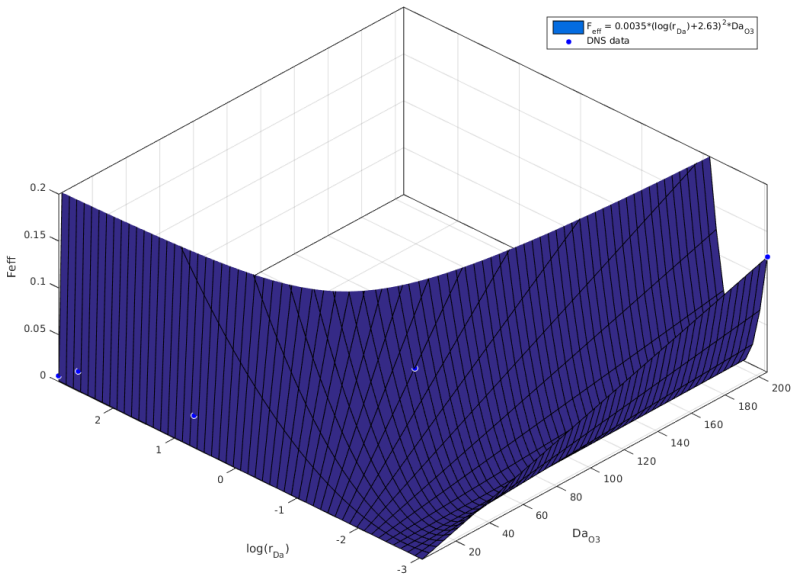

Figure 3.46: Fit with ozone chemistry of the normalised effective chemical reaction rate (k_{eff}/k) against Da_{O_3} and $\log r_{Da}$ for the 1 km-32 lev resolution-degraded model. The best-fit function is $F_{eff} = 0.003522(\log r_{Da} + 2.637)^2 \cdot Da_{\mathrm{O}_3}$. The SSE is 0.0004395 The R-square is 0.9653 and the adjusted R-square is 0.9653. The RMSE is 0.01048.

3.7 Conclusions and Discussion

To investigate the relations between turbulent motions and chemical reactions in an urban convective boundary layer, direct numerical simulations (DNS) are conducted with two initially-segregated reactive chemical species, with extension to cases with strong emission fluxes and heterogeneous emissions. The Damköhler number (Da), that is the ratio between the chemical and turbulent timescale, is used to classified the regime in which turbulence significantly affects the chemical reaction rate. Turbulence fails to mix the chemicals well in the boundary layer when the chemical reaction rate is fast or when the emission flux of the chemical is strong (which can be characterised with $Da \geq 1$). The effective chemical reaction rate (k_{eff}), which represents the actual reaction rate at which the species reacts in the turbulent flow, is used to quantify the impact of turbulence on chemical reaction. With tracer advection simulations with a homogeneous turbulent field, it can illustrate that both the tracer segregation and production in the turbulent-resolved model significantly differ from the averaged-values calculated in a single grid box in a large-scale model.

The DNS simulation is first configured with two reactive chemical species, one surface-emitted species at constant emission rate (Tracer A) and another species entrained from the free troposphere (Tracer B), reacting in a second-order chemical scheme

to form a product (Tracer C) (A+B $\longrightarrow$ C). Cases with 4 different values of reaction rate constants are simulated, in which two of them are in the slow-chemistry regime ($Da < 1$) and two are in the fast-chemistry regime ($Da > 1$). The simulations are terminated after $\sim$4.5 hours when statistical equilibrium is reached. When the effective chemical reaction rates of these cases are computed, it is revealed that a complete-mixing model, which assumes the species to be homogeneously distributed in the boundary layer, overestimates the actual reaction rate by 15% with initial $Da \sim 1$ and by $\sim$ 35% with initial $Da \sim 10$. This overestimation is induced by the segregation of the reactants due to inefficient turbulent mixing. The overestimation is most significant just below the top of the boundary layer, which varies between 8% and 45 %, increasing with the imposed reaction rate.

The DNS results are then degraded into coarser resolution with two horizontal resolutions (equivalent to 1 and 3 km respectively) and three vertical resolutions (containing 10, 20 and 40 levels in the boundary layer respectively) to mimic the calculations in a regional chemical-transport model (CTM). In the fast-chemistry regime, such model improves significantly when the horizontal resolution increases from $\sim$12 km to 3 km by reducing the overestimation of the effective chemical reaction rate from 15-35% to 4-22%. However, the improvement is less significant when the horizontal resolution increases from 3 km to 1 km, as at both resolutions the overestimation lies in the range of 4-13%. The improvement is more significant with increasing vertical resolutions. All coarse-grid models give a smoother vertical profile of the horizontally averaged effective reaction rate with no local minimum at the top of the surface layer and less prominent minimum in the entrainment zone, as the two zones are particularly sensitive to model resolution.

The experiment continues with strong fluxes of the surface-emitted species at 0.5 ppb m s^{-1} and 1.4 ppb m s^{-1}. The reaction between Tracer A and B transits from Tracer A-limiting to Tracer B-limiting condition. The corresponding effective chemical reaction rate drops dramatically to only less than 3% of the imposed rate in the fast-chemistry regime, and to 8-12% of the imposed rate even in an initially slow-chemistry regime. The depletion of Tracer B results in a very large segregation between Tracer A and B, and therefore only limited amount of Tracer A can react with Tracer B, mostly below the top of the boundary layer. It is later found out that, the transition of chemistry regime for Tracer A-limiting to Tracer B-limiting makes the effective reaction rate to be closer related to the Damköhler number of Tracer B, contrary to previous studies which always relate the effective reaction rate to the Damköhler number of Tracer A (e. g. de Arellano et al. (2015)[5]).

The investigation is then extended to heterogeneous emission of two species emitted

[5]Many of these studies only refer *Da* as the Damköhler number of Tracer A and seldom mention the Damköhler number of Tracer B.

from the surface at alternate strips with a width of 2 km. In the fast-chemistry regime, the effective reaction rate is 75% of the imposed value for $Da \sim 0.6$ and only 25% for $Da \sim 3.0$. The effective reaction rate is minimum at the surface and maximum at the top of the boundary layer. When degrading the model resolution, some coarse-grid models underestimate the actual reaction rate when the chemistry is very slow, in contrary to the cases with homogeneous emission, that the actual rate is always overestimated. In the fast-chemistry regime, the effect of degrading model resolution is significant, with an overestimated rate of at least 10%. For the coarse-grid model with resolution lower than the emission heterogeneity length scale (in this case the width of the alternate strips, i. e. 2 km), the coarse-grid model can even perform worse than a completely mixing model. As the vertical resolution increases, the model overestimation also becomes larger. This is because the model grid fails to resolve the separation of the emission sources of the two species, which leads to the premixing of the reactants within the same model grid at a higher concentration than in a lower-resolution model.

Following the simulations with the second-order chemistry scheme, a simulation with a chemical reaction involving nitrogen oxides and ozone is conducted. Nitrogen monoxide (NO) is uniformly emitted from the surface at 5 different emission fluxes, ranging from rural to highly-polluted environment (0.004 - 4.0 ppb m s^{-1}), while ozone (O_3) is entrained from the free troposphere at a fixed background value of 40 ppb. At low NO emission flux (< 0.4 ppb m s^{-1}), the overestimation is insignificant (within 5%). However, at the high emission fluxes (≥ 2 ppb m s^{-1}), the overestimation can reach 15%. Despite the emission fluxes in the case with the largest flux (4 ppb m s^{-1}) is 2 times larger than the the second-largest case (2 ppb m s^{-1}), their overestimation is similar. The overestimation is most significant again at the top of the boundary layer, and is larger than 50% when the emission flux reached 2 ppb m s^{-1}. Degrading the model resolution causes the models to overestimate the reaction rate by 6-13%.

At last, the parametrisation on the effective chemical reaction rate is formulated to represent the relation between turbulence and chemical reaction in the boundary layer based on the physical and chemical variables of the DNS runs. One can see that the effective reaction rate is significantly deviated from the imposed value when (1) the Damköhler number of the limiting reactant (Da_{lim}) is approaching or greater than 1, and/or (2) when the ratio between the Damköhler numbers of the two reactants (r_{Da}) is partially small/large. From these, it is speculated that the normalised effective reaction rate is a function of Da_{lim} and r_{Da}. The normalised effective reaction rate is derived empirically, which is found to be following an exponential relation with Da_{lim} and a Gaussian relation with $\log r_{Da}$. A formulation for the cases with NO_X-O_3 chemistry is specifically expressed as a function of the Damköhler numbers of O_3 (as the chemistry is O_3-limiting when the NO flux is larger than 0.4 ppb m s^{-1}), and the ratio between the NO and O_3 concentrations, and will be implemented int the WRF-Chem model of

Chapter 2 in the next chapter.

The DNS simulations conducted in this chapter only represent some idealistic atmospheric conditions due to computational limitations. First of all, the growth of the boundary layer is driven by a constant buoyancy flux, so that the boundary layer height gradually increases. Hence the simulation can only approximate the time when the PBL grows from sunrise to mid-afternoon (see Figure 1.2). This also raises the issue of the time it is required for statistical equilibrium to attain. In some cases, it may be possible that in some scenarios the statistical equilibrium can be attained in a turbulent environment if time is long enough. However, this duration may be longer than the duration of daylight, after which the atmosphere is no longer convective (such that the DNS condition also violates). This poses a greater problem to cases with strong emission fluxes, as the time required to attain statistical equilibrium is particularly long. Thus, it may not be practically to run more than the duration of daylight (say 9 hours) even though statistical equilibrium is not reached at some cases. Moreover, the simulations only address a convective boundary layer under clear-sky conditions. It cannot take into account of with different weather conditions (such as cloud-top boundary layer) or when the atmosphere is stably stratified (typical for nighttime conditions). The simulations also does not include any mean horizontal winds, or other forcings from the surface (such as surface roughness) other than the constant buoyancy flux. Therefore, the DNS simulation may be more valuable in addressing the vertical mixing caused by the turbulent motions the mixed layer relatively far away from surface features that may induce surface roughness and other additional forcings.

In simulations with strong emission fluxes, the entrained tracer starts depleting, both in the second-order and $NO-NO_2-O_3$ chemistry. In these cases, the segregation between the two reacting species is mainly caused by the depletion of one of these species. Despite the large deviation of the effective reaction rate from the imposed rate in those cases, the actual effect on the production term may not be as large as anticipated, as the concentration of the depleting species is particularly low, leading to an initially small production term. In most of the studies including ours, only the fluxes of the emitted tracers or the chemical reaction rate constant are varied. The boundary conditions of the entrained tracers are often kept constant. In principle, the determining factor is the ratio between the two reacting species (Schumann 1989; de Arellano et al. 2004), so it may not be necessary to change the boundary conditions of the entrained tracer. However, in reality, the boundary conditions of the entrained tracers may change, both in the entrainment flux (due to weather conditions (e. g. Albrecht et al. (2016)) and concentration in the free troposphere (transport from longer range (e. g Zyryanov et al. (2012)). It may be useful to also change the boundary conditions of the entrained tracers in future experiments.

In simulations with heterogeneous emissions, the only emission configuration considered is with horizontal strips with uniform width of 2 metres. However, it is also known that other factors may also affect the significance of heterogeneous emission on the segregation of the reacting species. Ouwersloot et al. (2011) has already addressed that the segregation is also affected by the length scale of heterogeneity (the width of the strips). Another common emission configuration is point sources. Karamchandani et al. (2000) studied the dispersion of reacting plume using a plume model and suggested that the segregation should be correlated to some physical variables such as the downwind distance from the point source. Future studies may also take these characteristics from the emission configurations into account.

Another important factor affecting the chemistry in the boundary layer in urban environments is undoubtedly the urban structures (buildings and streets in the urban canopy). The structure of turbulent flow can be significantly altered in the street canyons due to the exchange of heat fluxes and momentum with the urban structures (Oke 1997). Therefore, such turbulent flow within the urban canopy can be extremely complicated, and our DNS model is unfortunately incapable of addressing the effect under such environments. Therefore, our simulations are more suitable for addressing the scenarios in the mixed layer above the urban canopy. But in the mixed layer, the urban canopy still potentially affects the chemistry and dynamics in the boundary layer by means of surface roughness and emission heterogeneity. Auger and Legras (2007) addressed this issue by considering different configurations of emissions, and showed that the segregation also depends on the average size of gaps between the emission region. DNS may not be a suitable tool to account for such effect from an urban environment due to its difficulty to alter boundary conditions. One may need to use LES or CFD to study the atmospheric chemistry in turbulent flows in an extended urban canopy.

The formulation presented in Section 3.6 only depends on the Damköhler numbers, with the assumption that the instantaneous Damköhler numbers are adequate to provide information on both the turbulent and chemical state at a given time. However, this assumption may not be true, and other work suggest that the parametrisation should also include other variables such as updraft/downdraft fluxes (Petersen and Holtslag 1999), variance of the reacting species, entrainment/emission fluxes (Petersen and Holtslag 1999; Vinuesa and de Arellano 2003), turbulent fluxes (Dlugi et al. 2014), variance of the emission (Galmarini et al. 1997), magnitude and direction of mean horizontal wind, length scale of heterogeneity (Ouwersloot et al. 2011) and distance from the sources (Karamchandani et al. 2000). Also, it is clear from the study with degrading model resolution that the formulation is also a function of model resolution if implemented into a large-scale chemical transport models. Further studies on such parametrisation may take these factors into account. Lenschow et al. (2016b) also developed a one-dimension second-order closure model to account for the vertical turbulent mixing of

chemical species ready to be incorporated into larger-scale models. Despite the presence of a number of parametrisations or tools to account for the effect of turbulent mixing on chemical reaction in the boundary layer, none of them has actually been applied in a CTM. It may be more advantageous to first apply a simpler parametrisation scheme to a CTM to estimate its effect on model calculation.

At last, the overall subject highly relies on the work from modelling, but the observations for validation is comparatively inadequate. Some related work on observations address the issue of surface and boundary layer exchange of chemical species (Ganzeveld et al. 2008; Vilà-Guerau de Arellano et al. 2009) and turbulent dispersion of inert chemical species (Dinger et al. 2018). Dlugi et al. (2010) is perhaps the most comprehensive study using field campaign data to infer the turbulent exchange and segregation of HO_X radicals and biogenic VOCs in a forest. However, these studies are all conducted in rural areas, focusing on the isoprene and the HO_X radicals. One of the main reasons to conduct measurement in rural conditions because most studies assumes that the segregation between isoprene and OH are most prominent due to the short chemical lifetime of OH. For example, Dlugi et al. (2010) inferred a segregation of maximum 15% between isoprene and OH in its field campaign. however, from our study it has been learnt that the segregation between NO and O_3 may also reach a comparable level when the emission flux of NO is high, which is more commonly found in urban areas. In urban areas, the observations are available mainly on the turbulent profiles in the urban boundary layer (Barlow et al. 2010). Observations addressing the effect of turbulent mixing on chemical segregation are scarce, and hence potentially useful. Such observation is anticipated to be challenging as higher temporal resolution is necessary for the measurements in the urban area than in the rural areas due to the complicated and uneasily controlled environment in urban areas.

Chapter 4

Bridging chemical calculations in the turbulence-resolved scale into a regional chemical transport model: Application to an urban area

4.1 Introduction

From Chapter 2, we have learnt that increasing model resolution changes the calculation of chemical reactions in aspects of pollutant distributions, ozone production rates, and the segregation between ozone and its precursors. The effect is potentially amplified in urban areas due to the localised and intense emission sources. However, the difference in the statistics of the model results become not significant as the model resolution increases from 3 km to 1 km. One possible reason is speculated to be the misrepresentation of subgrid-scale processes. One example of this is the failure to resolve turbulent motions in the boundary layer which may mix the chemicals inefficiently and hence affect the actual reaction rate.

Therefore in Chapter 3, direct numerical simulations are employed to explicitly resolve turbulent motions in a convective boundary layer. The results show that the inability of a complete-mixing model to resolve the segregation of reactants due to inefficient turbulent mixing can cause an overestimation of 15-35% on the actual reaction rate for a second-order chemistry scheme in a fast chemistry regime (with Damköhler number greater than 1). The effect is even more significant in cases with strong emission fluxes and heterogeneous emissions, which are common conditions in an urban environment. A simulation with $NO-NO_2-O_3$ chemistry is also conducted and a $\sim 15\%$ reduction in the actual reaction rate is found when the NO_X emission is strong. The effective chemical reaction rate (k_{eff}) is adopted to quantify the deviation between the actual

and imposed reaction rate due to the segregation of reactants in the boundary layer, and is parametrised as a function of the Damköhler numbers and the concentration ratios of the reactants. In this chapter, the formulation derived based on the DNS results with the NO_X-O_3 chemistry in Section 3.6 will be implemented into the WRF-Chem model in Chapter 2 as an attempt to estimate its significance and feasibility in its implementation in an operational regional chemical-transport model. Its impact on the model calculations will then be examined with comparison with the results in Chapter 2.

4.2 Methods

In this chapter, the rate constant k of the reaction

$$k : \mathrm{NO} + \mathrm{O_3} \longrightarrow \mathrm{O_2} + \mathrm{NO_2}, \tag{4.1}$$

will be modified with the formulation in Section 3.6 based on the results of the DNS simulations in the convective boundary layer in Section 3.5.

Before listing the implemented equations, some boundary conditions of the DNS simulations in Section 3.5 and the WRF-Chem simulation in Chapter 2 are first briefly intercompared. The results from the WRF-Chem simulations in January 2017 are used as an illustration. Figure 4.1 shows the colour maps of the emission fluxes of NO in the domain d04 at the resolution of 9 km and 1 km. At the resolution of 9 km (the left panel), the maximum emission flux of NO is around 10 ppb m s^{-1}. which is slightly higher than the maximum emission fluxes in the DNS runs (4 ppb m s^{-1}). However, at the resolution of 1 km, the maximum emission flux of NO can reach the level of 100 ppb ms^{-1}, which is much higher than the range of the NO emission fluxes adopted in the DNS simulation. For the boundary condition of O_3, the concentration at the top of the boundary layer at both resolutions is around 60 ppbv, which is slightly higher than the fixed concentration adopted in the free troposphere in the DNS simulations. However, since the O_3 concentration decreases with height in the free troposphere in the WRF-Chem simulations, the value of 40 ppbv adopted in the DNS simulation is not much underestimated from the mean value in the free troposphere.

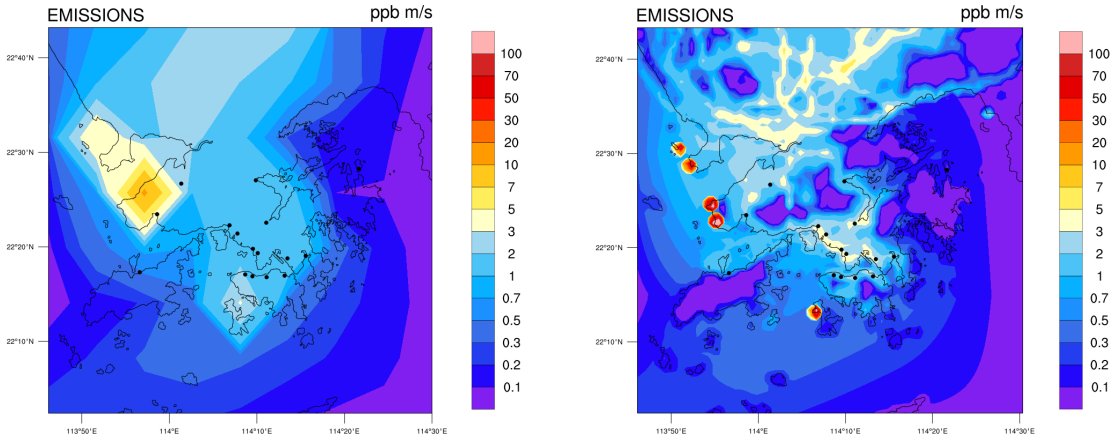

Figure 4.1: Colour maps of NO emissions in January 2017 at the resolution of 9 km (left) and 1 km (right).

Figure 4.2 shows the colour maps of some variables in Equation 4.3 at the surface level at 11 am on 27$^{\text{th}}$ January 2017 calculated from the results in the WRF-Chem simulations in Chapter 2. One may refer to the colour maps of the corresponding temperature (Figure 2.9), NO (Figure 2.14) and O_3 (Figure 2.16) concentration distributions. The turbulent timescale (top-left panel) on the landmass lies between 5 and 10 minutes, which is in the range of turbulent timescale associated with DNS simulation (bottom-right panel of Figure 3.15). In some regions along the coastline, the turbulent timescale is longer than 15 minutes. For the ratio between the O_3 and NO concentrations, the high ratios (positive logarithmic values) occur at the east side of the domain due to the high O_3 but low NO concentration. The low ratios (negative logarithmic values) occur at and in the downwind regions of the point sources (refer to Figure 2.3 for the locations of main point sources), all located in the west, where the NO concentration is high contributed from the emission of the power points and ports. The concentration of O_3 is also low there due to the titration of NO.

The Damköhler numbers of NO and O_3 are shown on the bottom panels. For NO, the Damköhler number is typically $\sim 5-10$ over the land mass, and can raise above 10 in some coastal regions and over the sea due to the longer turbulent timescale there. However, the Damköhler number of NO is relatively small (< 5) in the downwind region of the point sources, attributed from the low concentration of O_3 ($Da_{\text{NO}} \propto \langle O_3 \rangle$). But over the area of the simulated domain, $Da_{NO} > 1$. For O_3, the Damköhler number is small (< 1) on the east half of the domain. It is large (~ 50) near the point sources and in their downwind regions owing to the high NO concentration there. For instance, at the Castle Peak Power Plant, Da_{O_3} can reach the level of 200.

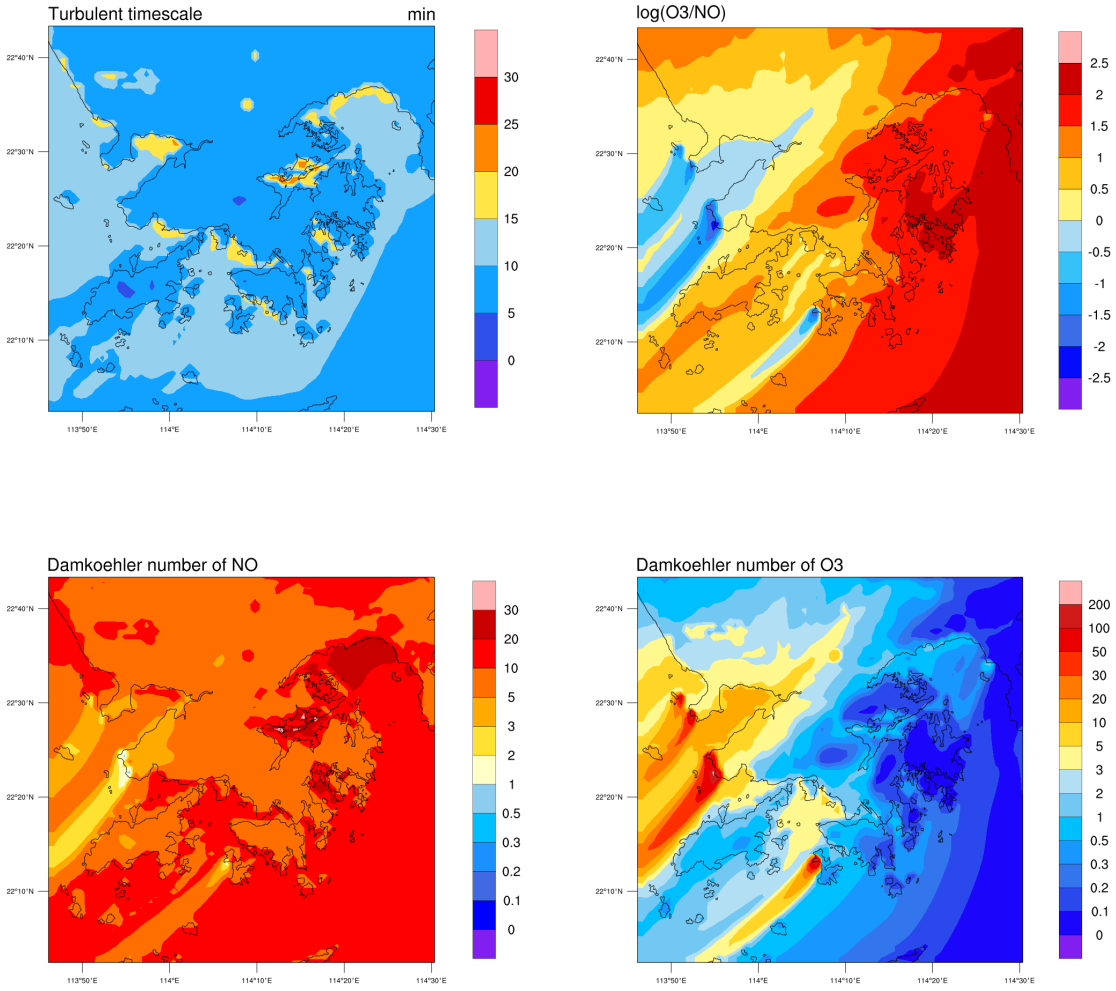

Figure 4.2: Colour maps of the turbulent timescale (top-left panel), the ratio between O_3 and NO concentrations (top-right, in logarithmic scale), the Damköhler number of NO (bottom-left) and O_3 (bottom-right) calculated from the results of the WRF-Chem simulation at 11 am on 27 January 2017 at resolutions of 1 km . These are calculated using the temperature and concentration fields shown in Figure 2.9, 2.14 and 2.16.

From Equation 3.8, the effective reaction rate between initially-segregated sources of NO and O_3 under the influence of turbulence can be expressed as:

$$\frac{k_{eff}}{k} = 1 - \alpha(\log r_{Da} + 2.637)^2 \cdot Da_{\mathrm{O_3}}, \tag{4.2}$$

where the Damköhler number of O_3 is

$$Da_{\mathrm{O_3}} = k\langle \mathrm{NO} \rangle \left(\frac{z_i^2}{B_0} \right)^{\frac{1}{3}}$$

and the ratio between the Damköhler number of NO and O_3 is

$$r_{Da} = \frac{Da_{\mathrm{NO}}}{Da_{\mathrm{O_3}}} = \frac{\langle \mathrm{O_3} \rangle}{\langle \mathrm{NO} \rangle}.$$

k here refers to the originally-imposed reaction rate constant of Reaction 4.1 in the WRF-Chem model. z_i refers to the boundary layer height, and B_0 is the surface buoyancy flux, which is given by

$$B_0 = \frac{g}{T}\overline{w'\theta'},$$

where g is the gravitational constant and T is the absolute temperature. $w'\theta'$ is the vertical kinematic flux of the virtual potential temperature θ.

To express the surface buoyancy flux B_0 in variables inside the WRF model, the above formula is rewritten into functions of the surface sensible heat flux SHF and the surface latent heat flux LH (Stull 2012):

$$\begin{aligned} B_0 &= \frac{g}{\rho c_p T}\left[SHF + 0.61\frac{c_p T}{L}LH\right] \\ &= \frac{g}{\rho c_p T}\left[SHF + 0.07LH\right], \end{aligned}$$

where ρ is the air density, c_p is the specific heat capacity of air at constant pressure, and LH is the surface latent heat. The ratio of $\frac{c_p T}{L}$ can be approximated to be 0.07 under normal atmospheric condition (Stull 2012).

Expanding Equation 4.3 with the above-mentioned physical and chemical variables, the effective reaction rate for Reaction 4.1 is formulated as:

$$\frac{k_{eff}}{k} = 1 - \alpha\left(\log\frac{\langle \mathrm{O_3} \rangle}{\langle \mathrm{NO} \rangle} + 2.637\right)^2 \cdot k\langle \mathrm{NO} \rangle \left(\frac{z_i^2}{\frac{g}{\rho c_p T}\left[SHF + 0.07LH\right]}\right)^{\frac{1}{3}}. \tag{4.3}$$

The effective chemical reaction rate k_{eff} is implemented into the WRF-Chem model in Chapter 2 to replace the originally-imposed k, with the impact factor $\alpha = 0.004331$ at the resolution of 9 km and $\alpha = 0.003522$ at the resolution of 1 km. The impact factor is smaller at the resolution of 1 km due to the compensation from the increased resolving power at higher resolution. In the simulation, it is adjusted that $k_{eff}/k = 1$ when $B_0 < 0$ or when $\langle NO \rangle = 0$ to avoid computational errors. Since Equation 4.3 is based on conditions in a convective boundary layer, $B_0 < 0$ would violate the the convective conditions, and therefore the effect addressing in Equation 4.3 should also be neglected. When $k_{eff}/k < 0$, the value is set to zero. When the impact of inefficient turbulent mixing significantly affects the rate of chemical reaction, k_{eff}/k approaches to 0. When the effect of inefficient turbulent mixing is unimportant, k_{eff}/k approaches to 1.

The expected values of k_{eff}/k based on the results in Chapter 2 at 11 am on 27$^{\mathrm{th}}$

January 2017 are shown in Figure 4.3 at the resolutions of 9 km (left panel) and 1 km (right panel) respectively. One can see that k_{eff}/k is generally smaller in the west half of the domain at both resolutions, as the NO concentrations are higher there with the presence of the point sources. At the downwind region of the point sources, k_{eff}/k can even drop to zero due to the intense concentration of NO. The ratio between O_3 and NO is also high there. The range of k_{eff}/k at the two resolutions both lies between 0.0 and 1.0, despite that the impact factor α is 18.7% larger at the resolution of 9 km.

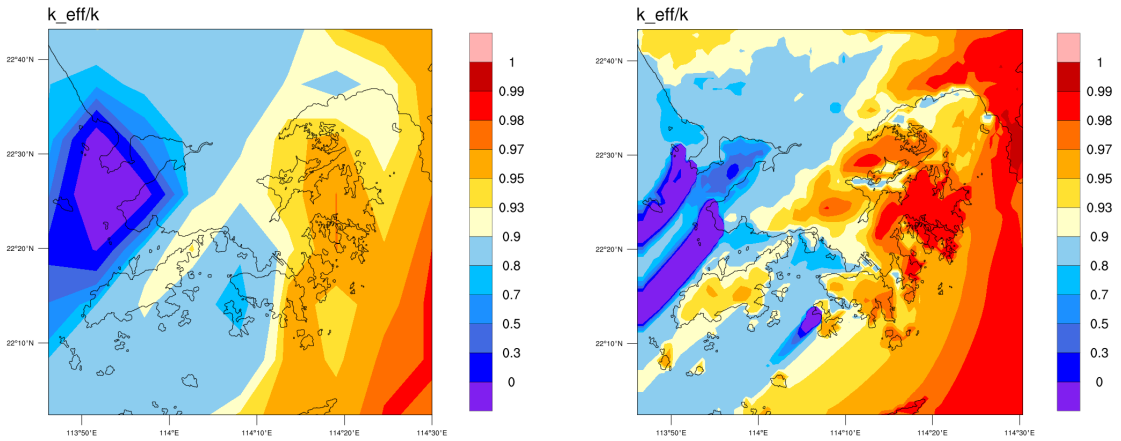

Figure 4.3: Colour maps of the normalised effective chemical reaction rate (k_{eff}/k) implemented in the WRF-Chem simulation at 11 am on 27th January 2017 at resolutions of 9 km (left panel) and 1 km (right panel) . These are calculated using the physical variables and concentration fields shown in Figure 2.14 and 2.16.

4.3 Results

4.3.1 Showcase on 27th January 2017

The results of the modified run are first illustrated with the colour maps of the surface concentrations of NO, NO_2 and O_3 at 11 am on 27th January 2017. One may refer to Section 2.1.2 for the locations indicated in this section. Figure 4.4 shows the results of the modified run at the resolution of 9 km, in which the left panels show the resultant concentrations of NO (top panel), NO_2 (middle panel) and O_3 (bottom panel), and the right panels show the deviations in the modelled concentrations of the modified run from the original run in percentage. One can refer to again to Figure 2.14 and 2.16 for the comparison with the original run. For NO (the top panels), the deviation between the two runs is typically less than +1.5%. The deviation is more significant in the the top-left corner of the domain and the south-west of the Lamma Island (downwind of the Lamma Power Plant). The deviation is larger at the west half of the domain. The difference

between the two runs is less than -1% for NO_2 and +1.5% for O_3. The deviation in the O_3 concentration is most significant downwind of the Shekou region. Despite the variation of k_{eff}/k can be as large as 100%, its influence to the modelled concentrations of NO and O_3 is only within 2%.

Figure 4.5 shows the similar plots as in Figure 4.4 but for runs at the resolutions of 1 km. The left panels show the resultant concentrations and the right panels show the deviations in its modelled concentrations from the original run. For NO, the deviation ranges from 0% to +2% The deviation is more significant again at the east half of the domain. The deviation for NO concentration is wider-ranged at the resolution of 1 km. The regions with relatively prominent deviations are north of Shekou, north of the simulation domain in Shenzhen, east of Castle Peak, near the Kwai Chung port and west of Kowloon, and south of the Lautau Island. For NO_2, the range of the deviation is within -1%. The deviation of NO_2 follows similar spatial distribution with NO, except the signs are opposite. For O_3 the deviation ranges between 0 and +25%. The areas with the larger deviations are located at the point sources and their downwind regions. In those areas, the O_3 concentrations are also low. The maximum deviation in O_3 concentration at the resolution of 1 km is larger than that at the resolution of 9 km.

From Figure 4.4 and 4.5, one can see that the deviation of the modified run from the original one is with larger maximum values and in a wider range at the resolution of 1 km, despite the correction factor α is $\sim$20% higher at the resolution of 9 km. The reason is speculated to be the larger variability of the concentrations with increasing resolution. Additionally, the effect from k_{eff}/k to the deviation in NO concentration is most significant when the NO concentration is at moderate level. When the NO concentration is low, k_{eff}/k is very close to 1, and hence does not have much impact. When the NO concentration is too high, although k_{eff}/k becomes close to zero, the concentration of O_3 is also low, hence diminishing the impact of the chemical term of their reaction ($k\langle O_3\rangle\langle NO\rangle$). The dominant processes affecting the NO concentrations at those regions are through emission and advection. For O_3, the deviation is larger near the point sources and their downwind regions due to the low values of k_{eff}/k there.

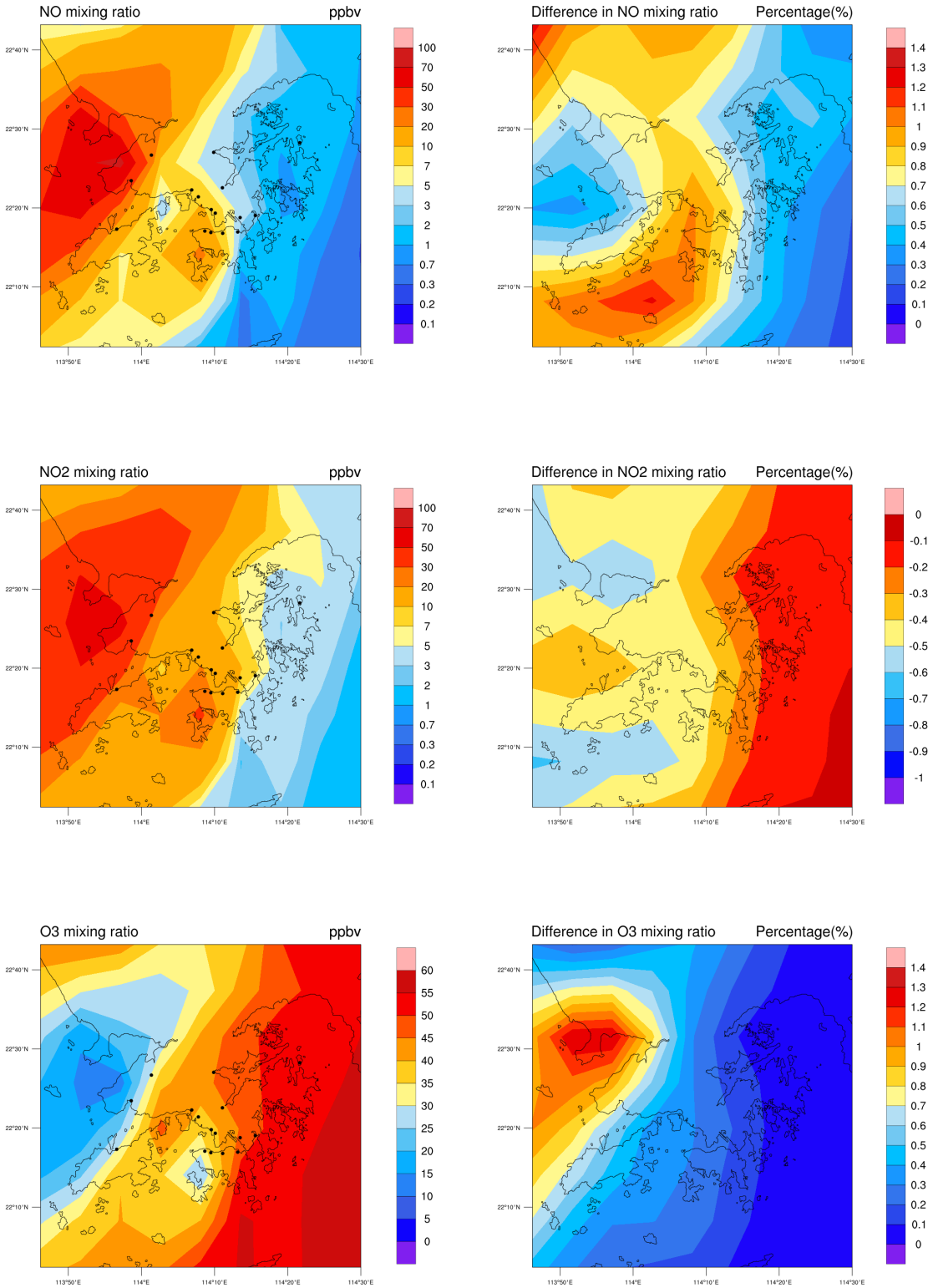

Figure 4.4: Colour maps showing the surface-level concentrations of NO (top-left panel), NO_2 (middle-left panel) and O_3 (bottom-left panel) at 11 am on 27th January 2017 from the modified run at the resolution of 9 km, and their corresponding deviation from the original run in the right panels. The deviation maps on the right panels are smoothed using nine-point local smoothing for better illustration.

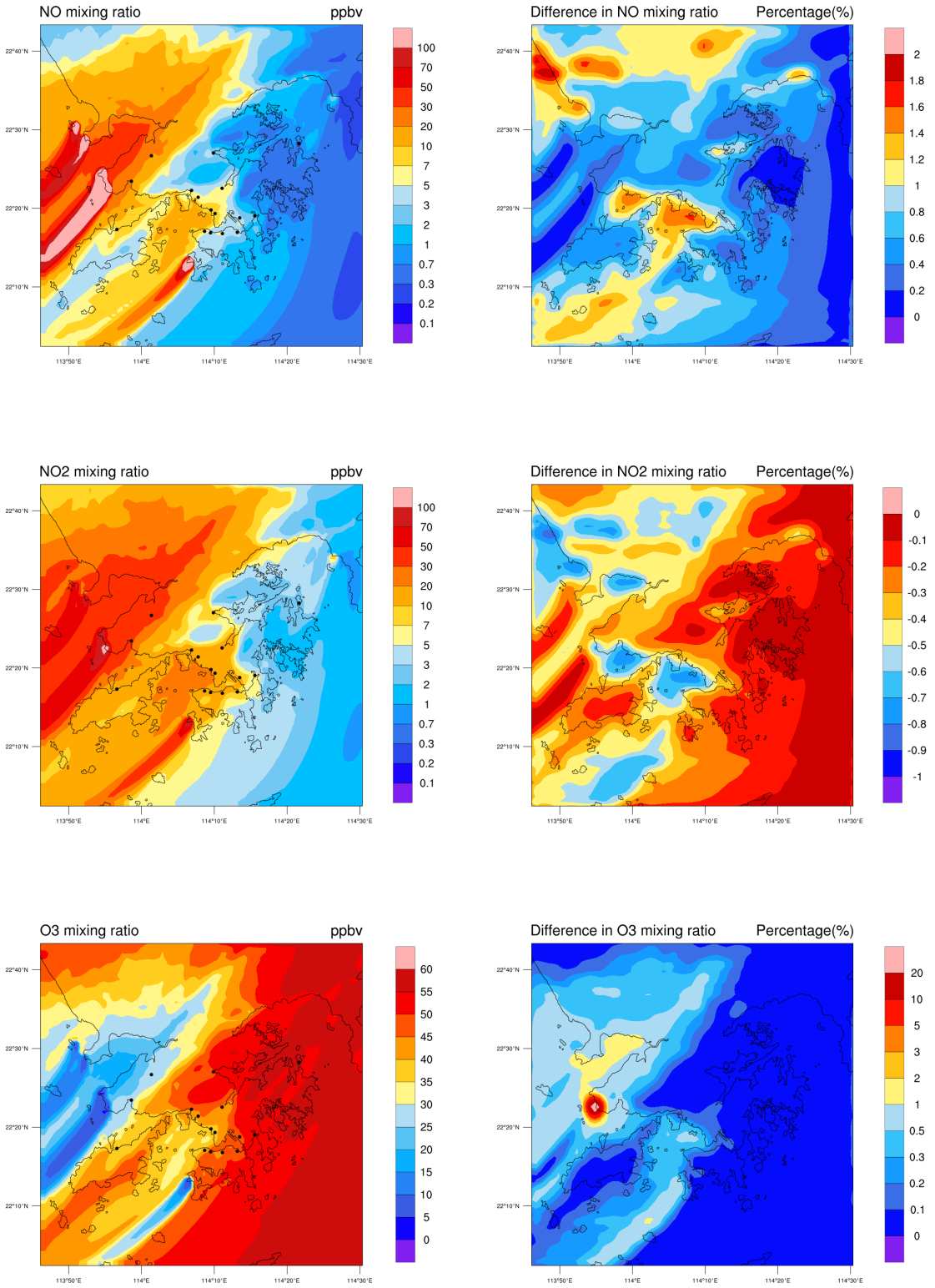

Figure 4.5: Colour maps with similar description in Figure 4.4 but from the modified run at the resolution of 1 km.

4.3.2 General statistics

Table 4.1 shows the statistics of the modified and original run over the daytime of the simulation days in January 2017, and the deviation between the two runs at the resolution of 1 km. Only the daytime data is considered here because Equation 4.3 is more applicable to the daytime conditions. One can see that the deviation between the statistics of the two runs is insignificant ($< 1\%$) for most of the variables, except that the maximum value of O_3 concentration is increased by 80% in the modified run. It shows that the parametrisation may be more sensitive to the extreme values of O_3 concentrations.

NO	MarcoPolo	kmod	kmod - MarcoPolo
Mean (ppbv)	13.46	13.51	+0.05 (+0.37%)
Standard deviation (ppbv)	38.95	39.13	+0.18 (+0.46%)
Maximum (ppbv)	1280.82	1283.26	+2.44 (+0.19%)
Total sum (Mg)	2.76	2.77	+0.01 (+0.35%)
NO_2	MarcoPolo	kmod	kmod - MarcoPolo
Mean (ppbv)	17.51	17.46	-0.05 (-0.29%)
Standard deviation (ppbv)	18.60	18.52	-0.08 (-0.43%)
Maximum (ppbv)	202.12	202.26	+0.14 (+0.07%)
Total sum (Mg)	6.24	6.22	-0.02 (-0.27%)
O_3	MarcoPolo	kmod	kmod - MarcoPolo
Mean (ppbv)	41.10	41.16	+0.06 (+0.15%)
Standard deviation (ppbv)	18.22	18.19	-0.03 (-0.16%)
Maximum (ppbv)	79.15	144.12	+64.97 (+82.02%)
Total sum (Mg)	8.65	8.66	0.01 (+0.15%)

Table 4.1: General statistics of the mixing ratios of NO, NO_2 and O_3 of the original (MarcoPolo) and modified (kmod) runs during the daytime of the simulation period in January 2017.

4.3.3 Vertical profiles and diurnal evolution

To examine whether the formulation in Equation 4.3 shows an effect on the vertical mixing of the pollutants, the vertical profiles at 2 pm averaged over the simulation days in January 2017 are shown for the mixing ratios of NO, NO_2 and O_3. The time of 2 pm is chosen because the boundary layer is most convective at that time, indicated by its maximum boundary layer height (refer to the top-left panel of Figure 2.23 for the diurnal variation of the boundary layer height). The boundary layer height at 2 pm is on average at 1,100 m, and one should only consider the height below 1,100 m, as the formulation in Equation 4.3 is only applicable within the boundary layer. One can refer to the results presented in Section 2.3.4 for the vertical profiles of the original runs.

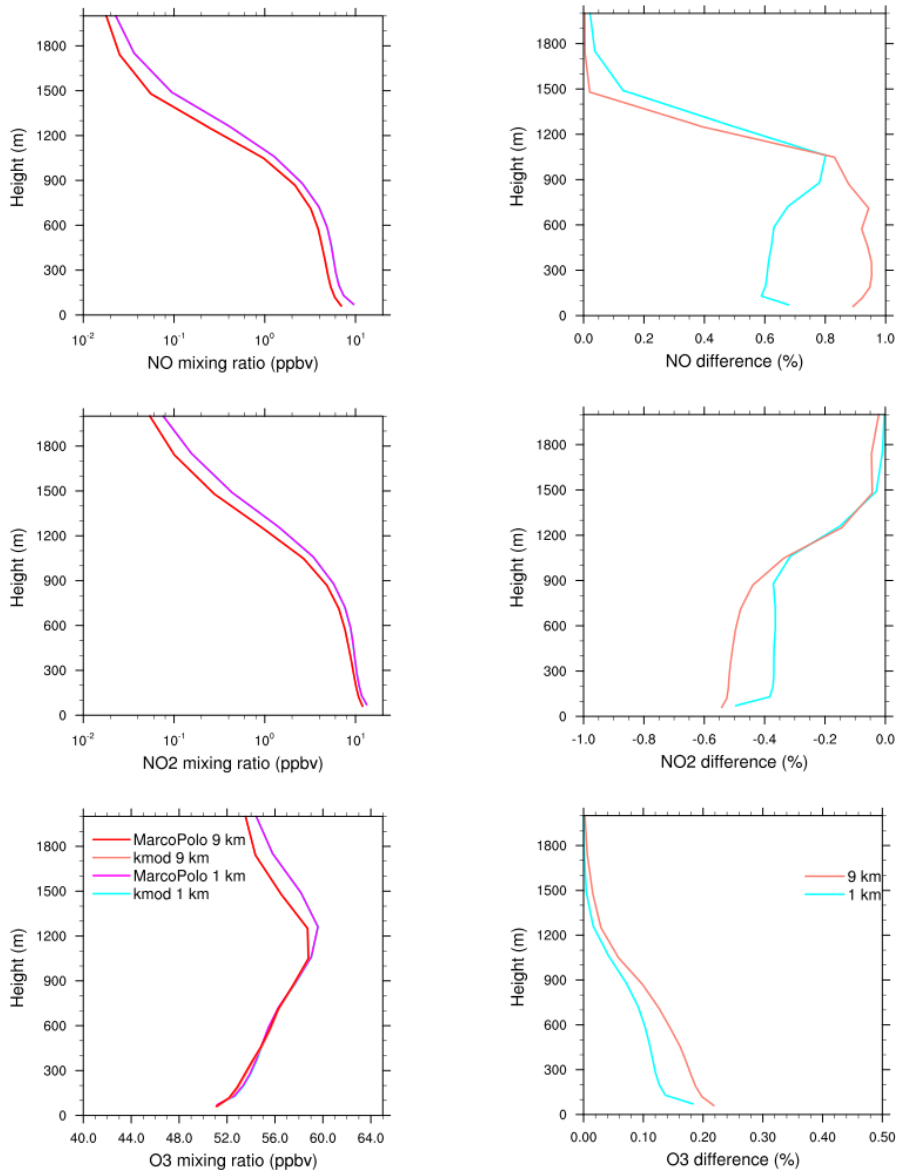

Figure 4.6: Vertical profile of the horizontally averaged concentrations of NO (top-left panel), NO_2 (middle-left panel) and O_3 (bottom-left) at 2 pm averaged over the simulation days in January 2017 at the resolution of 9 km and 1 km. The original (MarcoPolo) and modified (kmod) runs are plotted in red and orange respectively at the resolution of 9 km, and magenta and cyan at the resolution of 1 km. The deviation between the original and modified runs are small so that the two profiles are not well distinct at both resolutions. Their corresponding deviation from the original run are plotted on the right panels in orange (at the resolution of 9 km) and cyan (at the resolution of 1 km). One should only focus on the altitudes below 1,100 m (the average boundary layer height at 2 pm).

Figure 4.6 shows the horizontally-averaged mixing ratios of NO (top-left panel), NO_2 (middle-left panel) and O_3 (bottom-right) in the original and modified runs at the resolution of 9 km and 1 km. The original and the modified runs are plotted in red and orange respectively at the resolution of 9 km, and in magenta and cyan respectively

at the resolution of 1 km. The right panels show the deviation between the two runs, plotted in orange and cyan at the resolution of 9 km and 1 km respectively.

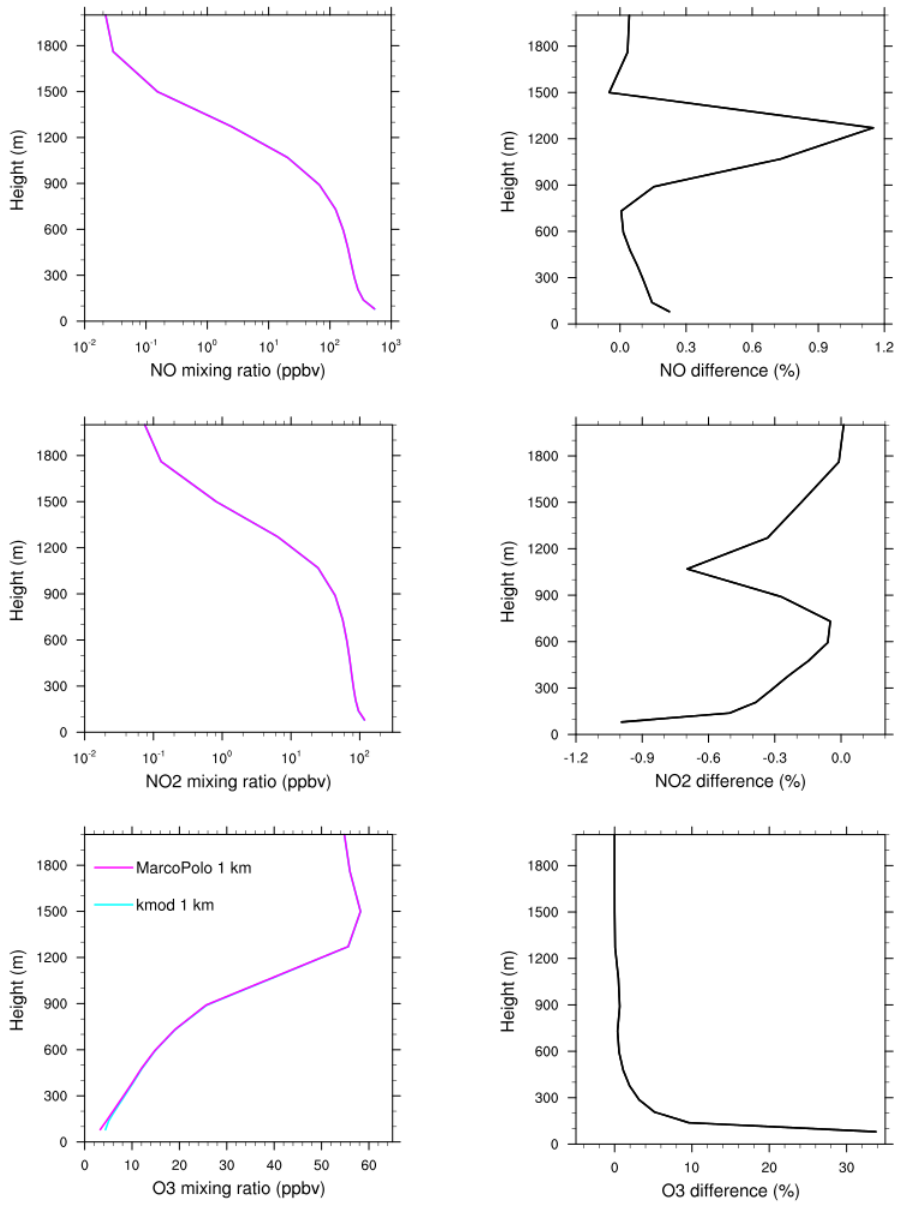

Figure 4.7: Vertical profile of the mixing ratios of NO (top-left panel), NO_2 (middle-left panel) and O_3 (bottom-left) at the Castle Peak Power Plant of the original and modified runs at the resolution of 1 km, and their corresponding deviation from the original run (right panels). Similar description as in Figure 4.6.

In general, the deviation of the modified run from the original run is insignificant for all 3 species throughout the boundary layer at both resolution, with $< 1\%$ for NO, $< 0.6\%$ for NO_2 and $< 0.25\%$ for O_3. That is why the lines of the modified runs are not clearly distinguished from the original runs in the profiles on the left panels. The deviation between the runs in general decrease with height for almost all species at both

resolutions. The horizontally-averaged deviations between the runs are larger in value for all species at the resolution of 9 km. The difference between the two resolutions is more prominent for NO ($\sim 0.4\%$ at maximum). At the resolution of 1 km, the deviation between the two runs shows a particularly steep gradient below 150 m, and transits to much smaller small gradient above that height. It shows that k_{eff}/k has a higher impact in and near the surface layer. One can also see from the DNS simulations that k_{eff}/k is larger near the surface layer (Figure 3.38). However, the vertical profiles do not show this characteristic and are relatively smooth at the resolution of 9 km.

The same vertical profiles are shown in Figure 4.7, but at the Castle Peak Power Plant (22.38°N, 113.92°E), where the deviation between the two runs is most significant. Here only the results at the resolution of 1 km are shown as the significant deviation can only been seen at the resolution of 1 km (see Figure 4.5). For NO, the deviation between the modified and original runs is only 0.24% at the surface, which is less than the horizontally-averaged value, and decreases with height. But the deviation rises again near the top of the boundary layer, that a level of 1% is reached. For NO_2, the deviation follows a similar pattern as that of NO. The deviation is 1% at the surface level (higher than the horizontally-averaged value). For O_3, the deviation reaches 34% at the bottom layer, then drastically decreases with height to less than 10% at 150 m.

The left panels of Figure 4.8 show the diurnal evolution of the surface mixing ratios of NO (top panel), NO_2 (middle panel) and O_3 (bottom panel) of the original run (plotted in magenta) and the modified run (in cyan) at the resolution of 1 km at the Castle Peak Power Plant, with time-averaged over the simulation days in January 2017. The right panels show the corresponding deviations between the two runs. Only the deviations during daytime between 8 am (0800) and 5 pm (1700) are shown here. For NO and NO_2, the deviation is relatively higher at 8 am and at 2 pm. However, the deviations are still insignificant ($< 0.24\%$ for NO and $< -1.1\%$ for NO_2). For O_3, the deviation is largest at 8 am (+150%) followed by at 2 pm (+30%). Note that the O_3 concentration is very low at 8 am, so the percentage change may have been exaggerated.

The peak occurs at 8 am (the time around sunrise) because the boundary layer begins to expand after sunrise. O_3 starts being entrained down from the free troposphere, and hence is highly segregated from NO, which is mostly emitted from the surface. Therefore at this time, the effect from Equation 4.3 is more significant. Other peak occurs at 2 pm because the boundary layer height (and hence the turbulent timescale) is maximum at that time. With a larger Da_{O_3}, the effect from Equation 4.3 is again more significant.

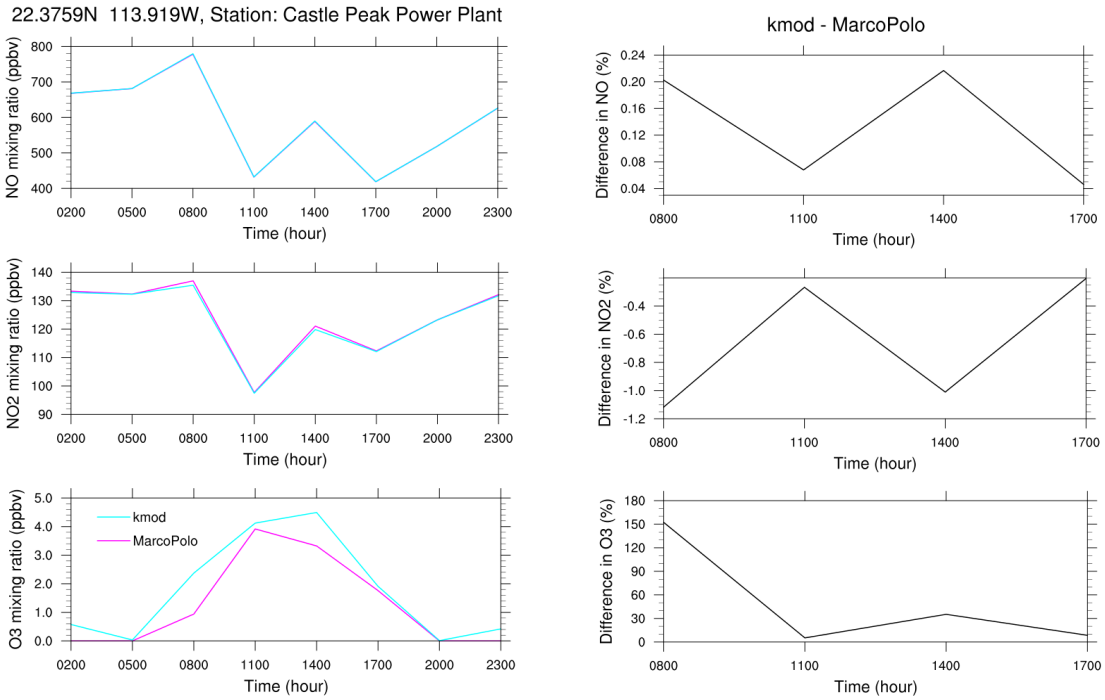

Figure 4.8: Left panels: Time series showing the mixing ratios of NO (first panel), NO_2 (second) and O_3 (third) of the modified (plotted in cyan) and the original run (plotted in red) at the resolution of 1 km at the Castle Peak Power Plant over the simulation days in January 2017. Right panels: Time series showing the corresponding deviation of the modified run from the original run in percentage.

4.3.4 Model comparison with observations

To investigate the diurnal variation arisen from the formulation and to compare the results with observations, the time series of the modified run and the original run are plotted together with the observational data at the observation stations of Shatin and Tuen Mun. In this section only the results at the resolution of 1 km are shown.

We first show the results at the Shatin station in Figure 4.9. The plot description is similar as in Figure 4.8, with the observation data plotted in black on the left panels. Shatin station is an suburban station located in the east of the domain. From the right panels, one can see the maximum deviation in NO concentration is 2.6%, almost 4 times higher than the horizontally-averaged value (see the top-left panel of Figure 4.6). Other than that, the deviation of both NO_2 and O_3 are both less than 1%. As seen from the left panels, the modified run is hardly deviated from the original run, hence the parametrisation does not show significant improvement to the model.

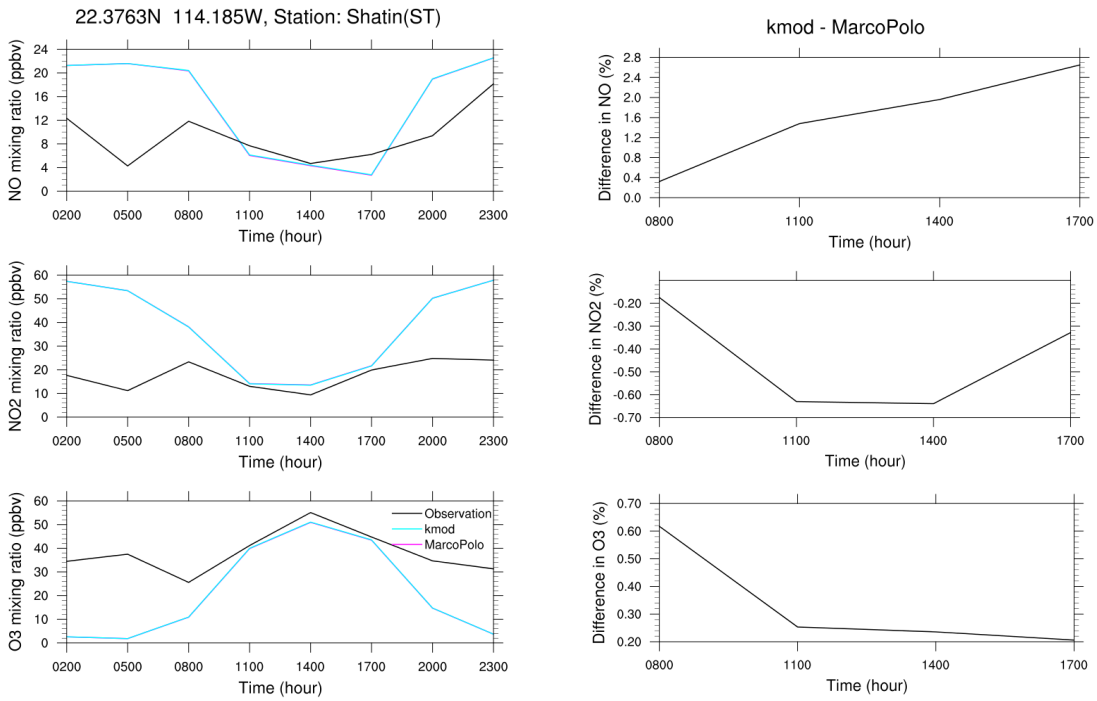

Figure 4.9: Left panels: Time series showing the mixing ratios of NO (first panel), NO_2 (second) and O_3 (third) of the modified (plotted in cyan) and the original run (plotted in red) at the resolution of 1 km, along with the observation data (plotted in black) at the Shatin station over the simulation days in January 2017. Right panels: Time series showing the corresponding deviation of the modified run from the original run in percentage at the Shatin station.

Figure 4.10 shows the same plots at Tuen Mun station, which is 7 km away from the Castle Peak Power Plant. The deviation at this station is expected to be higher due to its proximity to the power plant. However, one can see the deviations ($< 0.15\%$ for all species) are even less than those found at Shatin station. Although the Tuen Mun station is close to the power plant, it does not locate on its downwind direction. The station may therefore show much less deviation as at the power plant (see Figure 4.8). Additionally, at the resolution of 1 km, the model can well separate the location of the station from the periphery/downwind region of the power plant.

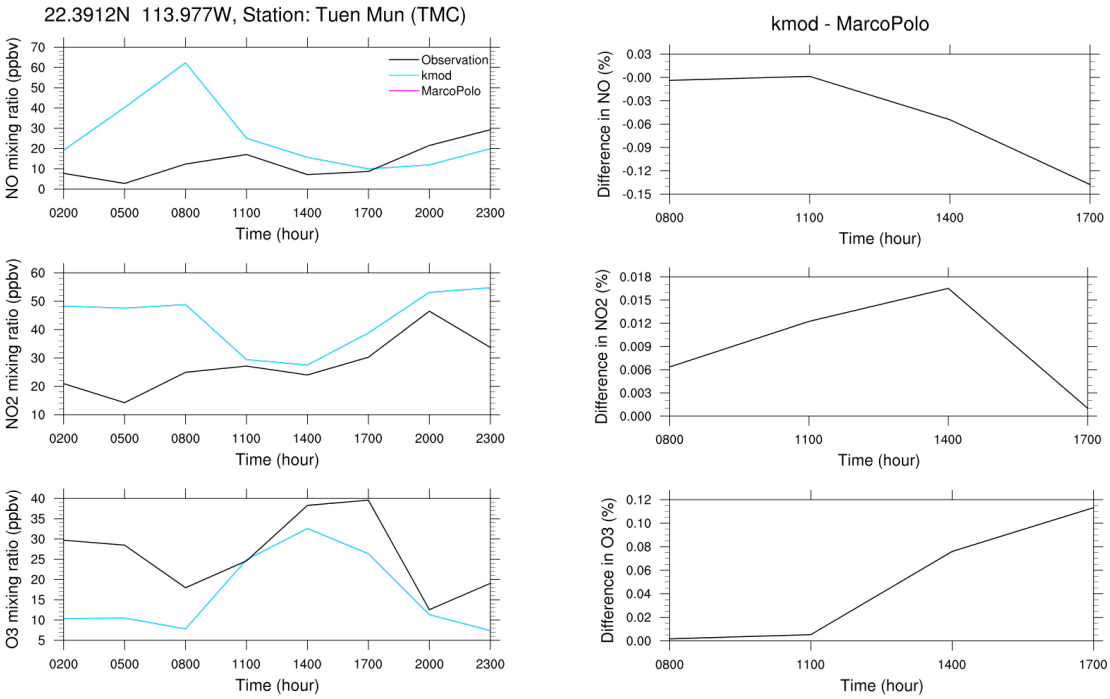

Figure 4.10: Left panels: Time series showing the mixing ratios of NO (first panel), NO_2 (second) and O_3 (third) of the modified (plotted in cyan) and the original run (plotted in red) at the resolution of 1 km, along with the observation data (plotted in black) at the Tuen Mun station over the simulation days in January 2017. Right panels: Time series showing the corresponding deviation of the modified run from the original run in percentage at the Tuen Mun station.

4.4 Conclusions and discussion

In this chapter, the parametrisation of the effective reaction rate of the reaction between NO and O_3 (Equation 4.1) is implemented into the WRF-Chem simulations presented in Chapter 2 with the formulation of Equation 4.3 constructed in Section 3.6 to account for the impact of segregated reactants due to inefficient turbulent mixing on the actual chemical reaction rate. The simulation at both resolution of 9 km and 1 km are once again conducted with the parametrised chemical reaction rate with different impact factor α. The results of these modified runs are then compared with the results of the corresponding runs in Chapter 2.

From the colour maps showing the deviation of NO and O_3 concentrations of the modified runs from the original runs at the resolution of 1 km, it is observed that the deviation during daytime is typically less than 2% for NO and NO_2, and is significant for O_3 only right above a point source. The effect is not as significant as expected from the colour maps of the effective chemical reaction rate, in which the actual reaction rate can drop to zero in some regions in the simulated domain. The deviation is most

significant for NO and NO_2 in areas where the NO_X concentration is moderate. It is because when the parametrised rate is largely deviated from the imposed rate, where the NO_X concentrations are high, the modelled concentrations are dominantly affected by other processes such as emission and advection. When the NO_X concentration is low, the parametrised rate would be close to the original rate. The deviations in mixing ratios of NO, NO_2 and O_3 between the runs at resolution of 9 km are all less than 2%, presumably due to the smaller variability in the concentration fields at lower model resolution.

The deviation may not be significant, but one should also reminded that only one chemical reaction (i.e. Reaction 4.1) is changed in the modified run. In principle, similar parametrisation should be implemented to other chemical reactions with fast chemistry and extreme concentration ratios between the two reactants. The number of chemical reactions that fit into this category is expected to be quite high in an urban environment, thus a comprehensive study with the rates of all these reactions parametrised may potentially have a significant effect on the modelled concentrations. Also, there are therefore a number of other reactions that may contribute to the chemical transformation of NO and O_3 in the WRF-Chem simulation. For instance, in the chain reaction involving ozone presented in Section 1.2, Reaction 4.1 is not the limiting reaction in the VOC-limited regime. In the high-NO_X emission region, where the effective reaction rate is most deviated from the imposed rate, ozone chemistry is always in the VOC-limited regime. Therefore, the concentration of O_3 is less sensitive to the concentration of NO, further hindering the impact of the modified chemical rate.

One should also evaluate whether the assumption made in the formulation are fully applicable in the WRF-Chem runs. First, the formulation is constructed in Section 3.6 based on the DNS simulation in which NO is homogeneously emitted from the surface. However, in the simulated domain, the emission of NO is mostly attributed to point sources in the west half of the domain. From what is learnt in Section 3.4, the heterogeneous emission sources may further decrease the effective reaction rate. On the other hand, in the east half of the domain where NO emission is relatively scarce, NO would have already been partially mixed as NO is transported from the sources. In this case, the formulation may underestimate the effective reaction rate (or overestimate the segregation of the chemicals).

Second, the clear-sky convective boundary layer is considered in the DNS simulation. Therefore, the formulation is only applicable during daytime, when the atmospheric is convective. Also, the boundary layer only grows in height throughout the DNS simulation. This is different from the evolution of the boundary layer height in the WRF-Chem model that the boundary layer undergoes a diurnal cycle that the boundary layer height attains its maximum height at around 2 pm and shrinks after that. Therefore, the formulation may even only correctly described the situation between 8 am and 2 pm in the

WRF-Chem run.

Third, the formulation is based on the assumption that solely the Damköhler number can provide the information on the instantaneous state of chemical and turbulent state. In the modified model, the Damköhler numbers are calculated from the modelled physical and chemical variables[1]. However, these modelled variables may have already tampered by the deficiency of the model. For example, the dilution of NO emissions at the resolution of 9 km tends to give a smaller Damköhler number, hence a less deviated effective chemical reaction rate than at the resolution of 1 km. That may explain why the deviation has a wider range and high maximum value at the resolution of 1 km. Despite the deviation factor in the formulation is $\sim 20\%$ large at the resolution of 9 km than of 1 km, it may not compensate the reduction from the dilution of concentrations due to low resolving power.

It should be also reminded that in the WRF-Chem model, the boundary layer scheme[2] provides a parametrisation for vertical mixing of chemical species in the boundary layer. Although this scheme is a function of height and a prescribed eddy diffusion coefficient, which is independent of chemical reactions and therefore inadequate to account for the effect of turbulence on chemistry, it contributes to reduce the segregation between the reactants, in turn also reduce the effect of our parametrisation on the modelled results.

To evaluate the effect of the formulation, one can compare roughly the deviations of the mean mixing ratios (refer to Table 4.1) with those when changing the grid and emission resolution (refer to Table A.7 and 2.6). For instance, when the grid resolution increases from 9 km to 1 km (refer to Table A.7), the deviations are +35% and -3.75% for the mean surface concentrations of NO and O_3 respectively. When the emission resolution is downgraded from 1 km to 10 km (refer to Table 2.6), the deviations in the former case are -64.29% and -3.05% for the concentrations of NO and O_3 respectively. When the formulation on the effect of turbulent motion on chemical reaction (Equation 4.3) is implemented at the 9-km resolution run, the deviation is only +0.89% for NO and +0.25% for O_3 (refer to Figure 4.6). From these, one can see that the implementation of the formulation is relatively insignificant compared wit the change in grid or emission resolution.

[1] As this parametrisation adopts mainly modelled variables in the calculation of the parametrised process, it is said to be a local parametrisation scheme.

[2] The YSU boundary layer scheme is adopted in the WRF-Chem model (Hong et al. 2006).

Chapter 5

Conclusion and Outlook

5.1 Summary

Chemical transport models resolve atmospheric processes at a spatial resolution that is generally much coarser than the size of important processes, such as localised surface emissions, that occur in particular in the boundary layer of urban areas. For instance, the resolution of regional chemical transport models is typically $\sim O(1-10)$ km. In urban areas, where different chemical species are often emitted from sources in separated locations, chemical species can be therefore segregated when turbulent mixing is not efficient. However, in an Eulerian model, they are assumed to be fully mixed inside a grid box, and thus react together much more easily than in the real world. A major goal is this thesis was to assess the importance of reactive species segregation in the calculation of chemical reactions, particularly in the turbulent boundary layer of a subtropical metropolitan area such as Hong Kong. The city has a complex topography with a large number of high-rise buildings and street canyons, in which emissions are clearly segregated.

To examine the importance of model resolution and the consequence of chemical segregation, I adopted two different and complementary approaches - a regional-scale and a turbulence-resolving model. First I analysed how the increase in the resolution of a regional chemical transport model from 27 km to just 1 km changes the predicted concentrations of secondary species like tropospheric ozone, whose formation results from nonlinear chemical processes. Ozone is thus sensitive to the degree of mixing in the boundary layer of primary fast reacting species such as nitrogen oxides. Second, to investigate the importance of very small scale effects, in particular turbulent motions in the urban boundary layer, I used direct numerical simulations to measure the relation between the segregation and the reactive rates between two reactive species.

The major conclusion of this investigation is that, under conditions representative of an urban boundary layer, segregation associated with turbulent motions and separated emission hotspots can considerably reduce the value of the chemical rate constant from

the measured value in a contained laboratory vessel. This reduced chemical reaction rate depends on the chemical lifetime of the reactants. It is close to one (no reduction) if both chemical species is well mixed. For example, no significant segregation is expected to occur for the reaction between methane and the OH radical since the lifetime of methane is close to 10 years during which complete mixing occurs. The situation changes if the primary species is a non-methane hydrocarbon such as isoprene whose lifetime is of the order of minutes during which turbulent motions may not be efficient enough to mix the species to allow chemical reactions. In an urban areas such as Hong Kong, a large amount of nitrogen oxides is emitted from the localised emissions of vehicles along major roads in street canyons, its reaction with ozone entrained from the free troposphere is fast and significant segregation occurs. I have estimated from my direct numerical simulation that, with strong emission fluxes of typical urban values, the rate constant to be used in the urban boundary layer can be reduced by as much as 95% due to the strong segregation of the primary species. Specifically for the $NO-NO_2-O_3$ reaction, the rate should be reduced by at least 15% when the NO_X emission flux is strong. This effective reaction rate can be parametrised as a function of the chemical and turbulent timescales and the concentrations of the reactants.

To provide realistic results, large-scale models should also adapt rate constants to account for the segregation between fast reactive species when calculating the respective chemical reactions. The correction applied to the reaction rate between NO and O_3, however, shows that the effect of this particular correction on the calculated ozone concentrations is small. Such correction should be applied to all fast reactions for a more comprehensive assessment of the subgrid segregation effect of a range of primary species.

More detailed conclusions are provided below as key points resulting from my investigation of research questions addressed in Section 1.5:

How does the calculation of ozone chemistry change with grid and emission resolution in a regional chemical-transport model over an urban environment?

In order to address this question, WRF-Chem simulations in the region of Hong Kong are conducted at four different horizontal resolutions (27, 9, 3, 1 km) and with emission inventory at resolutions of 1 and 10 km in *Chapter 2*. Unlike previous similar studies (e. g. Schaap et al. (2015)) in other regions which focus on the comparison between modelled and observed data to assess the improvement of model performance with increasing model resolution, I choose to focus on the intercomparison between the modelled results at different resolutions to see how the calculation of processes related to ozone chemistry changes in the model with increasing model resolution. Regarding the changes in model calculation with increasing resolution of horizontal grids, I present

the following key results:

- The modelled concentration shows more significant influence from local topography (mainly terrains) and emission heterogeneity with sharper and more extended tails of minima/maxima at the downwind areas of the emission point sources and in urbanised areas with increasing resolution. I advise to adopt a resolution of at least 3 km to adequately resolve the heterogeneity from the topography and emissions for this case in Hong Kong.

- The net ozone production rate per NO_X concentration decreases when the resolution increases from 27 km to 3 km, as expected from the non-linearity of ozone chemistry together with the increase in the mean NO_X mixing ratios. However, when the resolution increases to 1 km, the rate increases again. The reason behind is speculated to be a combined effect of the slightly drop of mean NO mixing ratio when the resolution increases from 3 km to 1 km and a substantial increase in the contribution of VOCs to ozone production.

- The segregation coefficient between the mixing ratios of NO and O_3 increases with increasing resolution in daytime in both Winter and Summer, but decreases in nighttime in Winter. Similar phenomenon is also noticed for the segregation coefficient between NO and NO_2. The change of pattern between daytime and nighttime suggests the change of processes in the $NO-NO_2-O_3$ cycle between day and night. From the correlation between the mixing ratios of NO_X and $O_X(= O_3 + NO_2)$, the local contribution to O_X in levels of NO_X is found to increase by 3% when the resolution increases from 27 km to 1 km.

- Overall, the modelled results show a distinct statistical difference between the resolution of 27 km and the higher resolutions. However, for some analysis parameters, the statistical relations of the modelled results between the resolution of 3 km and 1 km are not very clear.

Regarding the changes in modelled concentrations between the simulations with an emission inventory at resolutions of 1 km an 10 km, the most noticeable impact is that more NO is converted to NO_2 in the run with the 10 km-resolution emission inventory. The impact of changing emission resolution to the calculation of ozone chemistry is more significant to that of changing the grid resolution (from 9 km to 1 km) in this case.

How does turbulent motion affect the rate of chemical reactions of two initially-segregated species in the boundary layer under urban conditions?

In *Chapter 3*, I employed a DNS model which explicitly resolves turbulent motions in a convective boundary layer to quantify the effect of turbulence on chemical reactions

of initially-segregated reactants. Unlike most of the previous studies (e. g. Ouwersloot et al. (2011)), which focus on the question on rural or forested conditions, I extended my simulations with considerations of urban conditions, particularly with strong emission fluxes and heterogeneous emissions. he Damköhler number (Da) is used to classified the regime in which turbulence significantly affects the chemical reaction rate. The results from the DNS are then compared with a complete-mixing model, which assumes the reactants to be homogeneously distributed in the whole boundary layer, to examine how the segregation of the reactants due to inefficient turbulent mixing affects the effective chemical reaction rate between two reactants A and B. Here I summarise the key results of the simulations:

- With homogeneous surface emission of reactant A at fluxes in rural level and entrainment of reactant B from the free troposphere undergoing a second-order chemical reaction ($A + B \longrightarrow C$), the inefficient turbulent mixing of the segregated reactants causes a 15-35% reduction with fast chemistry ($Da = 1 - 10$), consistent with the previous results of LES studies (Vinuesa and de Arellano 2005). Heterogeneous surface emission and strong emission flux in urban level can increase the reduction in reaction rate to 24-76% and $> 95\%$ respectively. Increasing the emission flux to urban level changes the chemical regime from Tracer A-limiting to Tracer B limiting. I also find that with strong emission fluxes, the effective chemical reaction rate is more closely related to the Damköhler number of Tracer B, instead of to the Damköhler number of Tracer A as in cases with rural-level emission fluxes.

- With the $NO-NO_2-O_3$ scheme, the resultant reduction in the reaction rate between NO and O_3 is $< 5\%$ when the NO emission flux is weak (≤ 0.4 ppb m $^{-1}$), but is $\sim 15\%$ when the NO emission flux is strong (2 -4 ppb m s^{-1}).

- Effective chemical reaction rate is significantly reduced from the imposed rate when (1) the Damköhler number of the limiting reactant is approaching or greater than 1, or (2) when the ratio between the final Damköhler numbers of the two tracers is particularly small or large (so that one of the tracers is depleting).

How significant is this effect of inefficient turbulent mixing on chemical reaction in models with grid resolution commensurable with regional chemical-transport models?

Instead of comparing the DNS results with the complete-mixing model, which is equivalent to assuming the whole boundary layer to be in the same model grid in a CTM, I degrade the DNS results to lower resolutions to mimic the calculation from a regional CTM with horizontal resolution of 1 and 3 km, and with multiple vertical layers in the boundary layer. I find that

- In the homogeneous-emission cases with fast chemistry, the overestimation of the effective reaction rate is moderated from 15-35% by the complete-mixing model, to 4-22% by a mimicking regional model.

- A mimicking regional model at horizontal resolution of 3 km gives an overestimation even higher than that by the complete-mixing model in the heterogeneous-emission cases. As the width of the alternating emission is 2 km, the two heterogeneously-emitted reactants are premixed at a higher concentration in a 3 km-resolution model than in the complete-mixing model.

- With $NO-NO_2-O_3$ chemistry, the overestimation drops from 15% by the complete-mixing model, to 9% by a 1 km-resolution model.

How significant is this effect when applied to an operational regional chemical-transport model?

Based on the DNS results in Chapter 3, the effective chemical reaction rate due to the segregation of reactants by inefficient turbulent mixing is parametrised for the reaction rate between NO and O_3 as a function of the Damköhler number of O_3 and the ratio between O_3 and NO concentrations. This parametrisation is applied in the WRF-Chem model in *Chapter 4* at the resolutions of 9 km and 1 km. Here is the summary of the chapter:

- From the estimates of the effective chemical rates from the previously modelled concentrations, the effect is expected to be significant near the emission point sources and in their downwind regions. However, the effect on the modelled concentrations of NO and NO_2 is found to be small ($< \pm 2\%$ in general) in the modified run at the resolution of 1 km, and is significant ($\sim +20\%$) for the O_3 concentration only right above a point source.

- Despite the expectedly larger reduction in the effective reaction rate at the resolution of 9 km due to the lower resolving ability of the model, the effect of the parametrisation in the modified 9 km-resolution run is less significant than that at the resolution of 1 km, due to the smaller variability in the modelled concentrations at lower resolution.

- Since only one reaction is modified in this application of the parametrisation, parametrisations on other chemical reactions with fast enough chemistry or with extreme reactant ratios may be necessary to show a significant effect on the modelled concentrations.

5.2 Discussion and Outlook

Generalisation of the parametrisation Parametrisations similar to that in Chapter 4 should be applied to other chemical reactions with fast chemistry or extreme concentration ratios between the two reactants. In principle, the parametrisation addressed in Section 3.6 for the second-order chemical scheme should be able to apply to other real-life second-order chemical reactions, such as the reactions between $R\,O_2$ and NO. However, one has to beware of the high computation cost of such parametrisations in a regional model. By implementing the parametrisation only on the reaction between NO and O_3, the computation time of the modified WRF-Chem run is already doubled. Therefore, one may also need to assess whether the effect of such parametrisation is significant on particular chemical reactions before implementing in a CTM, presumably from the estimated values of the typical corresponding Damköhler numbers and the reactant concentration ratio .

Another consideration to generalise the parametrisation is to express it also as a function of model resolution. Equation 3.7 is fitted specifically with the data from the 1 km-32 level coarse-grid model with a different impact factor α from that in Equation 3.8 in order to be applied to the 1 km-resolution WRF-Chem model. However, theoretically, this impact factor should be a function of both the horizontal and vertical resolution, as both resolutions affect the ability of the model to resolve turbulent motions.

Representation of emission heterogeneity To ask whether a model can resolve the segregation of reactant due to inefficient turbulent mixing, one should in fact consider the abilities of the model to resolve the initial segregation of the reactants before mixing (that is the segregation of the emission sources), and to resolve the subsequent turbulent mixing of these reactants. While the main focus of this thesis is on the second consideration, the first consideration is also very important. The initial segregation of the reactants is actually an initial or a boundary condition of the calculation of the turbulent mixing process in the model. For example, the parametrisation used in Chapter 4 is a local scheme[1] , which is particularly sensitive to the initial and boundary conditions. For example, at the resolution of 9 km, the WRF-Chem model fails to resolve the emission heterogeneity, which in turn tampers the performance of the scheme. To redeem this, one may need to consider a non-local scheme which imposes functions with prescribed variables independent of the modelled variables, or to take extra measures to parametrise for example, the sub-grid emission variability (Valari and Menut 2010), or the sub-grid variability of landuse (such as MOSAIC scheme in WRF (Li et al. 2013)).

[1] A local parametrisation scheme mainly adopts the modelled variables in the calculation of the parametrised process

Validation with observations Observation data are important to validate such parametrisations. Observations on turbulent dispersion of reactive or non-reactive species are commonly done by eddy-correlation methods on aircraft campaigns. These measurements are usually done in rural areas, but cannot be conducted in urban areas. In the urban areas, a more feasible observation method is to obtain the vertical profiles of chemical species by DOAS and LIDAR methods. Such campaigns measuring street-level concentration profiles have been done in cities, including Hong Kong. However, these one-time campaigns cannot provide a real-time observation of the concentration vertical profiles. Setting up LIDAR system in on-site observational stations is invaluable to provide 3D data for the validation of pollution dispersion and transport.

Inclusion of urban structures and urban modelling One very important feature in urban environments, the urban structures, is neglected in this study. The urban structures can serve to increase the segregation of the emissions and to change the dynamics of the turbulent flows. Further study may consider including urban structures for similar studies in an urban environment. However, similar DNS model may not be applicable to the implementation of urban structures on the surface. One may need to use computational fluid dynamics models with a smaller simulation domain, or with large eddy-simulation with considerations of sub-grid parametrisations.

To ultimately remove the uncertainties from parametrisation scheme of turbulent mixing in regional CTMs, one may perform very-high resolution modelling that is capable to resolve turbulent structures. Owing to its highly-localised sources and complex topography with buildings and roads, high-resolution modelling is considered to be essential in urban areas for accurate pollutant concentration calculations. Thanks to the rapid advancement of computational power, regional-scale models are now capable to run at a resolution of $\sim O(100)$ m or even less. LES models at resolution of $\sim O(10)$ m with real urban topography of a specific area in a city implemented are also feasible. Such LES studies are at the moment mainly applied to study urban meteorology and pollution dispersion, and still rarely involve atmospheric chemistry. A coupled LES model to a regional CTM may be considered as the next generation of urban air quality modelling.

Appendix A

Supplementary materials for Chapter 2

VOC species	Energy	Industry	Domestic	Transport
alcohols	0.42	5.48	7.99	0
benzene	2.25	0.47	8.51	2.98
butanes	5.13	3.38	0.99	13.17
ethane	1.67	1.23	7.24	1.20
ethene	0.89	0.19	15.19	5.35
ethyne	0.96	0.15	5.57	3.51
formaldehyde	1.33	0.16	1.02	0.47
hexanes and higher alkanes	17.05	36.62	1.08	20.72
ketones	0.13	7.37	0.69	0.58
other alkanals	0.09	0.00	3.59	0.56
other alkenes and alkynes	8.97	1.76	6.92	6.44
pentanes	2.91	3.24	1.17	17.51
propane	2.00	1.62	2.58	0.82
propene	0.89	0.19	6.37	1.87
toluene	7.87	7.90	3.59	5.49
xylene	24.60	10.35	1.14	4.60

Table A.1: Speciation of VOC species in HTAPv2 emission inventory in the domain d04 - Mass ratio of different VOC species against the total non-methane VOC in percentage.

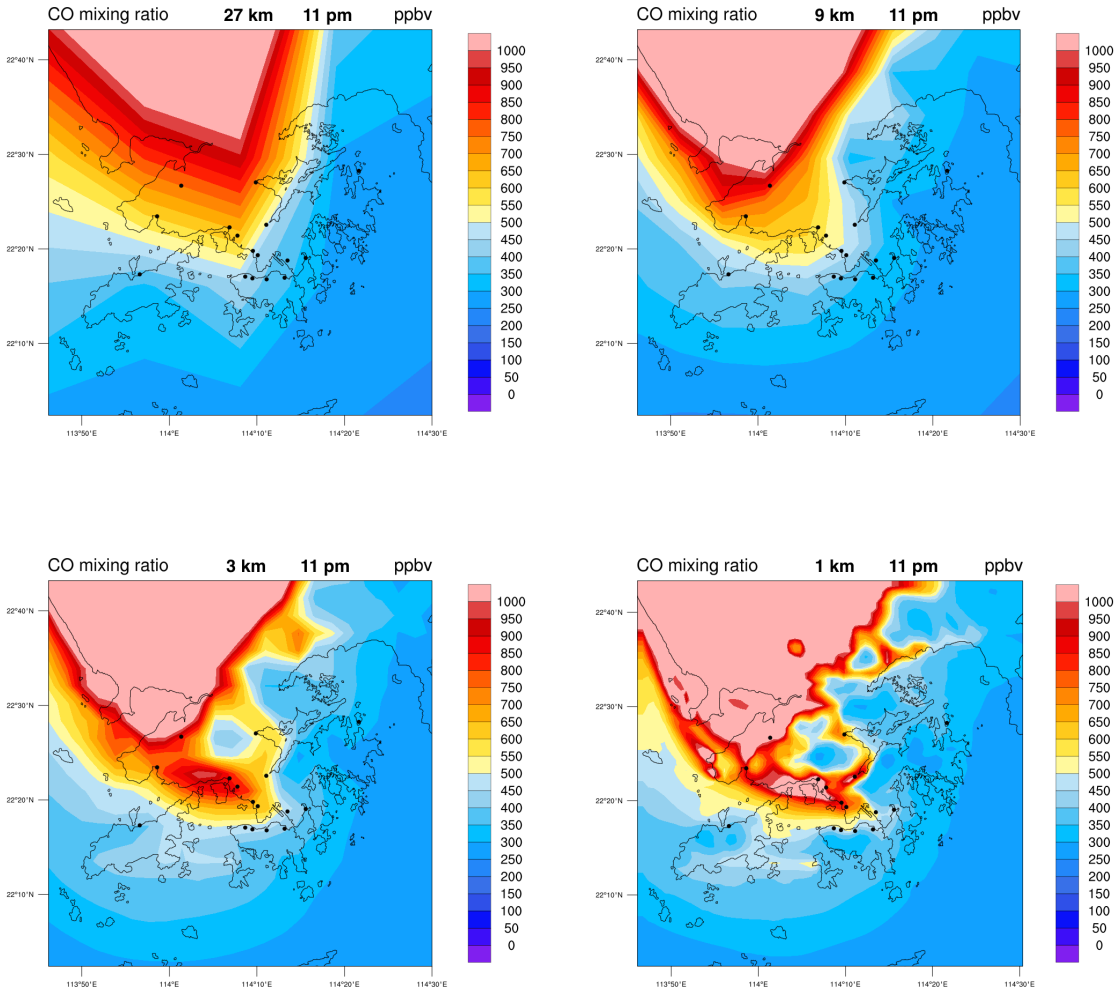

Figure A.1: The color map of O_3 surface mixing ratio at resolution of 27 km (top-left), 9 km (top-right), 3 km (bottom-left) and 1 km (bottom-right) in Domain d04 at 11 pm on 27th January 2017.

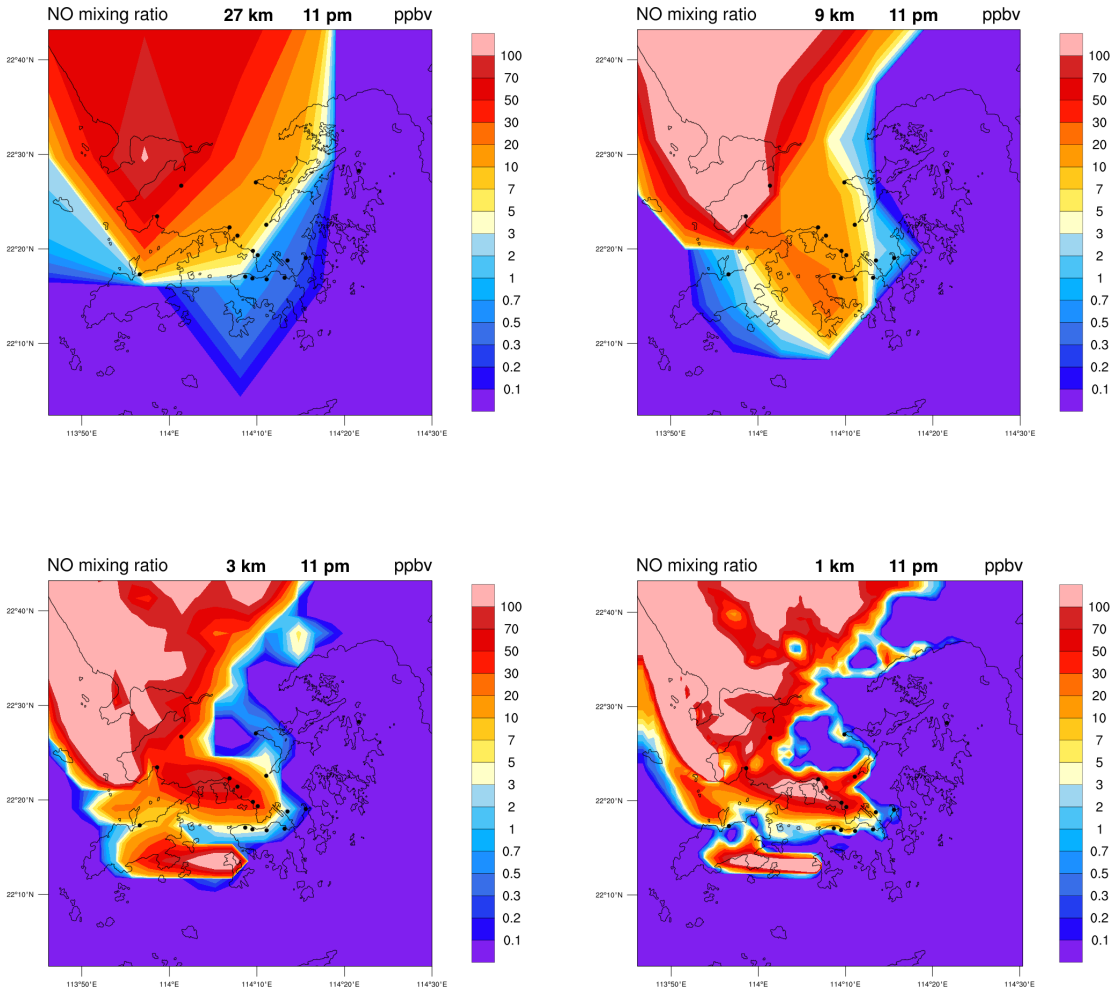

Figure A.2: The color map of NO surface mixing ratio at resolution of 27 km (top-left), 9 km (top-right), 3 km (bottom-left) and 1 km (bottom-right) in Domain d04 at 11 pm on 27$^{\text{th}}$ January 2017. Note that the contours of the NO mixing ratio are in logarithmic scale.

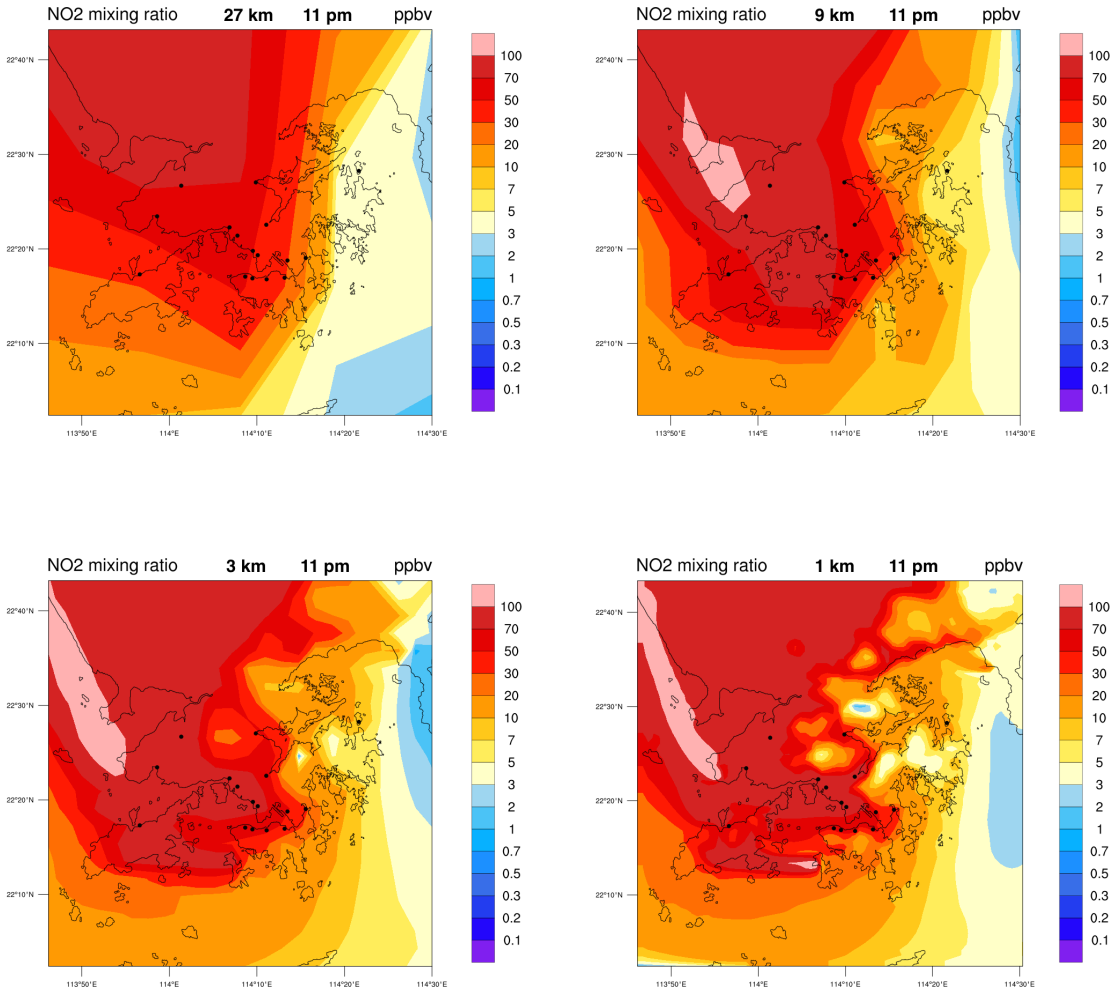

Figure A.3: The color map of NO_2 surface mixing ratio at resolution of 27 km (top-left), 9 km (top-right), 3 km (bottom-left) and 1 km (bottom-right) in Domain d04 at 11 pm on 27th January 2017. Note that the contours of the NO_2 mixing ratio are in logarithmic scale.

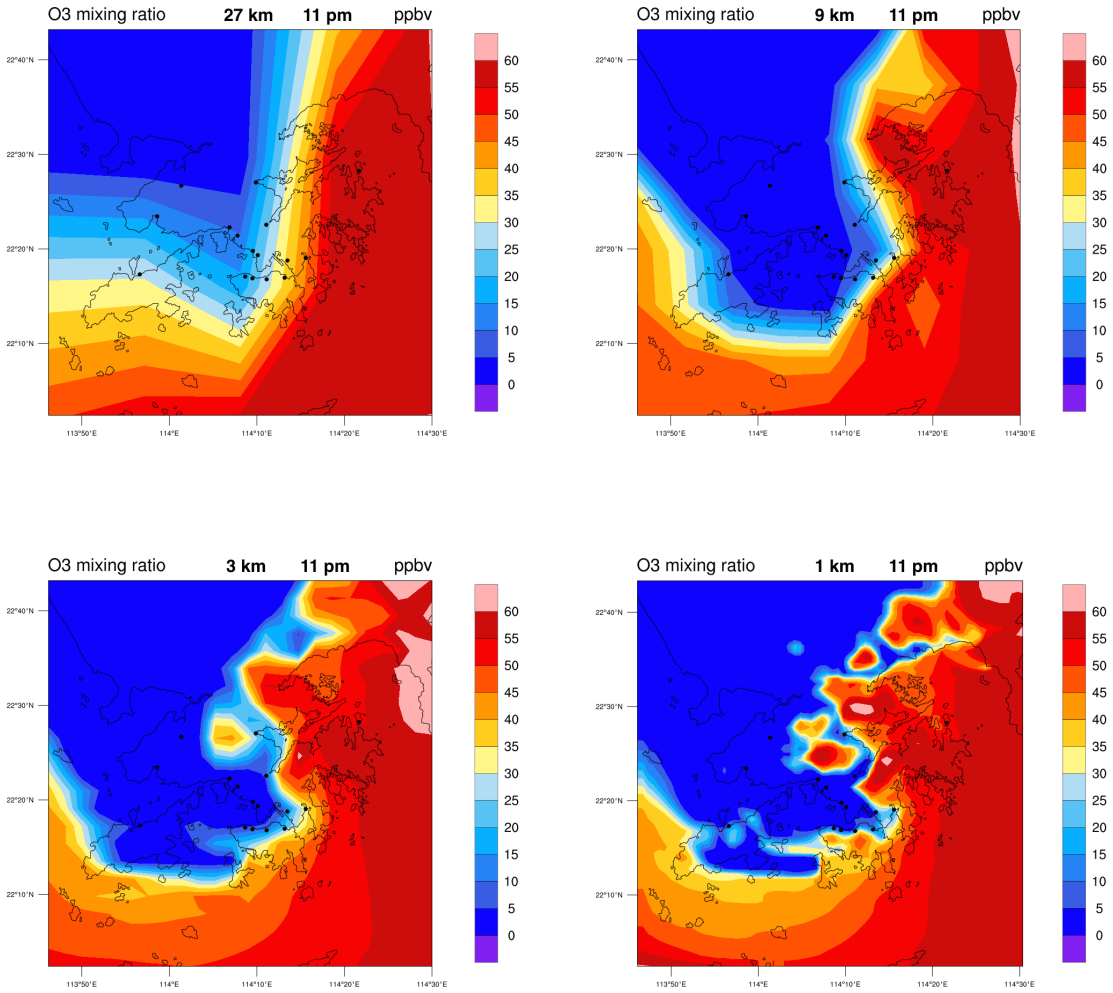

Figure A.4: The color map of O_3 surface mixing ratio at resolution of 27 km (top-left), 9 km (top-right), 3 km (bottom-left) and 1 km (bottom-right) in Domain d04 at 11 pm on 27th January 2017.

U (m s^{-1})	27-km	9-km	3-km	1-km
Mean	-3.3284	-3.2686	-2.9072	-2.8289
Median	-2.4461	-2.5489	-2.3466	-2.3280
Standard deviation	2.9255	2.7833	2.5261	2.4607
Maximum	2.6521	3.4281	3.8366	5.4934
Minimum	-12.4350	-12.3730	-12.2494	-12.2345

V (m s^{-1})	27-km	9-km	3-km	1-km
Mean	-2.2160	-2.0349	-1.8351	-1.7825
Median	-2.1555	-2.0021	-1.7724	-1.7108
Standard deviation	2.3223	2.2598	2.1765	2.1568
Maximum	3.6751	4.5038	4.6828	5.3041
Minimum	-10.7520	-11.1076	-10.8001	-12.7953

BL height (m)	27-km	9-km	3-km	1-km
Mean	430.0501	413.2439	398.3781	391.2053
Median	429.4047	422.9040	387.8741	376.6754
Standard deviation	267.8530	253.0949	255.9734	253.9113
Maximum	1501.4741	1518.5784	1526.4483	1622.0584
Minimum	0	0	0	0

T (°C)	27-km	9-km	3-km	1-km
Mean	17.7813	17.5659	17.4296	17.3672
Median	17.9270	17.8173	17.7480	17.7114
Standard deviation	2.0976	2.1779	2.3440	2.3992
Maximum	23.9470	23.9983	24.5111	24.3941
Minimum	9.3291	8.8314	8.0197	7.2408

Table A.2: General statistics of the meteorological variables at different resolutions over all the simulation time in January 2017.

U (m s^{-1})	27-km	9-km	3-km	1-km
Mean	-3.5800	-3.4049	-2.9955	-2.9090
Median	-2.6686	-2.6785	-2.3829	-2.3570
Standard deviation	2.6062	2.5018	2.2475	2.1821
Maximum	0.7983	1.8606	2.1468	2.8843
Minimum	-10.7444	-10.6576	-10.3984	-10.2811

V (m s^{-1})	27-km	9-km	3-km	1-km
Mean	-1.7892	-1.5368	-1.3060	-1.2363
Median	-1.9507	-1.7291	-1.4892	-1.4001
Standard deviation	2.0473	2.0095	1.8726	1.8581
Maximum	3.6751	4.5038	4.6828	4.7476
Minimum	-7.1084	-6.8953	-6.3593	-6.2187

BL height (m)	27-km	9-km	3-km	1-km
Mean	565.1754	531.1380	527.1436	521.0523
Median	538.2749	498.5362	492.1066	488.0930
Standard deviation	270.7518	251.1494	261.2925	258.3340
Maximum	1501.4741	1518.5784	1526.4483	1622.0584
Minimum	26.7564	26.4098	25.9472	25.6403

T (°C)	27-km	9-km	3-km	1-km
Mean	18.0896	17.9078	17.9413	17.9342
Median	17.9673	17.9277	18.0021	18.0257
Standard deviation	2.0510	1.9471	2.0765	2.1021
Maximum	23.9470	23.7657	23.9689	24.0108
Minimum	10.8565	10.1430	9.2157	8.8331

Wind direction(°)	27-km	9-km	3-km	1-km
Mean	65.7267	71.7417	74.4533	76.2907
Median	58.9790	62.5985	63.5754	65.1505
Standard deviation	39.0484	47.5806	52.0758	54.1590
Maximum	349.4326	359.2534	359.9754	359.9954
Minimum	0.8126	0.4154	0.1152	0.0041

Table A.3: General statistics of the meteorological variables at different resolutions over the daytime in January 2017.

U (m s^{-1})	27-km	9-km	3-km	1-km
Mean	-4.5633	-4.5642	-4.1197	-4.0023
Median	-3.6138	-3.9431	-3.5332	-3.4301
Standard deviation	3.1760	2.9381	2.6686	2.6018
Maximum	0.8945	0.5792	1.4948	2.0898
Minimum	-12.4350	-12.3730	-12.2494	-12.2345

V (m s^{-1})	27-km	9-km	3-km	1-km
Mean	-1.0666	-1.0426	-0.8673	-0.8835
Median	-0.9520	-0.9472	-0.8463	-0.8717
Standard deviation	1.8132	1.7402	1.6513	1.6459
Maximum	3.1596	4.1151	4.1132	5.3041
Minimum	-6.7277	-6.5074	-6.0629	-6.3577

BL height (m)	27-km	9-km	3-km	1-km
Mean	337.8073	337.0424	309.5324	301.4706
Median	337.8910	333.9608	280.8843	265.4619
Standard deviation	223.9229	217.4367	204.9224	200.6064
Maximum	915.9371	907.5319	876.5562	867.6135
Minimum	25.8608	25.7394	25.7290	25.7171

T (°C)	27-km	9-km	3-km	1-km
Mean	17.2774	16.8975	16.5821	16.4387
Median	17.6703	17.4662	17.2826	17.1647
Standard deviation	1.8103	1.9842	2.1229	2.1687
Maximum	21.7607	21.2940	21.6250	21.4642
Minimum	9.3291	8.9875	8.6860	7.3646

Wind direction(°)	27-km	9-km	3-km	1-km
Mean	85.2019	83.3600	84.2062	83.5040
Median	77.6932	77.3208	78.2052	77.4300
Standard deviation	39.7202	30.9296	32.1715	33.1144
Maximum	359.0695	357.0985	359.9638	359.9938
Minimum	4.3377	0.3848	0.7440	0.0066

Table A.4: General statistics of the meteorological variables at different resolutions over the nighttime in January 2017.

U (m s^{-1})	27-km	9-km	3-km	1-km
Mean	0.7871	0.8106	0.7395	0.7109
Median	1.1723	1.2849	1.2087	1.1962
Standard deviation	2.8240	2.7768	2.6144	2.5938
Maximum	7.9370	7.9314	7.6949	7.7048
Minimum	-6.7908	-6.6979	-6.6903	-7.4514

V (m s^{-1})	27-km	9-km	3-km	1-km
Mean	1.8581	1.7453	1.7136	1.6812
Median	1.9041	1.6919	1.6517	1.6253
Standard deviation	1.6895	1.6814	1.6417	1.6362
Maximum	6.5970	8.0676	8.1020	8.0606
Minimum	-2.8093	-2.9841	-4.8712	-7.7919

BL height (m)	27-km	9-km	3-km	1-km
Mean	449.9439	414.1591	418.2090	413.6932
Median	345.8975	332.4439	319.0197	313.9791
Standard deviation	393.5897	353.2595	361.4664	353.7976
Maximum	2122.8413	2123.4038	2148.4187	2261.8203
Minimum	0.0000	0.0000	0.0000	0.0000

T (°C)	27-km	9-km	3-km	1-km
Mean	30.6758	30.3914	30.5164	30.4975
Median	29.6060	29.5988	29.7706	29.8342
Standard deviation	2.2652	1.9350	1.9466	1.9022
Maximum	37.3592	36.8803	37.1354	37.0786
Minimum	28.3324	28.0116	26.2203	23.8926

Table A.5: General statistics of the meteorological variables at different resolutions over all the simulation time in July 2016

U (m s^{-1})	27-km	9-km	3-km	1-km
Mean	0.5910	0.5708	0.4798	0.4323
Median	0.6839	0.7359	0.6854	0.6209
Standard deviation	3.0318	2.9993	2.7991	2.7462
Maximum	7.9370	7.9314	7.6949	7.7048
Minimum	-5.5372	-5.5216	-5.5015	-6.3663

V (m s^{-1})	27-km	9-km	3-km	1-km
Mean 1.5795	1.4015	1.3621	1.2986	
Median	1.5644	1.3686	1.3261	1.2379
Standard deviation	1.5031	1.4667	1.4169	1.4168
Maximum	4.7725	5.6607	5.6573	6.1638
Minimum	-2.8093	-2.9841	-3.7419	-7.3173

BL height (m)	27-km	9-km	3-km	1-km
Mean	273.4735	250.0116	231.8154	220.2020
Median	247.6847	233.1097	201.7733	189.1690
Standard deviation	169.0472	159.7922	146.4578	142.1703
Maximum	787.6618	762.9449	758.1445	809.5045
Minimum	27.4953	27.4335	27.4457	27.3155

T (°C)	27-km	9-km	3-km	1-km
Mean	29.0867	28.7221	28.5637	28.4263
Median	29.1177	28.9682	28.8869	28.8001
Standard deviation	1.1053	1.1705	1.2957	1.3473
Maximum	33.6837	33.2810	33.3730	33.3421
Minimum	24.4225	23.9778	23.0146	21.0970

Wind direction(°)	27-km	9-km	3-km	1-km
Mean	188.5329	187.7471	186.9630	186.4017
Median	198.1346	200.9135	199.7467	199.0903
Standard deviation	62.3990	65.2547	65.0722	65.9830
Maximum	312.1699	304.6072	343.6091	359.8526
Minimum	59.7205	55.5681	44.7335	0.5745

Table A.6: General statistics of the meteorological variables at different resolutions over the nighttime in July 2016.

CO (ppbv)	27-km	9-km	3-km	1-km
Mean	506.8	531.2	568.5	569.0
Median	464.3	462.9	485.9	489.1
Standard deviation	242.2	307.0	334.9	335.9
Maximum	1596.8	2621.7	3056.1	3540.0
Minimum	190.2	184.6	185.7	183.7

NO	27-km	9-km	3-km	1-km
Mean	8.9	12.7	16.7	17.1
Median	8.9	12.7	16.7	17.1
Standard deviation	18.2	30.8	41.4	52.1
Maximum	128.5	534.1	1017.9	3115.6
Minimum	0	0	0	0

NO_2	27-km	9-km	3-km	1-km
Mean	22.0	23.0	25.6	25.2
Median	22.0	23.0	25.6	25.2
Standard deviation	22.4	23.8	25.0	25.1
Maximum	100.0	126.8	17.5	40.67
Minimum	0.5	0.3	0.3	0.4

O_3	27-km	9-km	3-km	1-km
Mean	34.8	34.7	32.7	33.4
Median	39.2	39.5	36.5	37.6
Standard deviation	20.7	21.4	21.7	21.3
Maximum	8.66	9.51	9.54	9.67
Minimum	0	0	0	0

Table A.7: General statistics of the mixing ratios of CO, NO, NO_2 and O_3 at different resolutions over all the simulation time in January 2017.

RO_2 species	Atomic composition
methylperoxy radical	CH_3O_2
hydroxyl ethene peroxyl radical	$HOCH_2CH_2O_2$
ethylperoxy radical	$C_2H_5O_2$
hydroxyl propene peroxy radicals	e.g., $CH_3CH(OO)CH_2OH$
propylperoxy radical	$C_3H_7O_2$
acetone peroxy radical	$CH_3COCH_2O_2$
lumped alkene peroxy radical	$CH_3CH(OH)CH(OO)CH_2$
lumped alkyl peroxy radical	$C_5H_{11}O_2$
methyl ethyl ketone peroxy radical	$CH_3COCH(OO)CH_3$
aromatic peroxy radical	$C_7H_9O_5$
peroxy radical derived from OH+Isoprene	e.g., $HOCH_2C(OO)CH_3CHCH_2$
terpene peroxl radical	$C_{10}H_{16}(OH)(OO)$
peroxy radical from NO_3+isoprene	$CH_2CHCCH_3OOCH_2ONO_2$
peroxy radical from OH+lumped unsaturated hydroxycarbonyl	e.g., $HOCH_2C(OO)CH_3CH(OH)CHO$

Table A.8: VOC species that contribute to ozone production in the MOZART scheme, which is used in the WRF-Chem simulations in this study (Emmons et al. 2010; Brasseur and Jacob 2017).

January 2017			
Resolution	HO_2−NO	RO_2−NO	Total
27 km	0.8091 (73.44%)	0.2925 (26.56%)	1.1016
9 km	0.8578 (73.73%)	0.3056 (26.27%)	1.1635
3 km	0.8570 (73.36%)	0.3112 (26.64%)	1.1682
1 km	0.9040 (73.39%)	0.3276 (26.60%)	1.2316
July 2016			
Resolution	HO_2−NO	RO_2−NO	Total
27 km	1.5486 (71.09%)	0.6296 (28.91%)	2.1782
9 km	1.4673 (70.68%)	0.6086 (29.32%)	2.0759
3 km	1.5121 (70.11%)	0.6446 (29.89%)	2.156826
1 km	1.7087 (69.99%)	0.7325 (30.01%)	2.4413

Table A.9: Corresponding ozone production rate contributed by HO_2 (Reaction 1.5) and RO_2 (Reaction 1.8) over all the simulation time in January 2017 and July 2016 in unit of ppbv hr^{-1}.

VOC species	Atomic composition
ethene	C_2H_4
propene	C_3H_6
methyl vinyl ketone (MVK)	$CH_2CHCOCH_3$
lumped monoterpenes	$C_{10}H_{16}$
isoprene	C_5H_8
methacrolein (MACR)	CH_2CCH_3CHO

Table A.10: VOC species that contribute to ozone loss by Reaction 1.13 in the MOZART scheme, which is used in the WRF-Chem simulations in this study (Emmons et al. 2010; Brasseur and Jacob 2017).

VOC species	Atomic composition
formaldehyde	CH_2O
propene	C_3H_6
acetaldehyde	CH_3CHO
peroxy radical from OH addition to MVK, MACR	e.g., $CH_3COCH(OO)CH_2OH$
peroxy radical derived from abstraction reaction of OH with MACR	$CH_2CCH_3CO_3$
lumped monoterpenes	$C_{10}H_{16}$
isoprene	C_5H_8
peroxy radical derived from OH+Isoprene	e.g., $HOCH_2C(OO)CH_3CHCH_2$
methylglyoxal	CH_3COCHO
peroxy radical from OH+HYDRALD	e.g., $HOCH_2C(OO)CH_3CH(OH)CHO$

Table A.11: VOC species that contribute to ozone loss by Reaction 1.20 in the MOZART scheme, which is used in the WRF-Chem simulations in this study (Emmons et al. 2010; Brasseur and Jacob 2017).

January 2017									
Resolution	$O^1(D)-H_2O$	O_3-OH	O_3-HO_2	O_3-VOC	$OH-NO_2$	RO_2-NO_2	NO_3-VOC	N_2O_5	Total
27 km	0.0742 (9.82%)	0.0176 (2.33%)	0.0202 (2.67%)	0.0101 (1.34%)	0.2499 (33.06%)	0.3696 (48.90%)	0.0136 (1.80%)	0.0002 (0.03%)	0.7558
9 km	0.0777 (10.00%)	0.0183 (2.36%)	0.0178 (2.29%)	0.0112 (1.44%)	0.2723 (35.02%)	0.3623 (46.61%)	0.0173 (2.22%)	0.0002 (0.03%)	0.7773
3 km	0.07617 (9.62%)	0.0170 (2.15%)	0.0168 (2.13%)	0.0131 (1.66%)	0.2855 (36.07%)	0.3552 (44.87%)	0.0273 (3.45%)	0.0002 (0.03%)	0.7916
1 km	0.0802 (9.81%)	0.0181 (2.21%)	0.0179 (2.19%)	0.0138 (1.69%)	0.2913 (35.62%)	0.3641 (44.51%)	0.0320 (3.92%)	0.0002 (0.03%)	0.8179
July 2016									
Resolution	$O^1(D)-H_2O$	O_3-OH	O_3-HO_2	O_3-VOC	$OH-NO_2$	RO_2-NO_2	NO_3-VOC	N_2O_5	Total
27 km	0.2763 (20.31%)	0.0393 (2.89%)	0.0305 (2.24%)	0.0118 (0.87%)	0.6142 (45.16%)	0.3515 (25.84%)	0.0361 (2.65%)	0.0001 (0.01%)	1.3601
9 km	0.2613 (20.40%)	0.0331 (2.58%)	0.0202 (1.57%)	0.0140 (1.09%)	0.6388 (49.86%)	0.2721 (21.24%)	0.0411 (3.21%)	0.0001 (0.01%)	1.2810
3 km	0.2616 (19.06%)	0.0306 (2.23%)	0.0206 (1.50%)	0.0177 (1.29%)	0.6650 (48.43%)	0.3219 (23.44%)	0.0550 (4.00%)	0.0001 (0.01%)	1.3729
1 km	0.2794 (18.17%)	0.0356 (2.31%)	0.0238 (1.54%)	0.0182 (1.18%)	0.7051 (45.85%)	0.4096 (26.64%)	0.0656 (4.26%)	0.0001 (0.01%)	1.5377

Table A.12: Corresponding ozone loss rate contributed by Reaction 1.10 ($O^1(D)-H_2O$), Reaction 1.11 (O_3-OH), Reaction 1.12 (O_3-HO_2), Reaction 1.13 (O_3-VOC), Reaction 1.18 ($OH-NO_2$), Reaction 1.19 (RO_2-NO_2), Reaction 1.20 and Reaction 1.17 (N_2O_5) over all the simulation time in January 2017 and July 2016 in unit of ppbv hr^{-1}.

*R*O2 species	Atomic composition
acetylperoxy radical	CH_3CHO
peroxy radical derived from abstraction reaction of OH with MACR	$CH_2CCH_3CO_3$

Table A.13: RO_2 species that contribute to ozone loss by Reaction 1.19 in the MOZART scheme, which is used in the WRF-Chem simulations in this study (Emmons et al. 2010; Brasseur and Jacob 2017).

Segregation coefficient	27-km	9-km	3-km	1-km
NO_X-O_3	-0.2931	-0.3431	-0.3512	-0.3540
NO-O_3	-0.4685	-0.4998	-0.4797	-0.4824
NO_2-O_3	-0.2660	-0.2909	-0.2911	-0.2865
NO-NO_2	1.3751	1.6533	1.3588	1.75310

Table A.14: Coefficients of segregation of NO, NO_2 and O_3 at the 4 different resolutions over all the simulation time in January 2017.

Segregation coefficient	27-km	9-km	3-km	1-km
NO_X-O_3	-0.1952	-0.2419	-0.2609	-0.2570
NO-O_3	-0.2882	-0.3743	-0.3807	-0.3795
NO_2-O_3	-0.1649	-0.1902	-0.1934	-0.1884
NO-NO_2	1.2695	1.6407	1.5400	1.7736

Table A.15: Coefficients of segregation of NO, NO_2 and O_3 at the 4 different resolutions over all the simulation time in January 2017 at daytime.

Segregation coefficient	27-km	9-km	3-km	1-km
NO_X-O_3	-0.4104	-0.4477	-0.4634	-0.4654
NO-O_3	-0.8194	-0.6993	-0.6703	-0.6555
NO_2-O_3	-0.3595	-0.3764	-0.3786	-0.3729
NO-NO_2	1.7964	1.4844	1.2086	1.4531

Table A.16: Coefficients of segregation of NO, NO_2 and O_3 at the 4 different resolutions over all the simulation time in January 2017 at nighttime.

Segregation coefficient	27-km	9-km	3-km	1-km
NO_X-O_3	-0.2279	-0.2783	-0.4285	-0.3132
NO-O_3	-0.4214	-0.4067	-0.5437	-0.4210
NO_2-O_3	-0.1824	-0.2312	-0.3479	-0.2364
NO-NO_2	0.9542	1.0101	0.9078	1.5900

Table A.17: Coefficients of segregation and correlations of NO, NO_2 and O_3 at the 4 different resolutions over all the simulation time in July 2016.

Segregation coefficient	27-km	9-km	3-km	1-km
NO_X-O_3	-0.1323	-0.1263	-0.1363	-0.1557
NO-O_3	-0.1954	-0.1861	-0.2005	-0.2315
NO_2-O_3	-0.0929	-0.0879	-0.0865	-0.0971
NO-NO_2	0.8972	0.8530	0.9252	1.3896

Table A.18: Coefficients of segregation and correlations of NO, NO_2 and O_3 at the 4 different resolutions over all the simulation time in July 2016 at daytime.

Segregation coefficient	27-km	9-km	3-km	1-km
NO_X-O_3	-0.4172	-0.5924	-0.9770	-0.6465
NO-O_3	-0.7335	-0.7886	-1.1429	-0.7886
NO_2-O_3	-0.3647	-0.5426	-0.8750	-0.5413
NO-NO_2	0.8359	0.5674	0.4471	0.7006

Table A.19: Coefficients of segregation and correlations of NO, NO_2 and O_3 at the 4 different resolutions over all the simulation time in July 2016 at nighttime.

Roadside					
CO	obs	27-km	9-km	3-km	1-km
Mean	781.97	416.08	451.59	432.63	431.93
σ	134.50	89.85	104.85	115.64	111.68
MB	-	-365.88	-330.38	-349.33	-350.04
NMB	-	-0.46	-0.42	-0.44	-0.44
MFB	-	-0.61	-0.54	-0.58	-0.58
r	-	0.39	0.32	0.22	0.19
NO	obs	27-km	9-km	3-km	1-km
Mean	87.87	5.84	9.85	7.69	8.02
σ	48.62	3.58	8.56	6.87	7.76
MB	-	-82.03	-78.03	-80.18	-79.85
NMB	-	-0.93	-0.87	-0.90	-0.90
MFB	-	-1.71	-1.55	-1.62	-1.60
r	-	0.39	0.24	0.10	-0.01
NO_2	obs	27-km	9-km	3-km	1-km
Mean	58.12	19.92	24.68	20.73	21.34
σ	15.24	7.39	11.52	10.01	11.09
MB	-	-38.20	-33.44	-37.39	-36.78
NMB	-	-0.66	-0.57	-0.64	-0.63
MFB	-	-0.99	-0.85	-0.97	-0.95
r	-	0.45	0.31	-0.01	-0.09
O_3	obs	27-km	9-km	3-km	1-km
Mean	14.11	37.55	33.13	36.84	37.18
σ	7.08	10.33	12.99	15.22	16.01
MB	-	23.45	19.03	22.74	23.07
NMB	-	1.74	1.50	1.70	1.71
MFB	-	0.95	0.76	0.81	0.80
r	-	0.52	0.44	0.40	0.35

Table A.20: Averaged Statistical metrics between the observed and modelled data of all the three roadside stations (Central, Causeway Bay, Mong Kok) of the chemical species CO, NO, NO_2 and O_3. The means of the modelled and observed data, the standard deviation of the modelled and observed data (σ) and the mean biases between the modelled and observed data (MB) are in units of ppbv. The normalised mean biases (NMB), the mean fractional biases (MFB), and the Pearson's correlation coefficients (r) are dimensionless.

Rural					
CO	obs	27-km	9-km	3-km	1-km
Mean	637.09	341.96	352.75	355.06	357.17
σ	66.57	71.82	79.11	79.43	87.21
MB	-	-295.13	-284.34	-282.03	-279.92
NMB	-	-0.46	-0.45	-0.44	-0.44
MFB	-	-0.61	-0.59	-0.58	-0.58
r	-	0.84	0.85	0.84	0.83
NO	obs	27-km	9-km	3-km	1-km
Mean	1.42	0.62	0.76	0.80	0.61
σ	0.54	0.49	0.61	0.71	0.48
MB	-	-0.80	-0.66	-0.62	-0.81
NMB	-	-0.56	-0.47	-0.44	-0.57
MFB	-	-0.87	-0.74	-0.69	-0.88
r	-	0.53	0.59	0.56	0.36
NO_2	obs	27-km	9-km	3-km	1-km
Mean	5.26	3.42	3.79	3.89	3.44
σ	1.43	2.33	2.06	2.11	2.64
MB	-	-1.84	-1.47	-1.37	-1.82
NMB	-	-0.34	-0.28	-0.25	-0.34
MFB	-	-0.50	-0.39	-0.35	-0.53
r	-	0.21	0.42	0.44	0.28
O_3	obs	27-km	9-km	3-km	1-km
Mean	53.91	52.91	52.74	52.49	51.94
σ	11.40	11.28	11.17	11.23	11.03
MB	-	-1.00	-1.16	-1.41	-1.97
NMB	-	-0.02	-0.02	-0.03	-0.04
MFB	-	-0.02	-0.02	-0.03	-0.04
r	-	0.90	0.90	0.88	0.86

Table A.21: Statistical metrics between the observed and modelled data of the Tap Mun Station. Similar description as Table A.20.

Tuen Mun					
CO	obs	27-km	9-km	3-km	1-km
Mean	691.72	704.31	746.36	760.41	725.49
σ	63.49	129.19	268.46	341.92	330.05
MB	-	12.59	54.64	68.70	33.78
NMB	-	0.02	0.08	0.10	0.05
MFB	-	0.01	0.02	0.01	-0.04
r	-	0.54	0.49	0.41	0.39
NO	obs	27-km	9-km	3-km	1-km
Mean	9.84	41.57	94.12	36.82	29.60
σ	7.93	20.78	63.71	38.35	34.16
MB	-	31.73	84.28	26.98	19.76
NMB	-	3.22	8.56	2.74	2.01
MFB	-	1.28	1.57	0.88	0.73
r	-	0.25	0.46	0.54	0.48
NO_2	obs	27-km	9-km	3-km	1-km
Mean	26.29	49.50	59.50	38.56	36.77
σ	7.39	11.29	11.40	15.13	13.82
MB	-	23.22	33.21	12.27	10.48
NMB	-	0.88	1.26	0.47	0.40
MFB	-	0.62	0.78	0.32	0.29
r	-	0.34	0.24	0.04	0.12
O_3	obs	27-km	9-km	3-km	1-km
Mean	32.34	14.27	9.29	21.75	23.34
σ	14.73	7.64	6.01	13.66	12.99
MB	-	-18.07	-23.04	-10.59	-9.00
NMB	-	-0.56	-0.71	-0.33	-0.28
MFB	-	-0.76	-1.13	-0.49	-0.39
r	-	0.38	0.30	0.39	0.43

Table A.22: Statistical metrics between the observed and modelled data of the Tuen Mun Station. Similar description as Table A.20.

New Town (East)					
CO	obs	27-km	9-km	3-km	1-km
Mean	NA	592.67	493.81	481.27	503.10
σ	NA	192.25	164.87	151.74	173.56
NO	obs	27-km	9-km	3-km	1-km
Mean	9.94	13.45	7.24	7.47	8.36
σ	8.56	14.84	9.44	9.05	10.91
MB	-	3.51	-2.71	-2.48	-1.58
NMB	-	0.40	-0.31	-0.22	-0.12
MFB	-	-0.04	-0.71	-0.50	-0.51
r	-	0.66	0.58	0.70	0.69
NO_2	obs	27-km	9-km	3-km	1-km
Mean	19.26	25.75	16.43	18.74	19.44
σ	8.56	13.11	11.34	11.22	12.79
MB	-	6.49	-2.83	-0.52	0.18
NMB	-	0.35	-0.16	-0.01	0.04
MFB	-	0.26	-0.28	-0.08	-0.09
r	-	0.69	0.66	0.71	0.67
O_3	obs	27-km	9-km	3-km	1-km
Mean	42.23	32.72	39.42	38.54	39.68
σ	16.21	16.37	16.76	16.82	18.41
MB	-	-9.50	-2.80	-3.69	-2.55
NMB	-	-0.22	-0.06	-0.09	-0.06
MFB	-	-0.33	-0.09	-0.11	-0.12
r	-	0.85	0.88	0.89	0.90

Table A.23: Averaged statistical metrics between the observed and modelled data of the New Town East Stations (Shatin and Tai Po). Similar description as Table A.20. Note that the biases and the Pearson's correlation coefficients of CO are not shown here as there are no observed data at both stations.

Tuen Mun			
CO	obs	MarcoPolo	MPlores
Mean	691.71	725.49	560.79
σ	63.49	330.05	243.07
MB	-	33.77	-130.92
NMB	-	0.05	-0.19
MFB	-	-0.04	-0.28
r	-	0.39	0.28
NO	obs	MarcoPolo	MPlores
Mean	9.84	29.60	19.52
σ	7.93	34.16	24.15
MB	-	19.76	9.68
NMB	-	2.01	0.98
MFB	-	0.73	0.36
r	-	0.48	0.55
NO_2	obs	MarcoPolo	MPlores
Mean	26.29	36.77	28.53
σ	7.39	13.82	14.29
MB	-	10.48	2.24
NMB	-	0.40	0.09
MFB	-	0.29	-0.01
r	-	0.12	0.01
O_3	obs	MarcoPolo	MPlores
Mean	32.34	23.34	29.53
σ	14.73	12.99	15.98
MB	-	-9.00	-2.81
NMB	-	-0.28	-0.09
MFB	-	-0.39	-0.18
r	-	0.43	0.51

Table A.24: Averaged Statistical metrics between the observed and modelled data in the MarcoPolo and MPlores runs of the Tuen Mun station of the chemical species CO, NO, NO_2 and O_3. Similar description as Table A.20.

New Town (East)			
CO	obs	MarcoPolo	MPlores
Mean	NA	487.57	382.40
σ	NA	132.77	96.87
NO	obs	MarcoPolo	MPlores
Mean	8.00	8.54	2.73
σ	7.11	8.70	2.29
MB	-	0.54	-5.27
NMB	-	0.07	-0.66
MFB	-	-0.12	-1.00
r	-	0.68	0.67
NO_2	obs	MarcoPolo	HTAPadj
Mean	17.51	22.21	11.84
σ	9.73	11.06	8.18
MB	-	4.70	-5.67
NMB	-	0.28	-0.32
MFB	-	0.26	-0.43
r	-	0.70	0.70
O_3	obs	MarcoPolo	HTAPadj
Mean	42.07	36.82	45.08
σ	15.16	16.76	15.30
MB	-	-5.24	3.02
NMB	-	-0.12	0.08
MFB	-	-0.21	0.09
r	-	0.87	0.88

Table A.25: Averaged statistical metrics between the observed and modelled data in the MarcoPolo and MPlores runs of the Shatin station of the chemical species CO, NO, NO_2 and O_3. Similar description as Table A.20.

Bibliography

Bruce Albrecht, Ming Fang, and Virendra Ghate. Exploring Stratocumulus Cloud-Top Entrainment Processes and Parameterizations by Using Doppler Cloud Radar Observations. *Journal of the Atmospheric Sciences*, 73(2):729–742, 2016. doi: 10.1175/JAS-D-15-0147.1. URL https://doi.org/10.1175/JAS-D-15-0147.1.

Saravanan Arunachalam, Andrew Holland, Bebhinn Do, and Michael Abraczinskas. A quantitative assessment of the influence of grid resolution on predictions of future-year air quality in North Carolina, USA. *Atmospheric Environment*, 40(26):5010–5026, 2006.

Ludovic Auger and Bernard Legras. Chemical segregation by heterogeneous emissions. *Atmospheric Environment*, 41(11):2303–2318, 2007.

Janet Barlow, Tyrone Dunbar, Eiko Nemitz, Curtis Wood, Martin Gallagher, Fay Davies, O'Connor E, and Roy Harrison. Boundary layer dynamics over London, UK, as observed using Doppler lidar. *Atmospheric Chemistry and Physics Discussions*, 10, 08 2010. doi: 10.5194/acpd-10-19901-2010.

Idir Bouarar, Katinka Petersen, Claire Granier, Ying Xie, Bas Mijling, A. van der Ronald, Michael Gauss, Matthieu Pommier, Mikhail Sofiev, Rostislav Kouznetsov, Natalia Sudarchikova, Lili Wang, Guangqiang Zhou, and Guy P. Brasseur. *Predicting Air Pollution in East Asia*, pages 387–403. Springer International Publishing, Cham, 2017. ISBN 978-3-319-59489-7. doi: 10.1007/978-3-319-59489-7_18. URL https://doi.org/10.1007/978-3-319-59489-7_18.

Guy Brasseur, John Joseph Orlando, Geoffrey Stuart Tyndall, et al. *Atmospheric chemistry and global change*. Oxford University Press, 1999.

Guy P Brasseur and Daniel J Jacob. *Modeling of Atmospheric Chemistry*. Cambridge University Press, 2017.

F. Brosse, M. Leriche, C. Mari, and F. Couvreux. LES study of the impact of moist thermals on the oxidative capacity of the atmosphere in southern West Africa. *Atmospheric Chemistry and Physics Discussions*, 2017:1–35, 2017. doi: 10.5194/acp-2017-969. URL https://www.atmos-chem-phys-discuss.net/acp-2017-969/.

Richard A Brost, Anthony C Delany, and Barry J Huebert. Numerical modeling of concentrations and fluxes of HNO_3, NH_3, and NH_4NO_3 near the surface. *Journal of Geophysical Research: Atmospheres*, 93(D6):7137–7152, 1988.

F. Chen and J. Dudhia. Coupling an Advanced Land Surface Hydrology Model with the Penn State NCAR MM5 Modeling System. Part I: Model Implementation and Sensitivity. *Monthly Weather Review*, 129:569, 2001. doi: 10.1175/1520-0493(2001)129⟨0569:CAALSH⟩2.0.CO;2.

Mian Chin, Paul Ginoux, Stefan Kinne, Omar Torres, Brent N Holben, Bryan N Duncan, Randall V Martin, Jennifer A Logan, Akiko Higurashi, and Teruyuki Nakajima. Tropospheric aerosol optical thickness from the GOCART model and comparisons with satellite and Sun photometer measurements. *Journal of the atmospheric sciences*, 59 (3):461–483, 2002.

Ming-Dah Chou, Max J Suarez, Chang-Hoi Ho, Michael MH Yan, and Kyu-Tae Lee. Parameterizations for cloud overlapping and shortwave single-scattering properties for use in general circulation and cloud ensemble models. *Journal of climate*, 11(2): 202–214, 1998.

Lynette J Clapp and Michael E Jenkin. Analysis of the relationship between ambient levels of O_3, NO_2 and NO as a function of NO_X in the UK. *Atmospheric Environment*, 35(36):6391–6405, 2001.

Daniel S Cohan, Yongtao Hu, and Armistead G Russell. Dependence of ozone sensitivity analysis on grid resolution. *Atmospheric Environment*, 40(1):126–135, 2006.

Gerhard Damköhler. Der Einfluss der Turbulenz auf die Flammengeschwindigkeit in Gasgemischen. *Zeitschrift für Elektrochemie und angewandte physikalische Chemie*, 46(11):601–626, 1940. ISSN 0005-9021. doi: 10.1002/bbpc.19400461102. URL `http://dx.doi.org/10.1002/bbpc.19400461102`.

P. V. Danckwerts. The definition and measurement of some characteristics of mixtures. *Applied Scientific Research, Section A*, 3(4):279–296, 1952. ISSN 1573-1987. doi: 10.1007/BF03184936. URL `http://dx.doi.org/10.1007/BF03184936`.

J Vilà-Guerau de Arellano, Alessandro Dosio, J-F Vinuesa, Albert AM Holtslag, and Stefano Galmarini. The dispersion of chemically reactive species in the atmospheric boundary layer. *Meteorology and Atmospheric Physics*, 87(1-3):23–38, 2004.

Jordi Vilà-Guerau de Arellano, Chiel C Van Heerwaarden, Bart JH Van Stratum, and Kees Van Den Dries. *Atmospheric boundary layer: Integrating air chemistry and land interactions*. Cambridge University Press, 2015.

James W. Deardorff. Convective Velocity and Temperature Scales for the Unstable Planetary Boundary Layer and for Rayleigh Convection. *Journal of the Atmospheric Sciences*, 27(8):1211–1213, 1970. doi: 10.1175/1520-0469(1970)027⟨1211:CVATSF⟩2.0.CO;2. URL `https://doi.org/10.1175/1520-0469(1970)027<1211:CVATSF>2.0.CO;2`.

Paul E Dimotakis. The mixing transition in turbulent flows. *Journal of Fluid Mechanics*, 409:69–98, 2000.

Anna Solvejg Dinger, Kerstin Stebel, Massimo Cassiani, Hamidreza Ardeshiri, Cirilo Bernardo, Arve Kylling, Soon-Young Park, Ignacio Pisso, Norbert Schmidbauer, Jan Henrik Wasseng, et al. Observation of turbulent dispersion of artificially released SO_2 puffs with UV cameras. 2018.

R Dlugi, M Berger, M Zelger, A Hofzumahaus, M Siese, F Holland, A Wisthaler, W Grabmer, A Hansel, R Koppmann, et al. Turbulent exchange and segregation of HO_X radicals and volatile organic compounds above a deciduous forest. *Atmospheric chemistry and physics*, 10(13):6215–6235, 2010.

R Dlugi, M Berger, M Zelger, A Hofzumahaus, F Rohrer, F Holland, K Lu, and G Kramm. The balances of mixing ratios and segregation intensity: a case study from the field (ECHO 2003). *Atmospheric chemistry and physics*, 14(18):10333–10362, 2014.

Coleman duP. Donaldson and Glenn R. Hilst. Effect of inhomogeneous mixing on atmospheric photochemical reactions. *Environmental Science & Technology*, 6(9):812–816, 1972. doi: 10.1021/es60068a004. URL `http://dx.doi.org/10.1021/es60068a004`.

CP Dullemond and HH Wang. Numerische Strömungsmechanik. University Lecture, 2009.

Dale R Durran. *Numerical methods for fluid dynamics: With applications to geophysics*, volume 32. Springer Science & Business Media, 2010.

Louisa K Emmons, Stacy Walters, Peter G Hess, Jean-François Lamarque, Gabriele G Pfister, David Fillmore, Claire Granier, A Guenther, Douglas Kinnison, Thomas Laepple, et al. Description and evaluation of the Model for Ozone and Related chemical Tracers, version 4 (MOZART-4). 2010.

Environment Bureau. A Clean Air Plan for Hong Kong. 2013.

JD Fast, WI Gustafson Jr, RC Easter, RA Zaveri, JC Barnard, EG Chapman, GA Grell, and SE Peckham. Evolution of ozone, particulates, and aerosol direct forcing in an

urban area using a new fully-coupled meteorology, chemistry, and aerosol model. *J. Geophys. Res*, 111(5):D21305, 2006.

Evgeni Fedorovich, Robert Conzemius, and Dmitrii Mironov. Convective Entrainment into a Shear-Free, Linearly Stratified Atmosphere: Bulk Models Reevaluated through Large Eddy Simulations. *Journal of the Atmospheric Sciences*, 61(3):281–295, 2004. doi: 10.1175/1520-0469(2004)061⟨0281:CEIASL⟩2.0.CO;2. URL `https://doi.org/10.1175/1520-0469(2004)061<0281:CEIASL>2.0.CO;2`.

J Flemming, A Inness, H Flentje, V Huijnen, P Moinat, MG Schultz, and O Stein. Coupling global chemistry transport models to ECMWFs integrated forecast system. Geoscientific Model Development, 2009.

J Flemming, V Huijnen, J Arteta, P Bechtold, A Beljaars, AM Blechschmidt, M Diamantakis, RJ Engelen, A Gaudel, A Inness, et al. Tropospheric chemistry in the Integrated Forecasting System of ECMWF. *Geoscientific model development*, 8(4): 975, 2015.

David Fowler, M Amann, F Anderson, M Ashmore, P Cox, M Depledge, D Derwent, P Grennfelt, N Hewitt, O Hov, et al. Ground-level ozone in the 21st century: future trends, impacts and policy implications. *Royal Society Science Policy Report*, 15(08), 2008.

SR Freitas, KM Longo, MF Alonso, M Pirre, V Marecal, G Grell, R Stockler, RF Mello, and M Sánchez Gácita. PREP-CHEM-SRC-1.0: a preprocessor of trace gas and aerosol emission fields for regional and global atmospheric chemistry models. *Geoscientific Model Development*, 4(2):419, 2011.

S Galmarini, J Vilà-Guerau De Arellano, and PG Duynkerke. Scaling the turbulent transport of chemical compounds in the surface layer under neutral and stratified conditions. *Quarterly Journal of the Royal Meteorological Society*, 123(537):223–242, 1997.

L Ganzeveld, G Eerdekens, G Feig, H Fischer, H Harder, R Königstedt, Dagmar Kubistin, M Martinez, FX Meixner, HA Scheeren, et al. Surface and boundary layer exchanges of volatile organic compounds, nitrogen oxides and ozone during the GABRIEL campaign. *Atmospheric Chemistry and Physics*, 8(20):6223–6243, 2008.

W. Gao and M. L. Wesely. Numerical modeling of the turbulent fluxes of chemically reactive trace gases in the atmospheric boundary layer. *Journal of Applied Meteorology*, 33 (7):835–847, 1994. doi: 10.1175/1520-0450(1994)033⟨0835:NMOTTF⟩2.0.CO;2. URL `https://doi.org/10.1175/1520-0450(1994)033<0835:NMOTTF>2.0.CO;2`.

Jade Rachele Garcia and Juan Pedro Mellado. The two-layer structure of the entrainment zone in the convective boundary layer. *Journal of the Atmospheric Sciences*, 71 (6):1935–1955, 2014.

Andreas Geyer and Jochen Stutz. The vertical structure of $OH-HO_2-RO_2$ chemistry in the nocturnal boundary layer : A one-dimensional model study. 2004.

Paul Ginoux, Mian Chin, Ina Tegen, Joseph M Prospero, Brent Holben, Oleg Dubovik, and Shian-Jiann Lin. Sources and distributions of dust aerosols simulated with the GOCART model. *Journal of Geophysical Research: Atmospheres*, 106(D17):20255–20273, 2001.

Georg A Grell and Saulo R Freitas. A scale and aerosol aware stochastic convective parameterization for weather and air quality modeling. *Atmospheric Chemistry & Physics Discussions*, 13(9), 2013.

Georg A Grell, Steven E Peckham, Rainer Schmitz, Stuart A McKeen, Gregory Frost, William C Skamarock, and Brian Eder. Fully coupled 'online" chemistry within the wrf model. *Atmospheric Environment*, 39(37):6957–6975, 2005.

Volker Grewe, Katrin Dahlmann, Sigrun Matthes, and Wolfgang Steinbrecht. Attributing ozone to NO_X emissions: Implications for climate mitigation measures. *Atmospheric environment*, 59:102–107, 2012.

A Guenther, T Karl, Pedro Harley, C Wiedinmyer, PI Palmer, and C Geron. Estimates of global terrestrial isoprene emissions using MEGAN (Model of Emissions of Gases and Aerosols from Nature). *Atmospheric Chemistry and Physics*, 6(11):3181–3210, 2006.

Neil Harris, Robert D Hudson, and Celine Phillips. *Assessment of trends in the vertical distribution of ozone*. SPARC, 1998.

HKEPD Air Science Group. Air quality in Hong Kong 2016. (EPD/TR 1/17), 2016.

Song-You Hong, Yign Noh, and Jimy Dudhia. A new vertical diffusion package with an explicit treatment of entrainment processes. *Monthly weather review*, 134(9):2318–2341, 2006.

H. Hooyberghs, N. Veldeman, and B. Maiheu. Monitoring and Assessment of Regional air quality in China using space Observations. *Deliverables*, 2016.

Antje Inness, A-M Blechschmidt, I Bouarar, S Chabrillat, M Crepulja, RJ Engelen, H Eskes, J Flemming, A Gaudel, F Hendrick, et al. Data assimilation of satellite-retrieved ozone, carbon monoxide and nitrogen dioxide with ECMWF's Composition-IFS. *Atmospheric chemistry and physics*, 15(9):5275–5303, 2015.

Daniel Jacob. *Introduction to atmospheric chemistry*. Princeton University Press, 1999.

Ji-Cheng Carey Jang, Harvey E Jeffries, Daewon Byun, and Jonathan E Pleim. Sensitivity of ozone to model grid resolution—I. Application of high-resolution regional acid deposition model. *Atmospheric Environment*, 29(21):3085–3100, 1995.

G Janssens-Maenhout, M Crippa, D Guizzardi, F Dentener, M Muntean, G Pouliot, T Keating, Q Zhang, J Kurokawa, R Wankmüller, et al. HTAP_v2: a mosaic of regional and global emission gridmaps for 2008 and 2010 to study hemispheric transport of air pollution. *Atmospheric Chemistry & Physics Discussions*, 15(8), 2015.

David Johnson and George Marston. The gas-phase ozonolysis of unsaturated volatile organic compounds in the troposphere. *Chemical Society Reviews*, 37(4):699–716, 2008.

Prakash Karamchandani, Lynne Santos, Ian Sykes, Yang Zhang, Cathryn Tonne, and Christian Seigneur. Development and evaluation of a state-of-the-science reactive plume model. *Environmental science & technology*, 34(5):870–880, 2000.

S.-W. Kim, M. C. Barth, and M. Trainer. Impact of turbulent mixing on isoprene chemistry. *Geophysical Research Letters*, 43(14):7701–7708, 2016. ISSN 1944-8007. doi: 10.1002/2016GL069752. URL `http://dx.doi.org/10.1002/2016GL069752`. 2016GL069752.

Maarten C Krol, M Jeroen Molemaker, and J de Vilu-Guerau. Effects of turbulence and heterogeneous emissions on photochemically active species in the convective boundary layer. *Journal of geophysical research*, 105:6871–6884, 2000.

Friderike Kuik, Axel Lauer, Galina Churkina, Hugo AC Denier van der Gon, Daniel Fenner, Kathleen A Mar, and Tim M Butler. Air quality modelling in the Berlin-Brandenburg region using WRF-Chem v3. 7.1: sensitivity to resolution of model grid and input data. *Geoscientific Model Development*, 9(12):4339, 2016.

PA Leighton. Photochemistry of Air Pollution (Academic, New York, 1961). *Google Scholar*, pages 235–53, 1960.

D. H. Lenschow, D. Gurarie, and E. G. Patton. Modeling the diurnal cycle of conserved and reactive species in the convective boundary layer using SOMCRUS. *Geoscientific Model Development*, 9(3):979–996, 2016a. doi: 10.5194/gmd-9-979-2016. URL `https://www.geosci-model-dev.net/9/979/2016/`.

Donald H Lenschow, David Gurarie, and Edward G Patton. Modeling the diurnal cycle of conserved and reactive species in the convective boundary layer using SOMCRUS. *Geoscientific Model Development*, 9(3):979–996, 2016b.

Dan Li, Elie Bou-Zeid, Michael Barlage, Fei Chen, and James A Smith. Development and evaluation of a mosaic approach in the WRF-Noah framework. *Journal of Geophysical Research: Atmospheres*, 118(21):11–918, 2013.

Meng Li, Qiang Zhang, Jun-ichi Kurokawa, Jung-Hun Woo, Kebin He, Zifeng Lu, Toshimasa Ohara, Yu Song, David G Streets, Gregory R Carmichael, et al. MIX: a mosaic Asian anthropogenic emission inventory under the international collaboration framework of the MICS-Asia and HTAP. *Atmospheric Chemistry and Physics*, 17(2):935, 2017.

Xian-Xiang Li, Chun-Ho Liu, and Dennis Y.C. Leung. Numerical investigation of pollutant transport characteristics inside deep urban street canyons. *Atmospheric Environment*, 43(15):2410 – 2418, 2009. ISSN 1352-2310. doi: https://doi.org/10.1016/j.atmosenv.2009.02.022. URL `http://www.sciencedirect.com/science/article/pii/S1352231009001198`.

Yang Li, Mary C Barth, Gao Chen, Edward G Patton, Si-Wan Kim, Armin Wisthaler, Tomas Mikoviny, Alan Fried, Richard Clark, and Allison L Steiner. Large-eddy simulation of biogenic VOC chemistry during the DISCOVER-AQ 2011 campaign. *Journal of Geophysical Research: Atmospheres*, 121(13):8083–8105, 2016.

Douglas K Lilly. Models of cloud-topped mixed layers under a strong inversion. *Quarterly Journal of the Royal Meteorological Society*, 94(401):292–309, 1968.

Fei Liu, Qiang Zhang, Bo Zheng, Dan Tong, Liu Yan, Yixuan Zheng, Kebin He, et al. Recent reduction in NO_X emissions over China: synthesis of satellite observations and emission inventories. *Environmental Research Letters*, 11(11):114002, 2016.

SC Liu, M Trainer, FC Fehsenfeld, DD Parrish, EJ Williams, D Wo Fahey, G Hübler, and P Co Murphy. Ozone production in the rural troposphere and the implications for regional and global ozone distributions. *Journal of Geophysical Research: Atmospheres*, 92(D4):4191–4207, 1987.

Jennifer A Logan, Michael J Prather, Steven C Wofsy, and Michael B McElroy. Tropospheric chemistry: A global perspective. *Journal of Geophysical Research: Oceans*, 86 (C8):7210–7254, 1981.

Neveen Mansour and Alan Wray. Decay of Isotropic Turbulence at Low Reynolds Number. *Physics of Fluids*, 6, 03 1994. doi: 10.1063/1.868319.

Nicolás A Mazzeo, Laura E Venegas, and Hipólito Choren. Analysis of NO, NO_2, O_3 and NO_X concentrations measured at a green area of Buenos Aires City during wintertime. *Atmospheric Environment*, 39(17):3055–3068, 2005.

Juan-Pedro Mellado, CS Bretherton, Bjorn Stevens, and MC Wyant. DNS and LES for simulating stratocumulus: Better together. *Journal of Advances in Modeling Earth Systems*, 2018.

Eli J Mlawer, Steven J Taubman, Patrick D Brown, Michael J Iacono, and Shepard A Clough. Radiative transfer for inhomogeneous atmospheres: RRTM, a validated correlated-k model for the longwave. *Journal of Geophysical Research: Atmospheres*, 102(D14):16663–16682, 1997.

Parviz Moin and Krishnan Mahesh. Direct numerical simulation: a tool in turbulence research. *Annual review of fluid mechanics*, 30(1):539–578, 1998.

Andreĭ Monin. *Statistical fluid mechanics, volume II: mechanics of turbulence*.

Paul S Monks. Gas-phase radical chemistry in the troposphere. *Chemical Society Reviews*, 34(5):376–395, 2005.

Paul Steven Monks, AT Archibald, Augustin Colette, O Cooper, M Coyle, R Derwent, D Fowler, Claire Granier, Kathy S Law, GE Mills, et al. Tropospheric ozone and its precursors from the urban to the global scale from air quality to short-lived climate forcer. *Atmospheric Chemistry and Physics*, 15(15):8889–8973, 2015.

A. Montornes, Cassom P., G. Lizcano, and B. Kosovic. WRF-LES in 250+ real sites: Learning and Challenges. Presented as 18th Annual WRF User's Workshop in Colorado, USA, 2017.

NCEP GFS. 0.25 Degree Global Forecast Grids Historical Archive, 2015. URL `https://doi.org/10.5065/D65D8PWK`.

Timothy R Oke. *Urban environments*. McGill–Queens University Press, 1997.

S. Onomura, C.S.B. Grimmond, F. Lindberg, B. Holmer, and S. Thorsson. Meteorological forcing data for urban outdoor thermal comfort models from a coupled convective boundary layer and surface energy balance scheme. *Urban Climate*, 11:1 – 23, 2015. ISSN 2212-0955. doi: https://doi.org/10.1016/j.uclim.2014.11.001. URL `http://www.sciencedirect.com/science/article/pii/S2212095514000856`.

World Health Organization et al. Air quality guidelines - global update 2005. 2005.

Paolo Orlandi. *Fluid flow phenomena: a numerical toolkit*, volume 55. Springer Science & Business Media, 2012.

HG Ouwersloot, J Vilà-Guerau de Arellano, CC van Heerwaarden, LN Ganzeveld, MC Krol, and J Lelieveld. On the segregation of chemical species in a clear boundary

layer over heterogeneous land surfaces. *Atmospheric chemistry and physics*, 11(20): 10681–10704, 2011.

Arthur C Petersen and Albert AM Holtslag. A first-order closure for covariances and fluxes of reactive species in the convective boundary layer. *Journal of Applied Meteorology*, 38(12):1758–1776, 1999.

GG Pfister, Stacy Walters, J-F Lamarque, J Fast, MC Barth, John Wong, James Done, Greg Holland, and CL Bruyère. Projections of future summertime ozone over the US. *Journal of Geophysical Research: Atmospheres*, 119(9):5559–5582, 2014.

Ashley Queen and Yang Zhang. Examining the sensitivity of MM5–CMAQ predictions to explicit microphysics schemes and horizontal grid resolutions, Part III—The impact of horizontal grid resolution. *Atmospheric Environment*, 42(16):3869–3881, 2008.

P. Rekacewicz. Strategic Plan for the U.S. Climate Change Science Program, 2003. URL `http://www.climatescience.gov/Library/stratplan2003/`.

James M Roberts. The atmospheric chemistry of organic nitrates. *Atmospheric Environment. Part A. General Topics*, 24(2):243–287, 1990.

Martijn Schaap, Cornelis Cuvelier, Carlijn Hendriks, Bertrand Bessagnet, José M Baldasano, Augustin Colette, Philippe Thunis, D Karam, Hilde Fagerli, Arno Graff, et al. Performance of European chemistry transport models as function of horizontal resolution. *Atmospheric Environment*, 112:90–105, 2015.

Ulrich Schumann. Large-eddy simulation of turbulent diffusion with chemical reactions in the convective boundary layer. *Atmospheric Environment (1967)*, 23(8):1713–1727, 1989.

C Seigneur and M Moran. Chemical transport models. *Particulate Matter Science for Policy Makers*, pages 283–323, 2004.

John H Seinfeld and Spyros N Pandis. *Atmospheric chemistry and physics: from air pollution to climate change*. John Wiley & Sons, 2012.

W.C. Skamarock, J Klemp, Jimy Dudhia, D.O. Gill, Dale Barker, W Wang, and J.G. Powers. A Description of the Advanced Research WRF Version 3. 27:3–27, 01 2008.

Fei Song, Jin Young Shin, Rafael JusinoAtresino, and Yuan Gao. Relationships among the springtime groundlevel NO_X, O_3 and NO_3 in the vicinity of highways in the US East Coast. *Atmospheric Pollution Research*, 2(3):374 – 383, 2011. ISSN 1309-1042. doi: https://doi.org/10.5094/APR.2011.042. URL `http://www.sciencedirect.com/science/article/pii/S130910421530492X`.

J. Stavrakou, J Mueller, and M. Bauwens. Monitoring and Assessment of Regional air quality in China using space Observations. 2016.

Douw G Steyn. *Introduction to Atmospheric Modelling*. Cambridge University Press, 2015.

Roland B Stull. *An Introduction to Boundary Layer Meteorology*, volume 13. Springer Science & Business Media, 2012.

Peter P Sullivan and Edward G Patton. The effect of mesh resolution on convective boundary layer statistics and structures generated by large-eddy simulation. *Journal of the Atmospheric Sciences*, 68(10):2395–2415, 2011.

Jiani Tan, Yan Zhang, Weicun Ma, Qi Yu, Jian Wang, and Limin Chen. Impact of spatial resolution on air quality simulation: A case study in a highly industrialized area in Shanghai, China. *Atmospheric Pollution Research*, 6(2):322–333, 2015.

Hendrik Tennekes, John Leask Lumley, JL Lumley, et al. *A first course in turbulence*. MIT press, 1972.

Gregory Thompson, Roy M Rasmussen, and Kevin Manning. Explicit forecasts of winter precipitation using an improved bulk microphysics scheme. Part I: Description and sensitivity analysis. *Monthly Weather Review*, 132(2):519–542, 2004.

Gregory Thompson, Paul R Field, Roy M Rasmussen, and William D Hall. Explicit forecasts of winter precipitation using an improved bulk microphysics scheme. Part II: Implementation of a new snow parameterization. *Monthly Weather Review*, 136(12): 5095–5115, 2008.

X Tie, G Brasseur, and Z Ying. Impact of model resolution on chemical ozone formation in Mexico City: application of the WRF-Chem model. *Atmospheric Chemistry and Physics*, 10(18):8983–8995, 2010.

H. L. Toor. Turbulent Mixing of Two Species with and without Chemical Reactions. *Industrial & Engineering Chemistry Fundamentals*, 8(4):655–659, 1969. doi: 10.1021/i160032a009. URL `http://dx.doi.org/10.1021/i160032a009`.

Myrto Valari and Laurent Menut. Does an increase in air quality models' resolution bring surface ozone concentrations closer to reality? *Journal of Atmospheric and Oceanic Technology*, 25(11):1955–1968, 2008.

Myrto Valari and Laurent Menut. Transferring the heterogeneity of surface emissions to variability in pollutant concentrations over urban areas through a chemistry-transport model. *Atmospheric Environment*, 44(27):3229–3238, 2010.

Chiel C Van Heerwaarden, Juan Pedro Mellado, and Alberto De Lozar. Scaling laws for the heterogeneously heated free convective boundary layer. *Journal of the Atmospheric Sciences*, 71(11):3975–4000, 2014.

GHL Verver, H Van Dop, and AAM Holtslag. Turbulent mixing of reactive gases in the convective boundary layer. *Boundary-Layer Meteorology*, 85(2):197–222, 1997.

J Vilà-Guerau de Arellano, S-W Kim, MC Barth, and EG Patton. Transport and chemical transformations influenced by shallow cumulus over land. *Atmospheric Chemistry and Physics*, 5(12):3219–3231, 2005.

J Vilà-Guerau de Arellano, K Dries, and D Pino. On inferring isoprene emission surface flux from atmospheric boundary layer concentration measurements. *Atmospheric Chemistry and Physics*, 9(11):3629–3640, 2009.

J-F Vinuesa and J Vilà-Guerau de Arellano. Introducing effective reaction rates to account for the inefficient mixing of the convective boundary layer. *Atmospheric Environment*, 39(3):445–461, 2005.

J-F Vinuesa and F Porté-Agel. A dynamic similarity subgrid model for chemical transformations in large-eddy simulation of the atmospheric boundary layer. *Geophysical research letters*, 32(3), 2005.

Jean-François Vinuesa and Fernando Porté-Agel. Dynamic models for the subgrid-scale mixing of reactants in atmospheric turbulent reacting flows. *Journal of the Atmospheric Sciences*, 65(5):1692–1699, 2008.

Jean-FrannÇois Vinuesa and Jordi Vilà-Guerau de Arellano. Fluxes and (co-) variances of reacting scalars in the convective boundary layer. *Tellus B*, 55(4):935–949, 2003.

T Wang, Vincent T.F Cheung, K.S Lam, G.L Kok, and J.M Harris. The characteristics of ozone and related compounds in the boundary layer of the South China coast: temporal and vertical variations during autumn season. *Atmospheric Environment*, 35(15):2735 – 2746, 2001. ISSN 1352-2310. doi: https://doi.org/10.1016/S1352-2310(00)00411-8. URL `http://www.sciencedirect.com/science/article/pii/S1352231000004118`.

Tao Wang, Likun Xue, Peter Brimblecombe, Yun Fat Lam, Li Li, and Li Zhang. Ozone pollution in China: A review of concentrations, meteorological influences, chemical precursors, and effects. *Science of the Total Environment*, 575:1582–1596, 2017.

Christine Wiedinmyer, Robert J Yokelson, and Brian K Gullett. Global emissions of trace gases, particulate matter, and hazardous air pollutants from open burning of domestic waste. *Environmental science & technology*, 48(16):9523–9530, 2014.

Cort J. Willmott, Scott M. Robeson, and Kenji Matsuura. A refined index of model performance. *International Journal of Climatology*, 32(13):2088–2094. doi: 10.1002/joc.2419. URL `https://rmets.onlinelibrary.wiley.com/doi/abs/10.1002/joc.2419`.

Min Xie, Kuanguang Zhu, Tijian Wang, Pulong Chen, Yong Han, Shu Li, Bingliang Zhuang, and Lei Shu. Temporal characterization and regional contribution to O_3 and NO_X at an urban and a suburban site in Nanjing, China. *Science of the Total Environment*, 551:533–545, 2016.

Karen Yu, Daniel J Jacob, Jenny A Fisher, Patrick S Kim, Eloise A Marais, Christopher C Miller, Katherine R Travis, Lei Zhu, Robert M Yantosca, Melissa P Sulprizio, et al. Sensitivity to grid resolution in the ability of a chemical transport model to simulate observed oxidant chemistry under high-isoprene conditions. *Atmospheric Chemistry and Physics*, 16(7):4369–4378, 2016.

Rahul A Zaveri, Richard C Easter, Jerome D Fast, and Leonard K Peters. Model for simulating aerosol interactions and chemistry (MOSAIC). *Journal of Geophysical Research: Atmospheres*, 113(D13), 2008.

S Zilitinkevich, A Grachev, and JCR Hunt. Surface frictional processes and non-local heat/mass transfer in the shear-free convective boundary layer. In *Buoyant convection in geophysical flows*, pages 83–113. Springer, 1998.

Denis Zyryanov, Gilles Foret, Maxime Eremenko, Matthias Beekmann, J-P Cammas, Massimo D'Isidoro, H Elbern, Johannes Flemming, E Friese, I Kioutsioutkis, et al. 3-D evaluation of tropospheric ozone simulations by an ensemble of regional Chemistry Transport Model. *Atmospheric chemistry and physics*, 12(7):3219–3240, 2012.

Declaration

Versicherung an Eides statt

Declaration of oath

Hiermit versichere ich an Eides statt, dass ich die vorliegende Dissertation mit dem Titel:

"Atmospheric Chemistry Reactions in a Turbulent Flow: Application to an Urban Environment" selbstständig verfasst und keine anderen als die angegebenen Hilfsmittel insbesondere keine im Quellenverzeichnis nicht benannten Internet-Quellen benutzt habe. Alle Stellen, die wörtlich oder sinngemäß aus Veröffentlichungen entnommen wurden, sind als solche kenntlich gemacht. Ich versichere weiterhin, dass ich die Dissertation oder Teile davon vorher weder im In- noch im Ausland in einem anderen Prüfungsverfahren eingereicht habe und die eingereichte schriftliche Fassung der auf dem elektronischen Speichermedium entspricht.

I hereby assure on oath that I am completing this dissertation with the Title: "Atmospheric Chemistry Reactions in a Turbulent Flow: Application to an Urban Environment" independently written and no other than the specified aids - especially none in the bibliography named Internet sources - used. All bodies that literally or are taken from publications, are identified as such made. I further assure that I have the dissertation or parts of it neither at home nor abroad in another examination procedure submitted and the submitted written version of the submitted on the corresponds to electronic storage medium.

Hamburg, 06.02.2019

Wing Yi Li

Hinweis / Reference

Die gesamten Veröffentlichungen in der Publikationsreihe des MPI-M
„Berichte zur Erdsystemforschung / Reports on Earth System Science“,
ISSN 1614-1199

sind über die Internetseiten des Max-Planck-Instituts für Meteorologie erhältlich:
http://www.mpimet.mpg.de/wissenschaft/publikationen.html

All the publications in the series of the MPI -M
„Berichte zur Erdsystemforschung / Reports on Earth System Science“,
ISSN 1614-1199

are available on the website of the Max Planck Institute for Meteorology:
http://www.mpimet.mpg.de/wissenschaft/publikationen.html